

Contrails

**RESEARCH ON ELASTOHYDRODYNAMIC
LUBRICATION OF HIGH SPEED
ROLLING - SLIDING CONTACTS**

Richard Smith
Jed Walowit
Pradeep Gupta
John McGrew

FOREWORD

This report was prepared by Mechanical Technology Incorporated, 968 Albany-Shaker Road, Latham, New York under USAF Contract No. F33615-69-C-1305. The contract was initiated under Project No. 3048 Task No. 304806. The work was administered under the direction of the Air Force Aero Propulsion Laboratory, with Mr. John Jenkins and Mr. M. R. Chasman acting as project engineers.

This report covers work conducted from 1 February 1971 - 1 February 1972.

Publication of this report does not constitute Air Force approval of the report's findings or conclusions. It is published only for the exchange and stimulation of ideas.



HOWARD F. JONES, CHIEF
Lubrication Branch
Fuels and Lubrication Division

ABSTRACT

The rolling disc apparatus that was built during Phase II of this research program has been used to obtain traction measurements for a MIL-L-7808 oil. A full matrix of data covering a range of loads, speeds, and temperatures are presented along with analytical correlation which reasonably describes the data over these parameters. Attempts have been made to measure film thickness with optical, capacitance, and X-ray measuring techniques. Optical measurements appear to be in reasonably good agreement with isothermal theory. Capacitance measurements obtained at higher loads and speeds indicate more significant load variations than existing theory would predict.

The partial elastohydrodynamic regime has been studied analytically and experimentally. Electrical continuity and resistance data have been obtained and comparisons between measured electrical resistance and predictions obtained with the asperity interactions analysis put forth in Task 2 have been obtained.

Contrails

Contrails

TABLE OF CONTENTS

	<u>Page</u>
I. INTRODUCTION _____	1
II. TRACTION DATA AND ANALYSIS _____	3
1. TEST DATA _____	3
2. ANALYSES OF TRACTION DATA _____	13
a. Film Thickness Predictions _____	13
b. Traction Predictions _____	22
III. CAPACITANCE FILM THICKNESS MEASUREMENT AND ANALYSIS _____	29
1. EXPERIMENTAL SETUP AND PRELIMINARY CHECK WITH ANALYSIS _____	30
2. ANALYTICAL ASSUMPTIONS _____	36
3. DIELECTRIC PRESSURIZATION AND CALIBRATION CURVES _____	36
4. TEST DATA _____	38
IV. OPTICAL FILM THICKNESS MEASUREMENT AND ANALYSIS _____	47
1. TEST SETUP _____	47
2. OPTICAL DISTORTION CORRECTION OF ELLIPTICAL BANDS _____	49
3. TEST DATA WITH ANALYTICAL EXPECTATIONS _____	56
V. X-RAY FILM THICKNESS MEASUREMENT _____	71
VI. ASPERITY INTERACTION AND PARTIAL ELASTOHYDRODYNAMICS _____	81
1. TIME AVERAGED RESISTANCE VERSUS SPEED _____	84
2. SURFACE TOPOGRAPHY _____	84
3. ASPERITY LOAD SHARING _____	94
4. ELECTRICAL CONTACT RESISTANCE AND FILM THICKNESS _____	94
VII. CONCLUSIONS _____	103
APPENDIX I - PHYSICAL PROPERTIES OF MIL-L-7808 _____	105
APPENDIX II - COMPUTER PLOTS OF EXPERIMENTAL TRACTION DATA _____	111
APPENDIX III - ELASTIC DISTORTION ANALYSES USED FOR STATIC OPTICAL CALIBRATION AND CAPACITANCE CALIBRATIONS _____	131
APPENDIX IV - OPTICAL DISTORTION FACTOR DERIVATION _____	143
APPENDIX V - TEST EQUIPMENT LIST _____	147
REFERENCES _____	149

LIST OF ILLUSTRATIONS

	<u>Page</u>
1. Five Parallel Talysurf Tracings of Roller Specimen Surface Finish ___	4
2. Traction Data from Rolling Disc Rig for Four Loads _____	5
3. Range of Presently Available Traction Data From MTI Computer Data Storage _____	6
4. Typical Load Sensitivity of MIL-L-7808 Traction Versus Slip Data ___	8
5. Comparison of Disc Traction-Slip Data for Two Different Lubricants with Similar Viscosities _____	9
6. Typical Temperature Sensitivity of Traction Versus Slip Data _____	10
7. Typical Temperature Sensitivity of Traction Versus Slip Data _____	11
8. Typical Temperature Sensitivity of Traction Versus Slip Data _____	12
9. Peak Traction Dependence on Hertz Pressure and Speed _____	14
10. Low-Speed Low-Temperature MIL-L-7808 Traction Data _____	15
11. Low-Speed High-Temperature MIL-L-7808 Traction Data _____	16
12. Medium-Speed Low-Temperature MIL-L-7808 Traction Data _____	17
13. Medium-Speed High-Temperature MIL-L-7808 Traction Data _____	18
14. High-Speed Low-Temperature MIL-L-7808 Traction Data _____	19
15. High-Speed High-Temperature MIL-L-7808 Traction Data _____	20
16. Viscosity-Temperature Data at Atmospheric Pressure _____	21
17. Temperature-Pressure-Viscosity Data for MIL-L-7808 _____	23
18. Empirical Viscosity Time-Delay Function _____	26
19. Contact Ellipse Schematic of Crowned Disc-Specimens _____	31
20. Dielectric Conditions Considered Analytically _____	32
21. No-Load Gap Separation Capacitive Test Schematic _____	33
22. No-Load Gap Separation Capacitive Data _____	34
23. Load-Separation Capacitive Data _____	35
24. Disparity Between Elliptical and Numerically Calculated Loci of Constant Separation _____	37
25. Analytical Capacitive Film Thickness Variations With and Without Dielectric Pressurization Effects _____	39
26. Analytical and Calibration Data for Capacitance Versus Film Thickness _____	40

Contrails

LIST OF ILLUSTRATIONS (Continued)

	<u>Page</u>
27. Analytical and Calibration Data for Capacitance Versus Film Thickness	41
28. Test Rig Output of Capacitance Versus Speed Data	42
29. Capacitive Film Thickness Versus Speed Determinations	43
30. Capacitive Film Thickness Versus Speed Determinations	45
31. Capacitive Film Thickness Versus Speed Determinations	46
32. Lower Disc Specimen Shaft Showing Mounting Arrangement and Optical Access	48
33. Optical Disc Illumination Schematic	50
34. Contact Ellipse Distortion Schematic	52
35. Distortion Off-Set Schematic of Observed Fringes	53
36. Two Interference Fringe Patterns of Stationary Loaded Contacts Showing Load-Area Contact	55
37. Phase Relation of Thin Film Reflected Light	57
38. Dimensional Variations of Loaded Contact Ellipse	58
39. Photograph and Computer Plot of a Load Contact Ellipse	59
40. Photograph and Computer Plot of a Load Contact Ellipse	60
41. Photographs of Rolling Contact Zone Variations with Speed	61
42. Photographs of Rolling Contact Zone Variations with Speed	62
43. Rolling Contact Zone Reflective Intensity Variations with Speed	63
44. Rolling Contact Zone Photographs	64
45. Rolling Contact Zone Photographs	65
46. Rolling Contact Zone Photographs	66
47. Rolling Contact Zone Photographs	67
48. Optical Film Thickness Versus Speed Determinations	69
49. X-Ray Test Facility Schematic	72
50. Relative Dimensional Characteristics of X-Ray Beam and Contact Zone	73
51. Top View of X-Ray Beam Test Arrangement	74
52. Cadmium 109 Energy Decay Spectrum	75
53. X-Ray Electric Detection Arrangement	76
54. X-Ray Film Thickness Determinations for Two Rolling Speeds	78
55. Lubricant Inlet Exit Schematic	79

Contrails

LIST OF ILLUSTRATIONS (Continued)

	<u>Page</u>
56. Typical Contact Resistance Versus Time Variations _____	82
57. Asperity Contact Data as a Function of Rolling Speed for Four Separate Loads _____	83
58. Asperity Contact Data as a Function of Rolling Speed for Five Resistance Detection Levels _____	85
59. Percent Contact Versus Contact Resistance for Five Speed Levels _____	86
60. Time-Averaged Rolling Contact Resistance as a Function of Speed _____	87
61. Nine Parallel Talysurf Tracings of Roller Specimen Surface Finish _____	88
62. Peak Height Distribution, $M = 0.342\mu''$ and $\sigma = 1.526\mu''$ _____	90
63. Radius of Curvature Distribution at the Peaks _____	91
64. Spectral Density Function _____	92
65. Autocorrelation Function _____	93
66. Average Normal and Friction Forces Supported by the Separations Between Mean Planes of the Interacting Asperities _____	95
67. Asperity Loads and Real Contact Area as a Function of Rolling Speed _____	96
68. Variations of Tunnel Resistivity as a Function of Adsorped Layer Thickness _____	98
69. Contact Resistance for a Unit Apparent Area as a Function of Separation Between Mean Planes _____	99
70. Resistance Speed Relationships for Rolling Discs at 760 lb. Load. Grubin's Formula is Used to Determine the Film Thickness _____	100
71. Density as a Function of Temperature and Pressure for 0-67-20 (MIL-L-7808) _____	106
72. Absolute Viscosity as a Function of Temperature and Pressure for 0-67-20 (MIL-L-7808) _____	107
73. Kinematic Viscosity as a Function of Temperature and Pressure for 0-67-20 (MIL-L-7808) _____	108
74. Isothermal Secant Bulk Modulus as a Function of Temperature and Pressure for 0-67-20 (MIL-L-7808) _____	109
75. Computer Plotted Experimental Traction Versus Slip Data _____	113
76. Computer Plotted Experimental Traction Versus Slip Data _____	114
77. Computer Plotted Experimental Traction Versus Slip Data _____	115
78. Computer Plotted Experimental Traction Versus Slip Data _____	116
79. Computer Plotted Experimental Traction Versus Slip Data _____	117
80. Computer Plotted Experimental Traction Versus Slip Data _____	118

Contrails

LIST OF ILLUSTRATIONS (Continued)

	<u>Page</u>
81. Computer Plotted Experimental Traction Versus Slip Data _____	119
82. Computer Plotted Experimental Traction Versus Slip Data _____	120
83. Computer Plotted Experimental Traction Versus Slip Data _____	121
84. Computer Plotted Experimental Traction Versus Slip Data _____	122
85. Computer Plotted Experimental Traction Versus Slip Data _____	123
86. Computer Plotted Experimental Traction Versus Slip Data _____	124
87. Computer Plotted Experimental Traction Versus Slip Data _____	125
88. Computer Plotted Experimental Traction Versus Slip Data _____	126
89. Computer Plotted Experimental Traction Versus Slip Data _____	127
90. Computer Plotted Experimental Traction Versus Slip Data _____	128
91. Computer Plotted Experimental Traction Versus Slip Data _____	129
92. Schematic of Hertz Profile _____	132
93. Hertz Contact Parameters _____	135
94. Dimensionless Elastic Distortion Along Minor Axis of Contact _____	136
95. Elastic Distortion Along Major Axis of Contact _____	137
96. Dimensionless Fringe Lines for $R/R' = 1/24$ _____	138
97. Schematic of Elliptical Fringe Lines Used in Capacitance Calculations _____	140
98. The Relationship Between Major and Minor Axis for Fringe Lines _____	141
99. Optical Distortion Off-Set Diagram _____	144

Contrails

ABBREVIATIONS

a	Semi-major axis of contact ellipse, in.
a_i	Micro asperity contact radius, in.
A	Area, in ²
\tilde{A}	Constant in Lorenz-Lorenz Equation
$\overline{(A/h)}$	Effective area to separation for capacitance, in.
b	Semi-minor axis of contact ellipse, in.
C	Capacitance, pico-farads
E'	Combined elastic modulus of contacting materials, lb-in ⁻²
E_1, E_2	Elastic moduli of bodies number 1 and 2, lb-in ⁻²
f	Frequency, in ⁻¹
f_D	Optical distortion factor
F_x	Tractive force in rolling direction, lbs.
h	Film thickness, in.
i	Increment parameter, non-negative integers
I, I ₀	X-Ray intensity
J_1, J_2, J_3	Dimensionless integrals
k	Dimensionless variable, $\sqrt{1-\beta}^2$
k^{\wedge}	Harmonic number
K, K ₀	Dielectric coefficients
K_f	Thermal conductivity of lubricant lb-sec ⁻¹ -o _F ⁻¹
K_{α}, K_{β}	Electron orbital shell
L	Half thickness of disc, in.
L_1	Observation length, in.
m_i	ith moment of spectral density function
\hat{m}	Maximum harmonic number
M	Mean asperity peak height, in.
n, n_p, n_o, n_G	Refractive indices
\bar{n}	Dimensionless Hertz parameter
p	Pressure, lb-in ⁻²
P_{HZ}	Maximum Hertz contact pressure, lb-in ⁻²
r	Inside radius of optical test disc, in.
R, R'	Relative radii of curvature, in.

ABBREVIATIONS (Continued)

R_1, R_2	Radii of bodies number 1 and 2, in.
R_1', R_2'	Crown radii of bodies number 1 and 2, in.
\hat{R}_i	Contact resistance, ohms
s	Sample interval for Talysurf data, in.
S	Actual arc length to fringe in rolling direction, in.
S'	Observed arc length to fringe in rolling direction, in.
t	Adsorbed surface film thickness, (\AA)
T	Temperature, $^{\circ}\text{F}$
T_A	Absolute temperature, $^{\circ}\text{R}$
T_o	Inlet oil temperature, $^{\circ}\text{F}$
u	Local velocity in rolling direction, in-sec^{-1}
U_1, U_2	Surface velocity of disc 1 and disc 2, in-sec^{-1}
\bar{U}	Mean rolling speed, in-sec^{-1}
W	Load, lb.
x, x_o	Coordinates in rolling direction, in.
y, y_o	Coordinate in axial direction, in.
z	Coordinate across film, in.
α, α_T	Viscosity pressure coefficients, $\text{in}^2\text{-lb}^{-1}$
$\bar{\alpha}$	Surface parameter
β	Viscosity temperature coefficient, $^{\circ}\text{F}$
$\bar{\beta}$	Dimensionless parameter, b/a
γ	Viscosity-pressure-temperature coefficient, $\text{in}^2\text{-}^{\circ}\text{F-lb}^{-1}$
ϵ_o	Permittivity of free space, 8.85×10^{-12} Farad/meter
ϵ_r	Relative permittivity of adsorbed material
η, η_o	Dimensionless coordinates in axial direction
θ	Angle to observed fringe, deg.
λ	Wavelength of light, in.
μ, μ_T	Viscosity, lb-sec-in^{-2}
μ_o	Base viscosity coefficient, lb-sec-in^{-2}
$\tilde{\mu}$	Adsorption coefficient, in^{-1}
ν_1, ν_2	Poisson's ratio of bodies number 1 and 2
ξ, ξ_o	Dimensionless coordinates in rolling direction

Contrails

ABBREVIATIONS (Continued)

ρ	Tunnel resistivity, ohm-cm ²
ρ, ρ_0	Lubricant density, lbs/in ²
ρ^A	Electrical resistivity of discs, ohm-in.
σ	RMS Surface roughness, in.
$\bar{\sigma}$	RMS Film thickness variations, in.
τ_x	Shear stress, lb-in ⁻²
Φ	Work function for electron emission (ev)
$\bar{\Phi}$	Dimensionless elastic separation parameter
χ	Viscosity-rolling speed factor
ψ	Spectral density function of surface profile, in ³ .

Contrails

SECTION I

INTRODUCTION

At the conclusion of Phase I of this research program, a compendium of the state of the art of elastohydrodynamic technology was compiled and a computer program was prepared to predict elastohydrodynamic performance characteristics on the basis of the best available theory and experimental data. It was found that considerable data were lacking in areas such as elastohydrodynamic tractions, measurement of elastohydrodynamic film thicknesses, and general behavior of partial elastohydrodynamic performance.

A rolling disc elastohydrodynamic test apparatus was built and instrumented (1)* as a result of the findings in Reference (2), for measurement of elastohydrodynamic performance characteristics including tractions and film thicknesses. A full matrix of traction data was obtained for a 5P4E polyphenyl ether during Phase II of this research program along with analytical predictions to describe the data. An asperity interaction computer program was also published in Reference 1 as a vehicle for studying the partial elastohydrodynamic regime.

During Phase III of this program, a full matrix of traction data was obtained with a MIL-L-7808 oil. Comparisons made between this oil and polyphenyl ether showed radical differences in both quantitative and qualitative traction behavior even under conditions where conventional properties are relatively similar.

Attempts were made to obtain film thickness data using three different techniques; namely, optical, capacitance, and X-ray techniques. Optical data was obtained which showed good detail of the film thickness profile at lower loads. These were compared with capacitance data taken with steel discs under conditions of higher loads and speeds. Calibrating techniques were developed for relating capacitance measurements to film thickness and for checking out optical measurements under elliptical contact. Full dry contact elastic distortion analyses for Hertz contact were considered. The optical data taken at lower loads indicated relatively small load sensitivity as is predicted by elastohydrodynamic theory. Capacitance data taken at higher loads indicated much stronger load effects which are in qualitative agreement with X-ray data given in Reference 3.

Electrical continuity and resistance measurements were obtained with the use of an asperity contact measuring device developed by MTI and referred to as an "Asperitac." This device provides information regarding the percentage of time the electrical resistance falls below a preset discrimination level and, hence, is a measure of the relative extent of contact. It was found for the cases studied that no significant contact occurred in the higher speed regions where

* Numbers in parentheses refer to references listed at the end of this report.

Contrails

capacitance and traction measurements were obtained, and in order to get incipient contact, speeds well below the 100 in/sec range had to be used. In general, based upon elastohydrodynamic film thickness predictions, this would be the range in which the film thickness to surface roughness ratios are on the order of 1. Comparisons were performed with electrical resistance data and resistance predictions based upon the asperity interaction model; however, conclusions are not definite as a result of uncertainties in the distribution of asperities.

The following sections deal first with measurements and correlation of tractions for MIL-L-7808 fluid. This section is followed by three sections dealing with film thickness measurements obtained by capacitance, optical, and X-ray techniques. These are followed by the results of the asperity interaction studies. Appendices are presented to give the full matrix of traction data along with the various lubricant data and mathematical analyses that have been performed in relationship to the traction and film thickness data.

SECTION II TRACTION DATA AND ANALYSIS

This section presents a summary of the traction data collected from tests performed on a MIL-L-7808 lubricant along with a quasi-empirical model for predicting tractions. The test lubricant physical properties are included in Appendix I for reference purposes. The test rig used to generate the traction data discussed here was reviewed in Reference 1.

1. TEST DATA

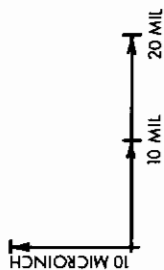
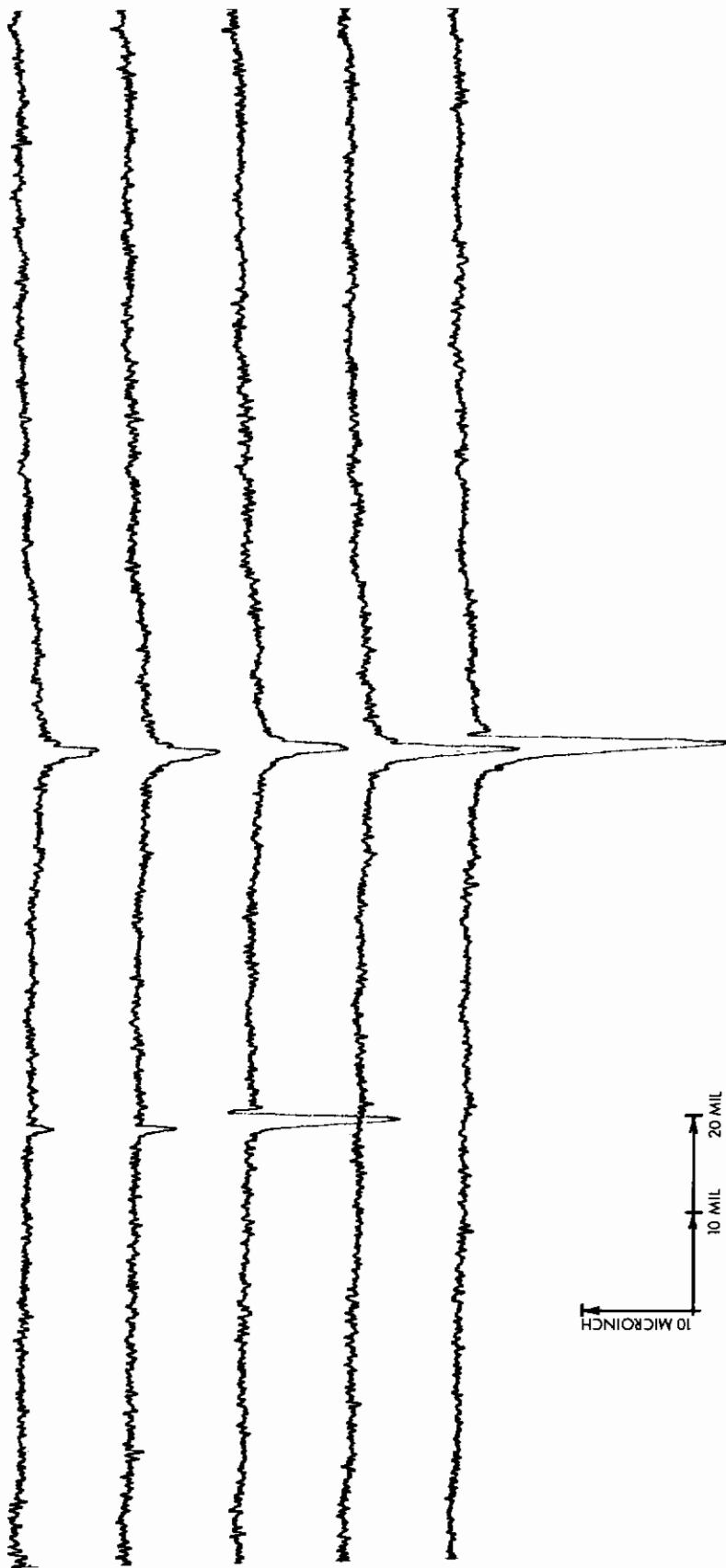
The test rig design is of the two-disc variety which permits the determination of traction and film thickness properties of most lubricants in a single rolling and/or sliding contact. In addition to accurate control and readout of rolling and sliding speeds, various levels of temperature can be maintained on the disc machine for investigating the dependence of traction on lubricant temperature. A sliding carriage supporting the upper disc specimen also provides a way to vary the load in order to study loading effects on a lubricated contact.

The basic geometry of the test disc specimens was identical to that used during the past year's work completed with polyphenyl ether. The traction data was taken from two crowned disc specimens, each with a three-inch diameter and a thirty-six-inch crown radius. Both were hardened and polished AISI 52100 bearing steel. The tested hardness of each was between fifty-eight and sixty Rockwell-C. The finish of the polished surfaces of the rollers was approximately two microinch rms. A topographical recording of five parallel tracings of a typical roller surface used for the tests is shown in Figure 1. Each tracing was recorded along a line perpendicular to the direction of rolling on the specimen surface. A complete discussion of test surface topology as related to asperity interactions of the test specimens is presented in Section VI.

Full traction-versus-slip curves for both positive and negative slips are a direct output of the rig instrumentation. A sample of four typical traction curves read out directly from the disc machine is shown in Figure 2. Each of the four sample curves was obtained at different loads but constant rolling speed and lubricant temperature.

Traction-versus-slip curves for a wide range of contact loading, rolling speed, and lubricant temperature have been investigated with a MIL-L-7808 lubricant. The range of conditions for presently available traction data, including the previous year's work performed on polyphenyl ether, is shown in Figure 3. In order to cover the range of variables, a large number of complete slip curves have been recorded (to date, 135). Enough combinations of loading, rolling speed, and lubricant temperatures have been recorded to reasonably describe the traction behavior of the two lubricants tested.

Since a large number of complete traction curves can be obtained in a short period of time, the data handling and storage has been tied into a computer



NOTE: PARALLEL SPACING OF EACH
RECORDING, 1 MIL

Fig. 1 Five Parallel Talysurf Tracings of Roller Specimen Surface Finish

MTI-13091

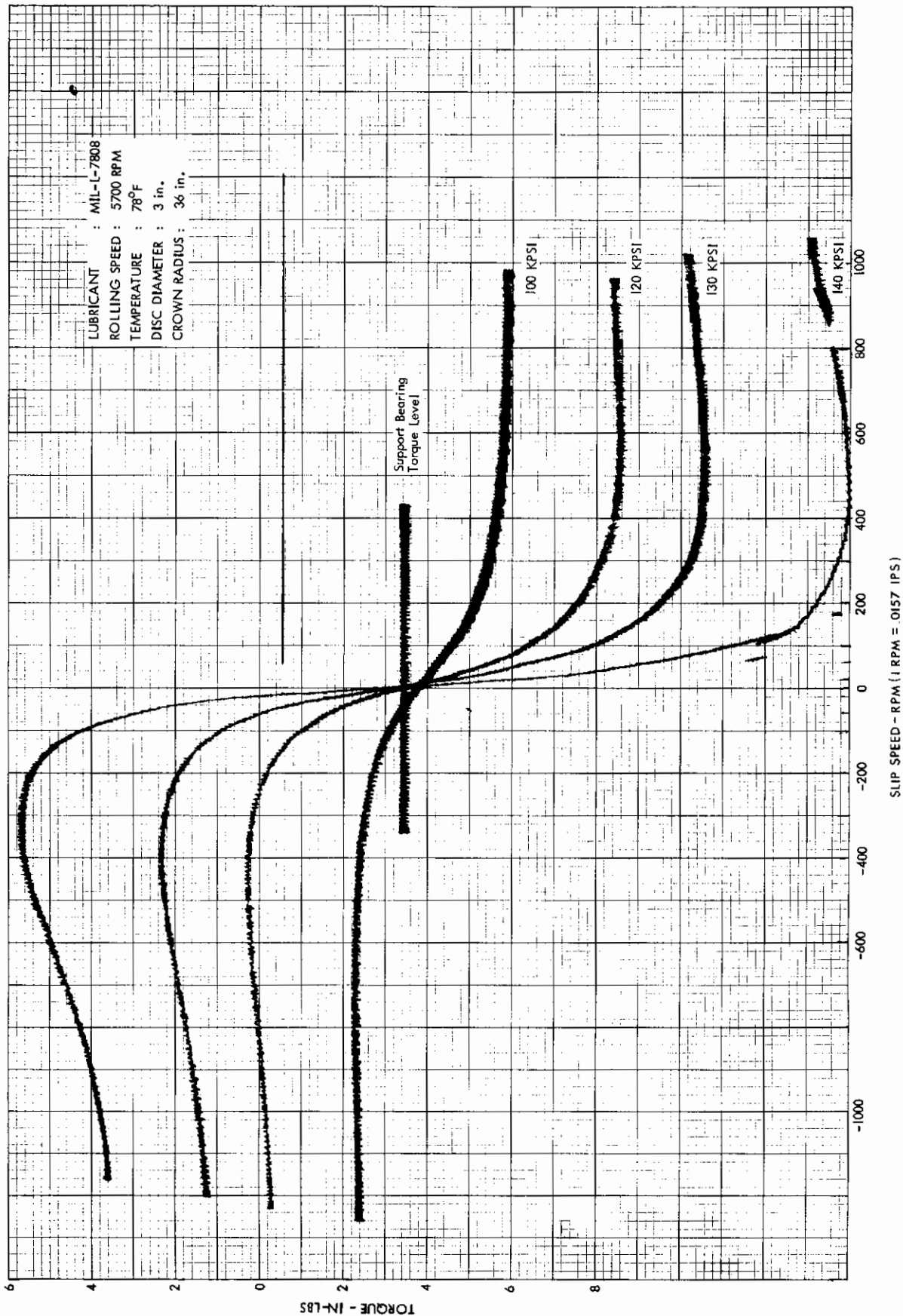
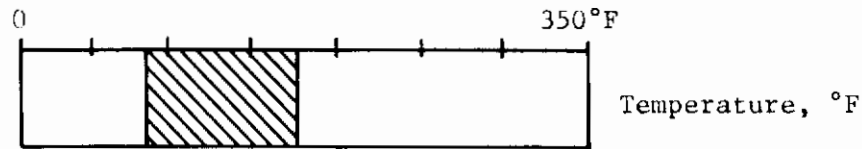
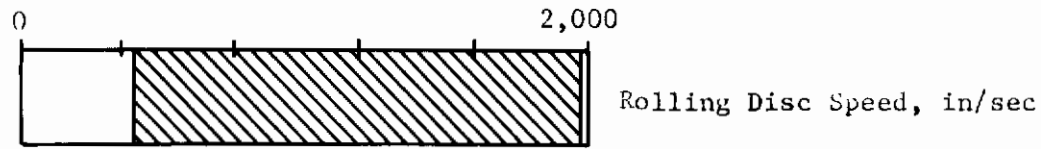
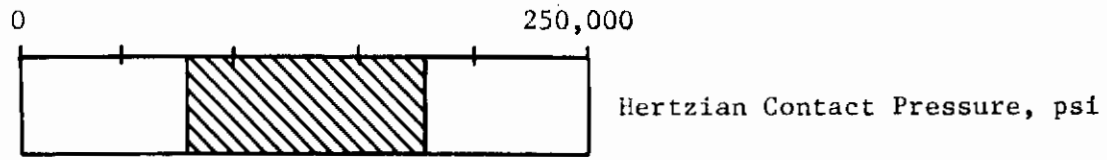


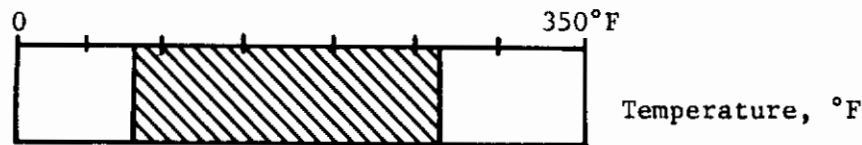
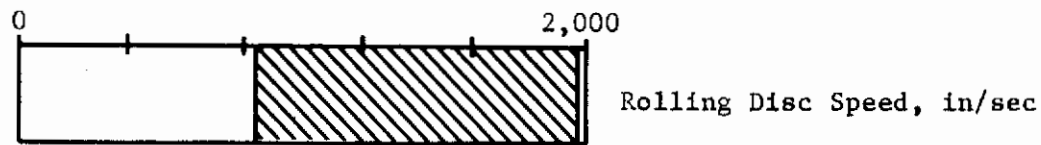
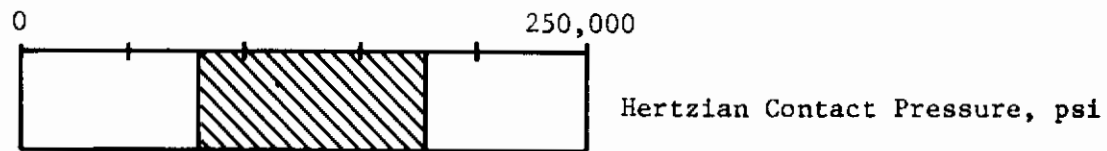
Fig. 2 Traction Data from Rolling Disc Rig for Four Loads

Contrails

MIL-L-7808 (Data Presented in this Report)



Polyphenyl Ether (5P4E) (Data Presented in Reference 1)




 Range of MTI Traction Data

Fig. 3 Range of Presently Available Traction Data From MTI Computer Data Storage

Contrails

via time-sharing terminal. The curves are digitized and transferred in total to the computer filing system at the present time by hand. The two-fold symmetry axes for each complete traction curve is found analytically and a single positive slip curve is stored in a computerized traction data bank.

Retrieval and analysis of the data is highly automated since the present time-sharing facility at MTI is linked to an onsite plotter which can display any stored curve within seconds. A sample set of the computer-plotted curves is shown in Figure 4, which shows a comparison of the four loads previously displayed as raw data in Figure 2. The scale of the abscissa and ordinate can be plotted in any convenient set of engineering units from the stored files of traction data. The present data handling system allows rapid comparison of gathered data taken under any set of test facility conditions.

The computer-plotted comparison of a 5P4E polyphenyl ether and a MIL-L-7808 oil is shown in Figure 5. The conditions of disc geometry, load, and rolling speed are identical. The lubricant temperature conditions were widely separated in order to match the viscosities of the fluids. Both fluids have a pressure coefficient of approximately $0.75 \times 10^{-4} \text{ in}^2/\text{lb}$. One curve shows the traction-slip rate for polyphenyl ether at 260°F , whereas the other curve shows traction data obtained from the MIL-L-7808 oil at 120°F . Both viscosities are approximately nine centipoise.

A marked difference is displayed even though the viscosity and viscosity-pressure coefficient characteristics are similar. Part of the displayed difference can be attributed to the fact that the temperature coefficient of viscosity for the MIL-L-7808 oil is about 80 percent greater than that for polyphenyl ether. However, this is insufficient for explaining the wide discrepancy revealed from the data.

Another indication of the fact that conventional viscosity characteristics are insufficient for describing elastohydrodynamic tractions results from the polyphenyl ether traction data obtained by MTI which indicates tractions for polyphenyl ether to be nearly insensitive to temperature. Conventional viscosity characteristics, such as the base viscosity and viscosity-pressure and temperature coefficients, vary markedly with temperature. The lack of sensitivity to temperature indicated by this data may result from additives introduced into the polyphenyl ether (Battelle data indicates considerable temperature sensitivity in tractions for polyphenyl ether without additives). The effect of these additives does not show up in conventional viscosity-temperature data.

The present test lubricant (MIL-L-7808), however, showed a strong effect with different operating temperatures. Shown in Figure 6 is a display of the temperature effect exhibited for one constant load and fixed rolling speed. As the temperature increases, the maximum transmittable peak traction is reduced. Figure 7 shows a 25 percent reduction of the peak traction was observed for an 85°F variation in temperature at the speed and load indicated. One additional set of traction curves taken at higher rolling speeds is plotted in Figure 8. Included in Appendix II for reference are computer plots of all the MIL-L-7808 traction curves stored to date for retrieval from the MTI computer data bank.

TRACTION DATA

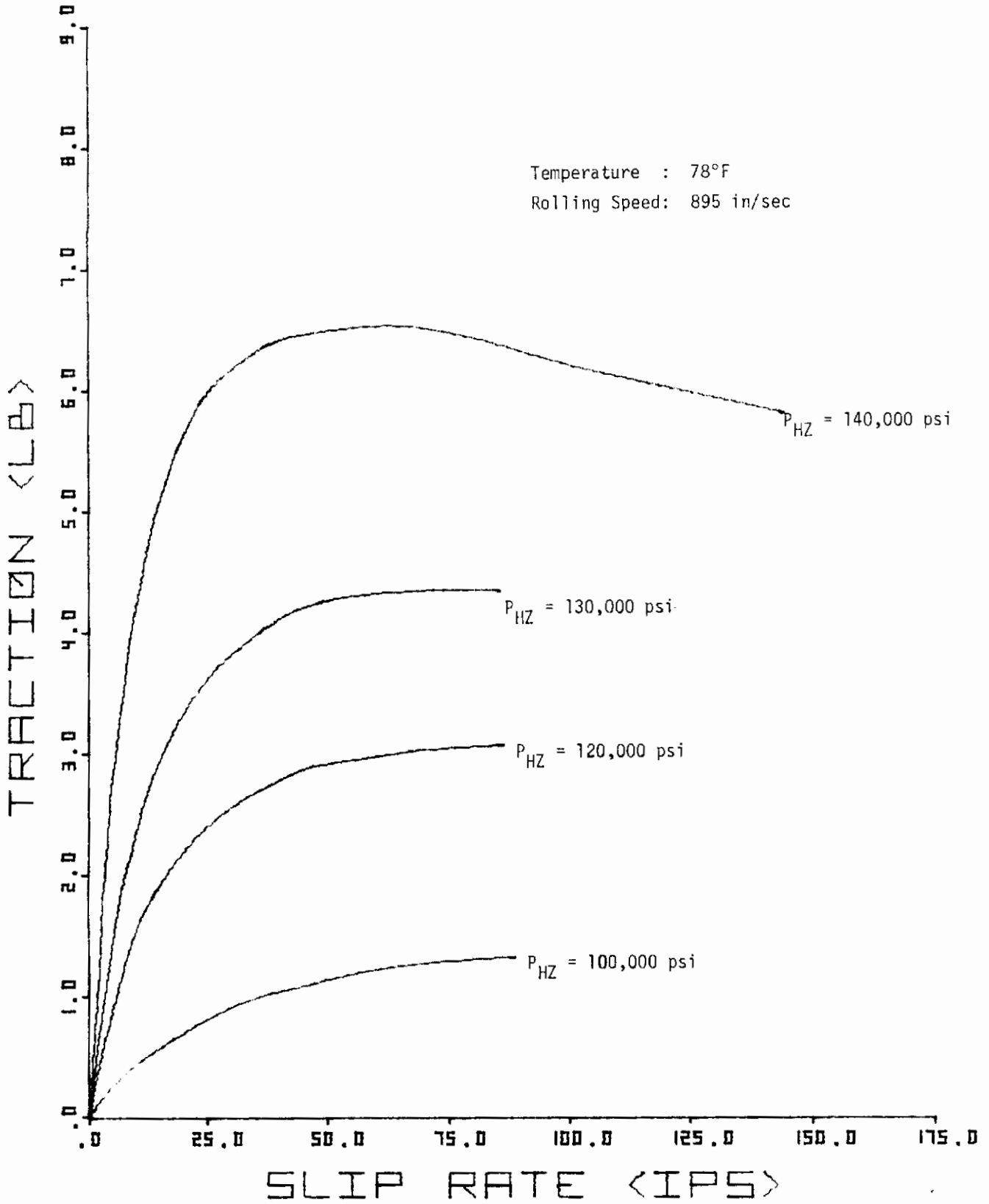


Fig. 4 Typical Load Sensitivity of MIL-L-7808 Traction Versus Slip Data

TRACTION DATA

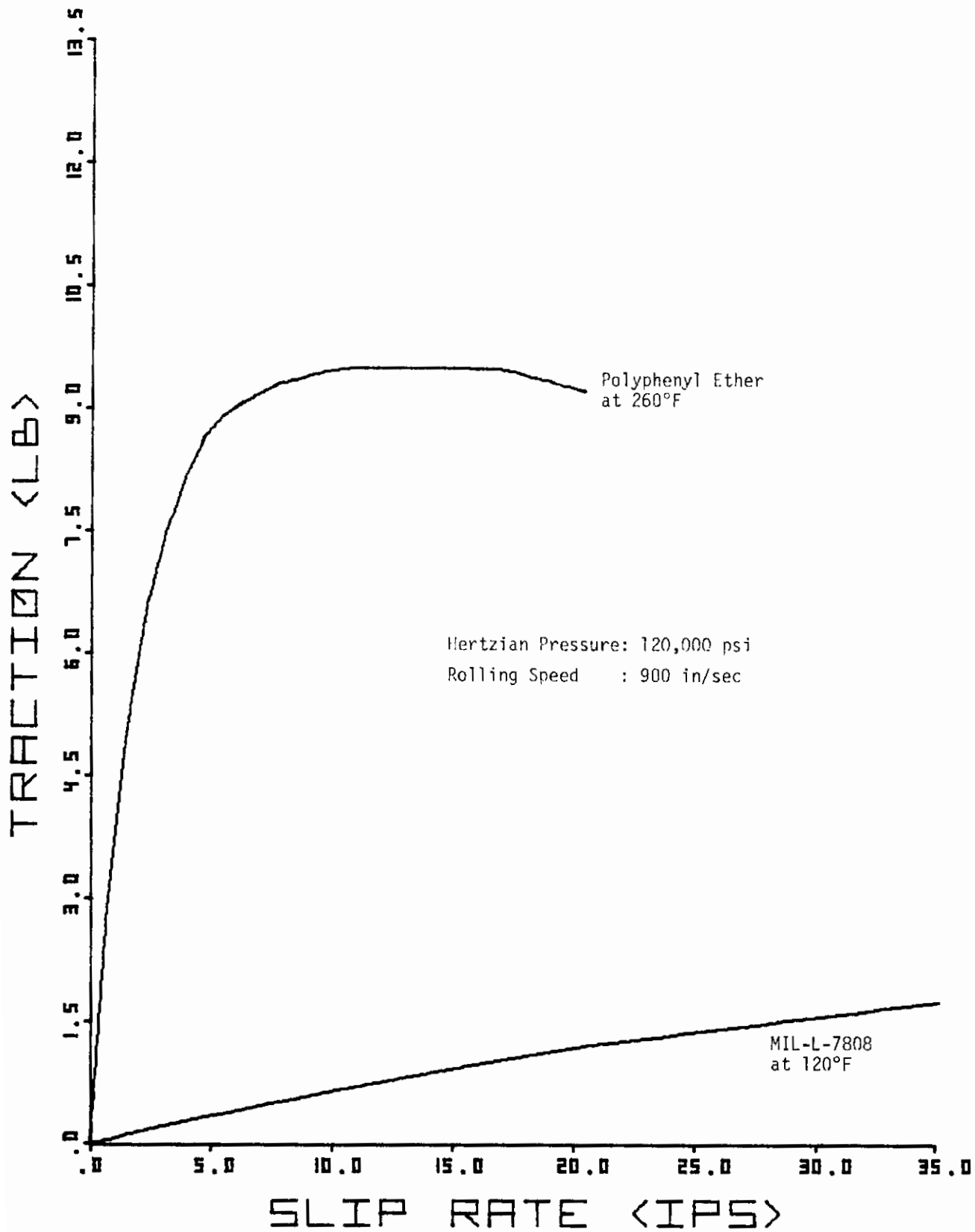


Fig. 5 Comparison of Disc Traction-Slip Data for Two Different Lubricants with Similar Viscosities

Contrails
TRACTION DATA

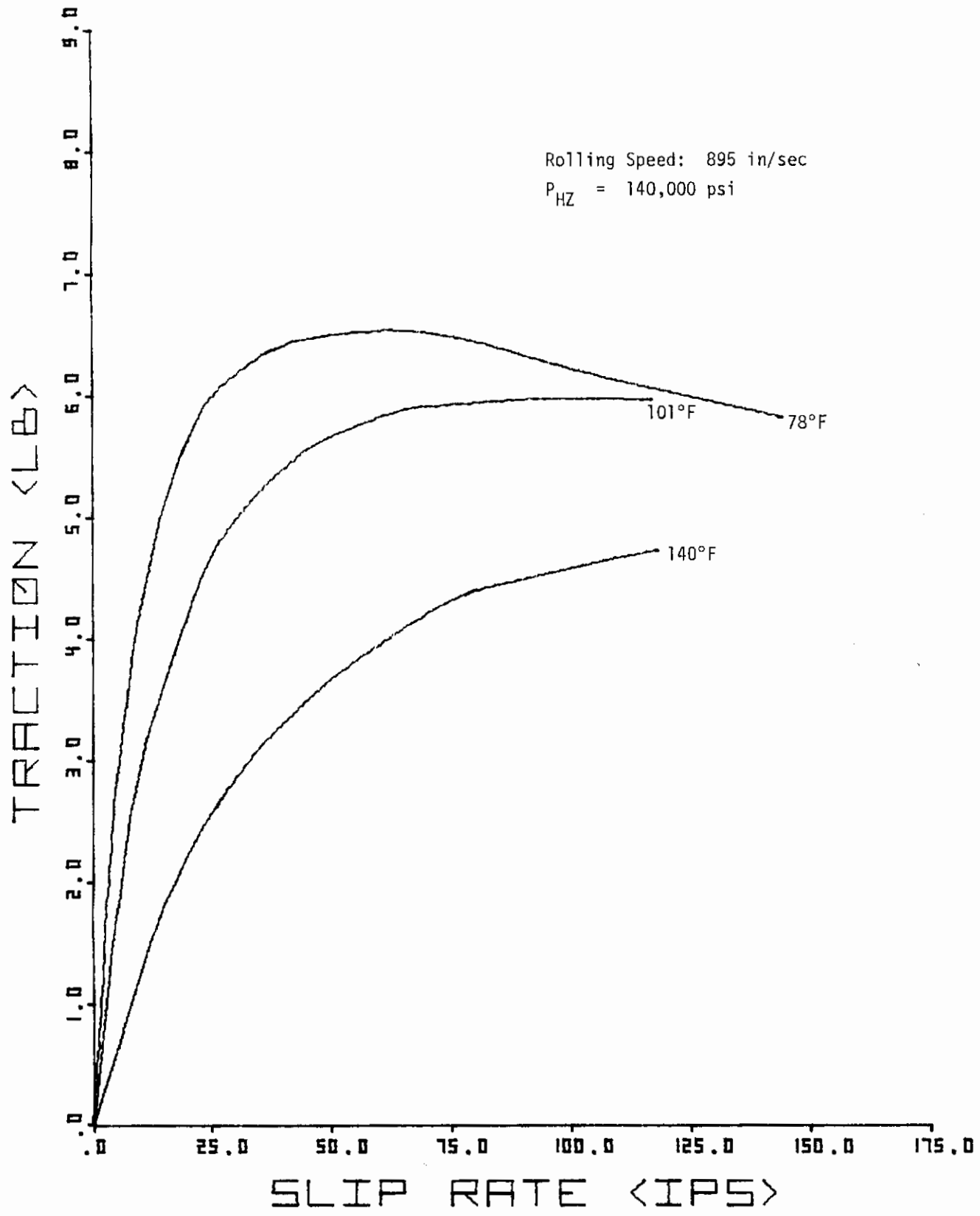


Fig. 6 Typical Temperature Sensitivity of Traction Versus Slip Data

TRACTION DATA

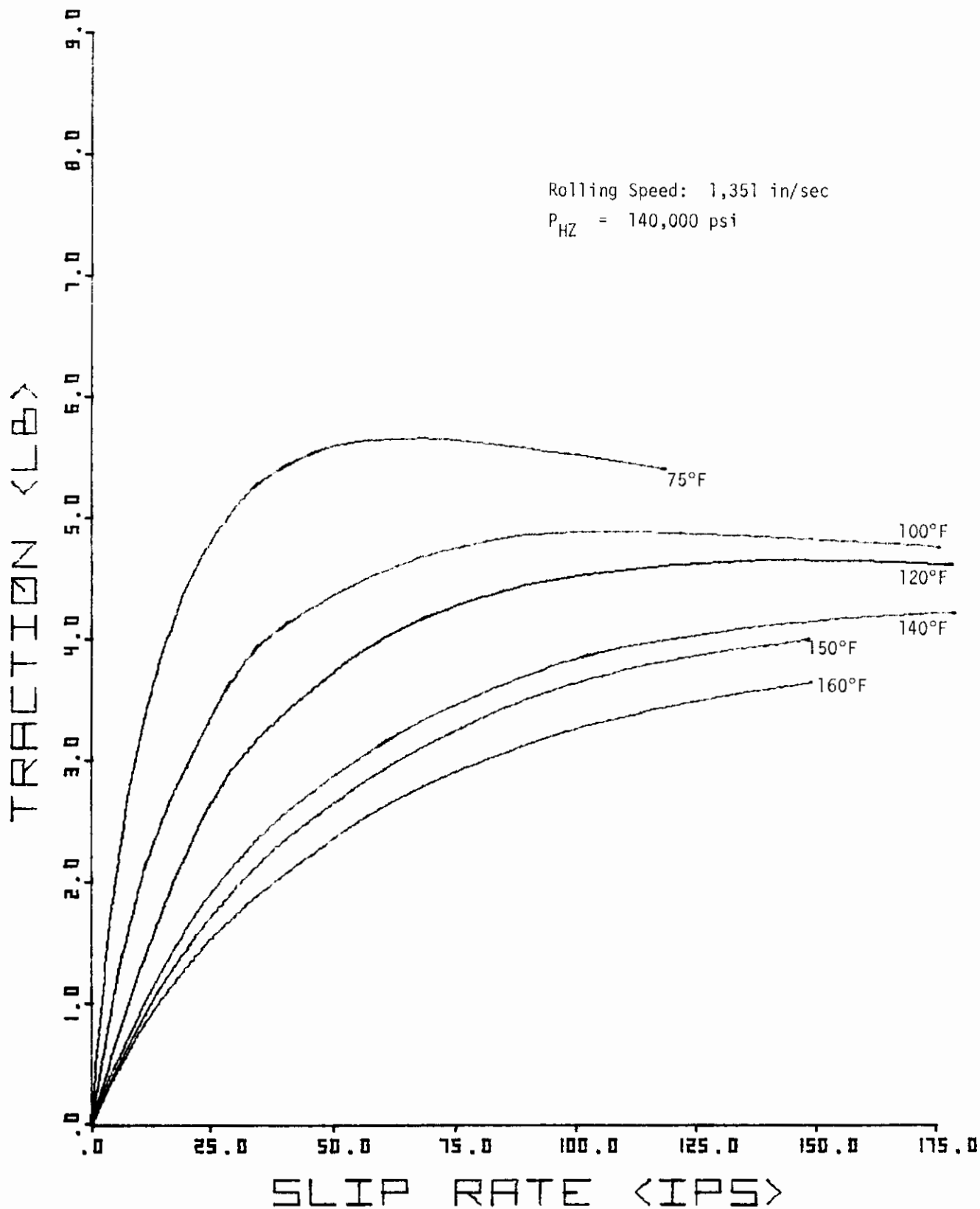


Fig. 7 Typical Temperature Sensitivity of Traction Versus Slip Data

TRACTION DATA

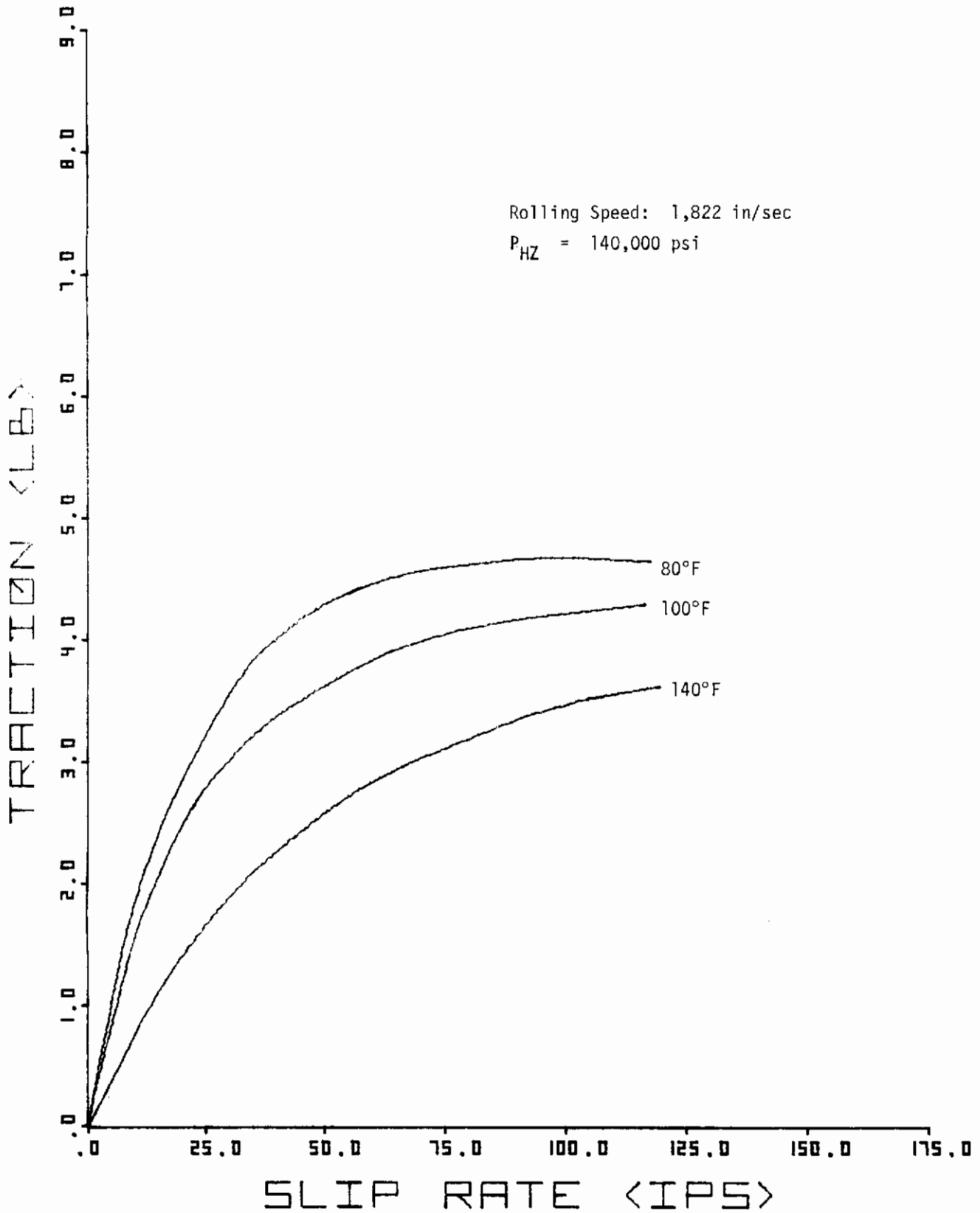


Fig. 8 Typical Temperature Sensitivity of Traction Versus Slip Data

Peak tractive forces varied widely as a function of the applied Hertzian pressure, rolling speed, and temperature. Since a large number (over 200) of complete traction-versus-slip curves were collected, cross plots of rolling speed versus Hertzian pressure for fixed peak tractive forces can be made. A single line for polyphenyl ether is shown in Figure 9 for a peak tractive force of four pounds. A range of peak tractions greater than one pound and less than four is shown for the MIL-L-7808 tested in Figure 9.

2. ANALYSIS OF TRACTION DATA

An attempt has been made to analyze the traction data and correlate it with the use of available viscosity data. A quasi-empirical model has been developed for predicting tractions based upon hypothetical but reasonable viscosity data.

The predicted tractions along with the measured ones are graphically displayed in Figures 10 through 15. The extremes in rolling speed and lubricant test temperatures have been plotted for comparison. For the range of test conditions, it can be seen that satisfactory predictions have been obtained which may be used to describe MIL-L-7808 tractions over the full test range of loads, rolling speeds, slip rates, and temperatures.

The methods that have been used for obtaining the traction correlation are described in the following sections.

a. Film Thickness Predictions

Any hydrodynamic traction prediction requires a knowledge of shear rate as input. In order to compute the shear rate from the known slip velocity, an estimate of the film thickness is required. This estimate is obtained with the use of the elastohydrodynamic performance code prepared for the Air Force and listed in Reference 2.

The hydrodynamic film thickness inputs to the film thickness portion of this computer program are the thermal conductivity of the lubricant and the viscosity coefficients μ_0 , α , and β corresponding to the formula.

$$\mu = \mu_0 e^{\alpha p} + (\beta + \gamma p) \left(\frac{1}{T + 460} - \frac{1}{T_0 + 460} \right) \quad (1)$$

where T_0 denotes the reference temperature in degrees Fahrenheit taken here to be the lubricant supply temperature and μ_0 is the viscosity at temperature T_0 . Values of μ_0 and β were determined from atmospheric viscosity-temperature measurements obtained at MTI and shown in Figure 16.

Values of β are obtained from the local slopes of a semi-log plot of h versus $1/T_A$ where T_A is the absolute temperature in accordance with the relationship

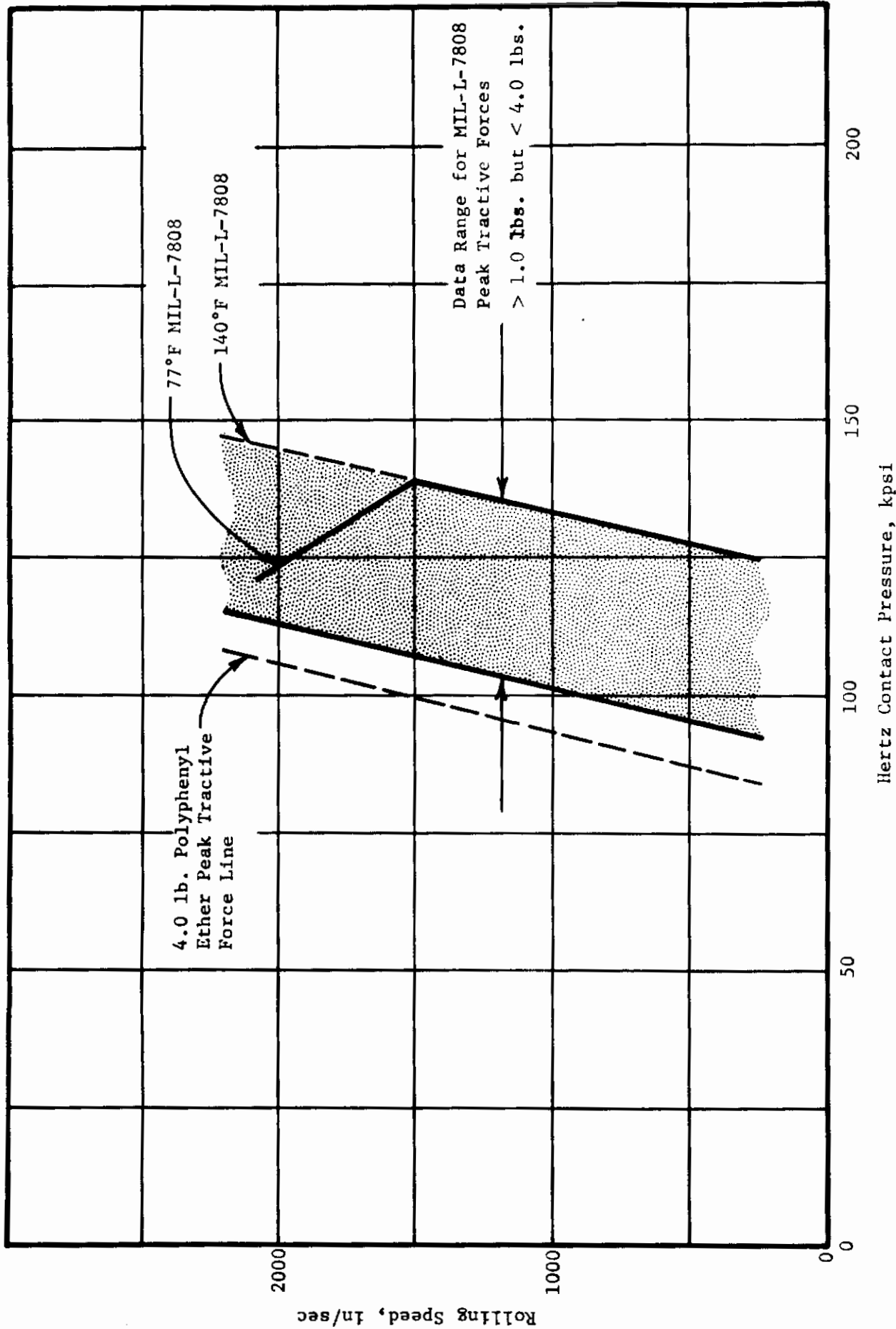


Fig. 9 Peak Traction dependence on Hertz Pressure and Speed

MTI-13370

Contrails

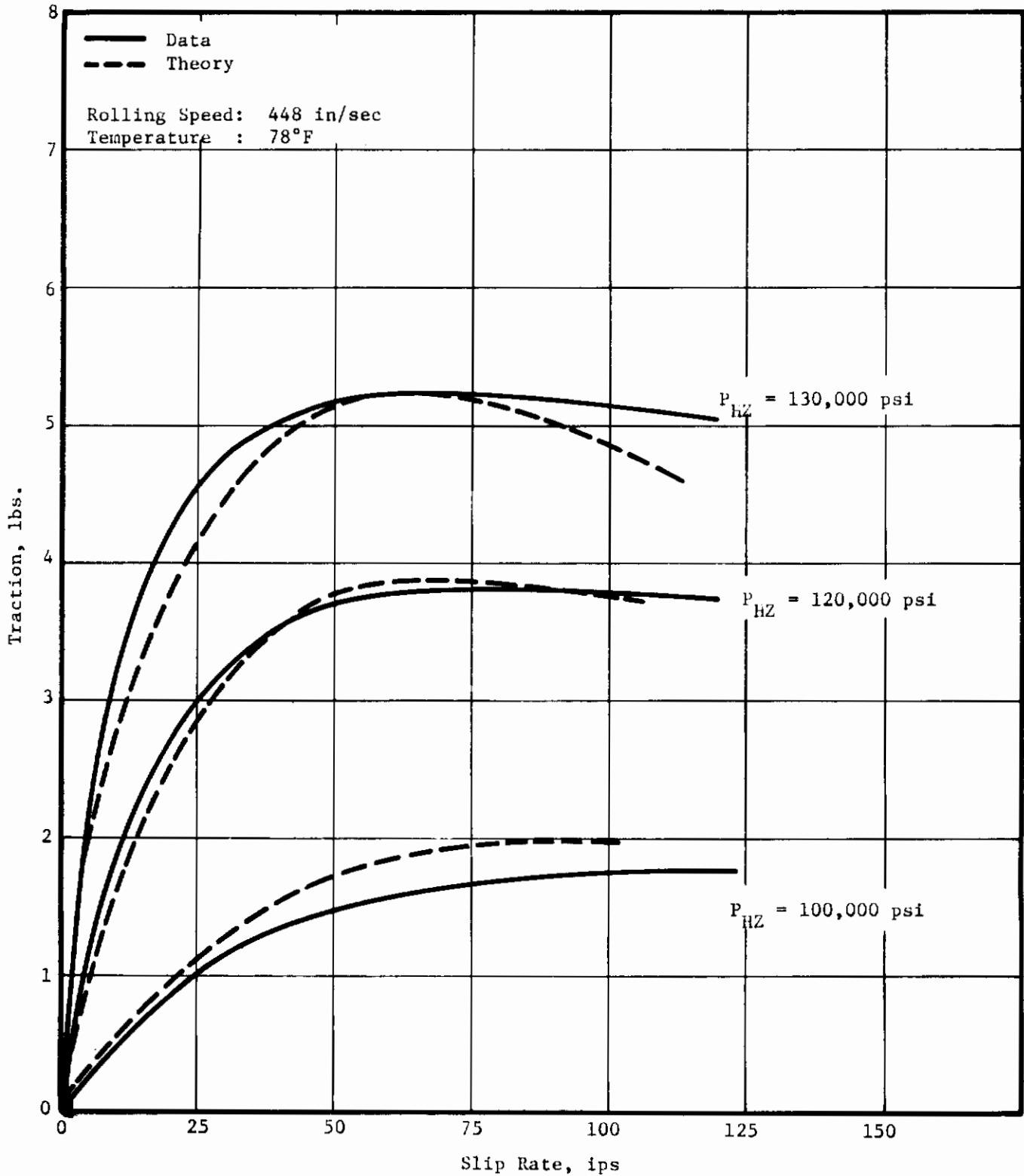


Fig. 10 Low-Speed Low-Temperature MIL-L-7808 Traction Data

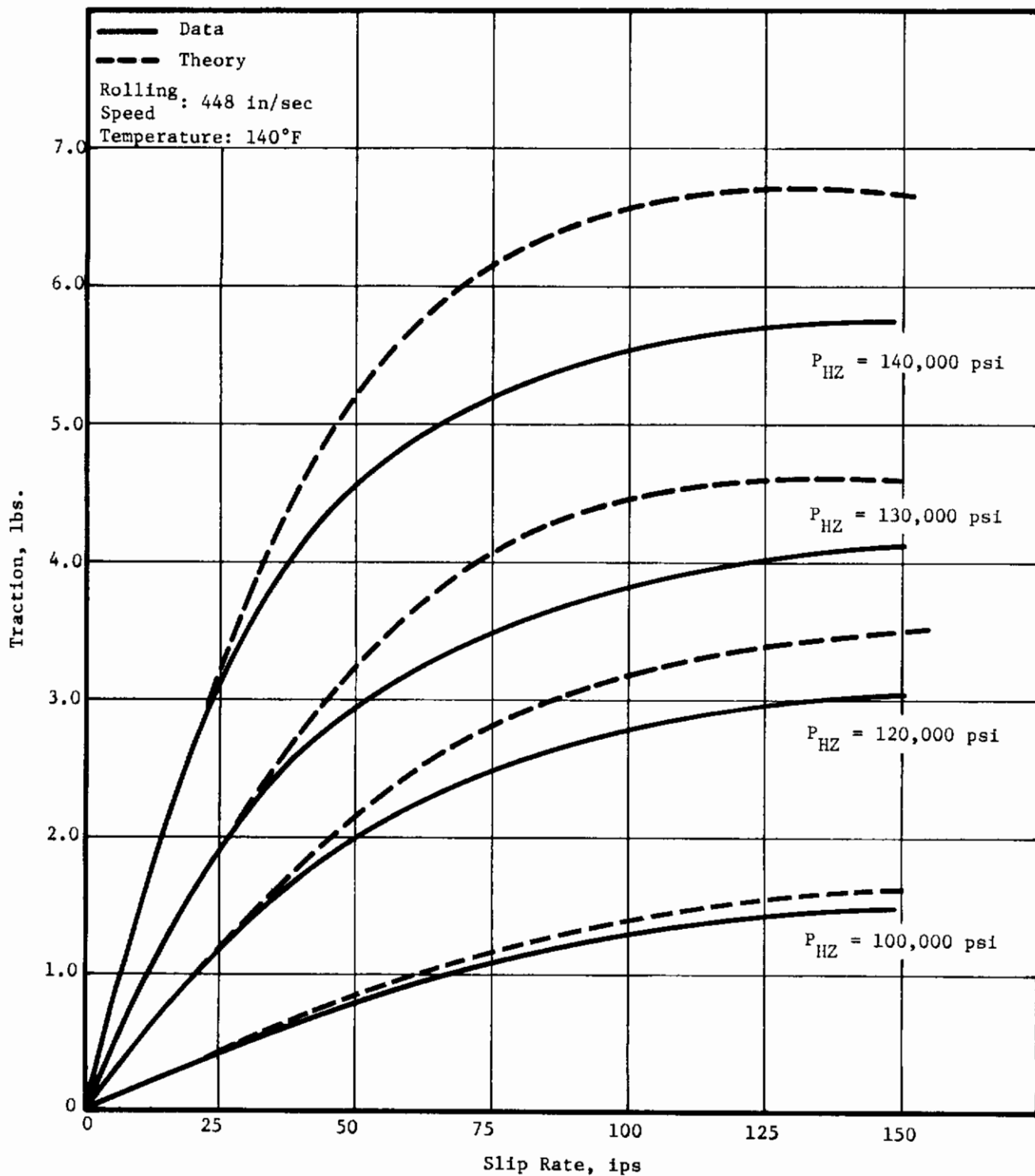


Fig. 11 Low-Speed High-Temperature MIL-L-7808 Traction Data

Contrails

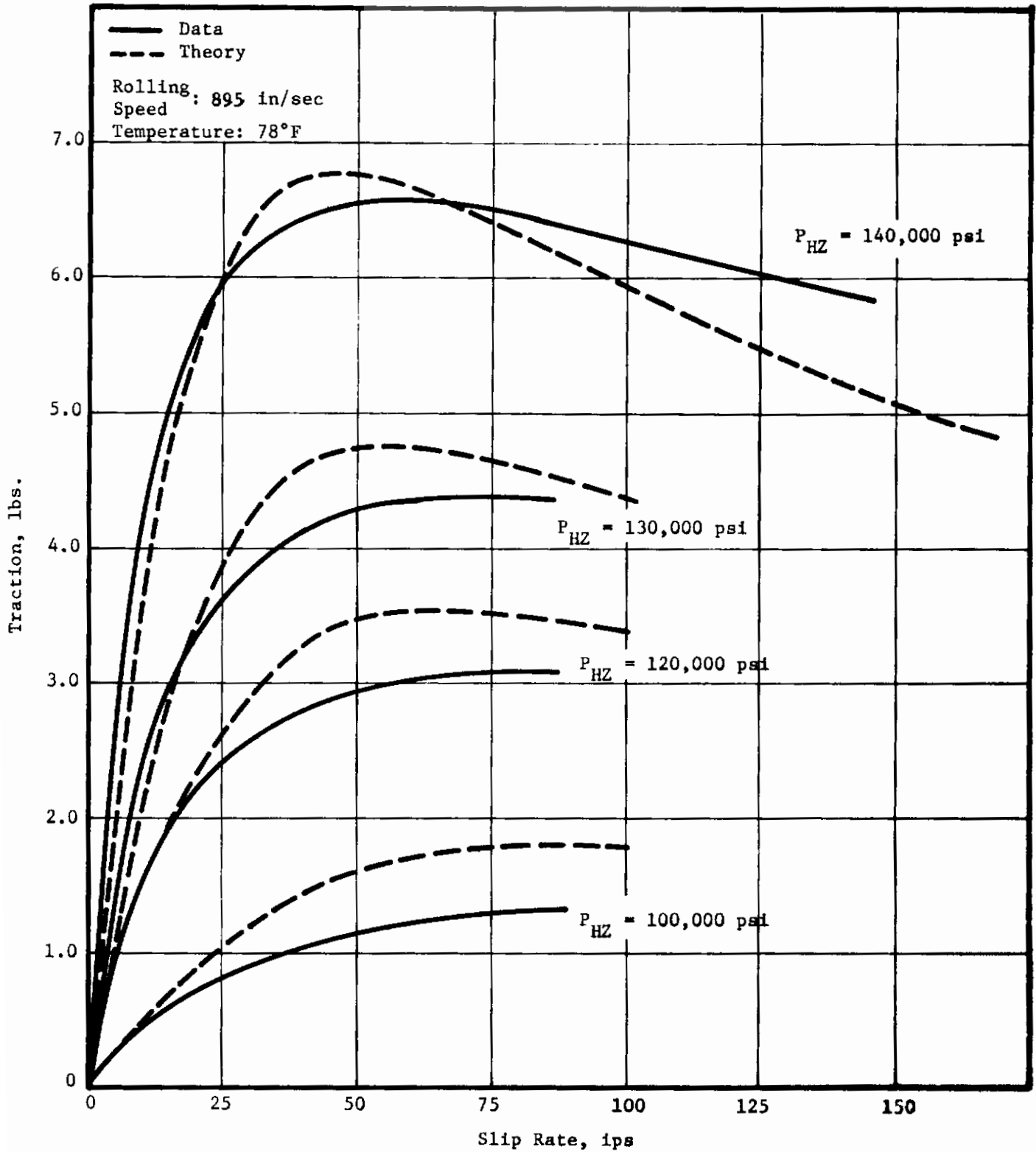


Fig. 12 Medium-Speed Low-Temperature MIL-L-7808 Traction Data

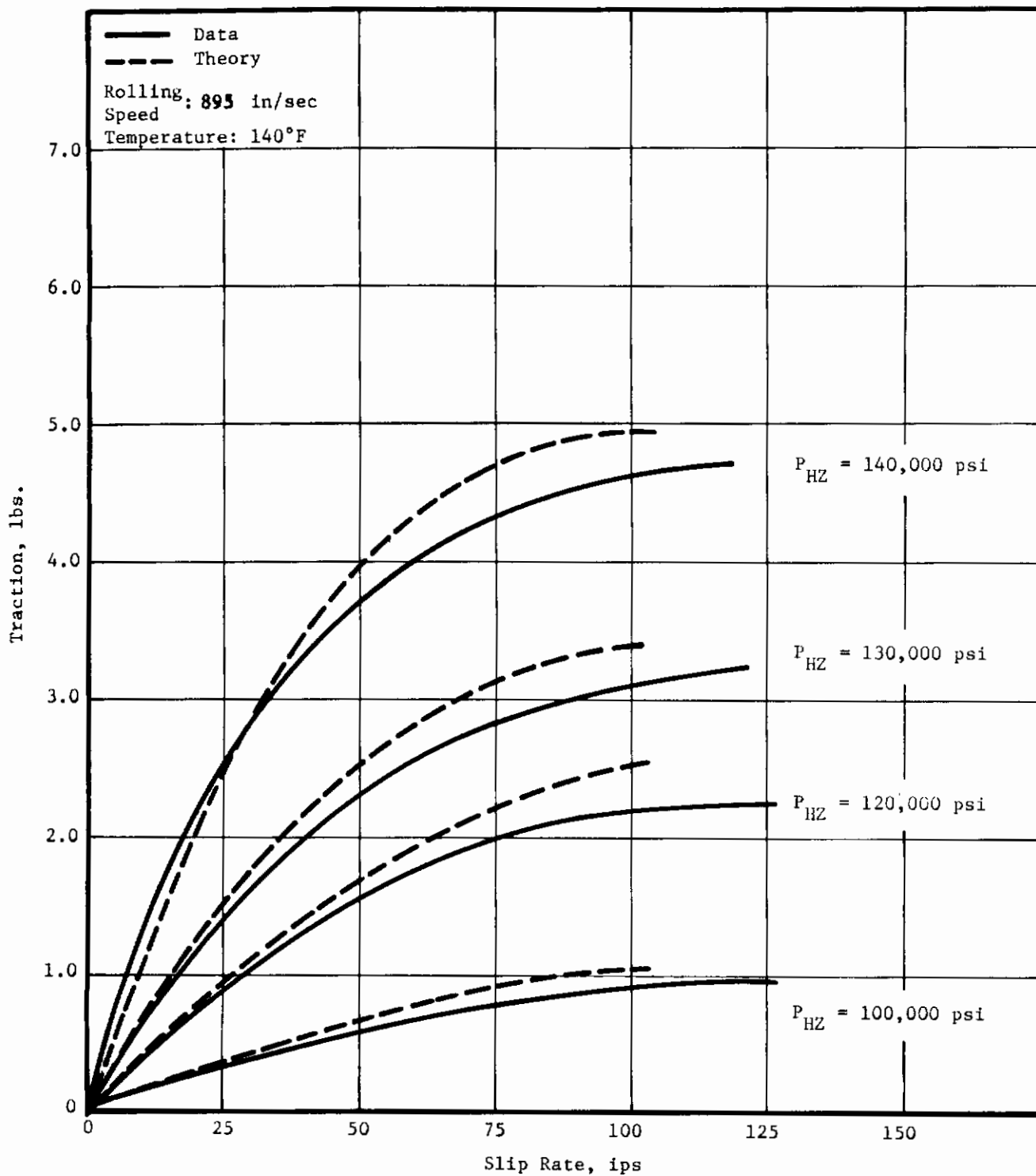


Fig. 13 Medium-Speed High-Temperature MIL-L-7808 Traction Data

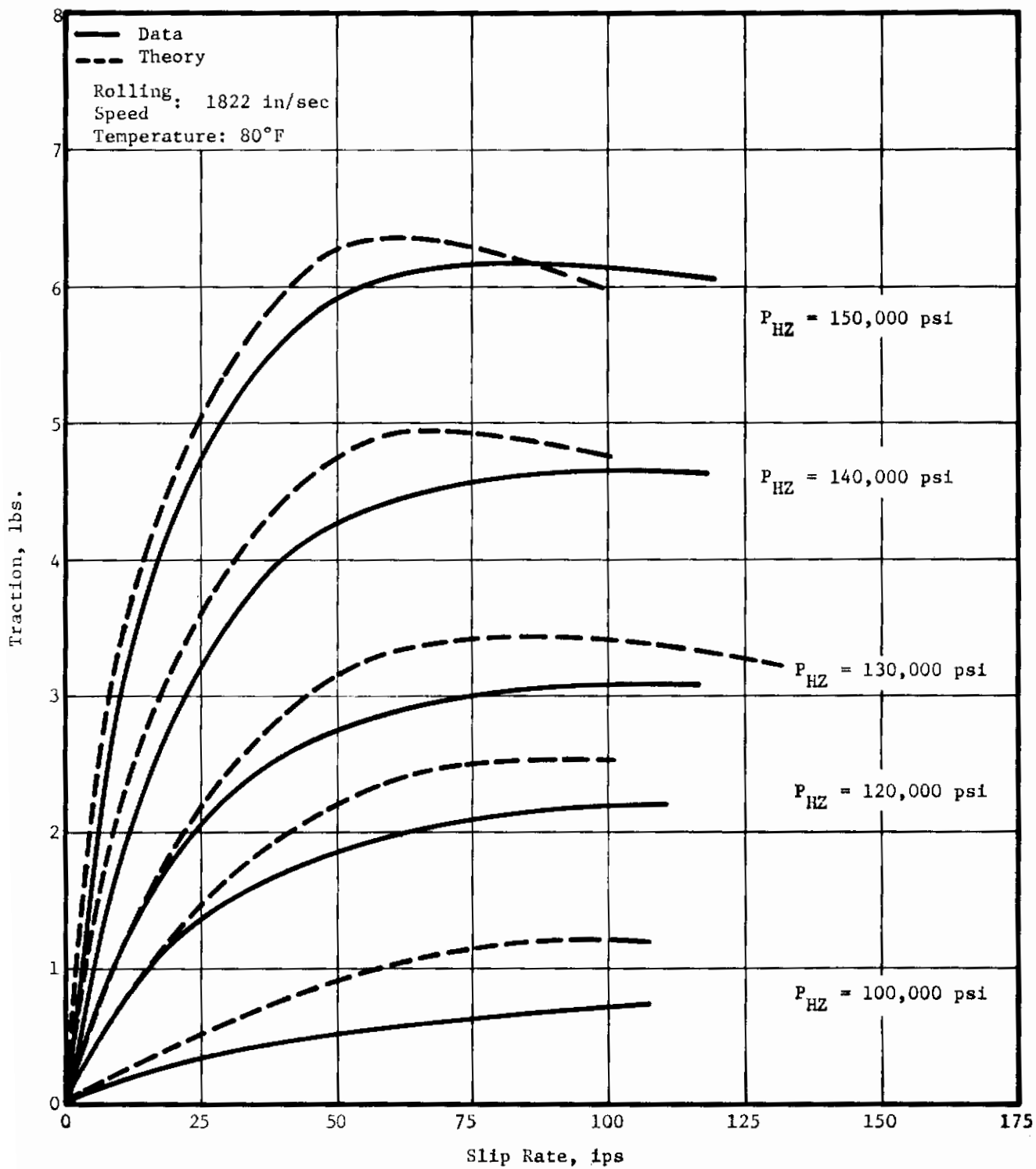


Fig. 14 High-Speed Low-Temperature MIL-L-7808 Traction Data

Contrails

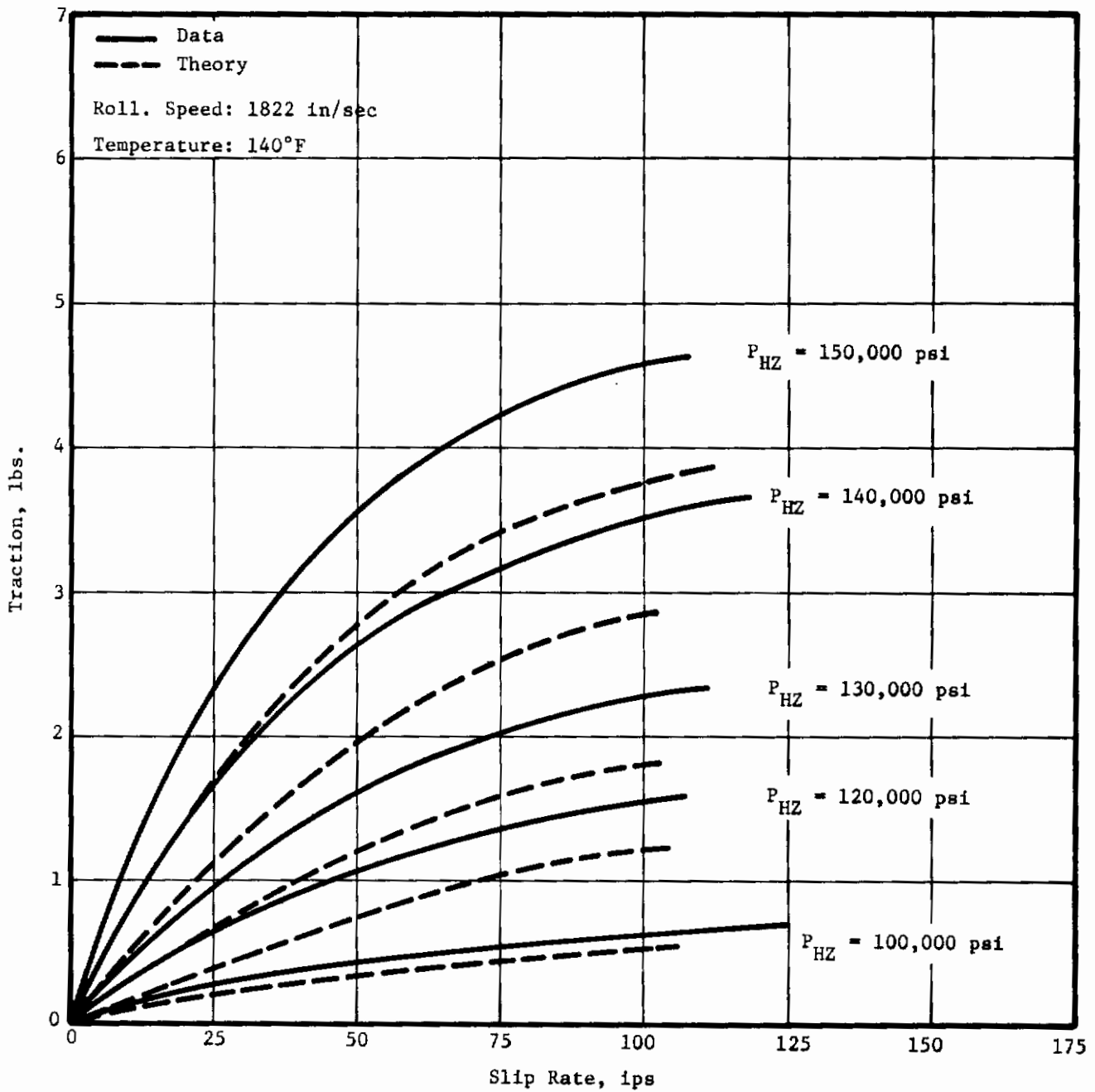


Fig. 15 High-Speed High-Temperature MIL-L-7808 Traction Data

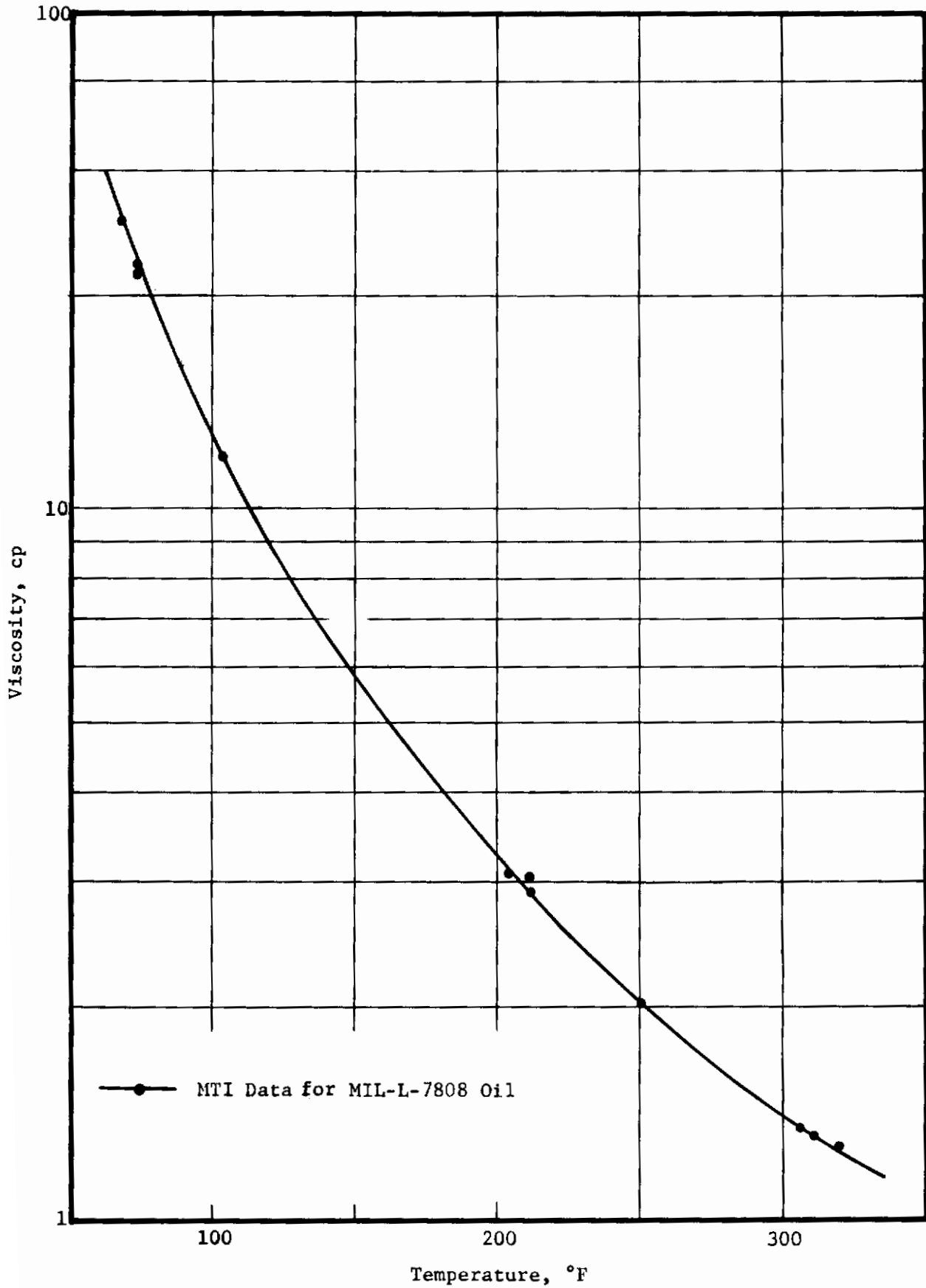


Fig. 16 Viscosity-Temperature Data at Atmospheric Pressure

Contrails

$$\beta = \left. \frac{d \ln \mu}{d(1/T_A)} \right|_{T = T_0} \quad (2)$$

The base viscosity μ_0 obtained from MTI viscosity measurements has been fitted with a viscosity index formula of the form

$$\mu_0 = 1.45 \times 10^{-7} \{ \exp[\exp(-3.705 \ln T + 460 + 24.39)] - .87 \} \quad (3)$$

where the viscosity μ is in units lb-sec/in². This formula corresponds to the solid line passing through the viscosity data appearing in Figure 16.

The viscosity data shown in Figure 16 were obtained at MTI for the MIL-L-7808 lubricant used in all of the traction and film thickness studies. This lubricant, which was supplied by the Air Force, was identified by code number 0-67-23. Viscosity-pressure data was obtained by Midwest Research Institute (Reference 4) for a different batch of the same lubricant identified by Air Force code number 0-67-20.

The MWRI data are shown in Figure 17. The pressure coefficients of viscosity were obtained from the slopes of the $\ln \mu$ versus p curves in the low-pressure region $0 < p < 50,000$ psi as shown by the solid lines in Figure 17. These slopes follow the relationship with temperature

$$\alpha = 5.227 \times 10^{-6} + \frac{.013332}{T + 72} \quad (4)$$

where α has units in²/lb and T is in °F.

Since film thickness is largely determined in the inlet zone where the pressures are somewhat lower than in the center of contact and with pressure coefficient of viscosity, this method of estimating α should be adequate. Equations (2) through (4), together with a thermal conductivity of .056 Btu/hr/ft/°F, completely describe all of the lubricant property input used in obtaining film thickness predictions.

b. Traction Predictions

The prediction of lubricant traction is sensitive to lubricant rheology at the high pressures occurring at the center of contact. The low pressure viscosity data used in determining film thickness is thus totally inadequate in determining traction. Comparisons between traction for 5P4E polyphenyl ether predicted on a basis of low pressure viscosity data with measurements were performed in Reference 1 and showed order of magnitude discrepancies between theory and experiment. Similar comparisons have been made here for MIL-L-7808 oil with similar results.

In order to correlate the traction data, it was necessary to extrapolate viscosity-pressure data outside of the range in which it had been obtained. The hypothetical viscosity relationship that was used at 895 ips is shown graphically by the broken high-pressure lines in Figure 17.

Contrails

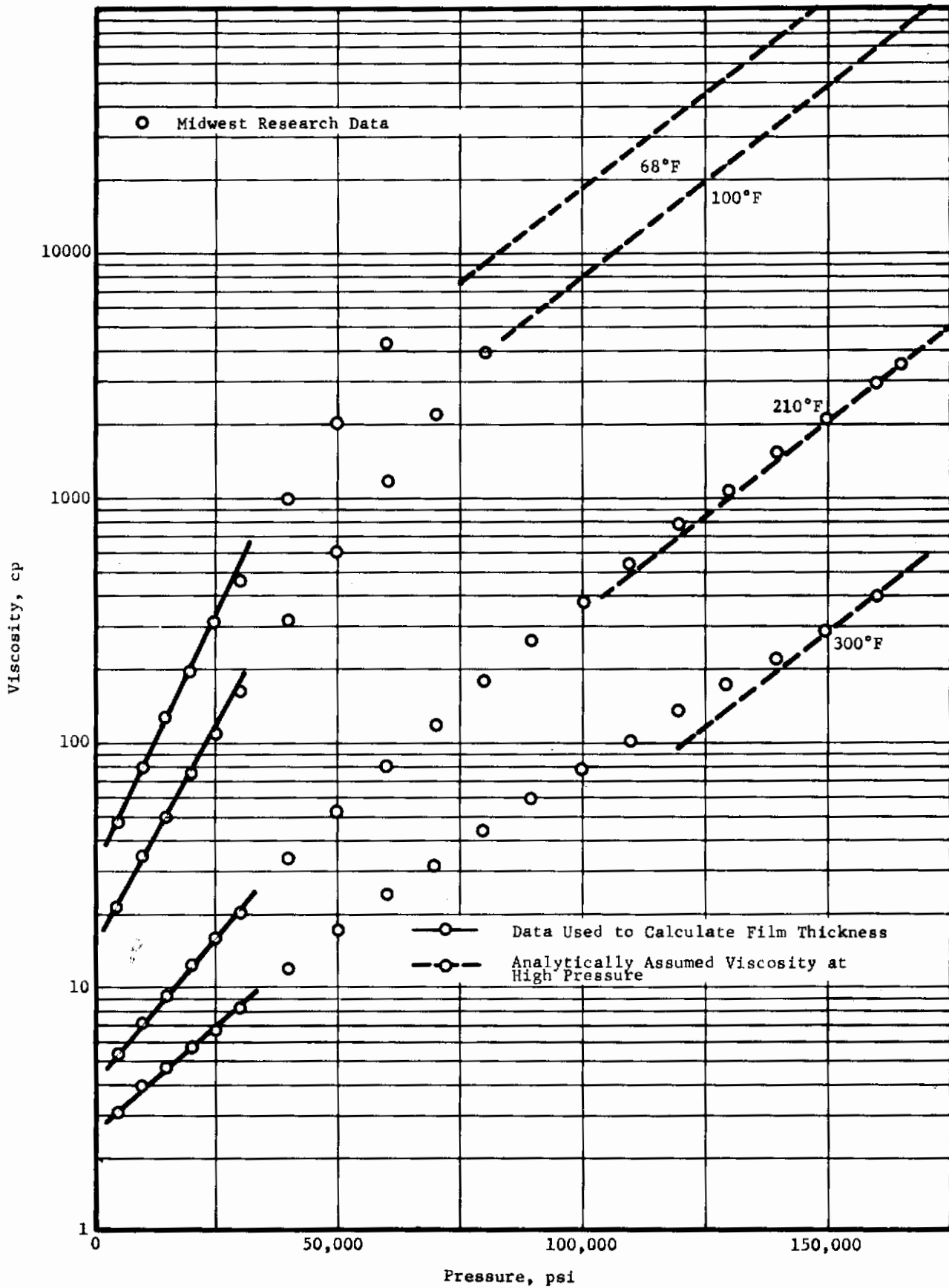


Fig. 17 Temperature-Pressure-Viscosity Data for MIL-L-7808

Contrails

These high-pressure lines are given by the formula

$$\mu_T = 1.45 \times 10^{-7} \chi(\bar{U}) \exp \left(-9.95 + \frac{5247}{T + 115} - \frac{4.189 \times 10^5}{(T + 115)^2} \right) + .36 \times 10^{-4} p \quad (5)$$

The above formula represents a compromise in regard to reasonability with respect to the MWRI viscosity data and the ability to obtain a reasonable fit to the traction data.

The quantity $\chi(\bar{U})$ is a rolling speed parameter that has been used as a multiplier to allow for the observed decrease in traction with increasing rolling speed that is not accountable to predicted film thickness variations alone. Equation (5) was developed by taking $\chi(\bar{U})$ to be 1 at 895 ips.

Tractions are predicted by solving the equations for the shear stress τ_x given in Reference 5 and integrating these shear stresses over the elliptical contact zone with the use of the assumption that the pressure is Hertzian as was performed in Reference 1. The equations for predicting traction as derived in the above references are summarized below. The Newtonian shear stress relationship is given by

$$\frac{\partial u}{\partial z} = \frac{\tau_x}{\mu_T} \quad (6)$$

where μ_T is the viscosity relationship given by Equation (5), u is the local lubricant velocity, and z is a coordinate variable which varies across the film $-h/2 \leq z \leq h/2$. The energy equation in accordance with Reference 5 assumes the form

$$K_f \frac{\partial T}{\partial z} = -\tau_x (u - \bar{U}) \quad (7)$$

There are three constraints on Equations (6) and (7) which are

$$T = T_0, \quad u = U_2 \text{ at } z = h/2 \quad (8)$$

and

$$u = \bar{U} \text{ at } z = 0 \quad (9)$$

Equation (8) may be regarded as providing the boundary conditions on the second order system given by Equations (6) and (7), and Equation (9) may be regarded as the additional constraint for determining τ_x .

Equations (4) through (9) together with the Hertzian pressure assumption

Contraails

$$p = p_{HZ} \sqrt{1 - \left(\frac{x}{b}\right)^2 - \left(\frac{y}{a}\right)^2}$$

and the elastohydrodynamic performance code prediction of film thickness provide all of the necessary equations for calculating the shear stress τ_x at any point in the contact zone. Solutions to the above system are readily obtained numerically with the use of the fourth order Runge-Kutta method.

The tractive force, F_x , is obtained by integrating the shear stress over the Hertzian contact area as shown mathematically by

$$F_x = 4 \int_0^a \int_0^b \sqrt{1 - (y/a)^2} \tau_x dx dy$$

which may be readily reduced to a single integral by expressing the coordinates in polar form.

The agreement between calculated and measured tractions at the extreme temperatures at 895 ips is shown in Figures 12 and 13. It can be seen that good agreement is obtained over a range of loads and temperatures.

The quantity $\chi(\bar{U})$ which has been used to modify viscosity to account for possible time effects is shown graphically in Figure 18. The points shown are those actually used in obtaining the theoretical curves shown in Figures 10 through 15. The solid line represents the formula

$$\chi(\bar{U}) = \begin{cases} 1 & \bar{U} < 900 \text{ ips} \\ \left(\frac{900}{\bar{U}}\right)^{0.23} & \bar{U} \geq 900 \text{ ips} \end{cases} \quad (10)$$

Hence, the traction correlation may be extended over a range of rolling speed as well as temperatures and loads.

The above correlation is not intended to represent a full theoretical description of lubricant traction, and the quasi-empirical nature of the correlation must be stressed.

Complete high-pressure-viscosity data for the fluid tested are lacking and whereas the description given by Equation (6) is a possible one, it does not necessarily represent true viscosity behavior. Similarly, tractions have been computed with predicted film thicknesses which could also be in considerable error. In light of these

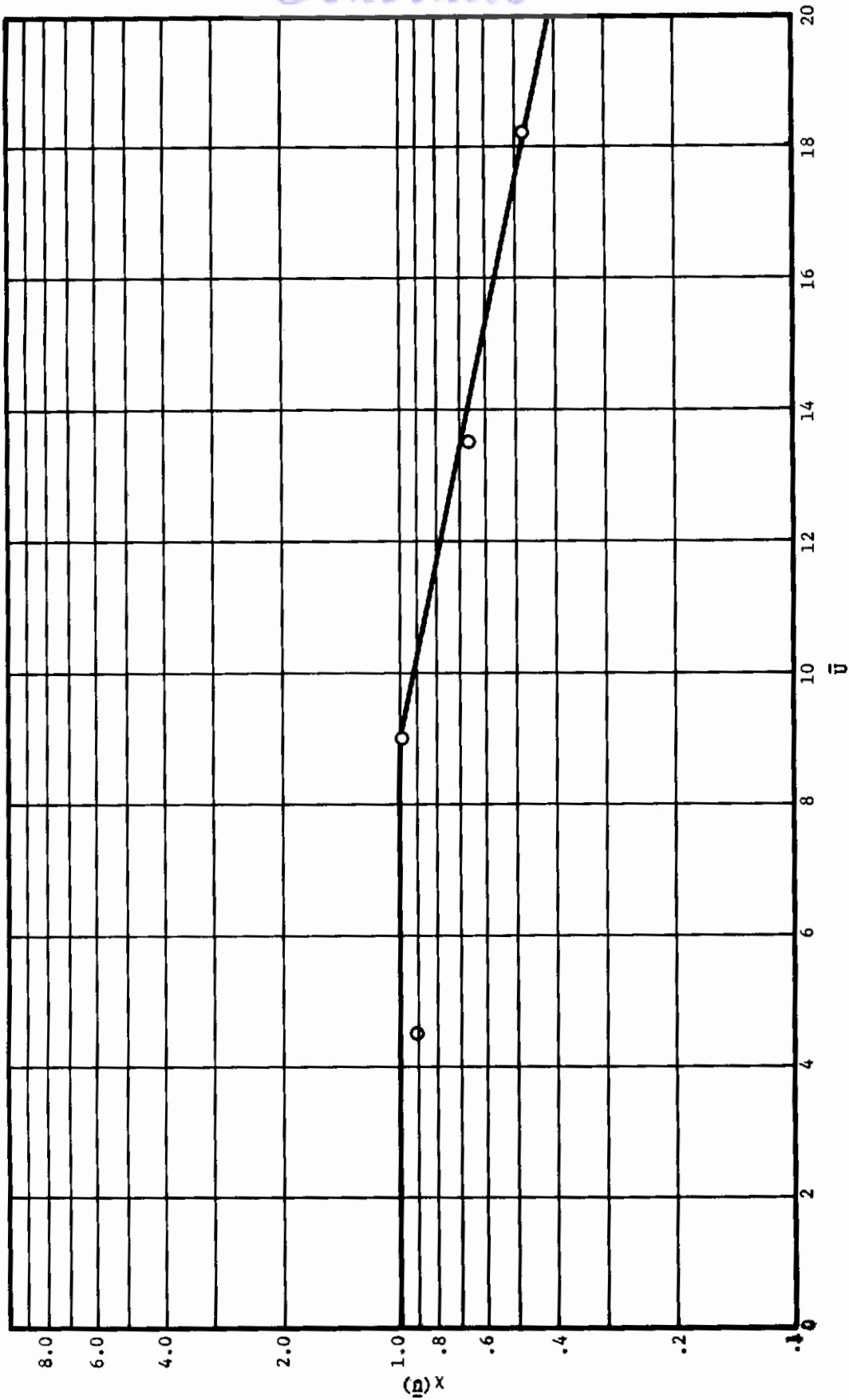


Fig. 18 Empirical Viscosity Time-Delay Function

Contrails

and other uncertainties, the analyses used here should be regarded primarily as a useful correlating device for interpolating and extrapolating traction data over reasonable ranges; but care should be taken before drawing any theoretical conclusions regarding the high pressure, high shear rate, short-time rheological behavior of the lubricant.

Contrails

SECTION III

CAPACITANCE FILM THICKNESS MEASUREMENT AND ANALYSIS

Capacitive film measuring techniques have been described in the literature since 1955. Crook (6), during the late fifties and early sixties, found through the use of the capacitive approach many of the unanticipated film thickness relationships between rolling speed and contact loading.

The measurement of film thicknesses with capacitive techniques requires that the test roller specimen be isolated electrically from the mating roller. The method used in the present study was explained in detail in Reference 1. The lower disc of the test rig was designed to use high compression plexiglass as inserts for electrical isolation. The choice of thickness and material was governed primarily by the necessity to minimize the fixed capacitance to ground. Direct electrical connection to each roller was made via two rotating cables ending in two mercury baths for positive electrical integrity to the capacitance bridge system. Any attempts to use electrical paths of grounding through the shaft support bearings resulted in an erratic, undesirable ground loop.

The total capacitance of such a design is the sum of the isolated disc to ground and the contact zone capacitance formed by the thin oil film. Since these capacitances are in parallel

$$C_{\text{total}} = C_{\text{constant to ground}} + C_{\text{contact zone}}$$

In the present design the capacitance of the contact zone was equal to or greater than the constant capacitance to ground when the test roller was running under loaded conditions.

The exact evaluation of the capacitance present at the lubricated contact point of the discs depends on a knowledge of the mating disc curvatures and the way in which the dielectric coefficient of the separating material varies with pressure and temperature. Thus,

$$C_{\text{contact zone}} = C(K, h, T, P_{\text{HZ}})$$

Several independent experiments were performed to check out the various independent parameters and the theoretical expectations. The contact zone capacitance was investigated for sensitivity of gap separation with and without contact loading. Lubricant dielectric coefficient sensitivity with temperature was also investigated.

The calculated capacitance of the contact area is obtained numerically from

$$C_{\text{contact zone}} = K \epsilon_0 \int \frac{dA}{h} = K \epsilon_0 \left(\frac{\bar{A}}{h} \right)$$

where $\left(\frac{\bar{A}}{h} \right)$ is evaluated numerically with the use of an analysis which corrects for Hertzian elastic distortion both interior and exterior to the contact

ellipse (see Appendix III for analyses). The integration is carried to infinity in the rolling direction but truncated at the disc edge perpendicular to the direction of rolling (see Figure 19). Capacitive contributions from surfaces beyond the edge are taken as a constant portion of the fixed isolated disc to ground capacitance.

1. EXPERIMENTAL SET-UP AND PRELIMINARY CHECK WITH ANALYSIS

Two conditions of filling the gap between the discs with dielectric material were considered analytically. The first case considered a single dielectric in and around the disc whereas the second considered a double dielectric filling of the gap (see Figure 20).

A preliminary check of analytically-determined capacitances and experimental variations with disc separation was performed with the test arrangement shown in Figure 21. The contact zone gap contained a single dielectric and varied from zero to one-hundred mils with increments as small as 2.8 microinch in the 10 to 100 microinch range of separation. Gap reading accuracy was 2.8 micro-inches from the standard dial micrometer bed and lever setup shown. The lower shaft was isolated electrically from the grounded upper shaft.

The contact zone capacitance as determined experimentally and analytically as a function of minimum gap separation is plotted in Figure 22. The fixed capacitance to ground was taken as the capacitance of the system determined with a gap of 100 mils and was subtracted from each subsequent reading. The measured capacitances were obtained with a standard carrier frequency capacitance bridge. The auto balance precision bridge combines speed of measurement with .01 percent accuracy and a digital display of capacitance to five significant places, as well as the conductance of the component under test. The bridge used has seven decade ranges from micro-farads to pico-farads. Each decade provided digital capacitance readings or analog signals with slightly less accuracy for automatic graphic display of measured capacitances.

In addition to knowing the unloaded capacitive dependence on separation, the fully loaded sensitivity must also be determined before lubricant film thickness can be found from capacitance data. Contact zone capacitance is very sensitive to loading since the area of the Hertzian zone increases as

$$\text{Contact Area} \propto \text{Load}^{2/3}$$

An experimental check of the expected capacitive changes with increasing loads was performed with mica separating shims. Thin cleavages 1.3 mils thick were successively stacked between the two stationary discs. Increases in capacitance with higher loads and decreases in capacitance with a greater number of mica shims were observed. The results are displayed in Figure 23. The use of mica as a load calibrating material presents some problems experimentally. The dielectric coefficient can vary depending upon the trace mineral content of the pieces used in testing. Published variations from 5.0 to 8.0 are common and are not accurate enough for calculating purposes. The two points at 80 ksi indicated in Figure 23 were used in determining ground capacitance results and the dielectric coefficient of the mica. The dielectric coefficient was determined to be 7.45 which lies within the range specified above. The coalescence of theory and experiment for both loaded and unloaded separations of the

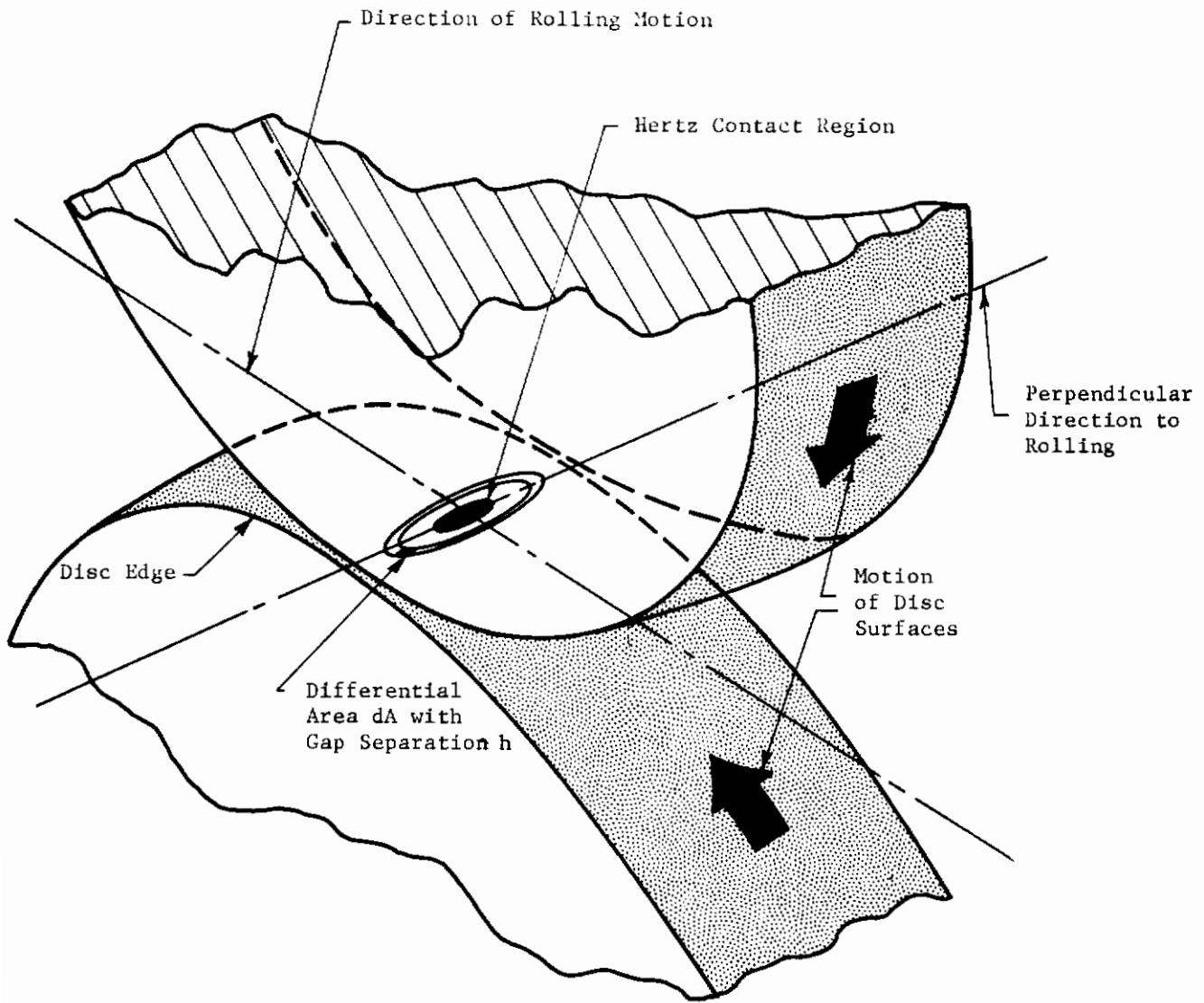


Fig. 19 Contact Ellipse Schematic of Crowned Disc-Specimens

Contrails

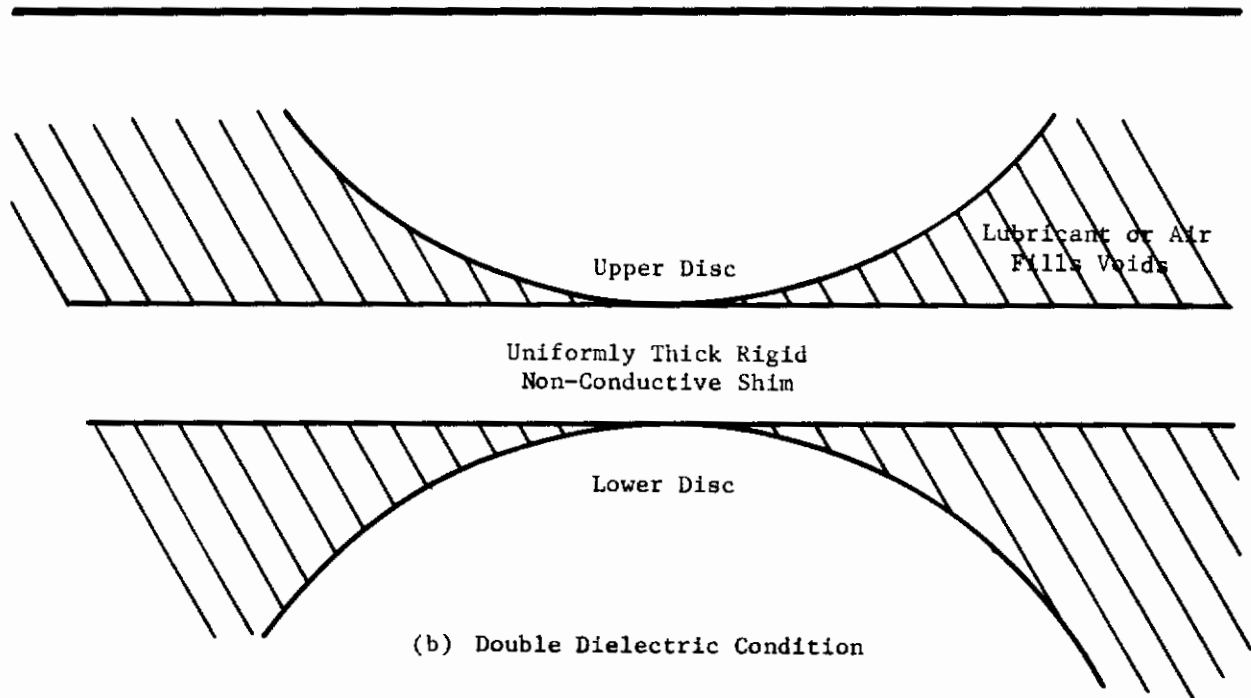
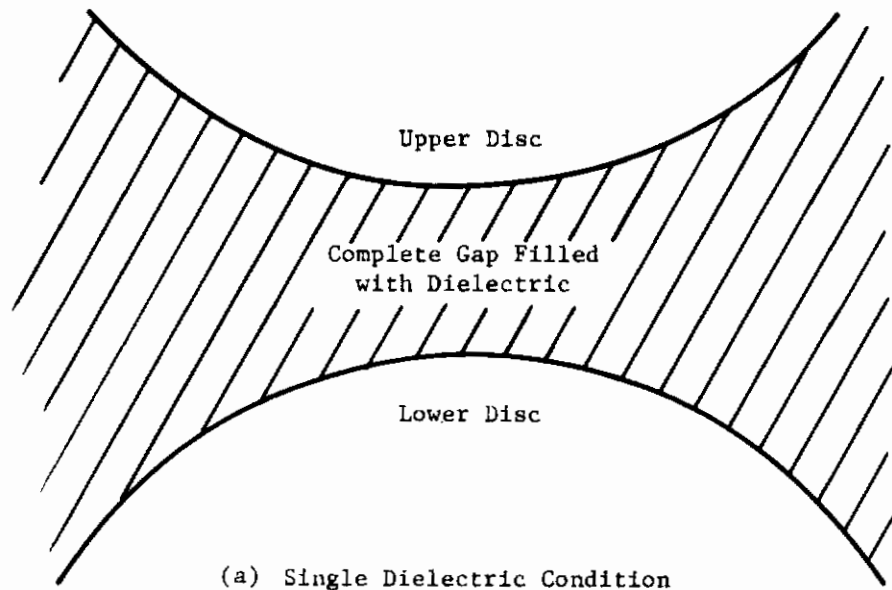


Fig. 20 Dielectric Conditions Considered Analytically

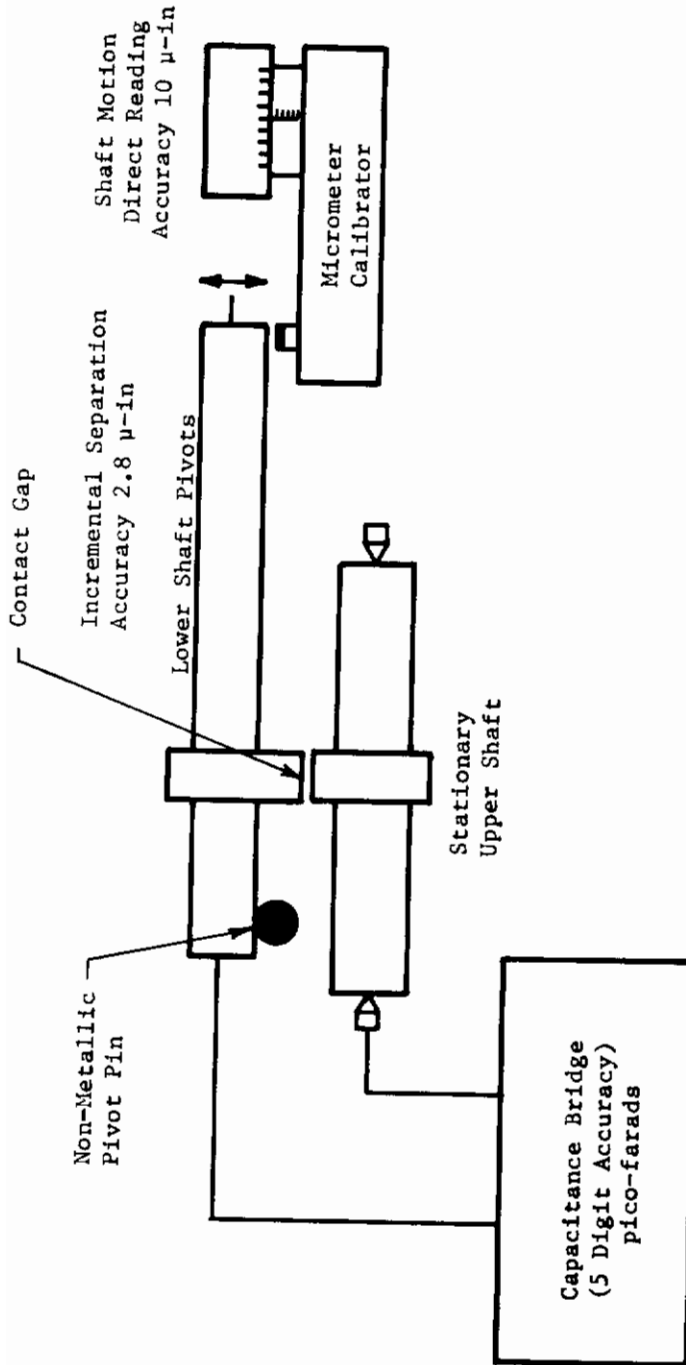


Fig. 21 No-Load Gap Separation Capacitive Test Schematic

Contrails

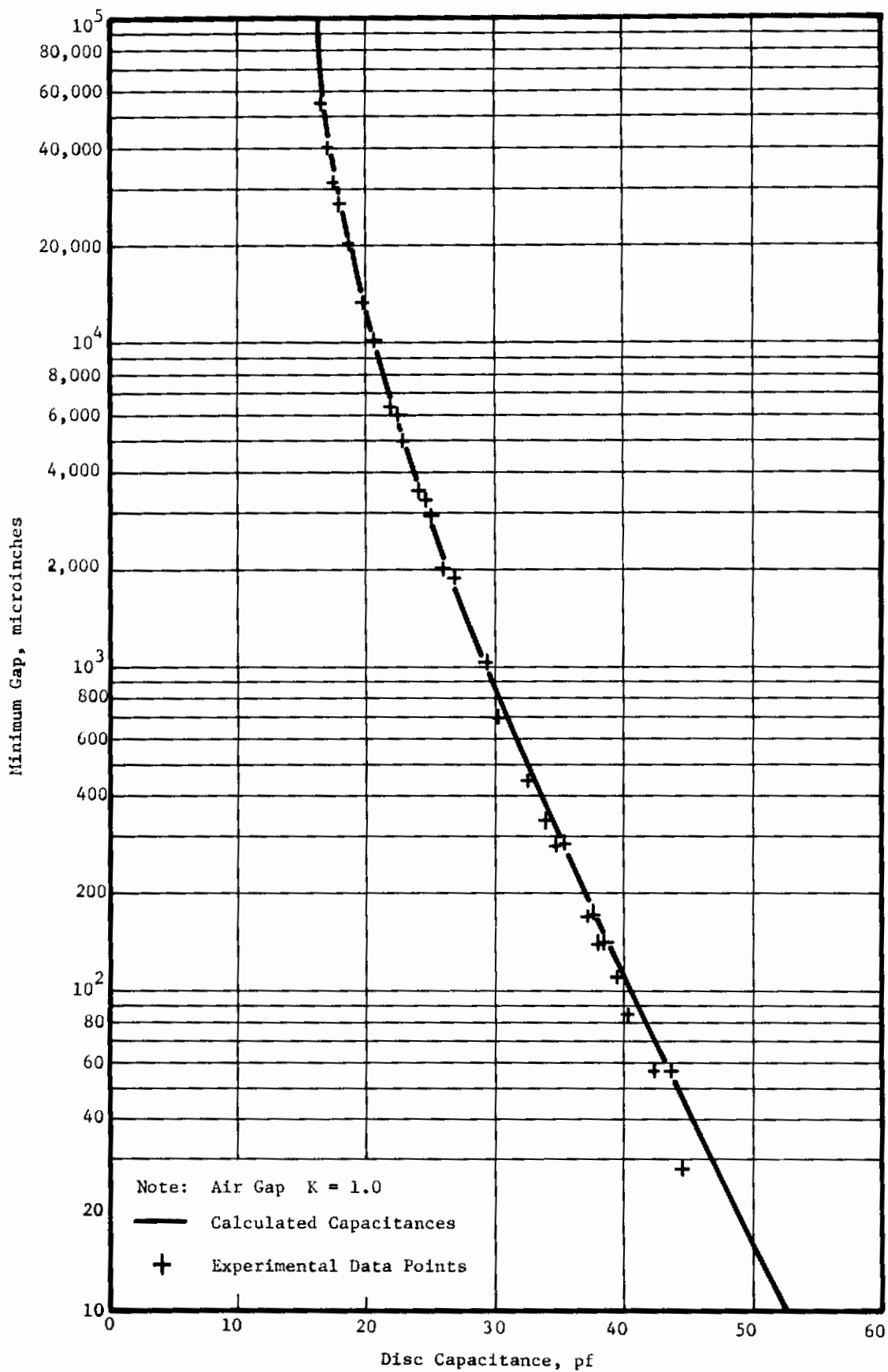


Fig. 22 No-Load Gap Separation Capacitive Data

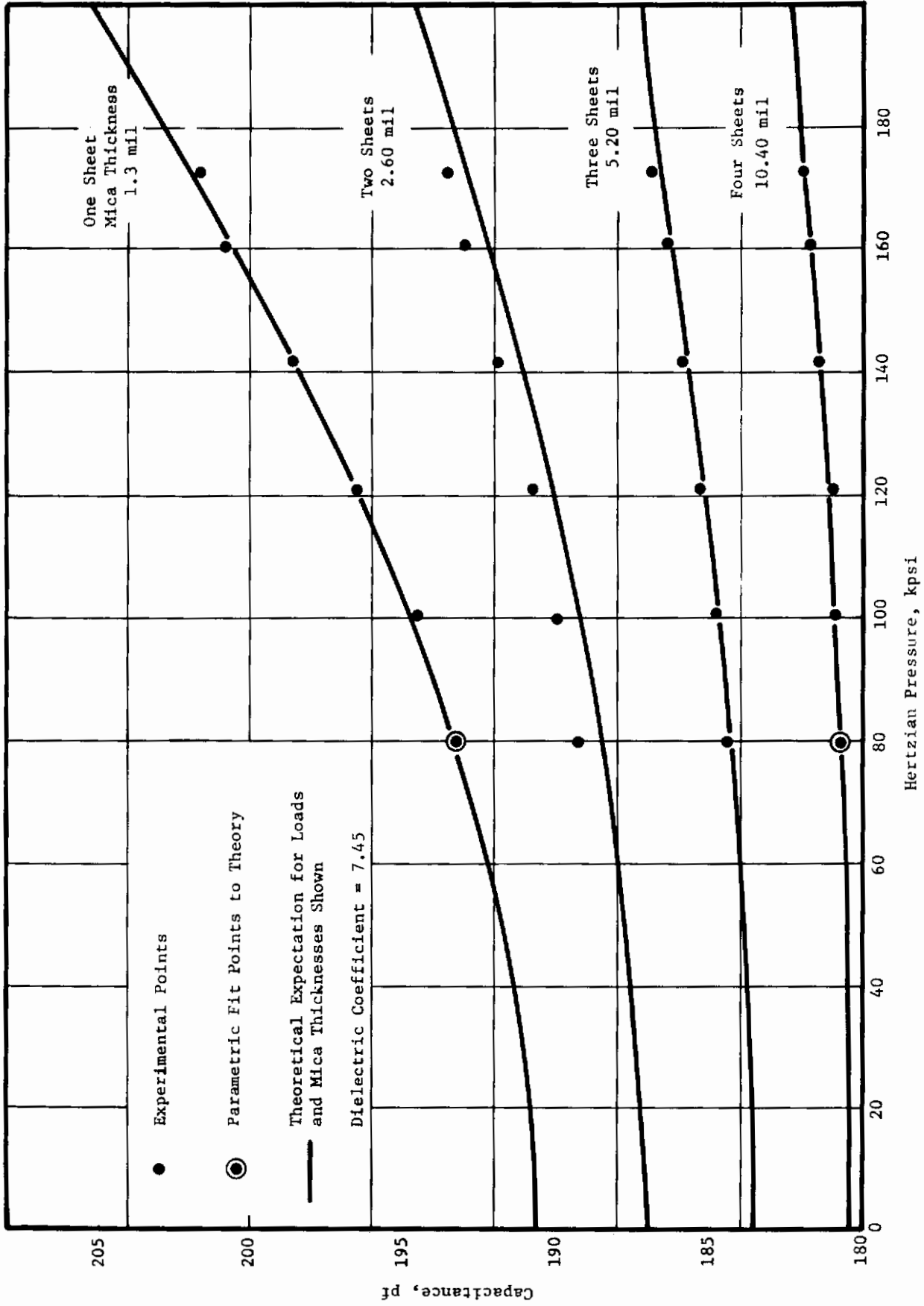


Fig. 23 Load-Separation Capacitive Data

NYT-13401

test specimens provided enough evidence to proceed in measuring full fluid film thicknesses under rolling conditions.

2. ANALYTICAL ASSUMPTIONS

Three basic assumptions were made in making the film thickness determinations from the capacitance data. Although full Hertzian distortions were used in calculating the contact area and gap distribution, the trailing edge dip present under rolling conditions was neglected. Since the dip was observed in the optical work (see Section IV) to extend over a minor portion of the contact area, this would result in a small percentage inaccuracy in the relative capacitances obtained. A twenty percent trailing edge dip occupying ten percent of the contact zone area could be expected to have no more than two percent error in expected capacitance produced by the contact zone.

The second simplifying assumption is related to the distribution of the loci of all points of equal separation in and around the contact zone between the discs referred to here as "fringe lines". Points of equal separation are calculated along the major and minor axes in and around the load-carrying zone of the test specimens. Although the fringe lines are not truly elliptical (a maximum radial difference of approximately 6 percent was observed analytically), they were assumed to be. For example, the numerical point by point distributions are compared to their elliptical counterparts and shown in the schematic of Figure 24. Elliptical distributions were assumed only to reduce calculating machine time. No significant error in calculating is generated with a maximum disparity of 6 percent, since the total capacitance is a summation of all differential areas with very small curvatures.

The third conceptual simplification made in calculating capacitances is related to the temperature within the rolling contact. The rolling zone was considered to have a sufficiently small temperature rise such that it could be neglected for the loads investigated. This assumption is valid since the temperature variations in the dielectric coefficient were found to be smaller than .04 percent per °F of a temperature rise from 70°F to 300°F for the MIL-L-7808 tested. It has also been observed by Hamilton and Moore (7) that the temperature rise in a pure rolling contact similar to the present setup is of the order of 1°F. Greater temperature rises would occur in sliding contacts; however, even 100°F increases in temperature would not significantly affect the results. In fact, experimentally some tests were observed with and without slip up to 10 percent and very little change in capacitance (~ 2 percent) was observed.

3. DIELECTRIC PRESSURIZATION AND CALIBRATION CURVES

Dielectric coefficients of non-polar fluids are known to respond to mass density changes as a result of applied pressure. The Clausius-Mossotti (8) equation is normally assumed in describing the reactive changes unless precise pressure-dielectric measurements are made on the test lubricant. Direct measurements by Galvin, Naylor and Wilson (9) have produced an explicit relation

$$K/K_0 = 1 + 2.59 \times 10^{-6} p - 29.8 \times 10^{-12} p^2$$

for a mineral oil where p is the pressure applied to the fluid in pounds per

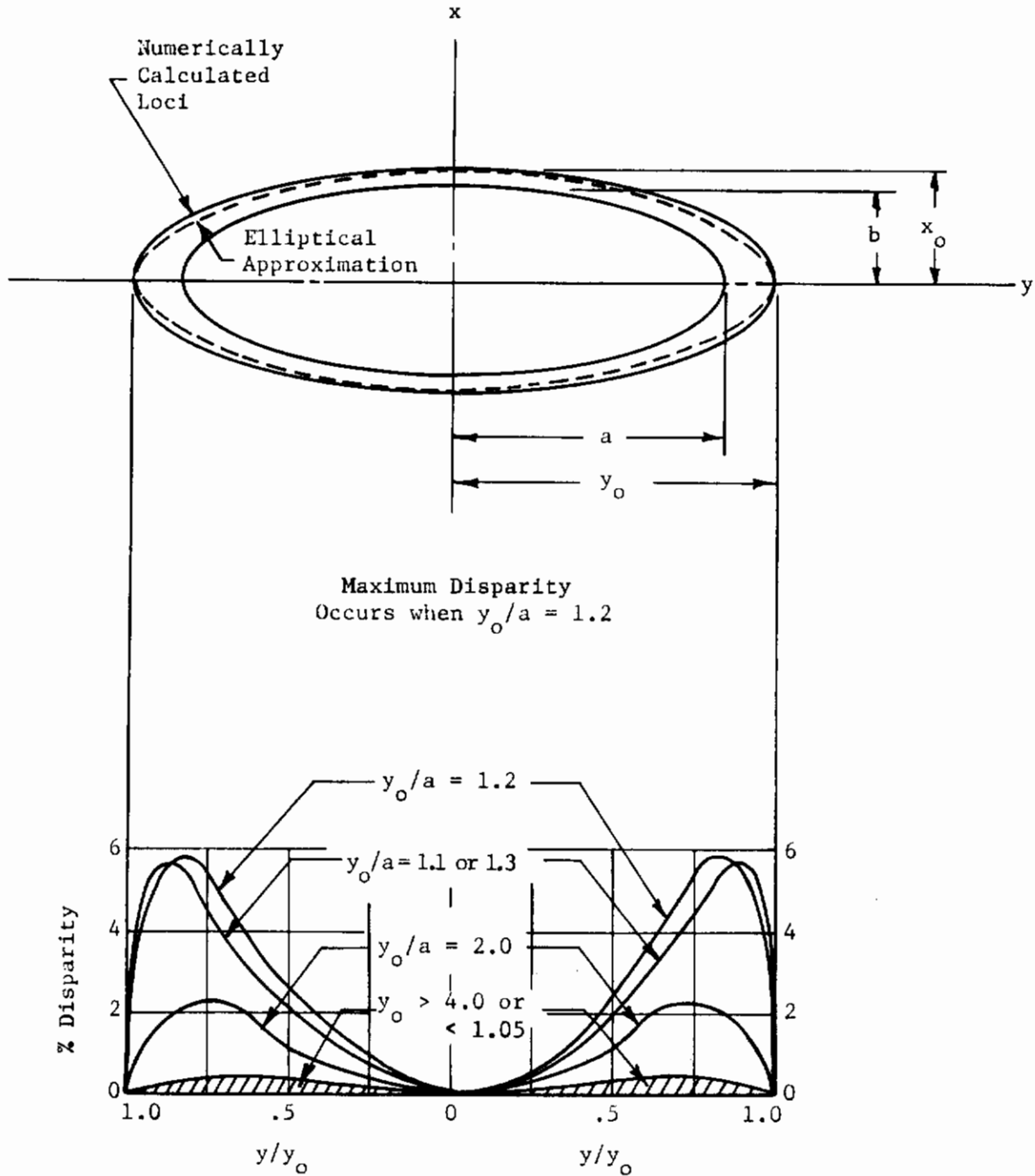


Fig. 24 Disparity Between Elliptical and Numerically Calculated Loci of Constant Separation

square inch. This estimation of the effective point wise dielectric coefficient throughout the contact region was assumed in the present film thickness determinations. It is apparent that pressure levels up to 80,000 psi would not significantly effect the dielectric coefficient. Film thicknesses below 100 microinches, as determined with and without the above pressure modifications, are presented in Figure 25 for comparison. Shown are two analytically-derived sets of calibration data from which film thicknesses can be taken for any level of disc loading. The dotted curves contain all significant load distortions and separation effects but do not include the point by point pressurization effect on the lubricant dielectric coefficient. The solid set of curves include the dielectric pressurization effect for each load depicted.

Although it appeared at first there was a possibility of getting a significant change when the dielectric pressurization was considered, the calculations are less sensitive than was anticipated for loading up to the 170,000 psi range.

Since there was shown with air to be a valid agreement between experimentally determined and calculated films for disc separations down to 30 microinches, five points between 1 and 10 mils disc separation were used for defining the no load under fully flooded conditions on the disc machine. A full set of analytically obtained capacitance data and the corresponding range of thicknesses for which experimental values were obtained is presented in Figure 26. A similar set of curves obtained analytically for polyphenyl ether is displayed in Figure 27.

4. TEST DATA

The capacitance data as taken from the disc machine is plotted automatically from analog signals as a function of rolling speed. A typical plot of actual recorded capacitance data is displayed in Figure 28. For the load and speed indicated, the MIL-L-7808 lubricant plot is not valid at disc rotational frequencies less than 800 rpm. The film at this point has become sufficiently small to allow some degree of asperity contacting which prevents the capacitance bridge from operating properly. Refer to Section VI for plots which show the nature of the asperity contact interactions below 1000 rpm. The capacitance obtained at each rolling speed is then used analytically to get true film thickness as a function of disc load and speed. Successive runs made at elevated temperatures show the dependence of film thickness on fluid viscosity.

Loading effects on MIL-L-7808 film thickness have been observed by various experimenters in the past. Kannel, Bell and Allen (3) presented evidence for a large load effect. The loading sensitivity in the present study made with capacitive techniques is functionally dependent upon the load level under examination. At heavy loads the film thickness was found to vary with load to the .2 power or less whereas at somewhat lighter loads power variations as high as .6 were encountered.

From a series of capacitance curves (similar to the one shown previously in Figure 28) taken at different loads, a functional plot of observed film thicknesses versus rolling speed may be obtained with the analysis. The observed film versus speed relation is the contents of Figure 29.

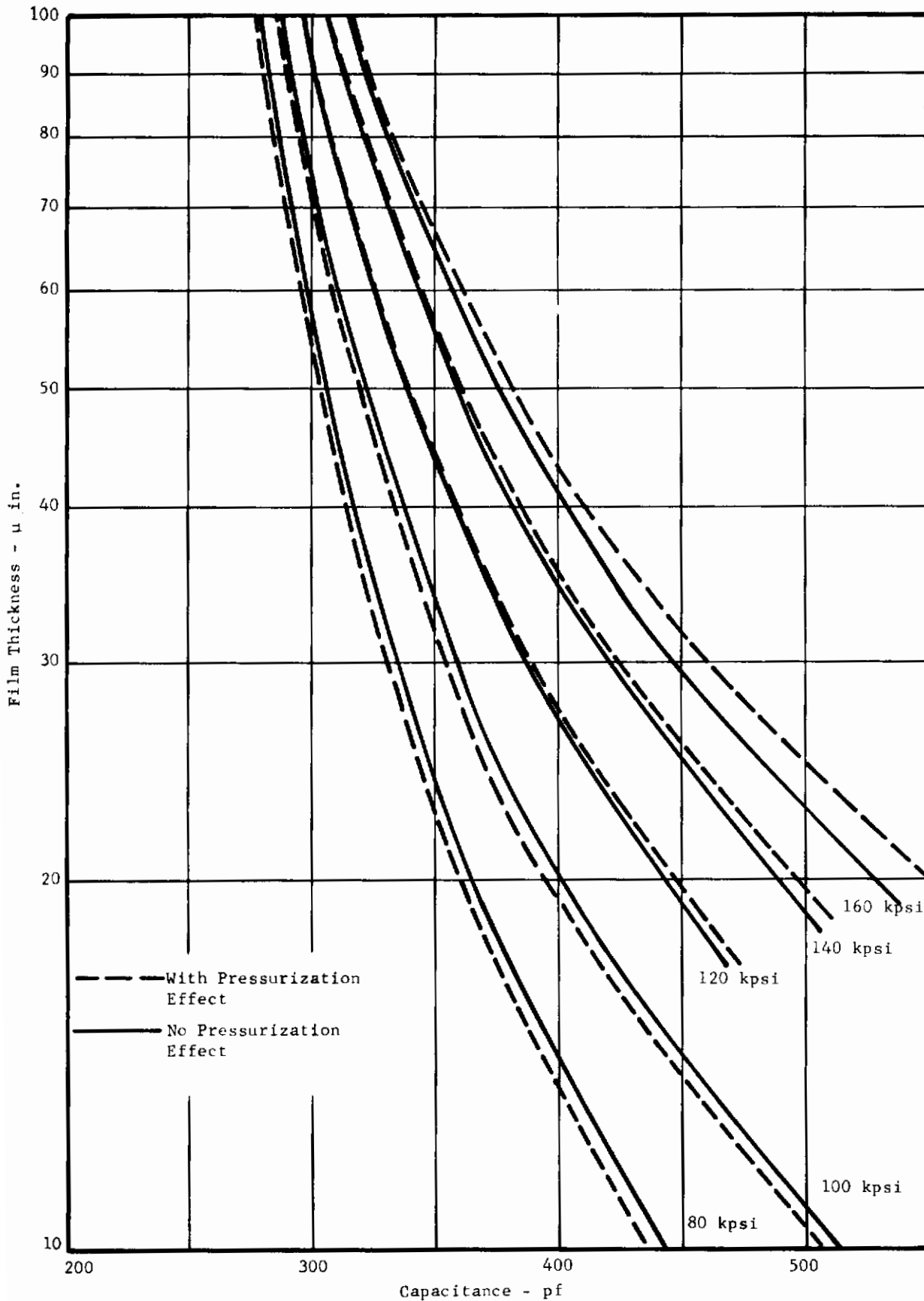


Fig. 25 Analytical Capacitive Film Thickness Variations With and Without Dielectric Pressurization Effects

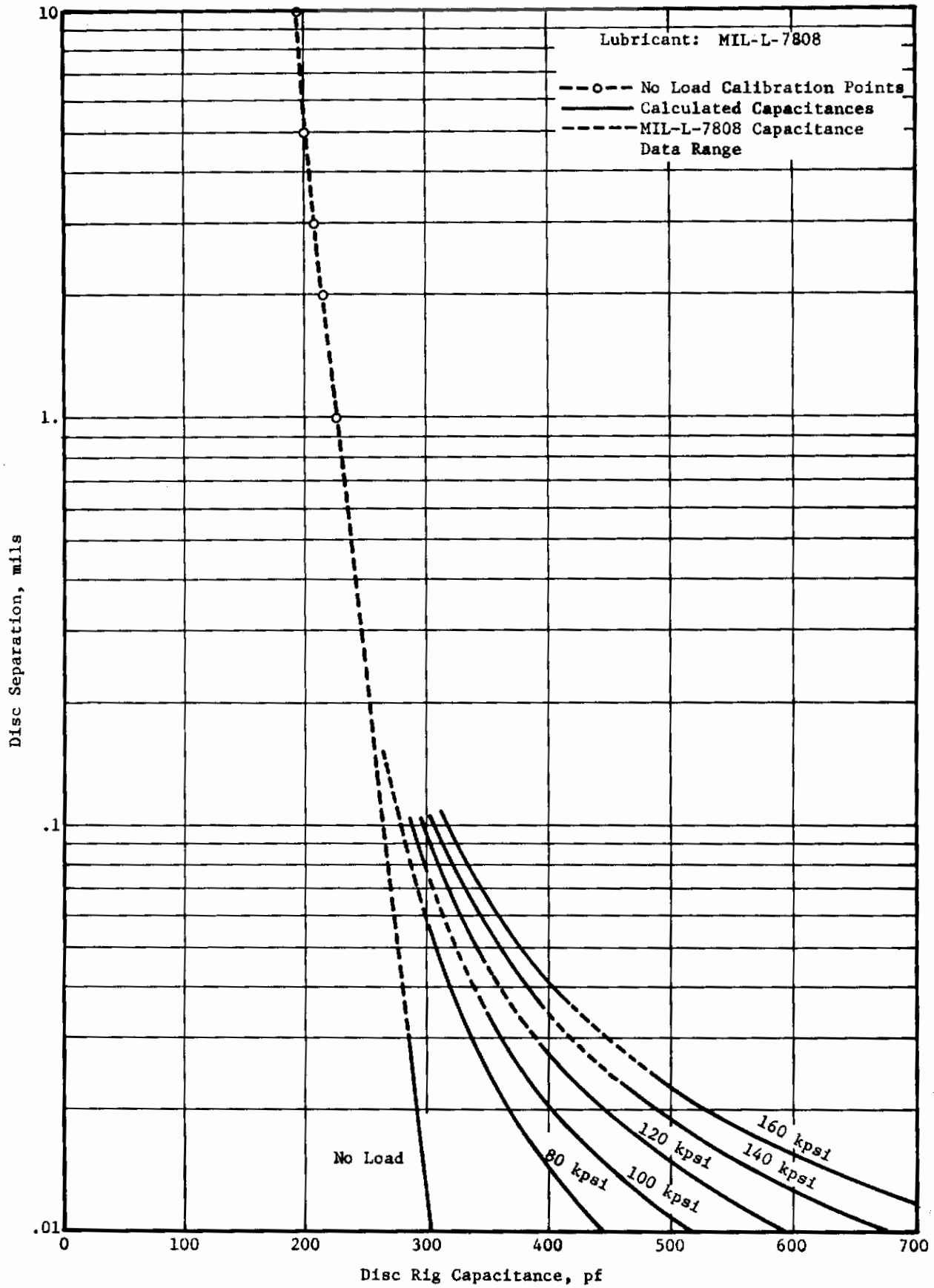


Fig. 26 Analytical and Calibration Data for Capacitance Versus Film Thickness

Contrails

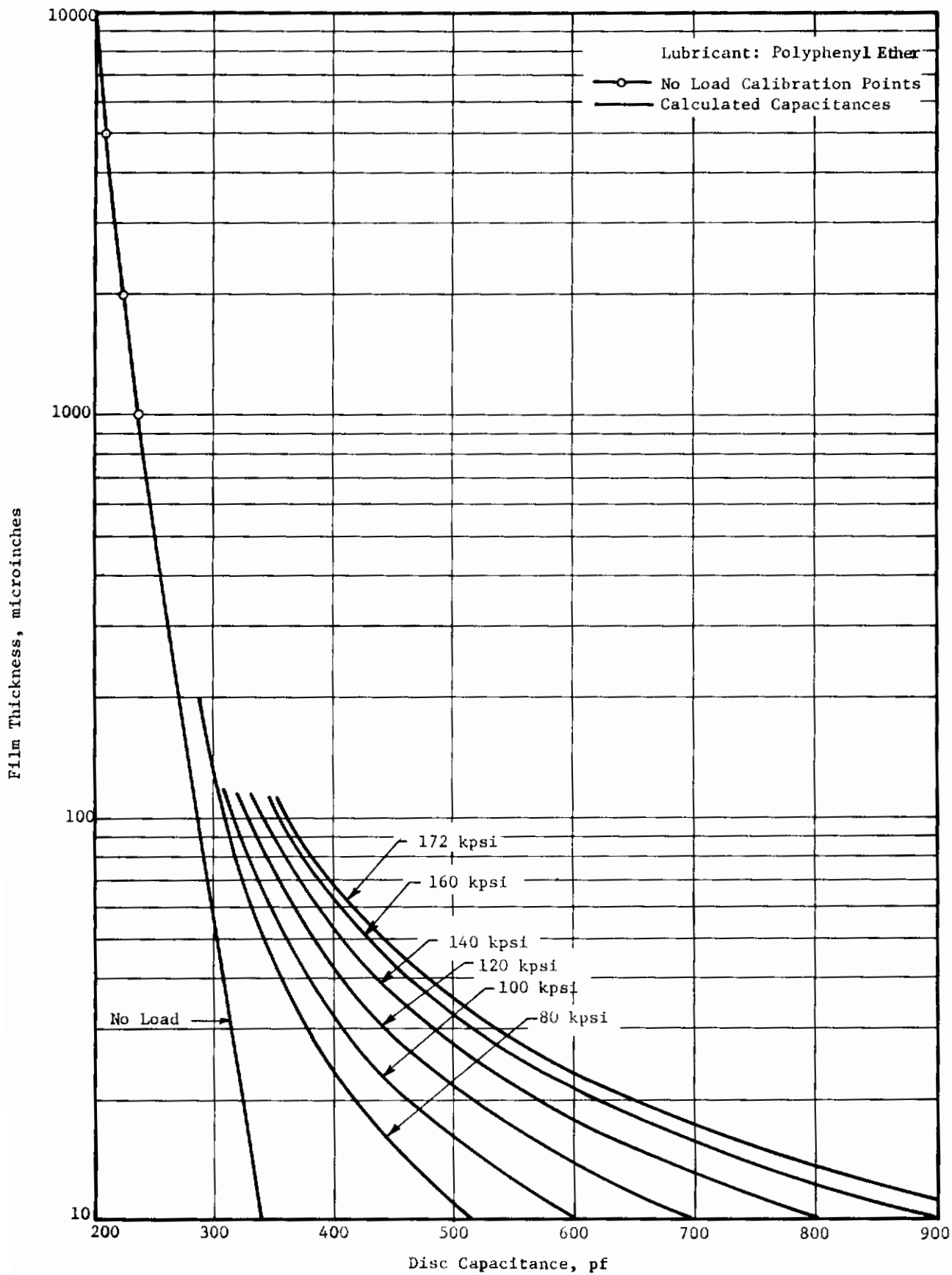


Fig. 27 Analytical and Calibration Data for Capacitance Versus Film Thickness

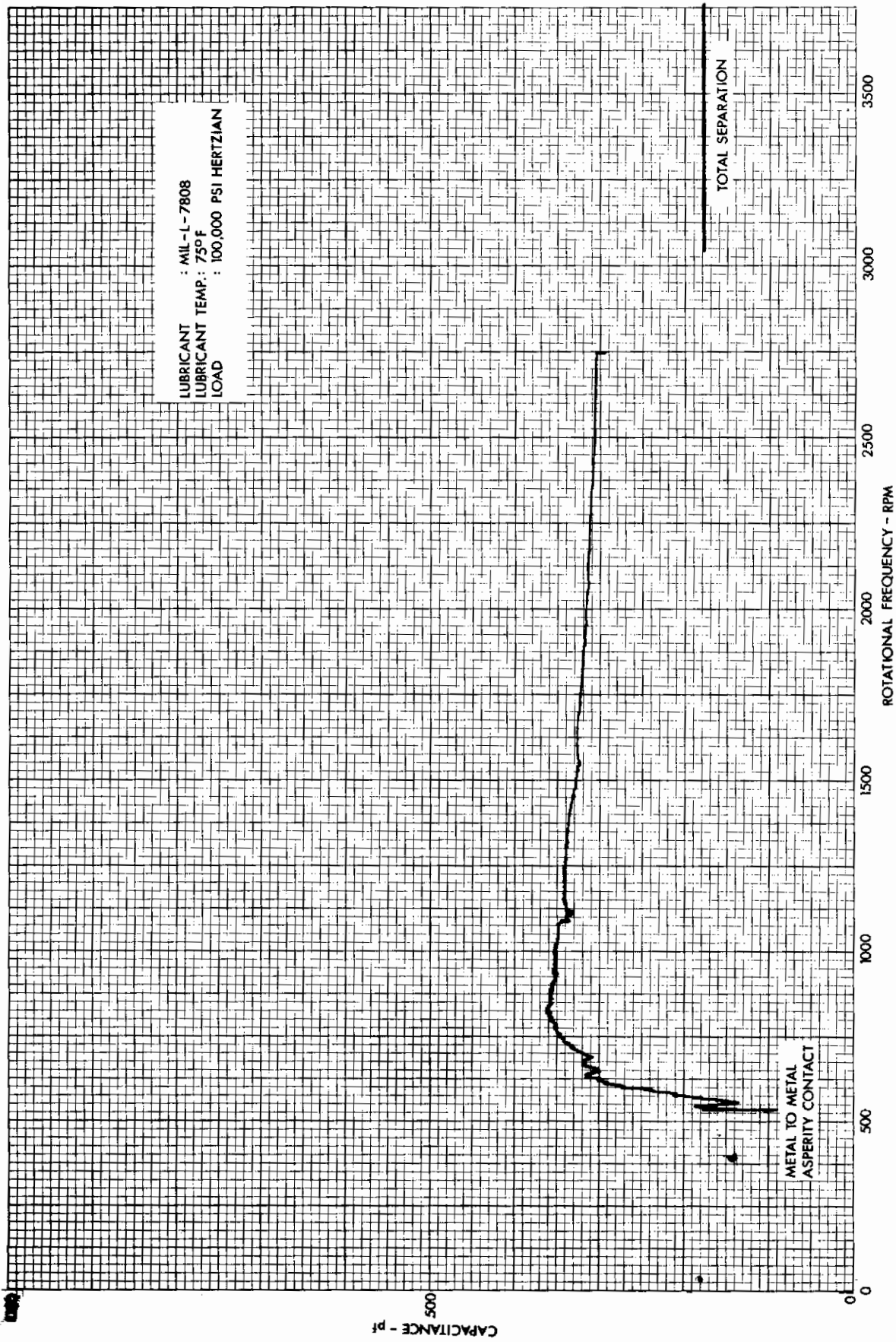


Fig. 28 Test Rig Output of Capacitance Versus Speed Data

Lubricant: MIL-L-7808

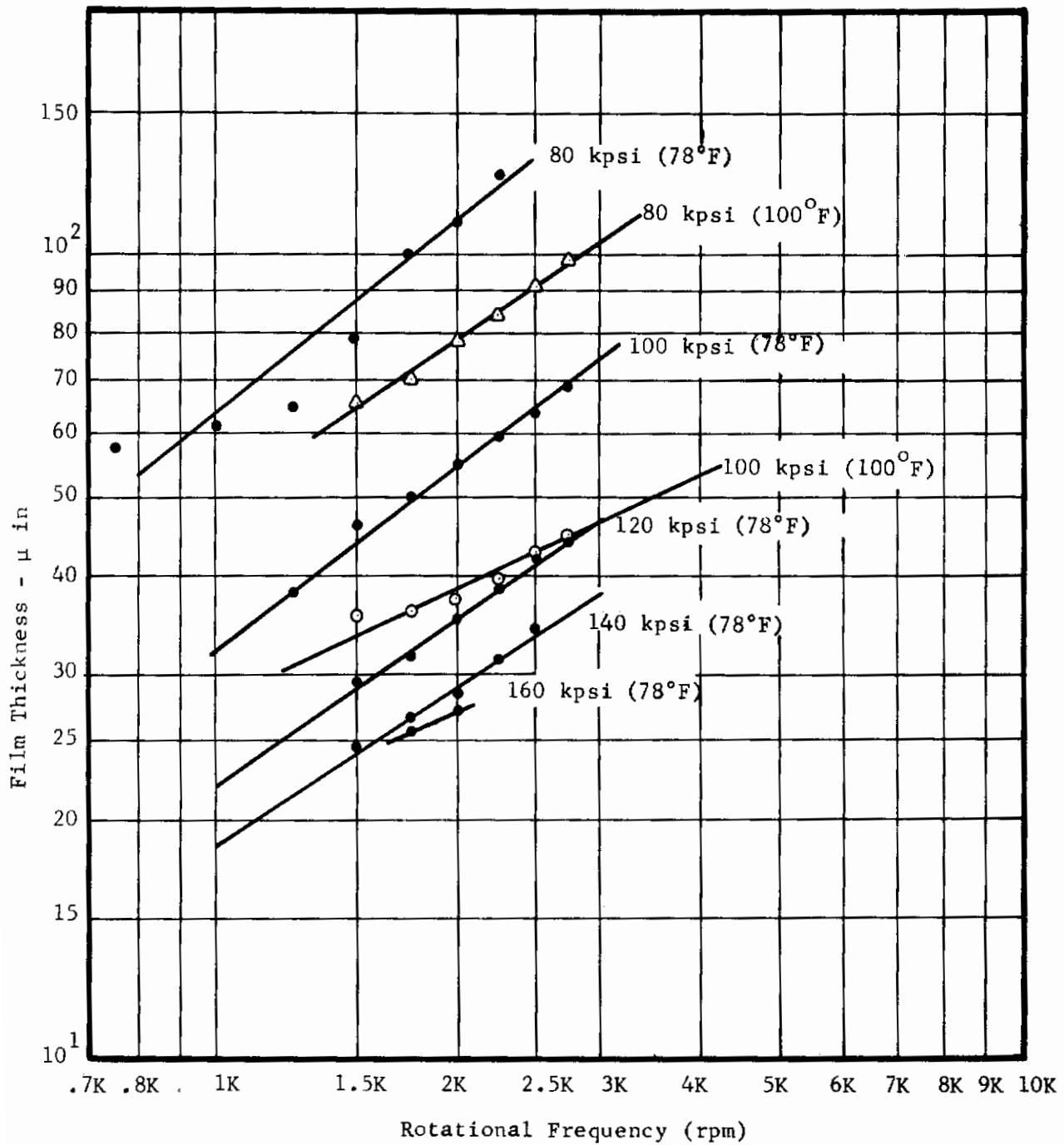


Fig. 29 Capacitive Film Thickness Versus Speed Determinations

Contrails

Examination of the slopes of the various film thickness vs. speed lines obtained at 78°F from the MIL-L-7808 indicates that film thickness varies with speed to the 0.79 power at 80 ksi and decreases to a 0.65 power variation at 140 ksi. These results are quite comparable with the 0.7 put forth by Dowson and Higginson (10). A wider range of power variations were observed from the polyphenyl ether data. The observed film thickness varied with speed to the .85 power with light loads and .40 power with heavy loads.

Similar recordings of capacitance data were taken with polyphenyl ether as a contact lubricant. A comparison of film thicknesses obtained with polyphenyl ether as the lubricating media show the test MIL-L-7808 maintains a thinner film for every load and speed measured. See Figures 30 and 31. In fact, at room temperature the observed film thickness for polyphenyl ether is nearly constant. Capacitive outputs are erratic when the polyphenyl was above 200°F and provide little film thickness information above that temperature.

Contrails

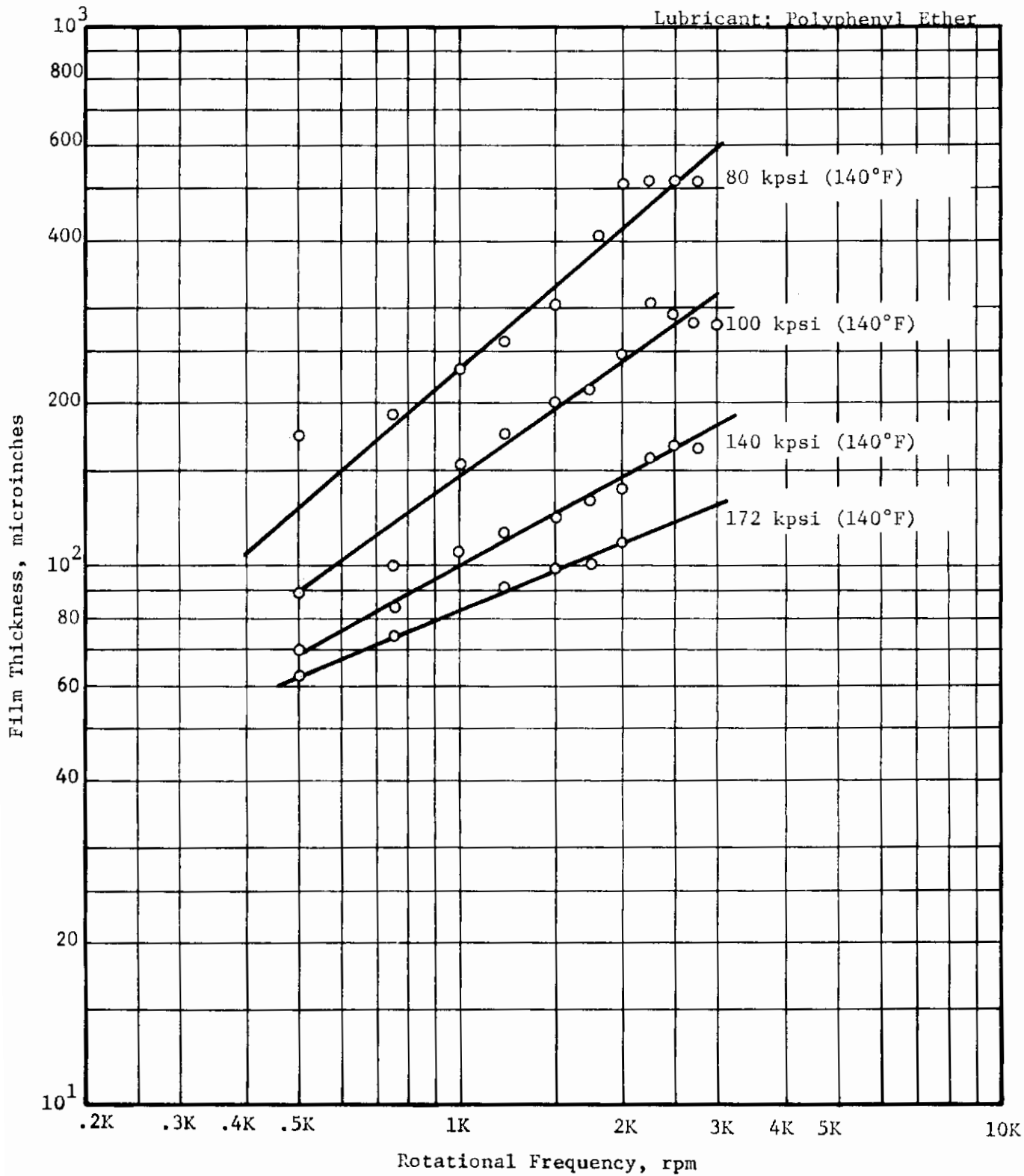


Fig. 30 Capacitive Film Thickness Versus Speed Determinations

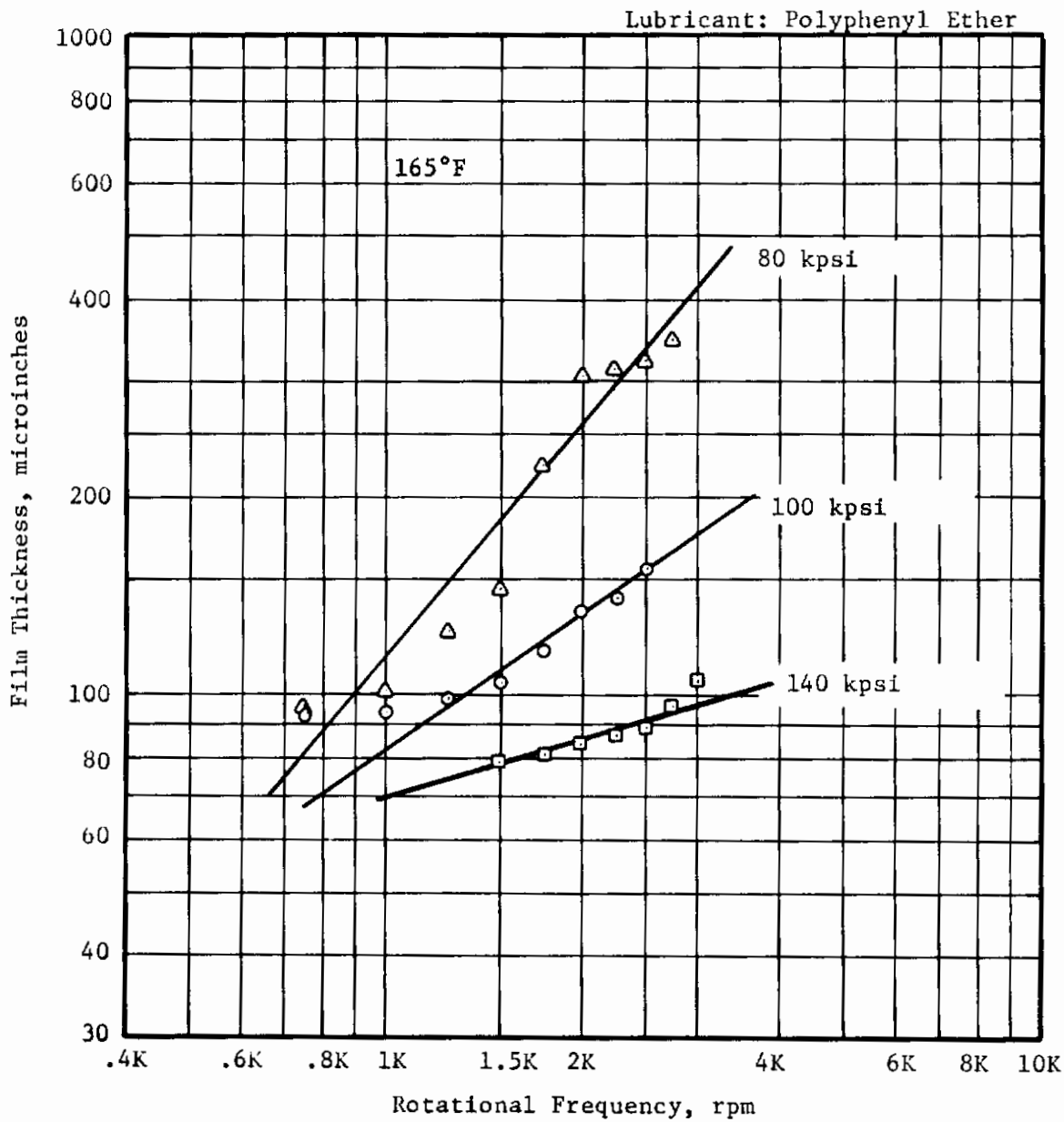


Fig. 31 Capacitive Film Thickness Versus Speed Determinations

SECTION IV

OPTICAL FILM THICKNESS MEASUREMENT AND ANALYSIS

The design details of the MTI optical test rig are described in a previous year's annual report (1). The first significant lubricated contact experiments made with optics were performed by Cameron (11). New approaches (12) in recent years have upgraded the quality of optical film thickness measurements in loaded rolling contacts. The advantage of the photographic technique is that a single picture reveals the full relative topological distribution in and around the observed contact region. If the finishes and coatings are carefully prepared, measured variations of film thickness as small as one-eighth of a wave length of light are common (typically 2 or 3 microinches).

1. TEST SET-UP

The complete test assembly was an intricate arrangement which provided:

- (a) Visual observance of the elliptical contact region
- (b) Monochromatic filtered illumination of the contact region
- (c) Variable speed control and detection of the rolling disc specimens
- (d) Variable loading capability of mating test discs
- (e) Stroboscopic illumination for photographic recording of the interference fringe pattern
- (f) An electrical triggering device to synchronize the optical access port with the illuminating strobe light.

The MTI optical setup used curved surface geometries for both the metal and transparent quartz mating discs. Before the present study only limited optical data related to lubrication experimentation have been available for geometries other than steel balls on an optical flat arrangement. The optical quality transparent disc was an uncrowned cylinder with a three inch outside diameter and a two inch inside diameter (see Reference 1 for photographs of specimens). The quartz disc was mounted with epoxy onto the disc machine lower shaft assembly as shown in the cross-sectional diagram of Figure 32. The shaft to which the transparent cylinder was attached was hollow for optical access at three points around the disc periphery.

The interference technique used in the present study makes use of thin film coating techniques with chromium in order to increase contrast of the interference fringes. A 20 percent reflective coat was deposited upon the outside diameter of the quartz disc. Standard microscopic components which were optically coated for reducing excess internal reflections were used in the main body of the optical setup.

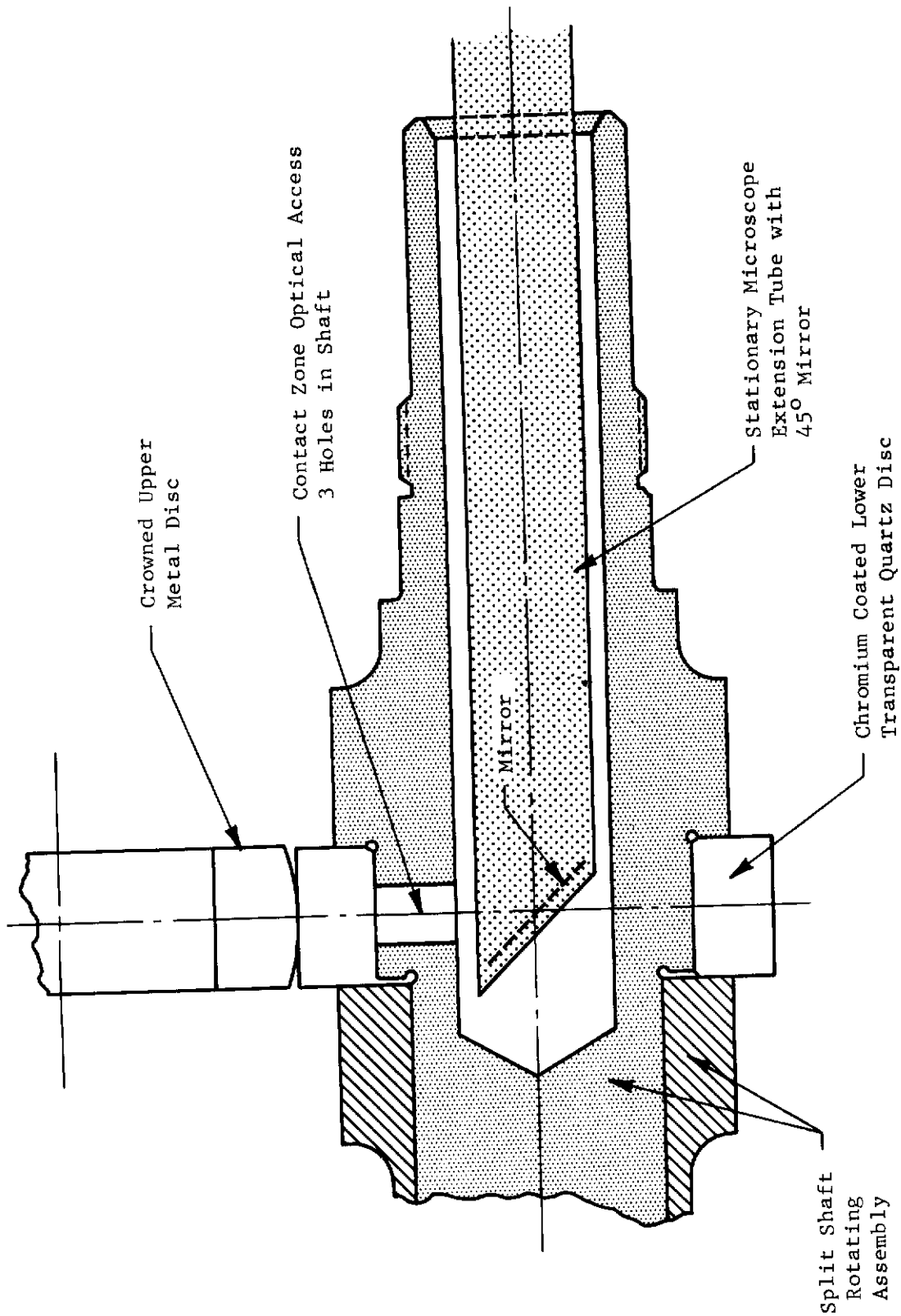


Fig. 32 Lower Disc Specimen Shaft Showing Mounting Arrangement and Optical Access

Loading was accomplished through the shaft bearings which supported each test specimen. This eliminated the common lubricant heating problem which arises when a sliding ball and cup made of teflon is used for contact loading purposes.

The test lubricants examined were the same as used in obtaining the traction and capacitive data described in the previous sections. The physical properties related to the test lubricant are given for reference in Appendix I. The synthetic turbine oil of MIL-L-7808 specification provided the best optical data of the two test fluids and allowed a comparison of nominal film thickness obtained by the separate methods of capacitive and optical measurement. Attempts to produce fringes with polyphenyl ether yielded unsatisfactory results. This was most likely related to the speed range with which the test rig could be varied. The polyphenyl at room temperature has a viscosity of approximately 600 centistokes and provided extremely high film thickness (> 100 microinch) at the lowest rolling speed obtainable on the present test rig.

A schematic of the illumination technique used in the test rig is displayed in Figure 33. The strobe unit used for photographic images was a single pulse unit with 1/10,000 second duration time. The unit was triggered via the "bulb" shutter position on the camera and a pair of sliding pin contacts on the shaft which held the quartz specimen. A yellow monochromic transmission filter was used between the light source and the contact zone. The transmitted yellow light wave length was independently measured with a dual slit diffraction test and the slit spacing determined with the 6328A light of a helium-neon laser. The predominate wave length of the contact illumination source after filtering was found to be 5890A (23.2 microinches) in air.

Visual observations of the contact zone were also made with a rapid cycle multi-flash unit of lower light intensity output. That system was also triggered synchronously with the shaft and light port alignment allowed visual observation of the contact interference pattern as it changed while adjusting the rolling speed.

The drive system was synchronized during the optical work for pure rolling operation. No investigations with slip between the discs were made. Shaft speeds were monitored with a Fotonic light probe, a striped decoding band, and a four-place digital counter. Rotational frequencies as low as 10 rpm could be maintained. However, motor cogging of the variable speed unit at such slow rotational frequencies limited the useful speed range to 20 rpm or greater.

2. OPTICAL DISTORTION CORRECTION OF ELLIPTICAL BANDS

The index of refraction used throughout the experiment were:

<u>Material</u>	<u>Refractive Index</u>
Polyphenyl Ether (5P4E)	1.630
MIL-L-7808	1.395
Quartz Test Disc	1.458

and was assumed constant. The quartz disc has a modulus of elasticity of approximately one-half of that of the steel disc and therefore requires Hertz

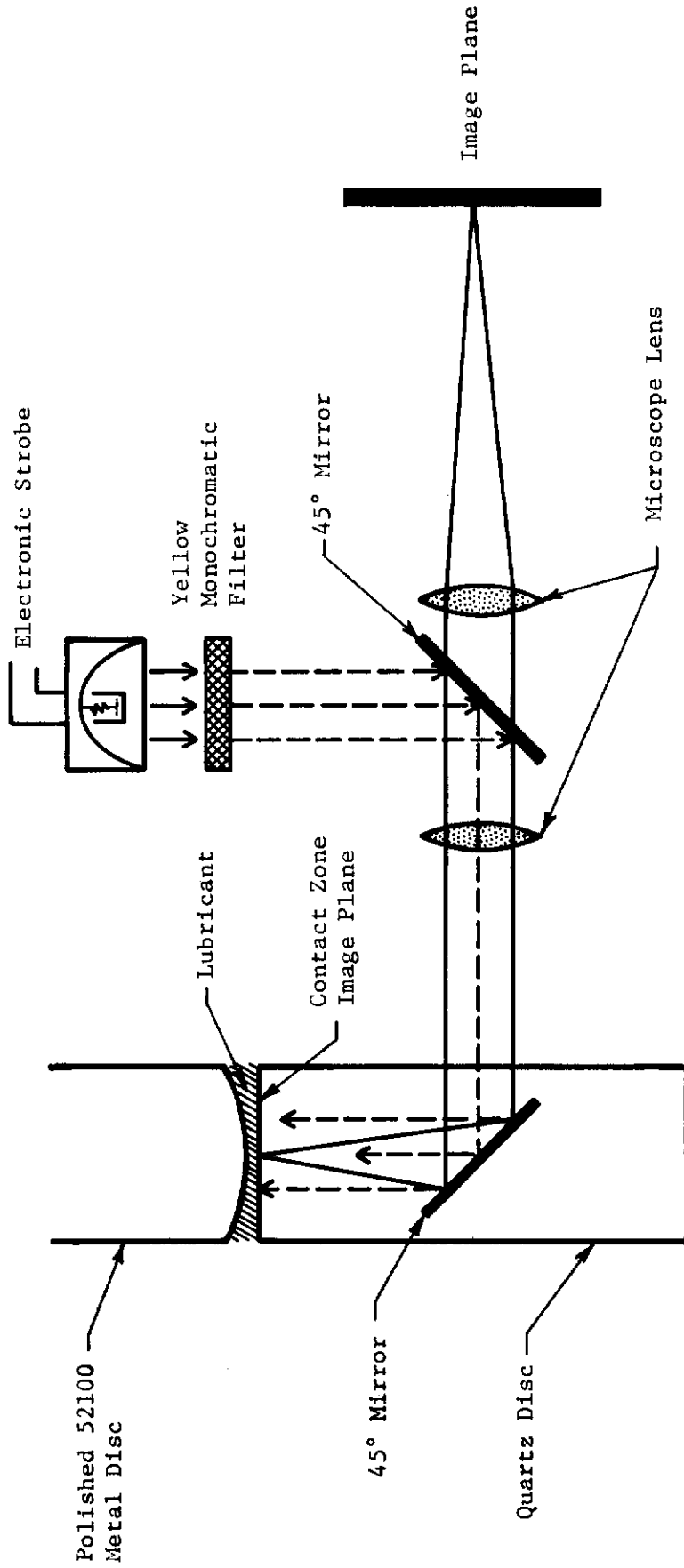


Fig. 33 Optical Disc Illumination Schematic

MTI-13381

Contrails

stresses of less than 50,000 psi for equivalent contact distortions equal to the 100,000 psi level with two steel mating discs. In fact, the choices of loading were made such that the minor axis (along the rolling direction) of the contact ellipse were the same for some tests made with the capacitive technique.

Hertz stresses of 50,000 psi would result in less than a 4 percent change in the refractive index and was not considered significant to adjust any film thickness data for pressurization. The 4 percent change would only occur over a limited area of the contact zone and was calculated from the classic Lorenz-Lorenz equation

$$n_p = \left(\frac{1 + 2\tilde{A}}{1 + \tilde{A}} \right)^{1/2}$$

where,

$$\tilde{A} = \frac{\rho}{\rho_o} \left(\frac{n_o^2 - 1}{n_o^2 + 2} \right)$$

with measured densities taken from the Midwest data in Appendix I. Hertz pressures up to 50,000 indicate

$$\frac{n_p - n_o}{n_o} \leq 4\%$$

Because of the geometry of the transparent test disc, it became necessary to apply a constant distortion correction factor to each observed fringe position along the contact rolling direction in order to interpret the actual spacing. The spacing perpendicular to the rolling direction needed no correction. The image distortion caused by using a cylindrical roller instead of the optical flat used by previous investigators is derived in Appendix IV. The correction factor

$$f_D = \frac{\text{Observed Fringe Position}}{\text{Actual Fringe Position}}$$

is found from the optical geometry to be

$$f_D = \frac{n_G}{\frac{R_1}{r}(n_G - 1) + 1}$$

The disparity between observed and actual dimensions is schematically represented in Figure 34. An understanding of the distortion expected can be obtained from the side view of the test discs shown in Figure 35. The distortion factor was evaluated to be

$$f_D = .8641$$

for the optical geometry or approximately 14 percent between observed and actual

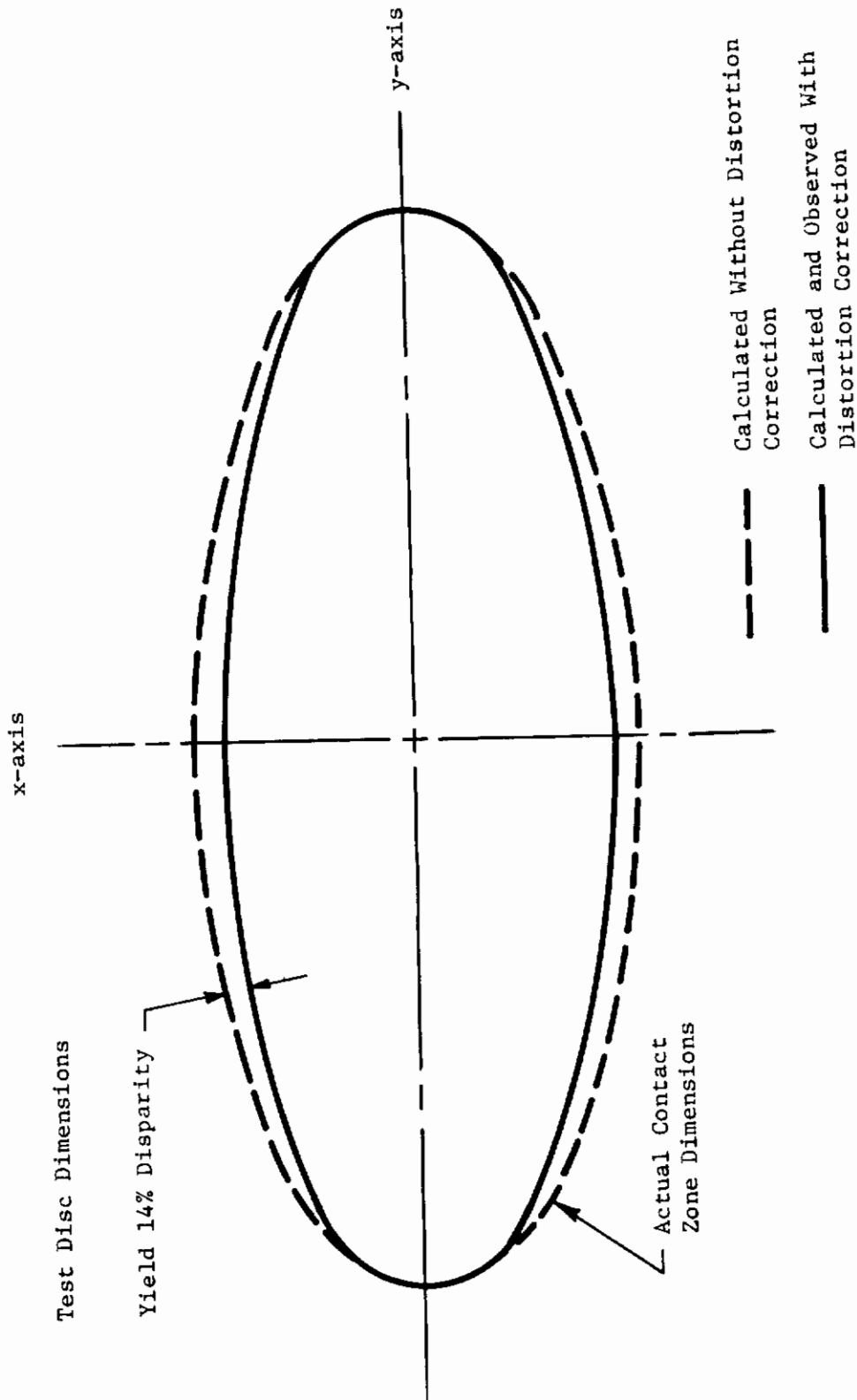
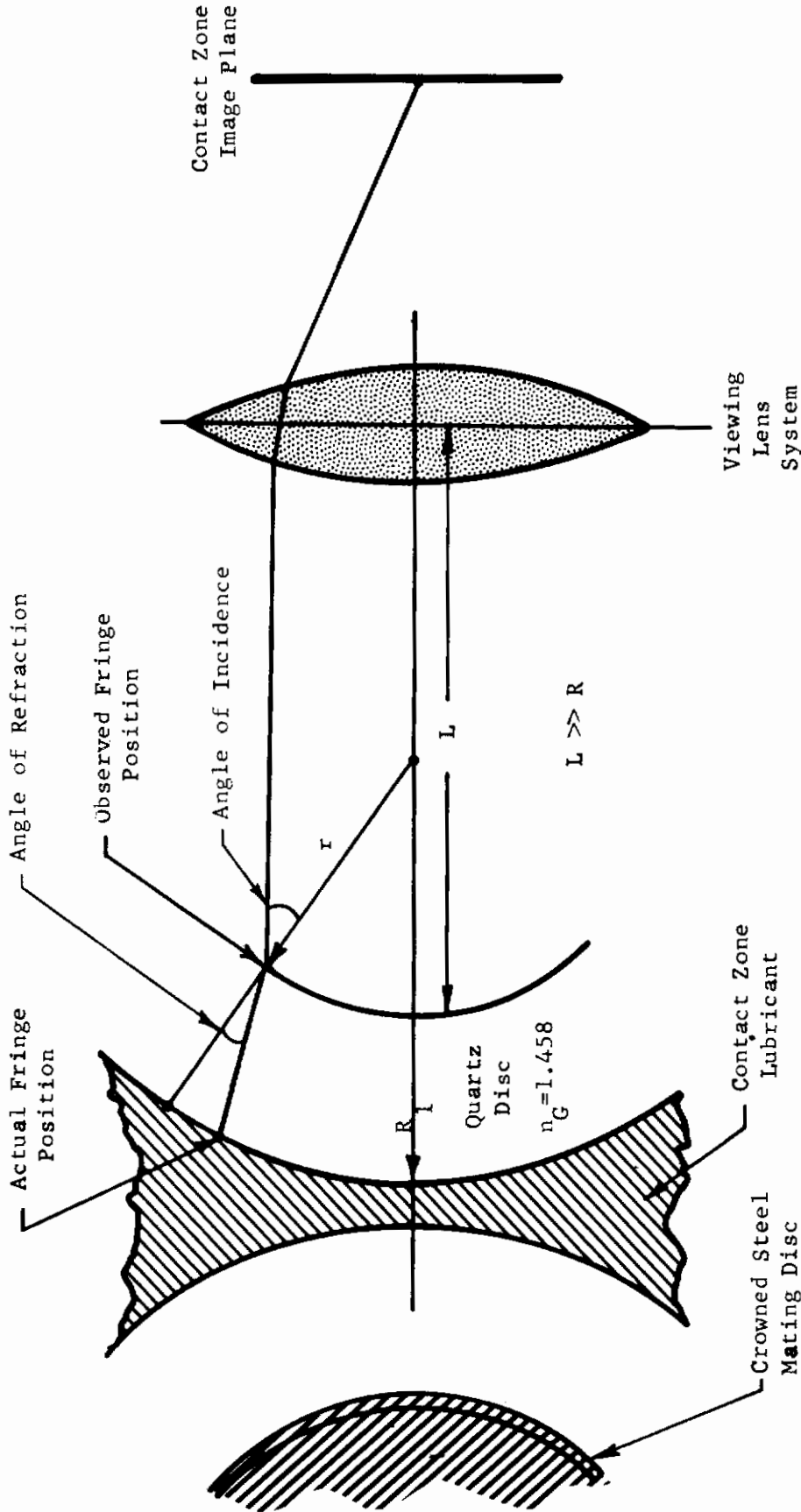


Fig. 34 Contact Ellipse Distortion Schematic



$$n_a \sin \gamma = n_\theta \sin \theta$$

Fig. 35 Distortion Off-Set Schematic of Observed Fringes

Contrails

spacings. This value was used to correct all observed dimensions in the rolling direction and is inherent in all photographs shown in this report.

In order to test the optical equipment and analysis, a preliminary static loading test was performed with MIL-L-7808 in the contact zone of the mating discs. Six loads giving Hertz pressures from 22,000 psi to 49,000 psi provided photos similar to those shown in Figure 36. The increase in contact zone area is apparent with increased loading although the actual points of metal to quartz contact within that zone cannot be seen in the photographs. Exhibited are the fringes of equal gap separation between the loaded discs for gaps greater than one-eighth of a wave length of the illuminating yellow light.

The interference intensity at the chromium coat depends upon the

- (a) Chromium film thickness deposited
- (b) Relative index of refraction compared to that of quartz
- (c) Separation gap between the discs
- (d) Phase change of the incident light at the polished metal surface.

The quartz mating disc used was coated with a 20 percent reflective coating of chromium which increases the contrast of the light interference bands in the contact region. The chosen coating was assumed to induce an even number of π phase shifts in the reflected light as indicated by Holden (13) from his thin film work with silver coatings. This means that the first surface reflection has the same phase as the incoming light since the index of refraction of the oil is less than that of the quartz used. The reflected light from the polished crown metal disc, however, undergoes a phase shift equal to (π) according to Andrews (14) which is the equivalent of one-half of a wave length of light. Light which has traveled a gap, h , such that

$$h = \left(\frac{2i + 1}{4}\right) \lambda$$

where,

$$i = 0, 1, 2, 3$$

when λ is the wave length of light in the separating lubricant, causes bright fringes at the chromium coat whenever the index of refraction of the lubricant is less than the refractive index of the transparent disc. In the present work dark fringes appear whenever the gap, h , is such that

$$h = \left(\frac{2i}{4}\right) \lambda$$

where,

$$i = 1, 2, 3, \dots$$

and λ is again the wave length of the illuminating light in the test lubricant.

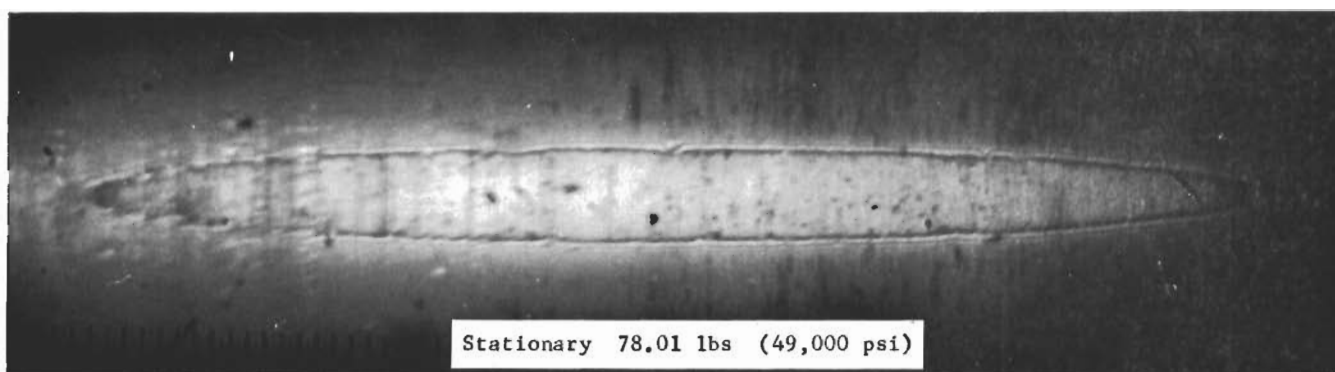
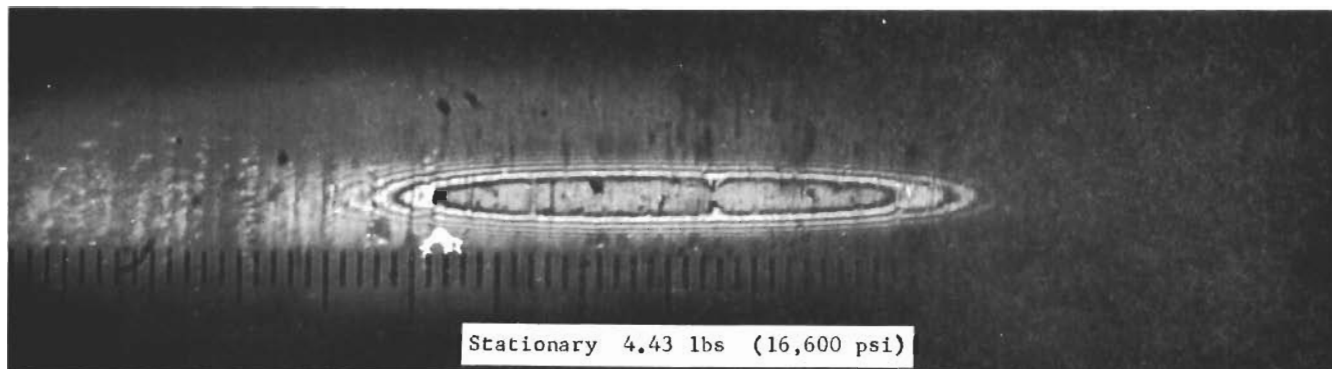


Fig. 36 Two Interference Fringe Patterns of Stationary Loaded Contacts Showing Load-Area Contact

Contrails

The inner most dark band which occurs is a special case of interference. There is enough lubricant trapped between the discs to allow a half wave phase shift in the light reflected at the chromium coat but not enough separation to provide a half wave length travel. Therefore, an interference minimum or a dark band appears. The central contact region contains little or no lubricant. The metal is so close to the chromium coat that very little light is transmitted and all light reflected is in phase so a central maximum or light gray area appears. A summary of the variations of intensity expected from a thin film gap is given by Figure 37.

The inner most bright ring (shown previously in Figure 36) occurs when the separation, h , between the discs is

$$h = \frac{\lambda_{air}}{4n_{oil}} = 4.15 \text{ microinches.}$$

3. TEST DATA WITH ANALYTICAL EXPECTATIONS

The actual load carrying contact area (such that $h = 0$) where micro-asperities support the normal load between the discs is well within the inner most white band. The analytically-calculated dimensions of the major and minor axes of the contact zone separation of 4.15 microinch points for six load levels are compared in Figure 38. The results of that figure indicate that the elasticity analysis used in describing the distribution of surface gaps in and around the contact area (given in Appendix III) are sufficient to accurately define the experimentally observed distributions with load under static contact. In fact, the locus of all points of equal separation for several loads were numerically evaluated and computer plotted. The results along with their corresponding contact photographs are shown in Figures 39 and 40. Overlaying the computer plots on the corresponding photographs reveal a positive matchup between theory and experiment.

Over three hundred photographs were taken of the contact region under various load-speed conditions. The photographs shown in Figures 41 and 42 reveal how the film pattern changes with increasing rolling speed. As the speed of the disc increases, the nominal film increases. The central minimum film region responds by changing alternately from light to dark and back again as the speed is brought to higher and higher levels. As shown in Figure 43, the outer bands move toward the center as the rolling speed increases. What was a dark ring about a central bright region, becomes a dark central contact region if the nominal gap increases by a quarter of a wave length of the illuminating light. A photograph showing a rolling contact taken at a speed where a dark band has moved in to lie partly in the central region and partly along the trailing edge dip is displayed in Figure 45c.

Photographs reproduced in Figures 44 through 46 were taken as the disc rolling speed was increased from 26 rpm to 488 rpm with a Hertz pressure of 22,000 psi. A 22,000 psi steel on quartz pressure was equivalent to 44,000 psi for the steel-on-steel test arrangement.

A pictorial summary of a second set of variable speed tests performed with a 36,000 psi Hertz stress is presented in Figure 47. The choice of load was made

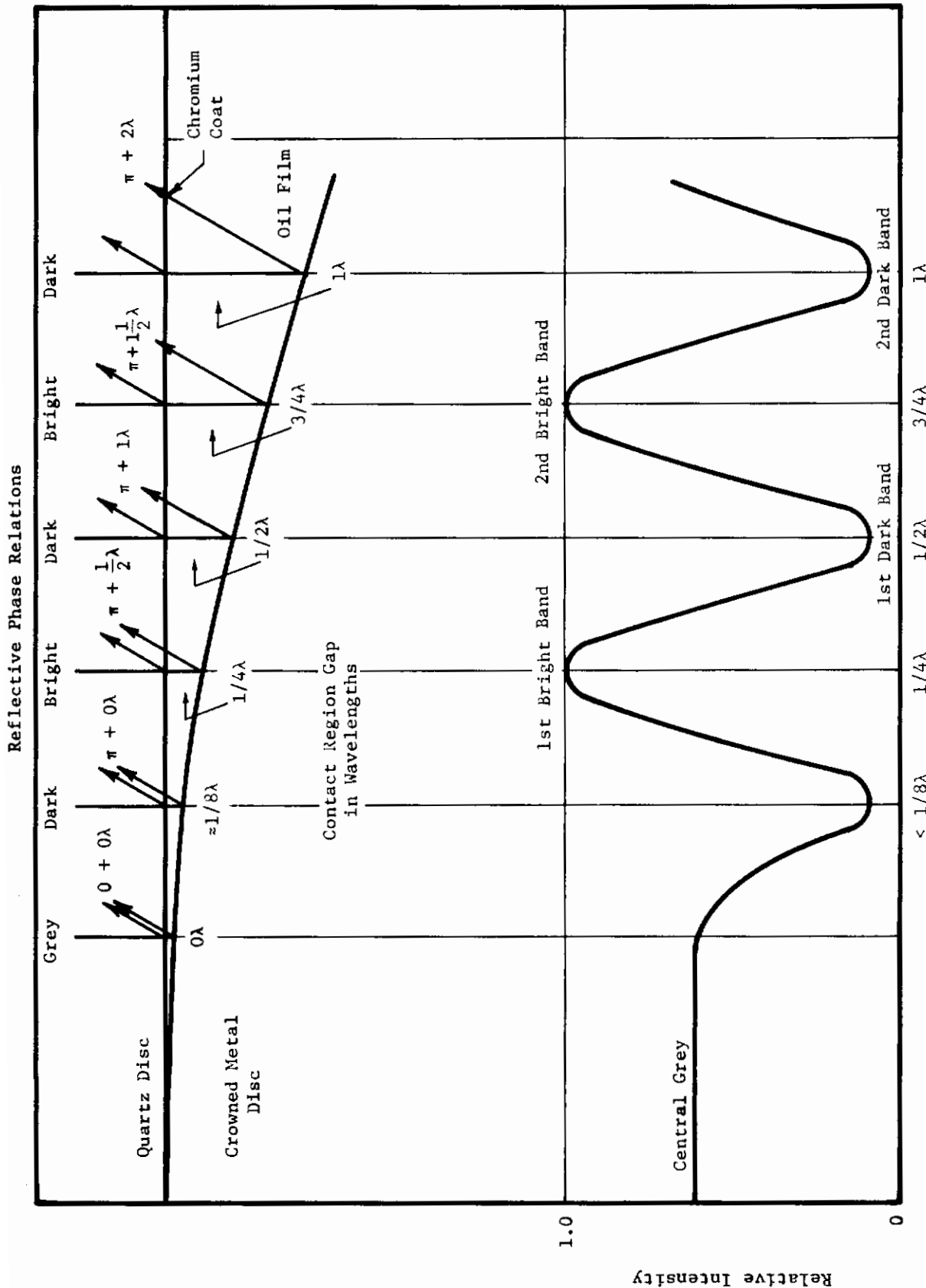


Fig. 37 Phase Relation of Thin Film Reflected Light

MTI-13607

Contrails

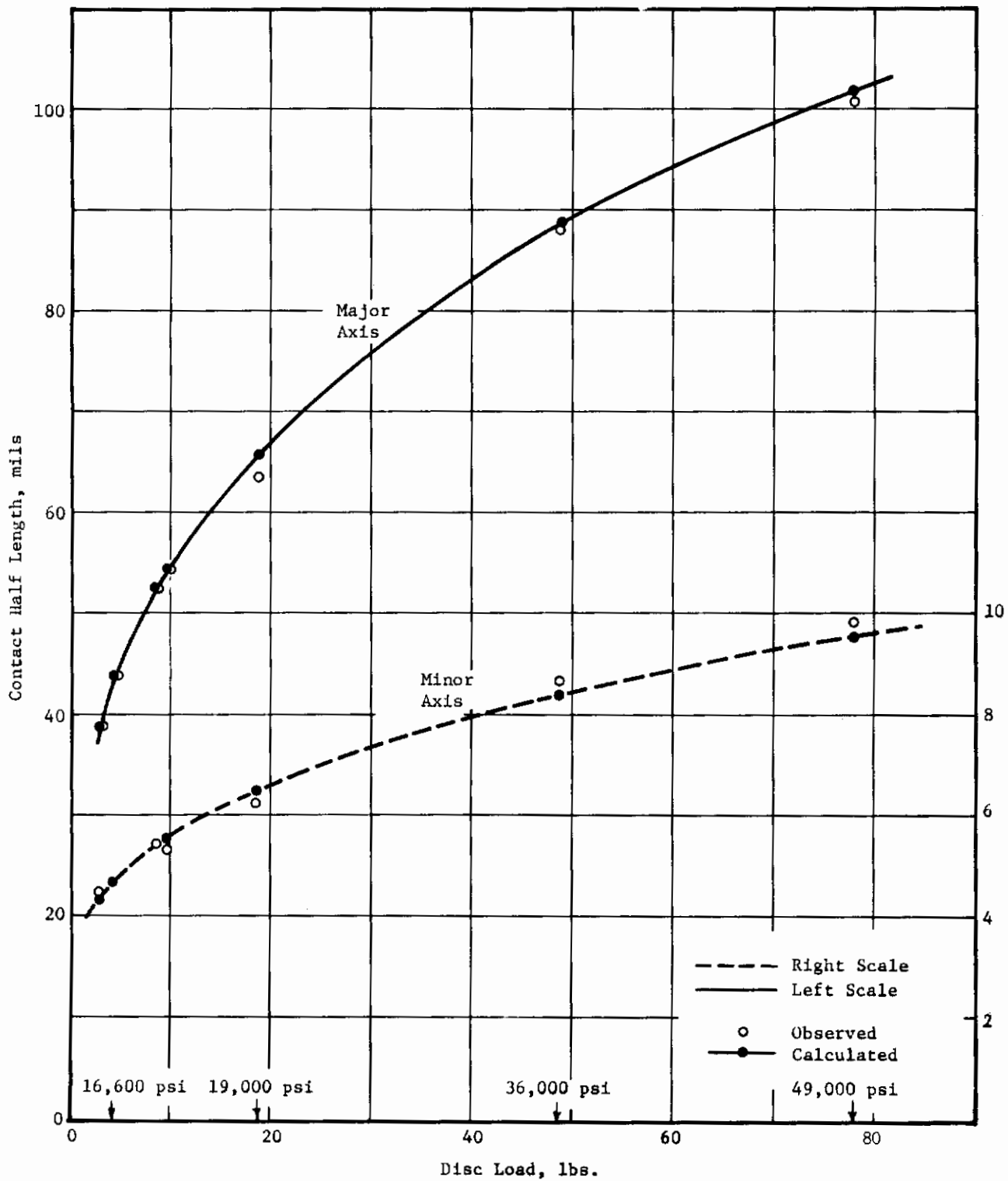


Fig. 38 Dimensional Variations of Loaded Contact Ellipse

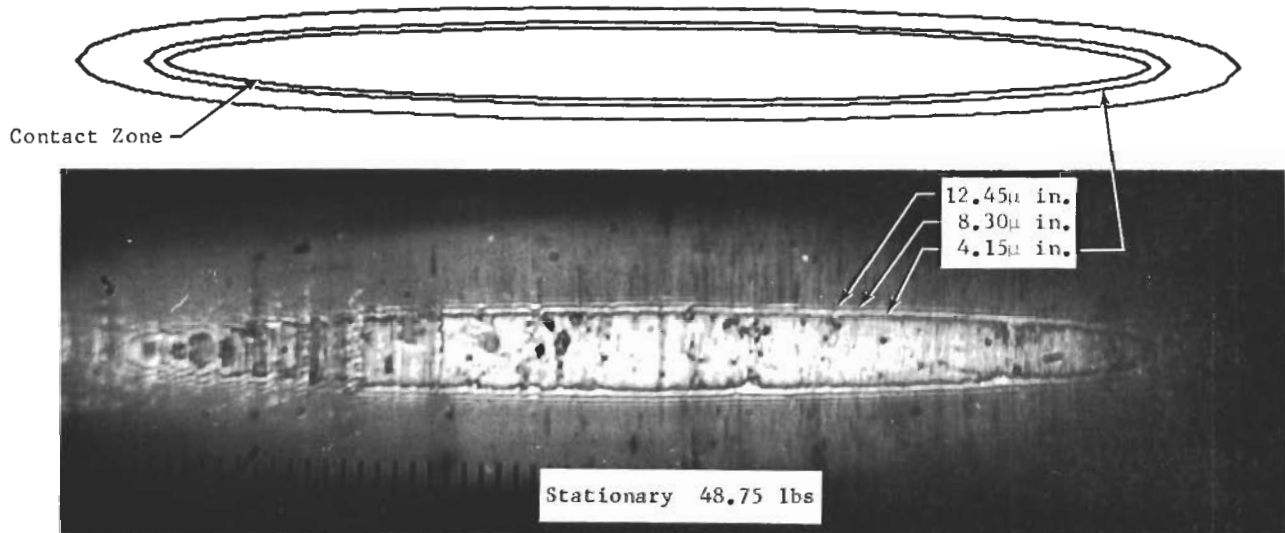


Fig. 39 Photograph and Computer Plot of a Loaded Contact Ellipse

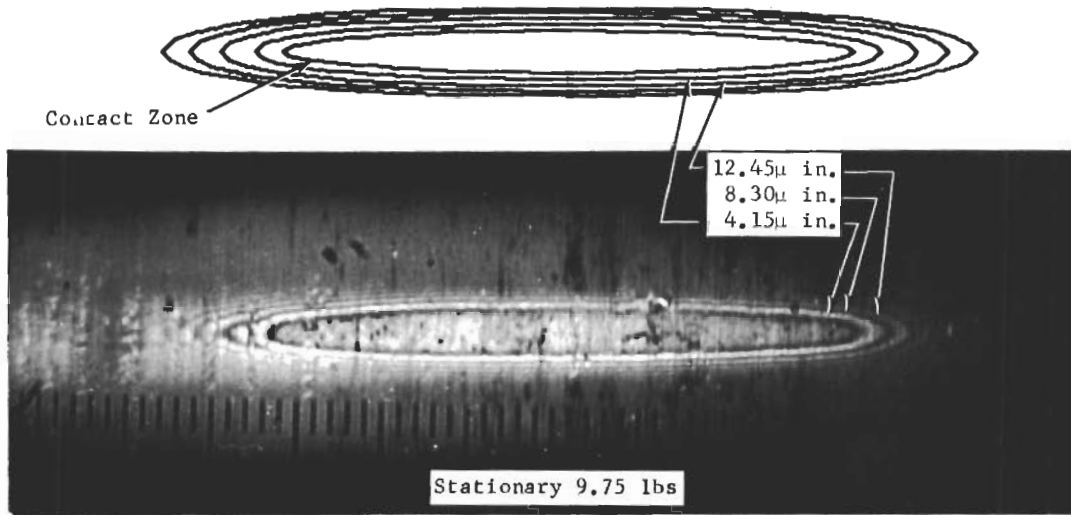


Fig. 40 Photograph and Computer Plot of a Load Contact Ellipse

Contrails

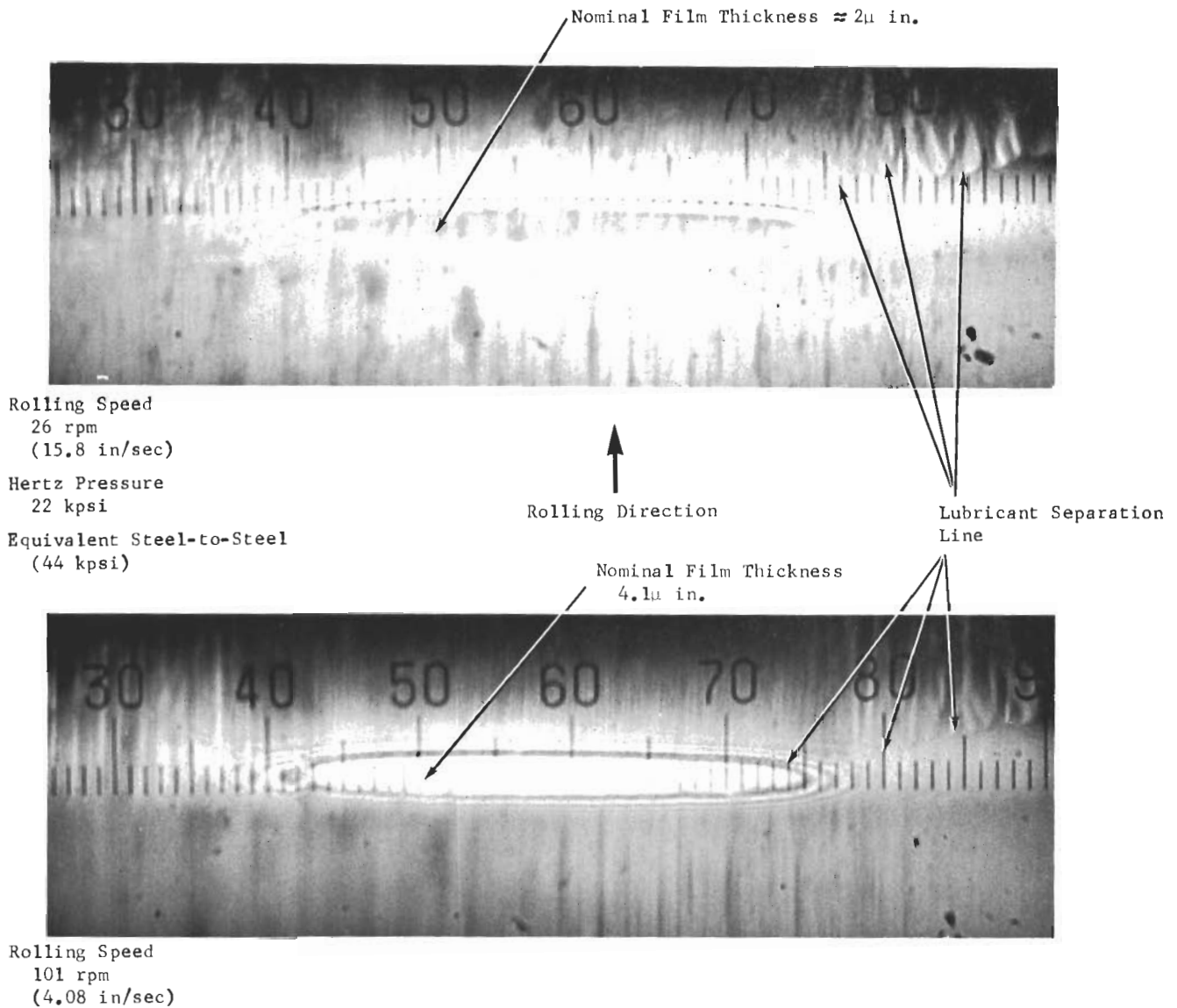


Fig. 41 Photographs of Rolling Contact Zone Variations with Speed

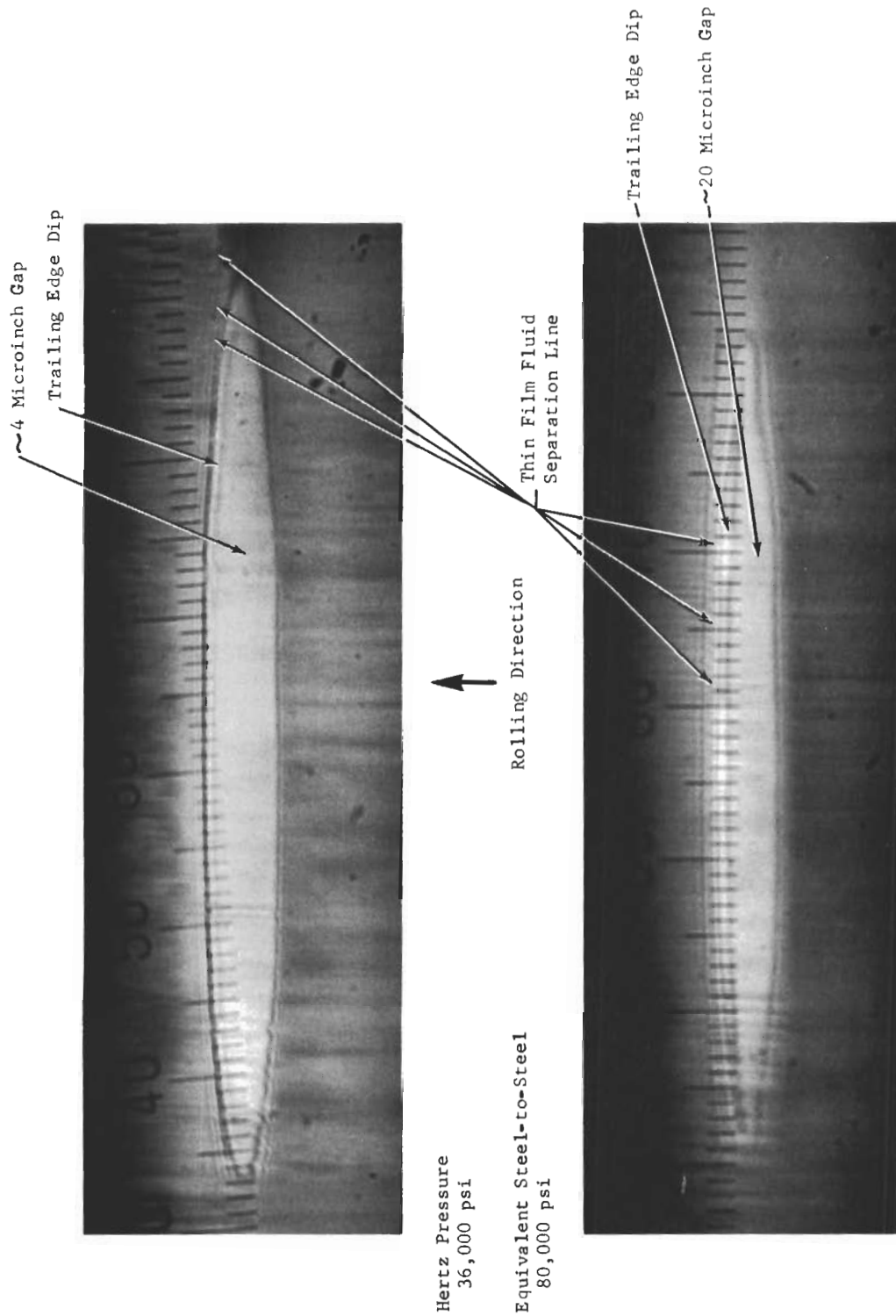
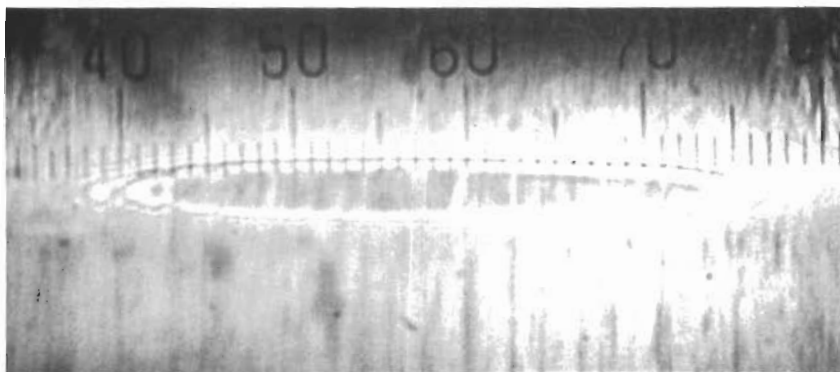


Fig. 42 Photographs of Rolling Contact Zone Variations with Speed

Contrails

ROLLING SPEEDS
(RPM)



26

(a)



60

(b)



101

(c)

Fig. 44 Rolling Contact Zone Photographs

Contrails

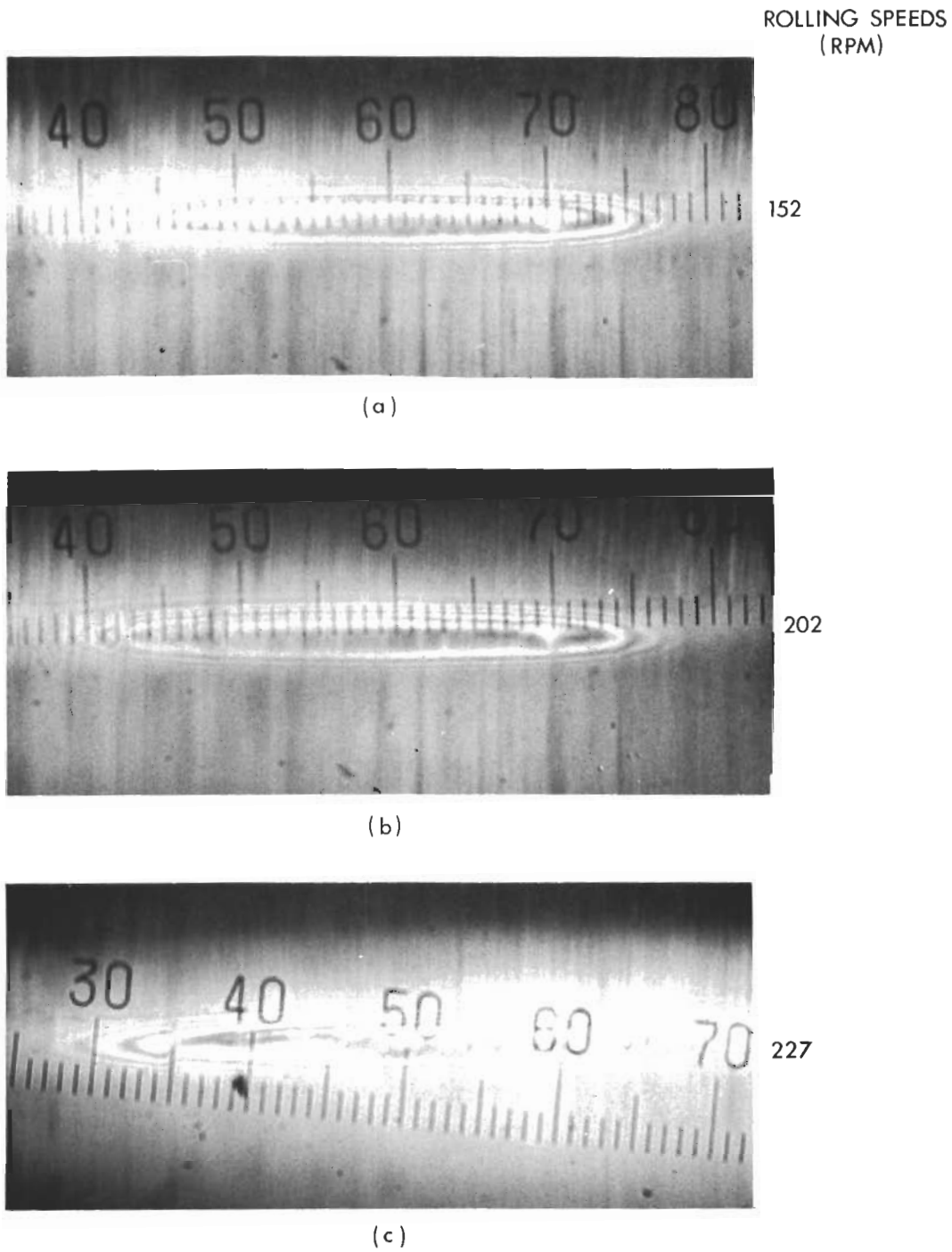
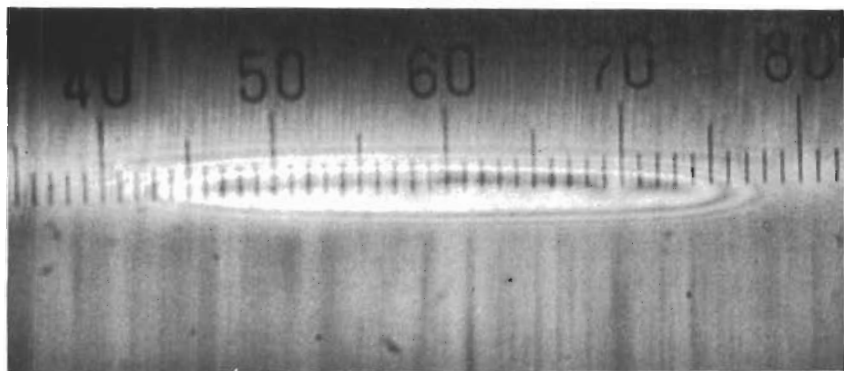


Fig. 45 Rolling Contact Zone Photographs

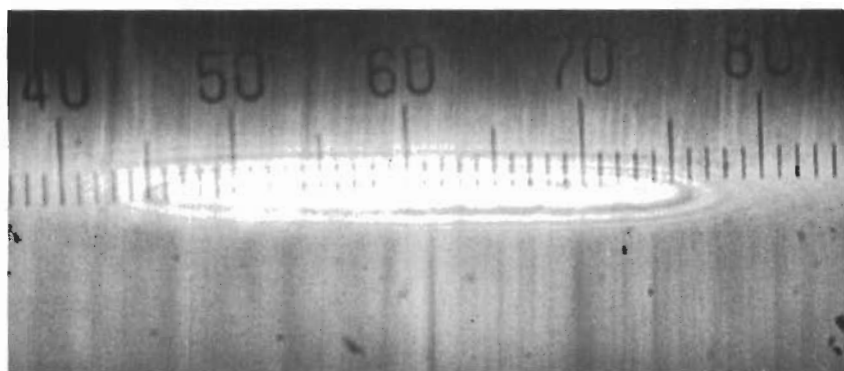
Contrails

ROLLING SPEEDS
(RPM)



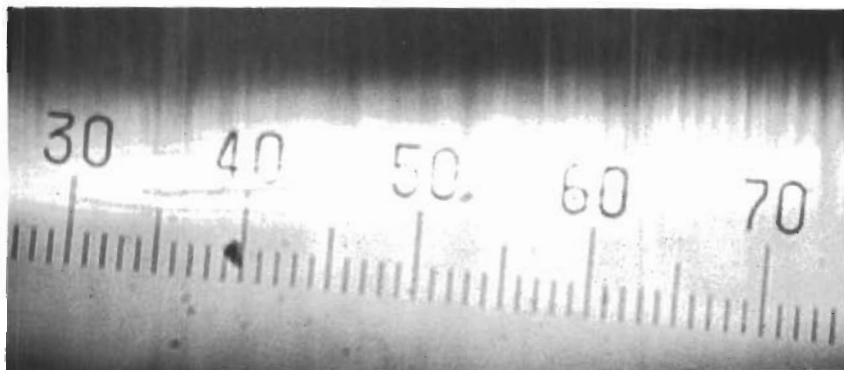
270

(a)



372

(b)



488

(c)

Fig. 46 Rolling Contact Zone Photographs

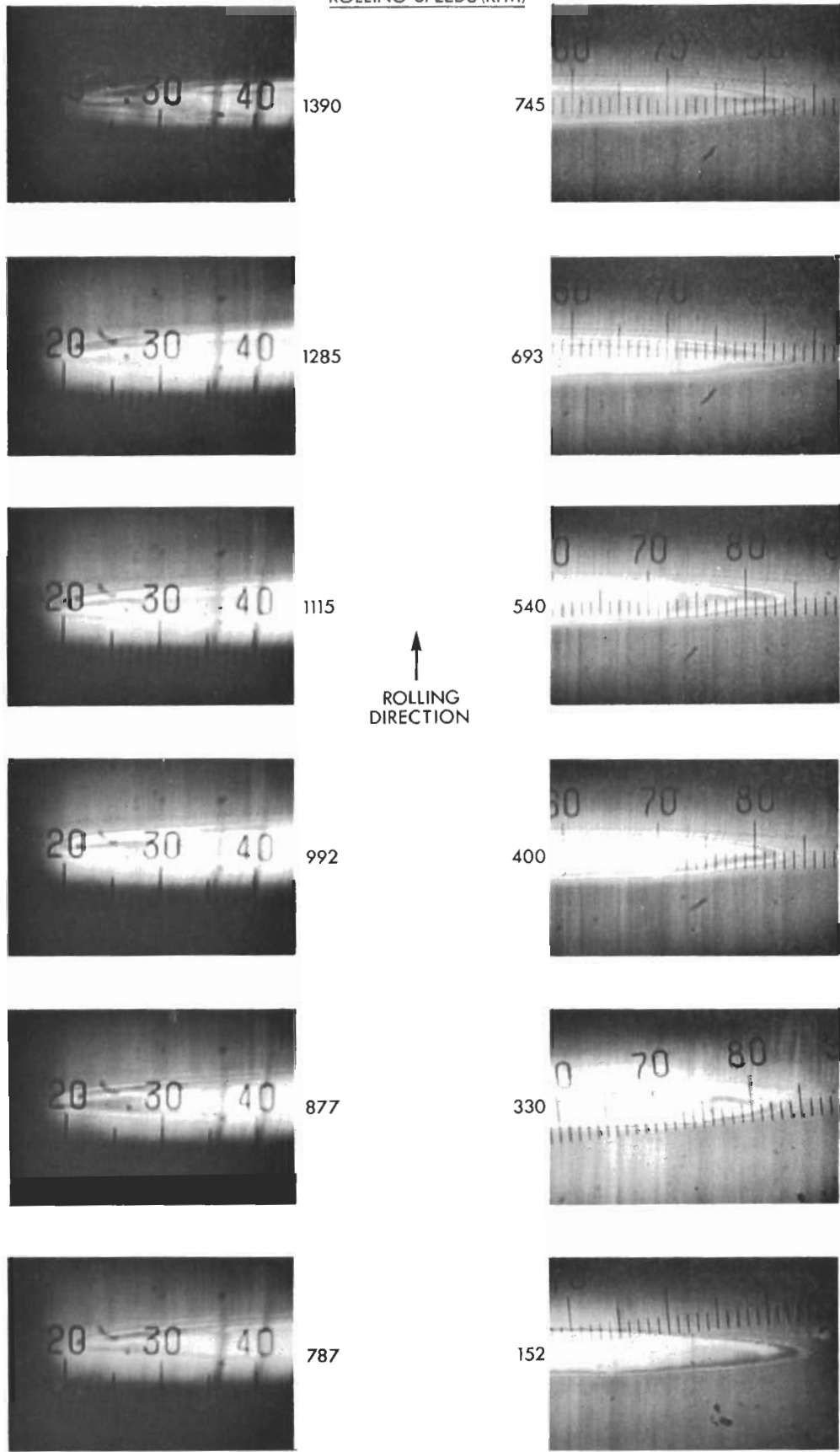


Fig. 47 Rolling Contact Zone Photographs

Contrails

so as to match the contact zone minor axis dimension in the rolling direction to the steel-on-steel contact dimensions of the capacitive test run at 80,000 psi. From both visual and photographic observations of the contact region over the full range of speeds from 0 to 1,400 rpm the plot shown in Figure 48 was compiled. The plot depicts five variable speed tests made with the MIL-L-7808; three capacitive runs and two optical runs under separate load conditions.

Although the film thickness speed data for the capacitive observations show a marked load dependence for the lighter loads, this is not evident from the optical data. The optical work indicates a simple film speed exponent relationship of 0.85 over the rolling speed range of 30 rpm (4.71 in/sec) to 1,400 rpm (220 in/sec) tested.

The analytical line shown in Figure 48 is the EHD performance code prediction corresponding to the conditions under which the 36 kpsi optical measurements were taken. The performance code prediction reduces very nearly to the Dowson and Higginson formula under these conditions since inlet zone heating effects are predicted to be small.

The optical data seems to substantiate conventional EHD predictions regarding load sensitivity at low pressures whereas the capacitance data obtained at higher pressures and higher speeds seems to indicate a more significant load dependence.

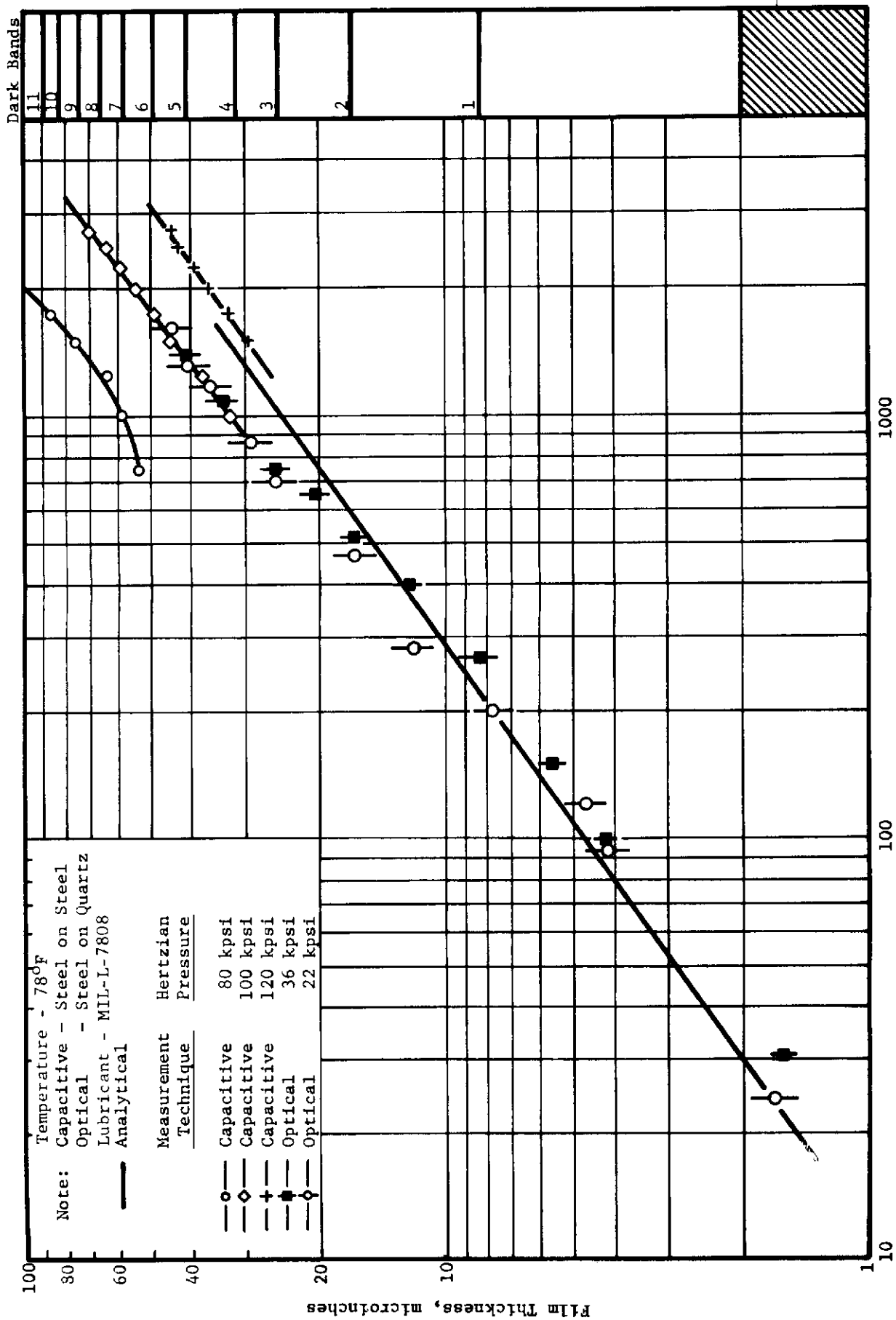


Fig. 48 Optical Film Thickness Versus Speed Determinations

NTI-13446

Contracts

SECTION V

X-RAY FILM THICKNESS MEASUREMENT

The X-ray film thickness measuring technique was initially developed by workers at Battelle Memorial Institute in the early 1960's. The work has since been heralded as the first valid proof of the existence of very thin films in rolling element contacts. The rolling disc machine described in a previous Air Force report (Reference 1) was designed to allow similar X-ray measurements. The conceptual layout is diagrammed in Figure 49. X-rays from a natural decay source are passed through the lubricating film of the disc machine in the direction of rolling.

A beam of X-rays with a width of .090 inch at the contact zone was passed between the rollers and detected with a photomultiplier tube. The dimensional characteristics and beam arrangement are shown in Figures 50 and 51.

The radioactive source was chosen for its desirable X-ray energy characteristics. Figure 52 displays the energy spectrum emitted from the Cadmium 109 decay source. The predominate X-ray peak appears at 22 kev and is emitted from the metastable silver state produced on decay. The 22 kev X-ray wave length is very close to that of the molybdenum target X-rays generated for the pioneering work originally performed by Sibley, Bell, Orcutt, and Allen (15). The radiation of the molybdenum target used by them exhibits peaks from the K_{α} and K_{β} shells which have energies of 16.5 kev and 18.6 kev respectively. X-ray energies less than 30 kev are desirable since they penetrate the lubricants quite well and yet will not penetrate bearing steels to any appreciable extent.

The X-ray detection instrumentation was identical to the original setup used in the Battelle work. A schematic of the electrical linkup used for monitoring and calibrating is shown in Figure 53 and a complete list of the test equipment is provided in Appendix V. The calibration procedure involved the determination of absorption coefficients of the X-rays in the test lubricants, as well as for count rate determinations for fixed disc separations.

If I is the intensity of X-rays on a piece of material of thickness dx , and dI is the decrease in intensity of the X-rays due to absorption within the material, then μ the absorption coefficient is defined such that

$$\mu = \frac{dI}{I dx}$$

Thus,

$$I = I_0 \exp(-\mu x)$$

where I_0 is the X-ray intensity when $x = 0$. The experimentally determined

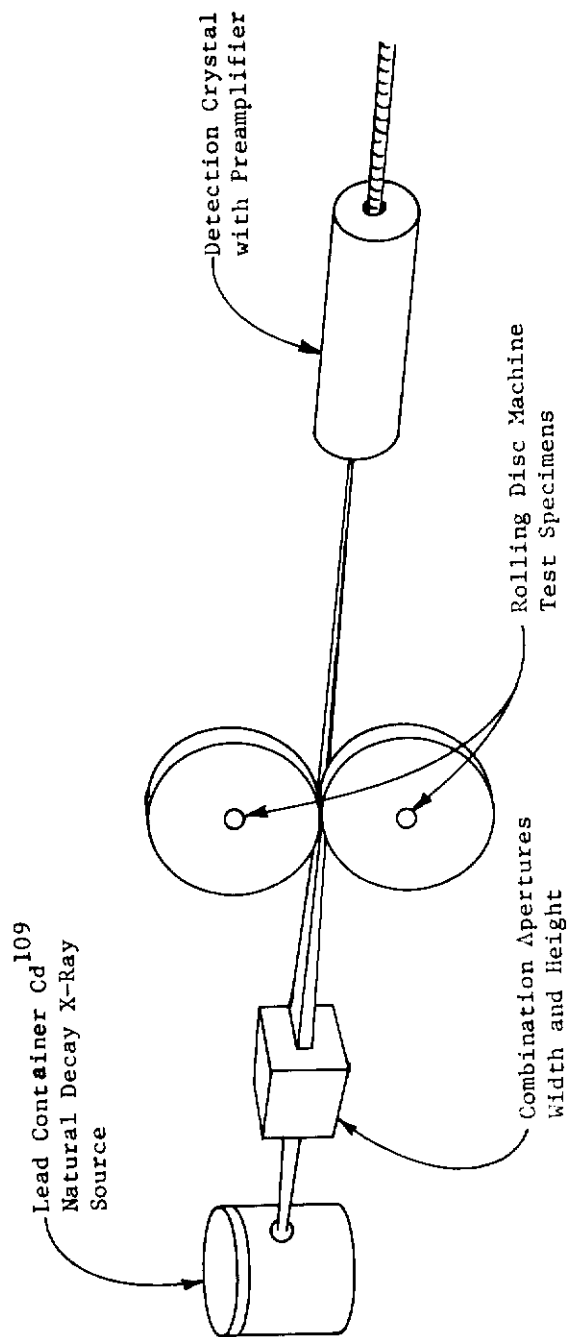


Fig. 49 X-Ray Test Facility Schematic

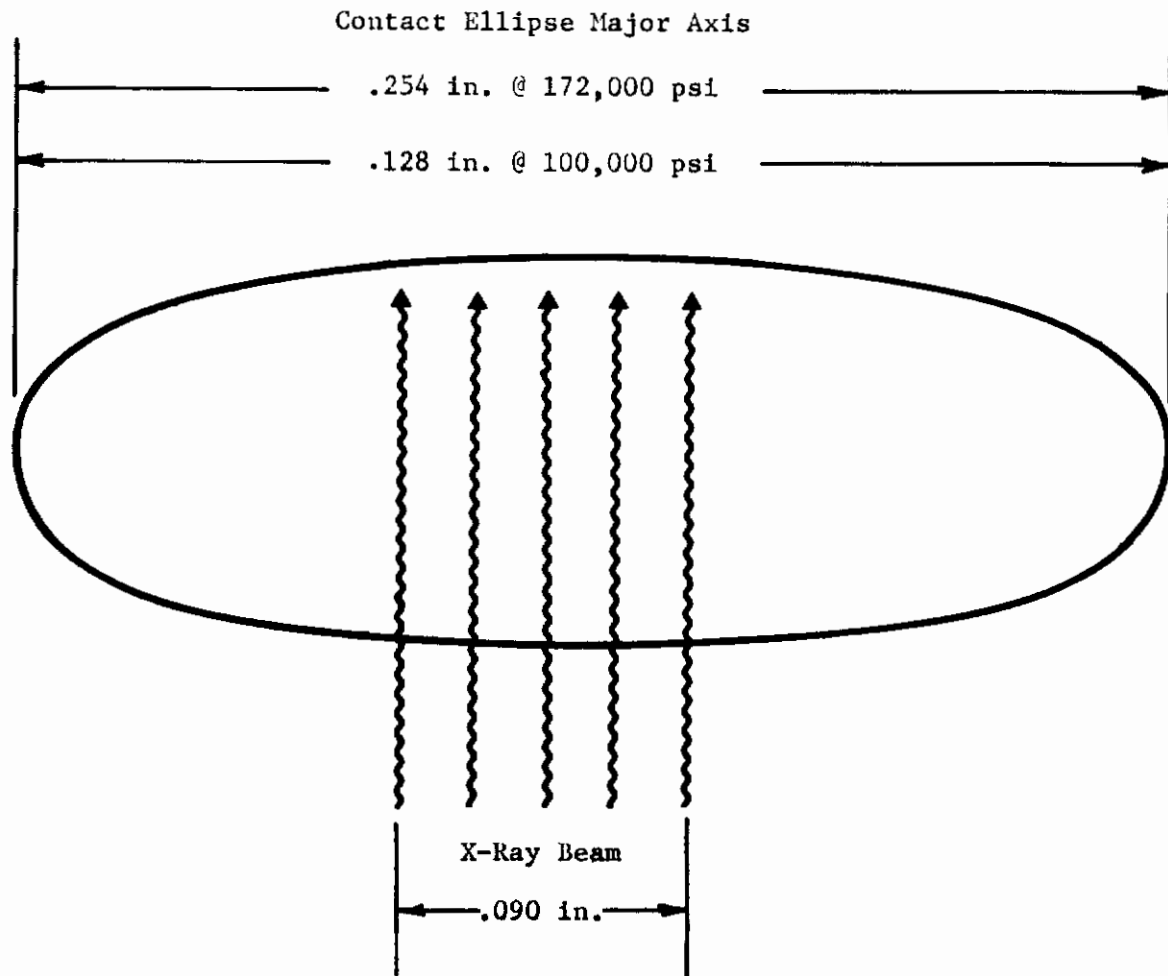


Fig. 50 Relative Dimensional Characteristics of X-Ray Beam and Contact Zone

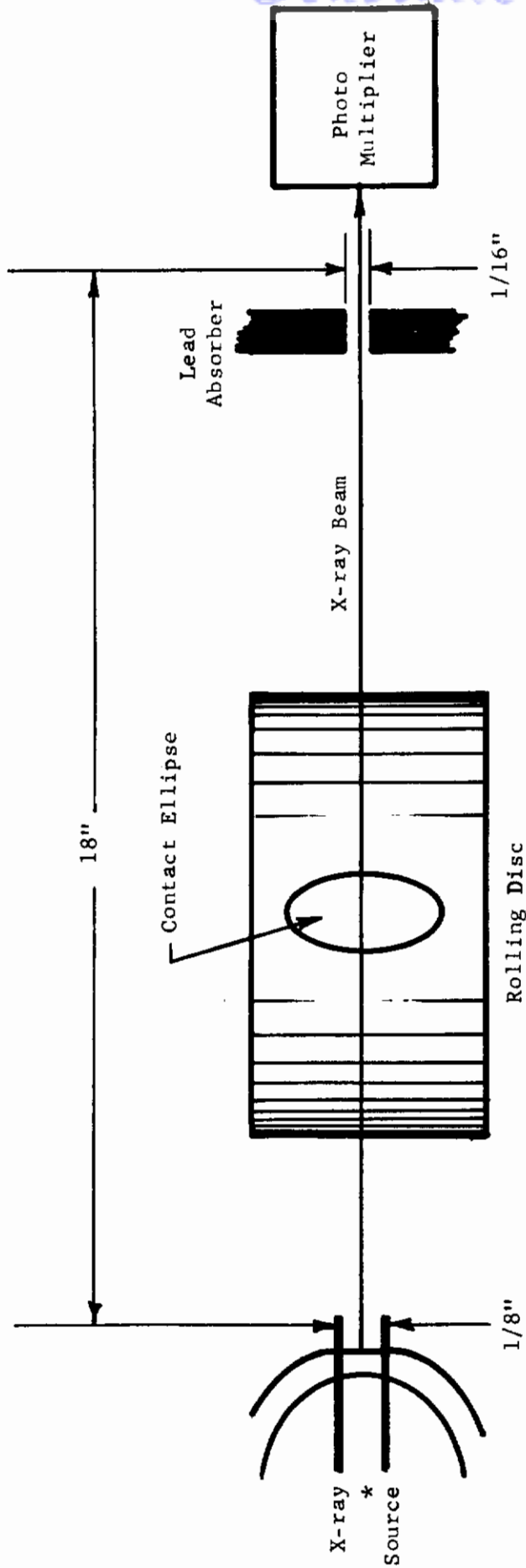


Fig. 51 Top View of X-Ray Beam Test Arrangement

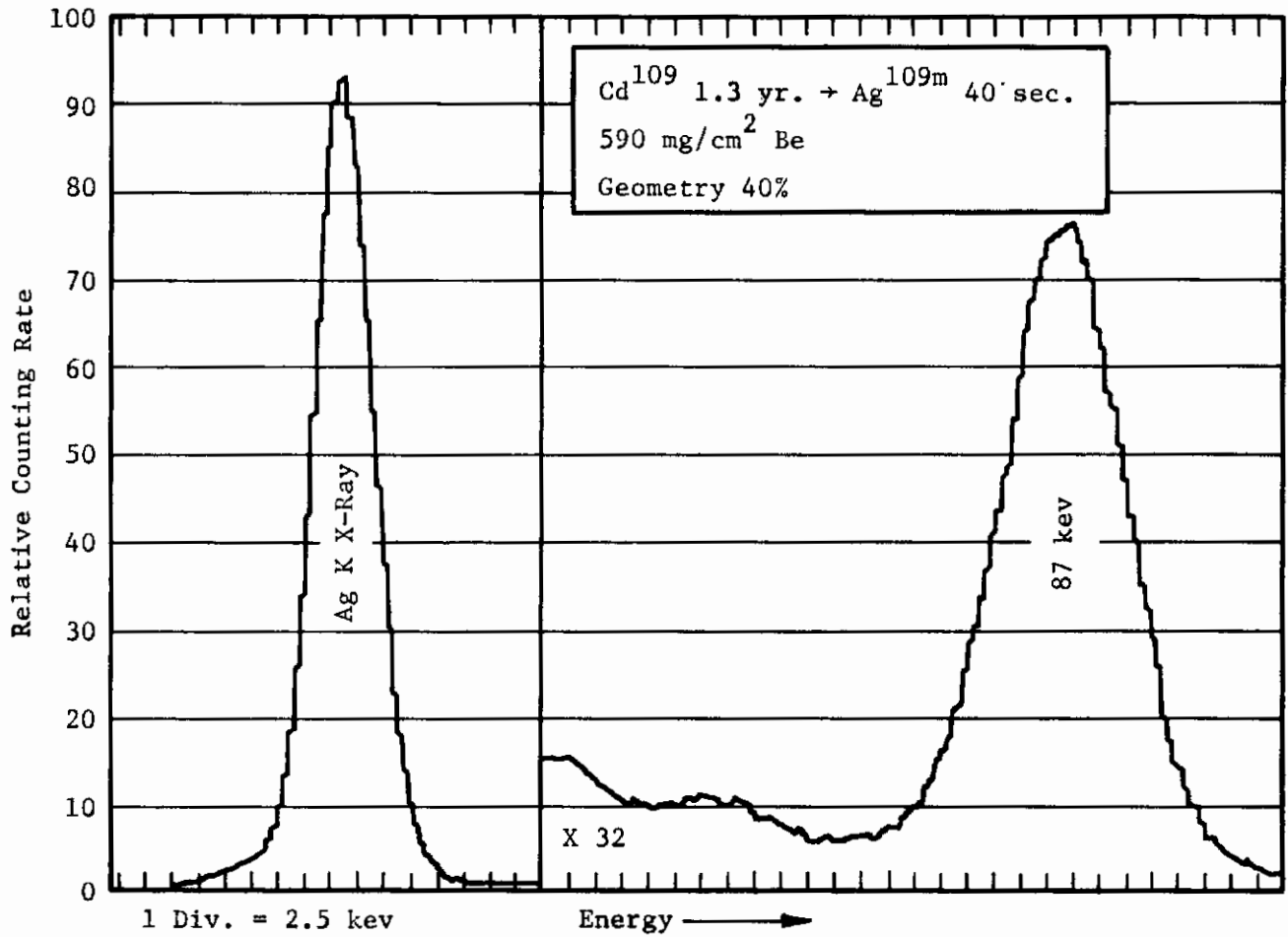


Fig. 52 Cadmium 109 Energy Decay Spectrum

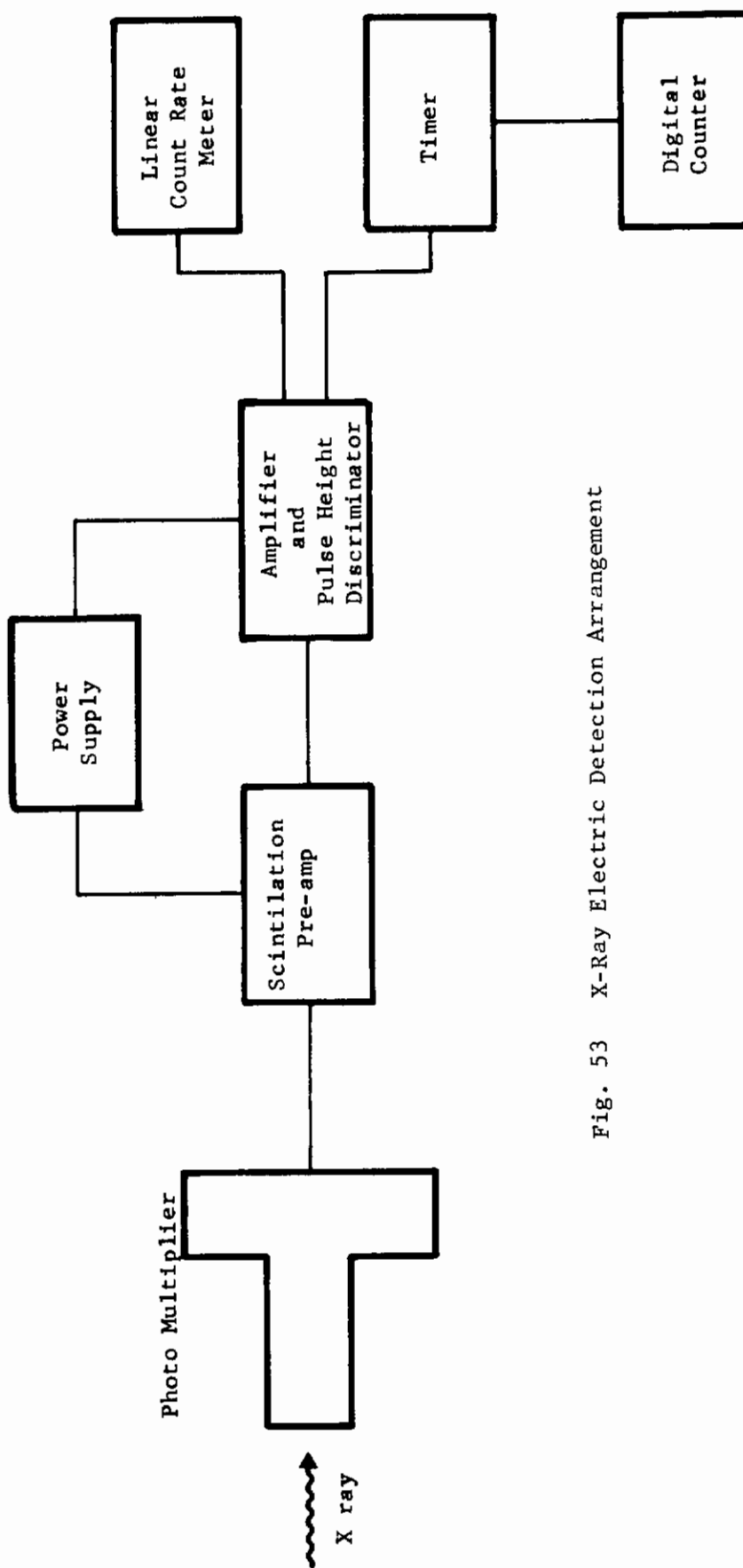


Fig. 53 X-Ray Electric Detection Arrangement

MTI-13369

Contrails

values of μ found from the two test fluids and X-ray source used were

<u>Test Material</u>	<u>Cd¹⁰⁹ X-Ray Absorption Coefficient</u> <u>μ</u>
MIL-L-7808	- .63 in ⁻¹
Polyphenyl Ether (5P4E)	- .82 in ⁻¹

The calibration of the disc separation was performed in the same manner as with the capacitance techniques. The count rate of X-rays was determined for fixed separations between the discs at 1, 2, 3, 5, and 10 mils separation. Since the beam width of the X-ray source was confined to less than 90 mils both in height and width at the contact zone, the calibration was made with no load on the discs. The relationship between separation and count rate was found to be both linear and a first power dependence as shown by the log-log plot in Figure 54. An extrapolation of the dependence into the microinch region was taken for the actual determination of film thickness from the count rate data taken under full load and rolling speed conditions.

Well over 150 sets of count rate data under dynamic conditions were recorded during testing. At least five recordings of X-ray count rate were taken for each of:

- (a) Three rolling conditions: zero, 470, and 920 in/sec
- (b) Five loads: 100, 120, 140, 160, and 172 kpsi
- (c) Two radiation conditions: beam-on and background (beam-off)

after beam alignment had been achieved. The disc machine contact zone was located with metal bluing and aligned with the exit hole of the radiation containment pig. A through hole in the container was opened whenever the Cadmium 109 source was rotated to the OFF position in the container. This through hole provided a convenient way (by insertion of a metal rod) to physically align the X-ray beam both in the vertical and horizontal directions with the contact zone.

The calibration of count rate with disc separation was determined when air filled the gap between the discs. The actual situation under rolling is similar to that shown schematically in Figure 55, where the X-rays must pass through a finite thickness of the test lubricant. The precise thickness is much greater than the minor axis of the contact zone, however, and was estimated to be $\leq .125$ inches from visual observation for the flooded conditions of actual running.

Net count rate data used to determine lubricant film thicknesses were obtained by subtracting the background recordings taken under identical loading conditions with no rotation of the discs. The mean values of film thicknesses obtained for each of the five load levels investigated are plotted in Figure 54 along the previously discussed calibration line. The nominal film thicknesses for rolling speeds of 920 in/sec and 470 in/sec were found to be approximately 30 microinches and were determined from the two mean values of all load data of the separate speeds investigated. Although the attenuation of the count rate signal was known, it was not used to modify the data. The X-ray

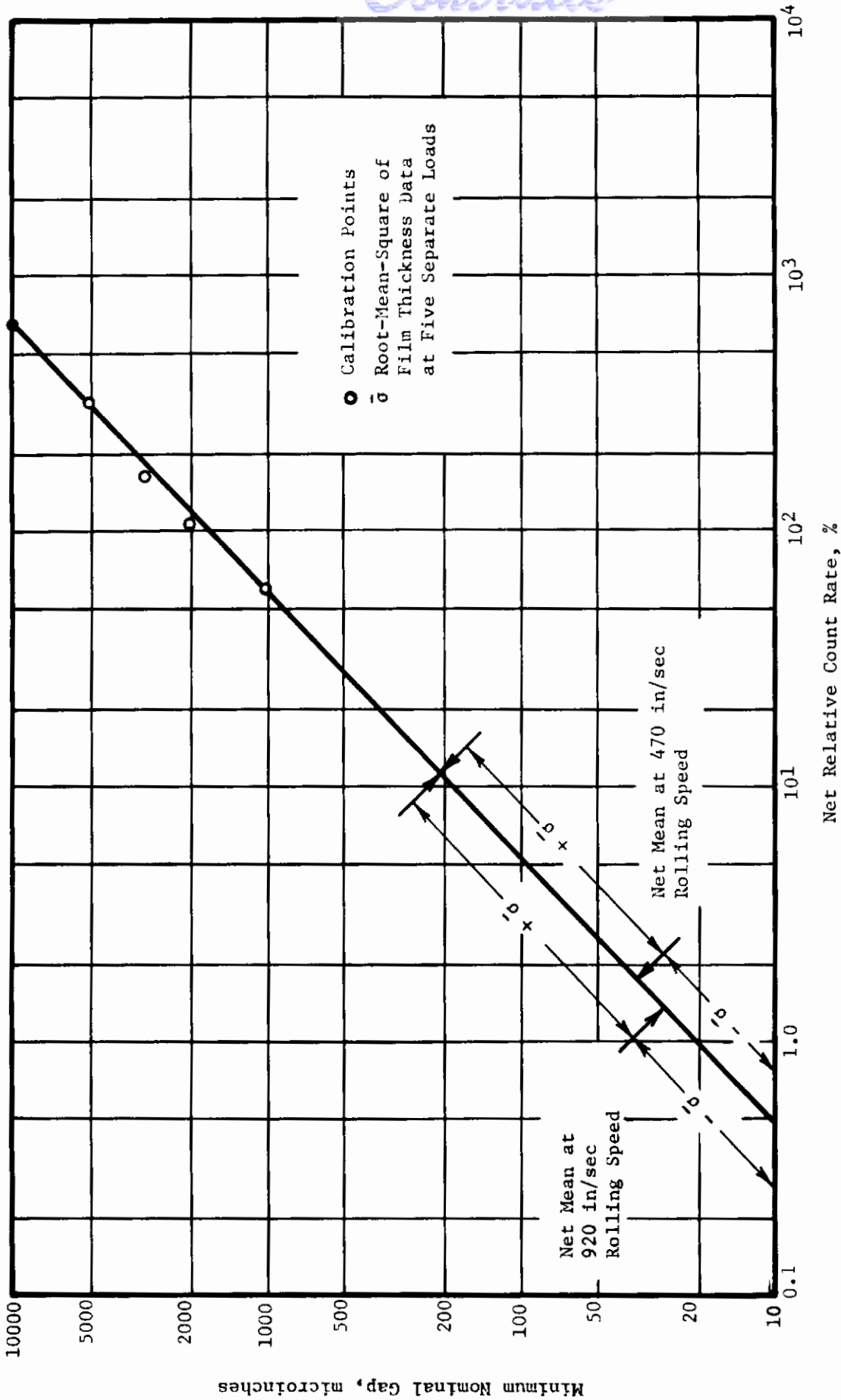


Fig. 54 X-Ray Film Thickness Determinations for Two Rolling Speeds

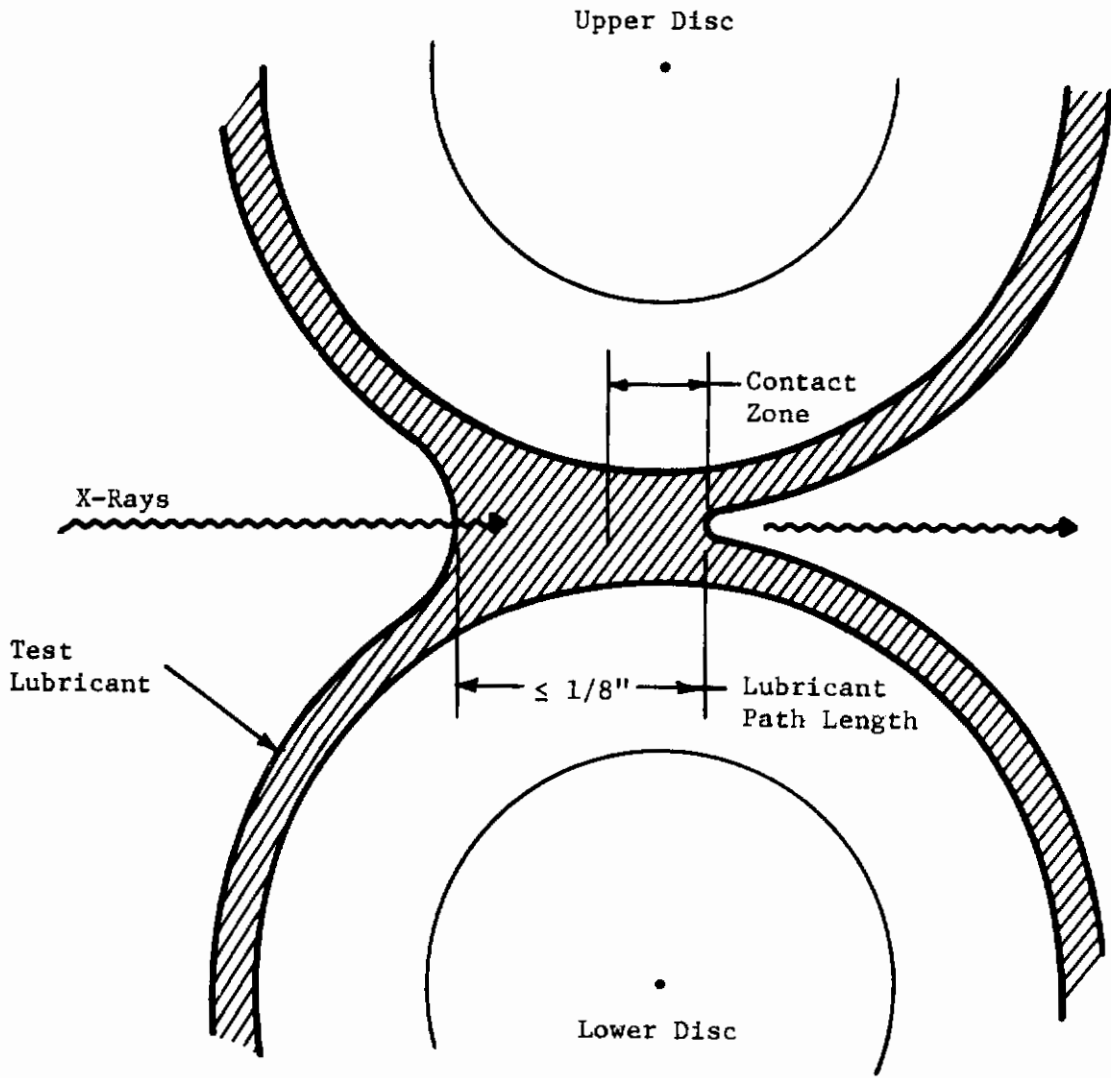


Fig. 55 Lubricant Inlet Exit Schematic

Contrails

attenuation is exponential with traversed length in lubricant and a lubricant path less than 1/8 inch would not significantly change the observed film thicknesses. Any consideration of the loss in X-rays in the lubricant, however, would be interpreted to give larger films than the 30 microinches found.

No correlation between variations in film thickness with speed and load could be obtained. Some of the lower loads revealed smaller films than some of the higher loads investigated and the mean film thickness of the slow speed was larger than that obtained at the higher test speed. The partial inconsistency in the data was assumed to be a result of a low signal-to-noise ratio obtained electronically from the available X-ray count rates. The root-mean-square of the data gathered under all loading conditions is shown also in Figure 54 as a measure of the scatter observed in the X-ray data.

SECTION VI

ASPERITY INTERACTION AND PARTIAL ELASTOHYDRODYNAMICS

Observation of asperity interaction was performed with the aid of the electronic "Asperitac" developed specifically for the work reported here. An overview of the operational characteristics of the electronics were reviewed in Reference 1. The development of the device centered around obtaining a real time electronic system which would generate characteristics of any typical resistance-time curve. Figure 56 is a schematic of a typical metal contact resistance-versus-time plot under partial lubrication conditions of sliding and/or rolling. The instantaneous fluctuation of the resistance is a complex function of

- (a) Lubricant film thickness, electrical properties, and
- (b) Contacting metal surface curvatures, surface finish roughness, and relative velocity between contacting surfaces.

The Asperitac provides a convenient means of determining for a given set of test conditions:

- (a) The percent of time spent in contact in any lubricated metal interface.
- (b) The number of contacts occurring per unit time across the interface.
- (c) The area of the shaded portion indicated in the schematic of Figure 56.
- (d) The nominal time-averaged resistance present in the contact zone.

In addition, the applied voltage, center-scale resistance, and resistance level of detection can all be preselected with the electronics used.

The percent of time a lubricated contact spends in the contact mode can be obtained either digitally or in an analog fashion. The observed percent contact is taken as the time spent below the preselected detection resistance relative to the total time of observation. Figure 57 displays a typical analog output of percent contact on the disc rig as a function of both Hertz contact pressure and rolling speed when polyphenyl ether is used as a lubricant. The discs used for the asperity work were the same as those used in determining capacitive film thickness measurements. The lower disc was isolated electrically from ground and held at a fixed voltage level of .391 volts D.C. for all contact work with the regulated power supply in the Asperitac.

Since nominal film thicknesses are typically in the microinch region for lubricated contacts, applied voltages in the one volt range may break down the lubricant through electrical discharge. No such breakdown of polyphenyl ether

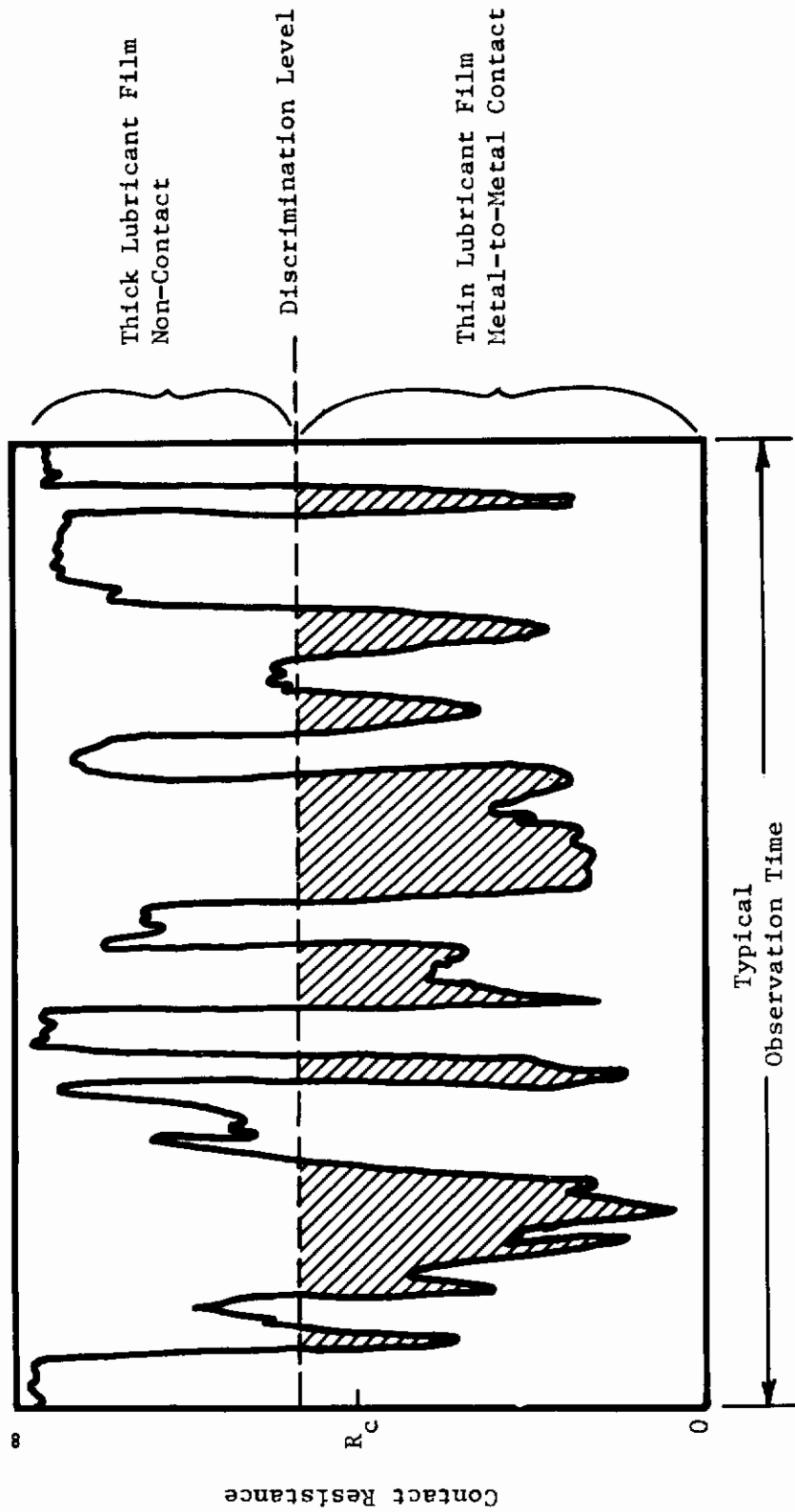


Fig. 56 Typical Contact Resistance Versus Time Variations

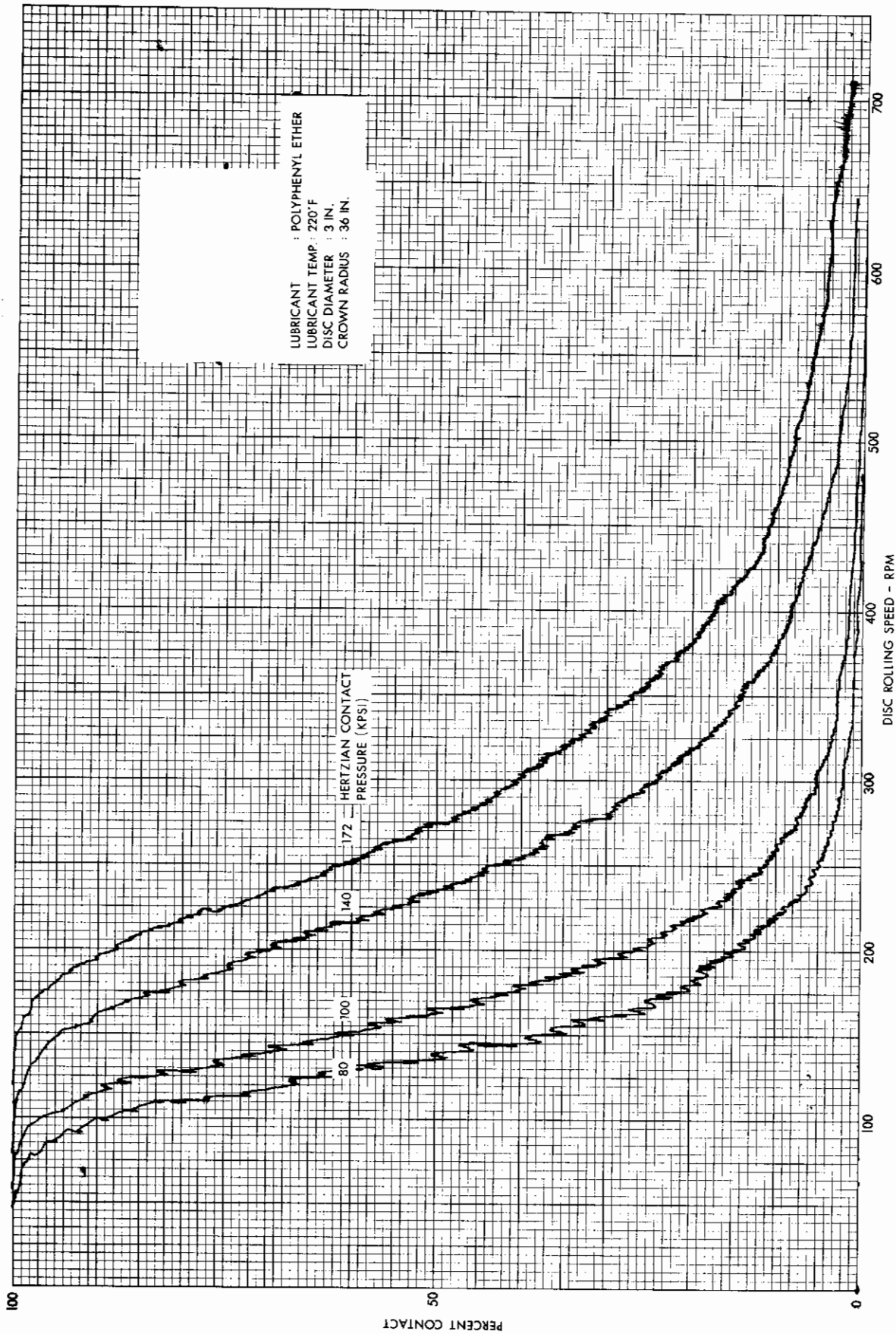


Fig. 57 Asperity Contact Data as a Function of Rolling Speed for Four Separate Loads

MTI-13095

was observed up to the 1.0 volt D.C. available with the power supply used. Percent contact and asperity count rate was observed to be constant for applied voltages up to 0.8 volts across the contact zone.

The Asperitac has in its present form a single level-crossing detection circuit and does not, with a single observation, determine the distribution of the resistance fluctuation levels. This information was determined by making separate observations using center-scale resistances of 10, 100, 1,000, 10,000, 100,000 ohms. The resulting analog signals are reprinted in Figure 58. Since each detection level determines the percent of time spent below that resistance, a full distribution of the fluctuating resistance levels with time can be determined for a given rolling contact condition.

1. TIME-AVERAGED RESISTANCE VERSUS SPEED

The distribution of fluctuations for any speed over the test range observed shows a log-normal dependence between resistance level and percent contact. The cross plots for several fixed speeds taken from Figure 58 are shown in Figure 59. By using the log-normal dependence, one is able to determine actual time-averaged resistances for every percent contact output of the Asperitac. The percent-contact-time-averaged-resistance points are connected in Figure 59 by the dotted line shown. Since percent contact is observed over a full range from 100 percent to zero, the functional dependence of nominal resistance averaged over time and the full contact zone was found. Figure 60 shows the exponential function for a Hertzian contact pressure of 172,000 psi. The experimentally-observed exponential increase in resistance with speed turns out to be a sensitive lubricant film detector under partial elastohydrodynamic conditions.

At large loads or low rolling speeds, the lubricant film thickness will be of the same order of surface roughness as the rolling surfaces. Thus, asperities will have metallic interactions and part of the applied load will be shared by interacting asperities. With the description of surface topography and of an appropriate model for the mechanics of interactions between a pair of asperities, such load sharing, real area of contact, and electrical contact resistance can be estimated. A detailed analysis of the problem has been described in References 1, 16 and 17. We shall present results for typical ball bearing surfaces having rms roughness of the order of 2 microinches. After summarizing the surface topographical data, results of asperity load sharing will be presented.

2. SURFACE TOPOGRAPHY

Steel specimens (AISI 52100) in the form of 3 inch diameter and 1 inch thick discs (no crown) were commercially prepared. The rms surface roughness of less than 2 microinches was ensured. Measurements of the surface topography consisted of obtaining several surface profiles along the axis of the disc using the Talysurf Model 4 profilometer with a standard 100 microinch stylus (see Figure 61 for another set of test surface tracings). An electrical signal proportional to the surface profile was picked up from the electronic unit of the profilometer and was recorded on an FM tape recorder. The data was then digitized at a suitable sampling rate determined by highest frequencies present in the data. A sampling interval of 40 microinches was found to be sufficient for

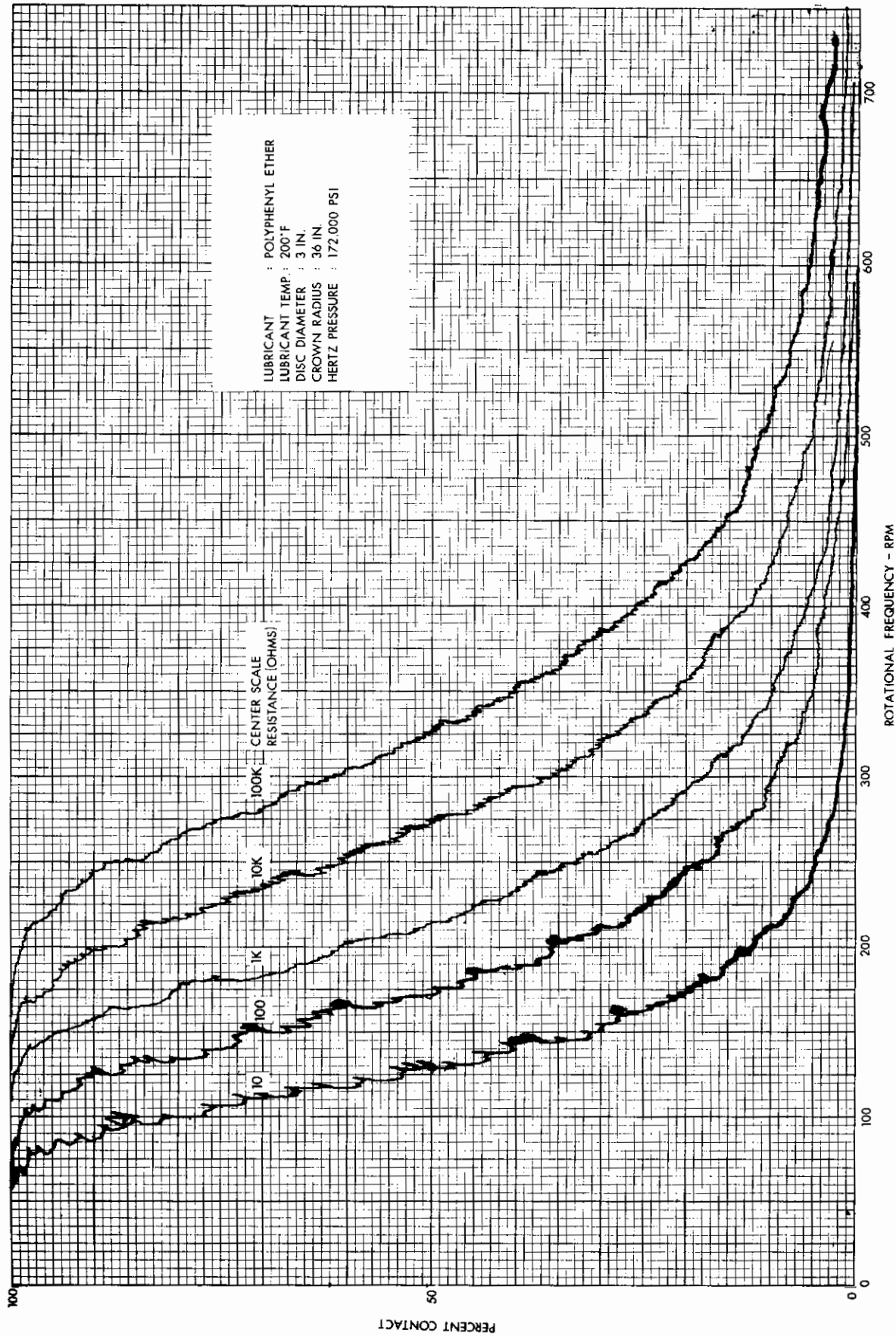


Fig. 58 Asperity Contact Data as a Function of Rolling Speed for Five Resistance Detection Levels

MTI-13093

Contrails

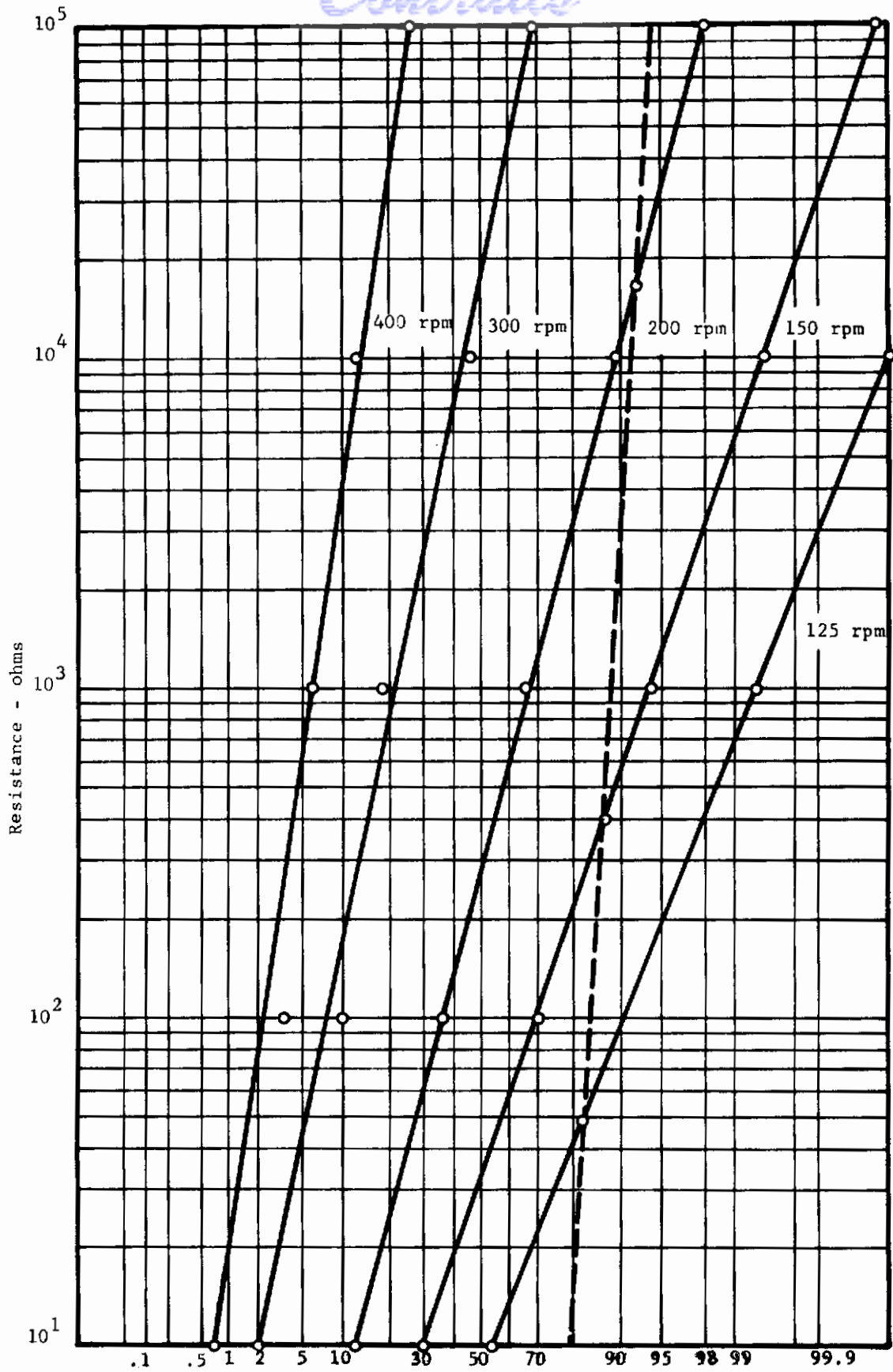


Fig. 59 Percent Contact Versus Contact Resistance for Five Speed Levels

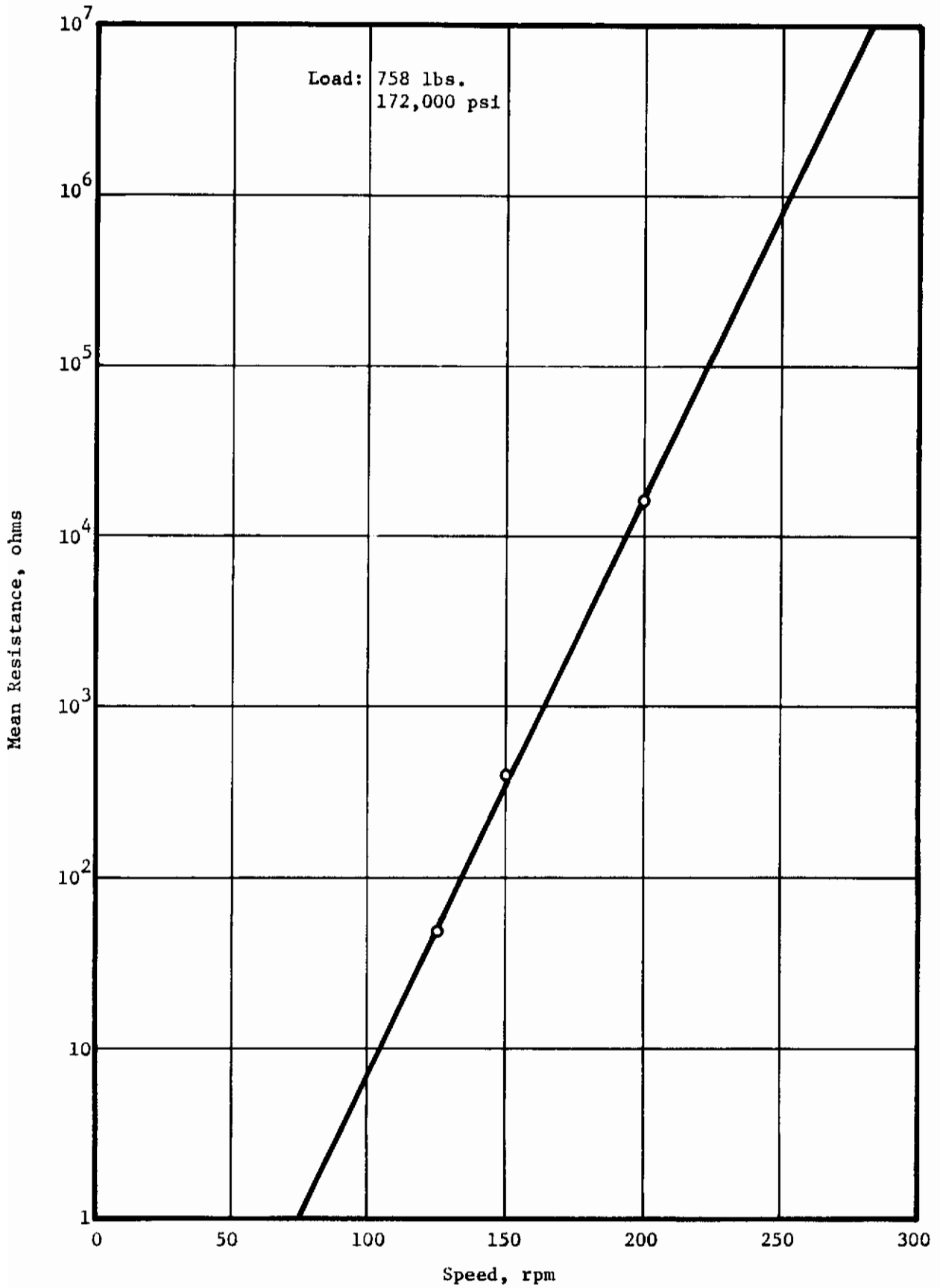


Fig. 60 Time-Averaged Rolling Contact Resistance as a Function of Speed

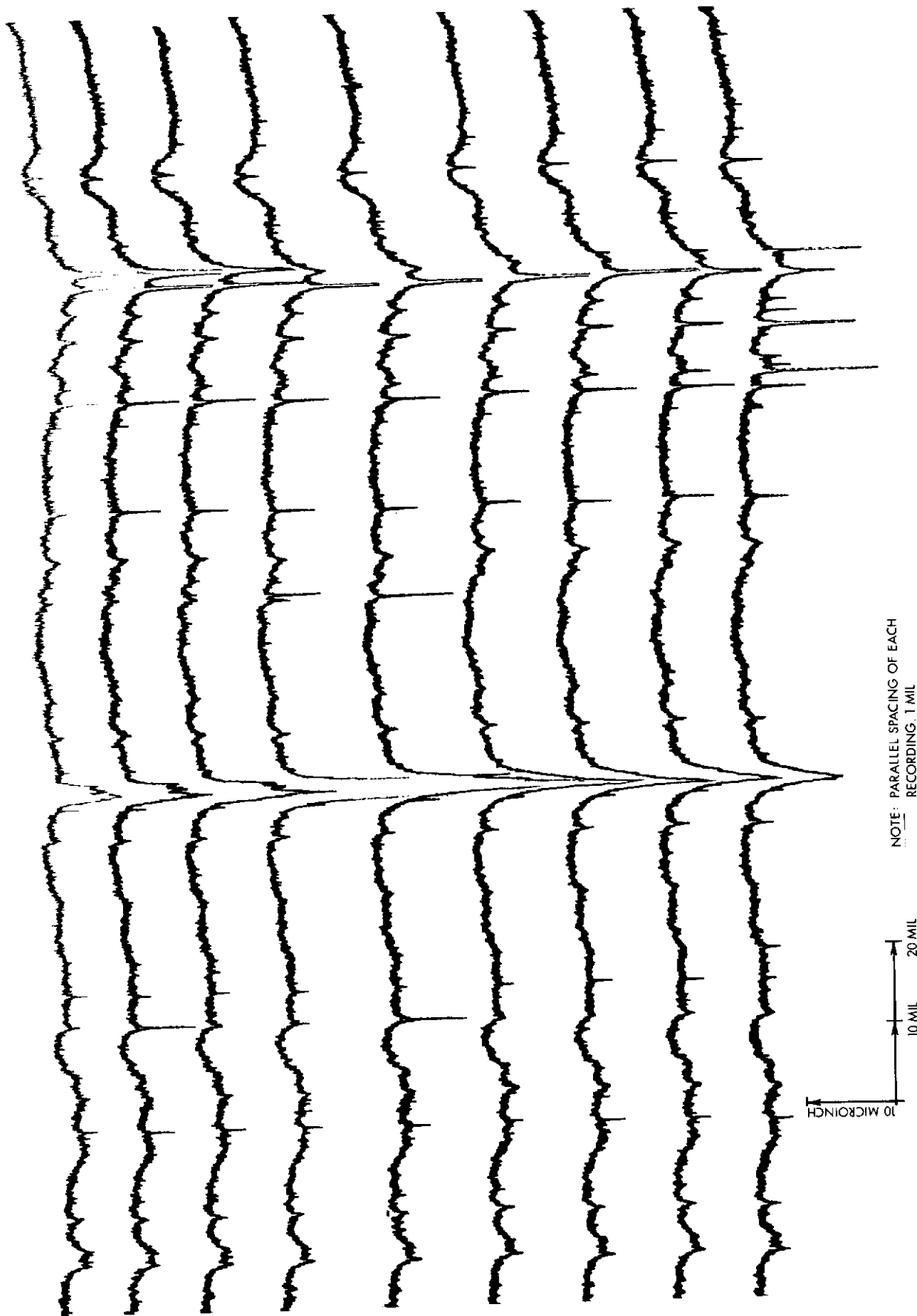


Fig. 61 Nine Parallel Talysurf Tracings of Roller Specimen Surface Finish

Contrails

most surface profiles analyzed. As will be shown later, most surfaces had very low frequencies and therefore sampling at large distances was necessary to obtain a reasonable spectral distribution of the data.

Peak asperity heights and radii of curvature were estimated by using the most common three-point definition for a peak. Statistical distribution of peak heights is shown in Figure 62. The data is fitted by a Gaussian function and the parameters of the distribution are used in the analysis of the surface interactions as described in Reference 1. Radii of curvature at the peaks is fitted by a log normal function as shown in Figure 63. Statistical correlation between the heights and radii was found to be less than 0.1. Thus, the assumption of independent heights and curvatures is valid.

Approximation of the three-dimensional hill or summits by peaks given by a surface profile has been a very controversial question for the last few years. Nayak (18) has performed a detailed mathematical analysis based on earlier work (20). It is shown that the differences between heights and curvatures of peaks can be substantially different from those of the summits. The differences are shown to be generally dependent on the spectral density function of the surface profile. If $\psi(f)$ is defined as the spectral density function where f is the frequency, the moments of $\psi(f)$ are defined as

$$m_i = \int_0^{\infty} \psi(f) f^i df$$

It is shown that an important parameter which represents the differences between profile and surface characteristics is

$$\bar{\alpha} = m_0 m_4 / m_2^2$$

For large $\bar{\alpha}$, heights and curvatures are essentially independent and the differences between profile and surface characteristics are expected to be quite small.

The data of five surface profiles (Fig. 1) were used to compute the autocorrelation and spectral density function. The recordings contained information directly related to the recording technique which was not representative of the local surface structure. The necessary components of the data which were removed before computing $\psi(f)$ included absolute shifts in D.C. level signals, linearly increasing or decreasing variations, and low frequency components with wavelengths of the order of the profile tracing length. The spectrum showed a large peak in the very low frequency region and was close to zero at higher frequencies. By sampling at large intervals the frequency band could be reduced to the region of interest but the upper cut-off frequency introduced some aliasing error on the trailing end of the spectrum. This is shown in Figure 64. The decay in the autocorrelation is also very slow; this is shown separately in Fig. 65, indicating dominance of low frequency waviness on the surface.

Moments of the spectral density functions were computed and α was found to be close to 25. Thus, the computed small correlations between peak heights and curvatures is probably in agreement with Nayak's analysis (18). Also, we are justified in approximating characteristics of the surface by those of the

Contrails

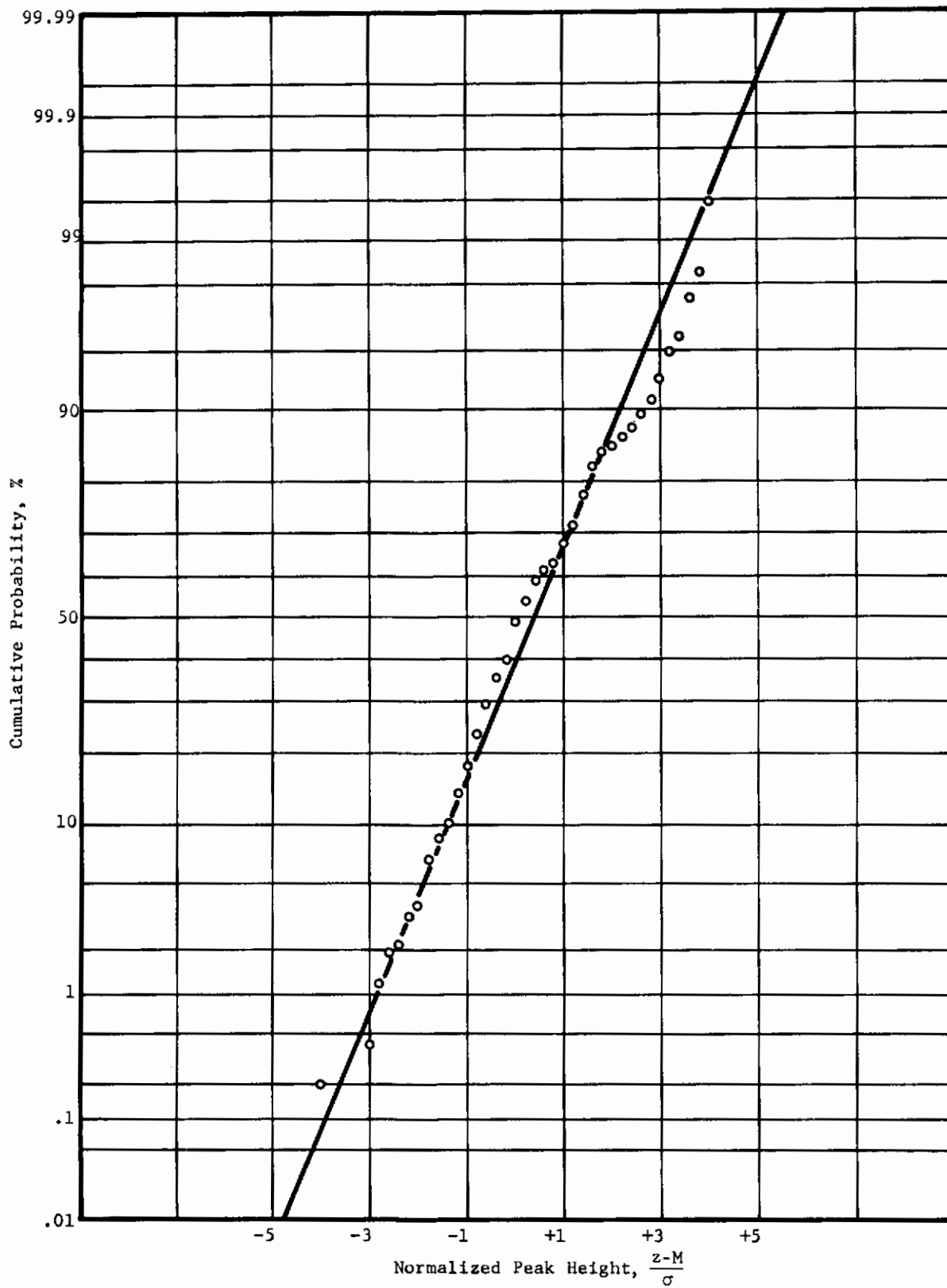


Fig. 62 Peak Height Distribution, $M = 0.342\mu''$ and $\sigma = 1.526\mu''$

Contrails

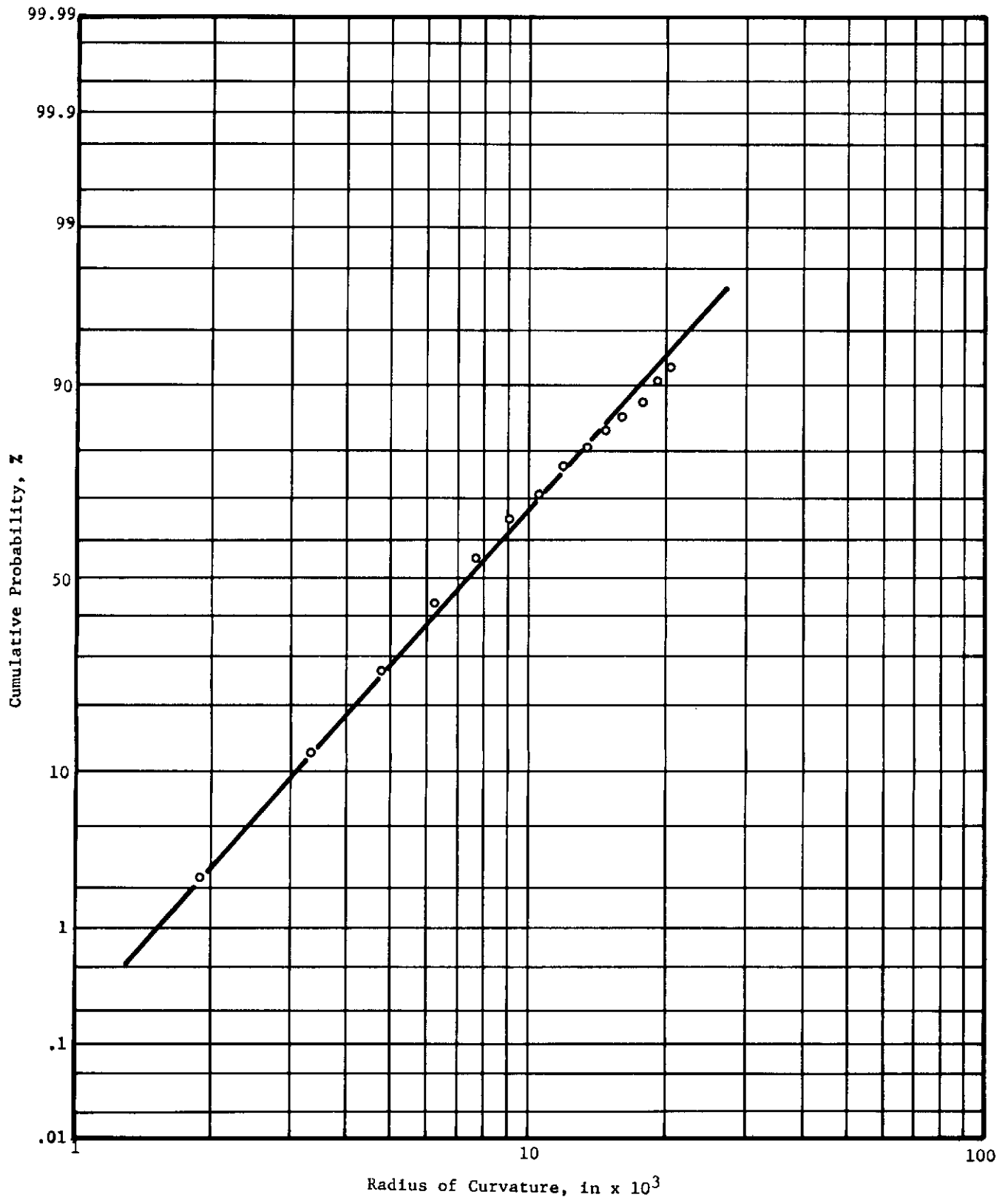


Fig. 63 Radius of Curvature Distribution at the Peaks

Contrails

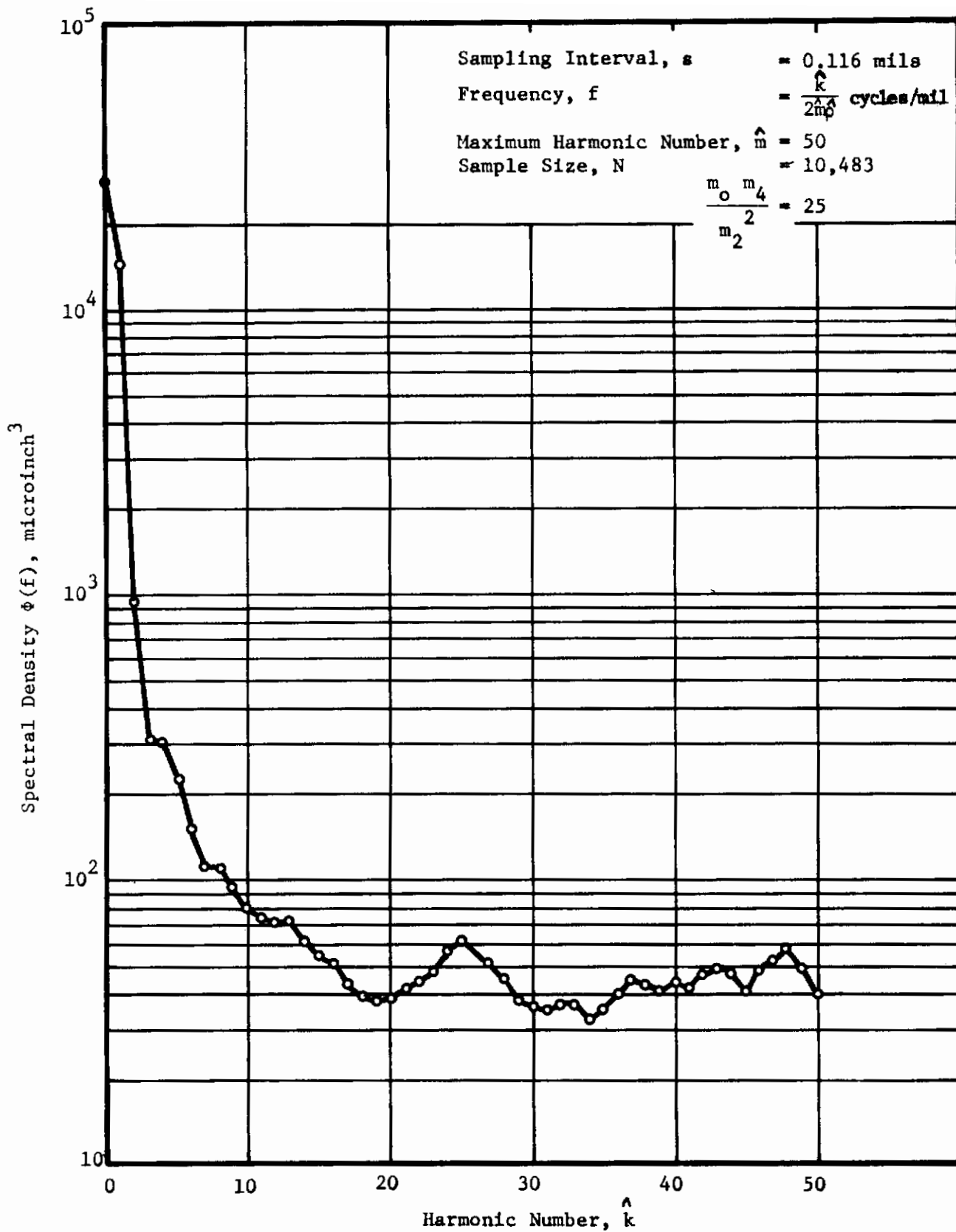


Fig. 64 Spectral Density Function

Contrails

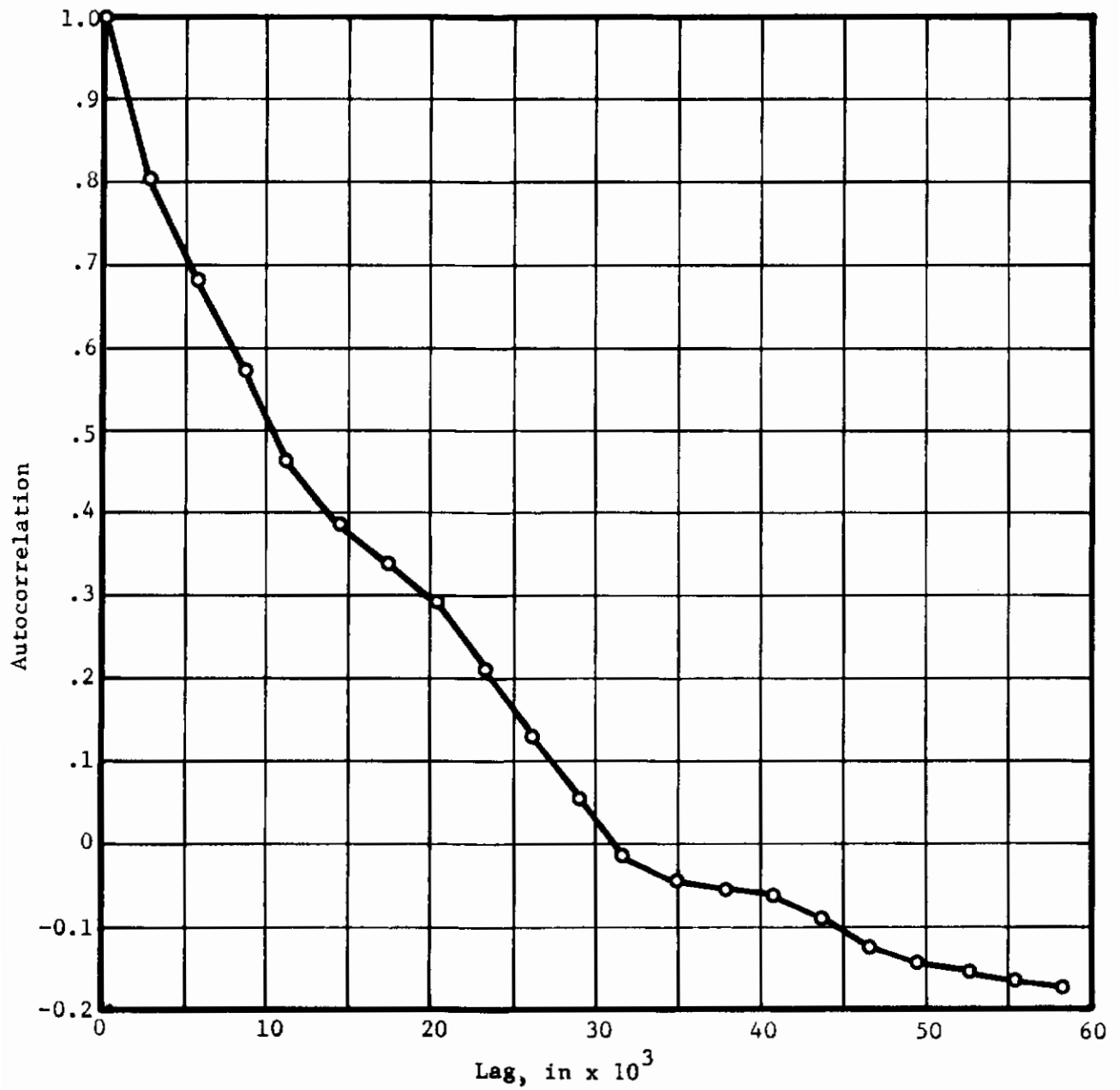


Fig. 65 Autocorrelation Function

profile produced by the talysurf trace recordings.

3. ASPERITY LOAD SHARING

With given statistical distributions of peak heights and curvatures, the loads supported by the asperities and the size distribution of microcontacts were calculated using the analysis described in Reference 1. All asperity interactions were found to be elastic in the range of mean plane separation 0.5σ to 4σ , where σ^2 is the combined variance of the peak height distribution of the two interacting surfaces. Identical surface topography was assumed on both surfaces and elastic junction models based on the Hertz solutions were used to calculate the real contact area and load supported by a pair of asperities with given geometric interference. Quasi-static sliding was allowed with a constant interfacial shear stress equal to the flow stress (\approx yield stress/2) of the deforming materials. The detailed analysis of the junction model is described in Reference 17.

Figure 66 shows the loads supported by the asperities as a function of the mean plane separation (i.e., the normal film thickness) for a unit apparent area. The real area of contact is also plotted. With computed micro contact size distribution and knowledge of the electrical properties of the materials and expected lubricant films, the electrical contact resistance was computed.

For any given geometry of interacting surfaces, in our case cylindrically crowned discs, the Hertzian contact area and the expected lubricant film thickness can be estimated. Dowson and Higginson's formula was used to compute the film thickness as a function of speed and lubricant properties. Knowing the film thickness and the Hertzian area (which will be the total effective apparent contact area) the total normal and friction load supported by the interacting asperities and the real contact area may be found directly from Figure 66. Solutions given in Figure 66 were assumed to be valid for crowned discs such as the one used experimentally since all specimens were produced at one time in a single lot with the same techniques. Thus, the loads shared by the asperities may be plotted as a function of rolling speed as shown in Figure 67. The speed ranges for full hydrodynamic, partial elastohydrodynamic and essentially dry contact are clearly evident from Figure 67.

4. ELECTRICAL CONTACT RESISTANCE AND FILM THICKNESS

For a given film thickness, it is possible to compute the size distribution of microcontacts and subsequently the electrical contact resistance. Contact resistance of a single microcontact is given by (19)

$$\hat{R}_i = \frac{\hat{\rho}}{4 a_i} + \frac{\hat{\xi}}{\pi a_i^2}$$

where $\hat{\rho}$ is the sum of electrical resistivity of the two materials, $\hat{\xi}$ is the tunnel resistivity due to adsorbed layers on the mating surfaces, and a_i is the microcontact radius. Tunnel resistivity $\hat{\xi}$ depends very strongly on the thickness of the adsorbed layer (19) and may be approximately expressed as

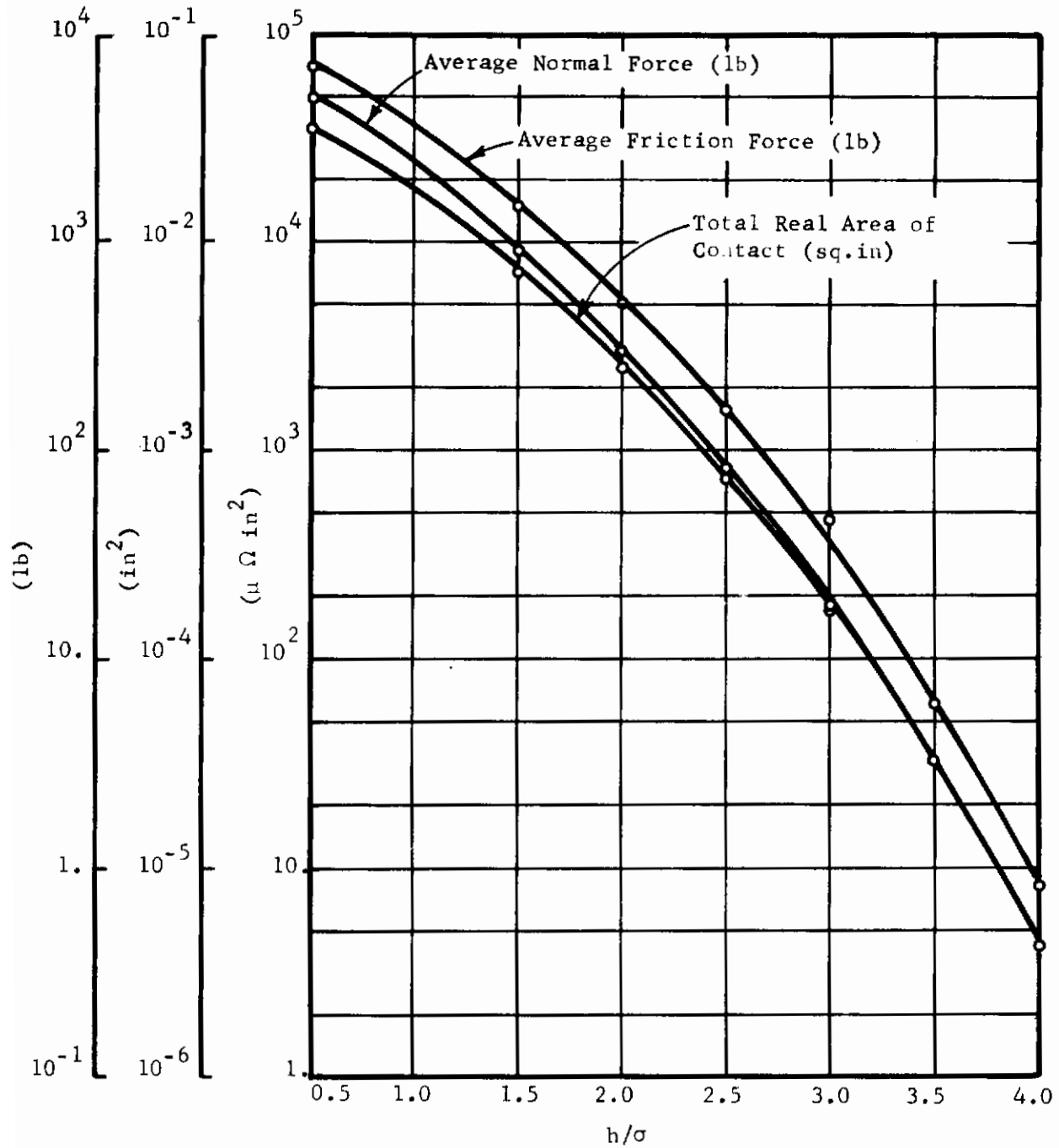


Fig. 66 Average Normal and Friction Forces Supported by the Separations Between Mean Planes of the Interacting Asperities

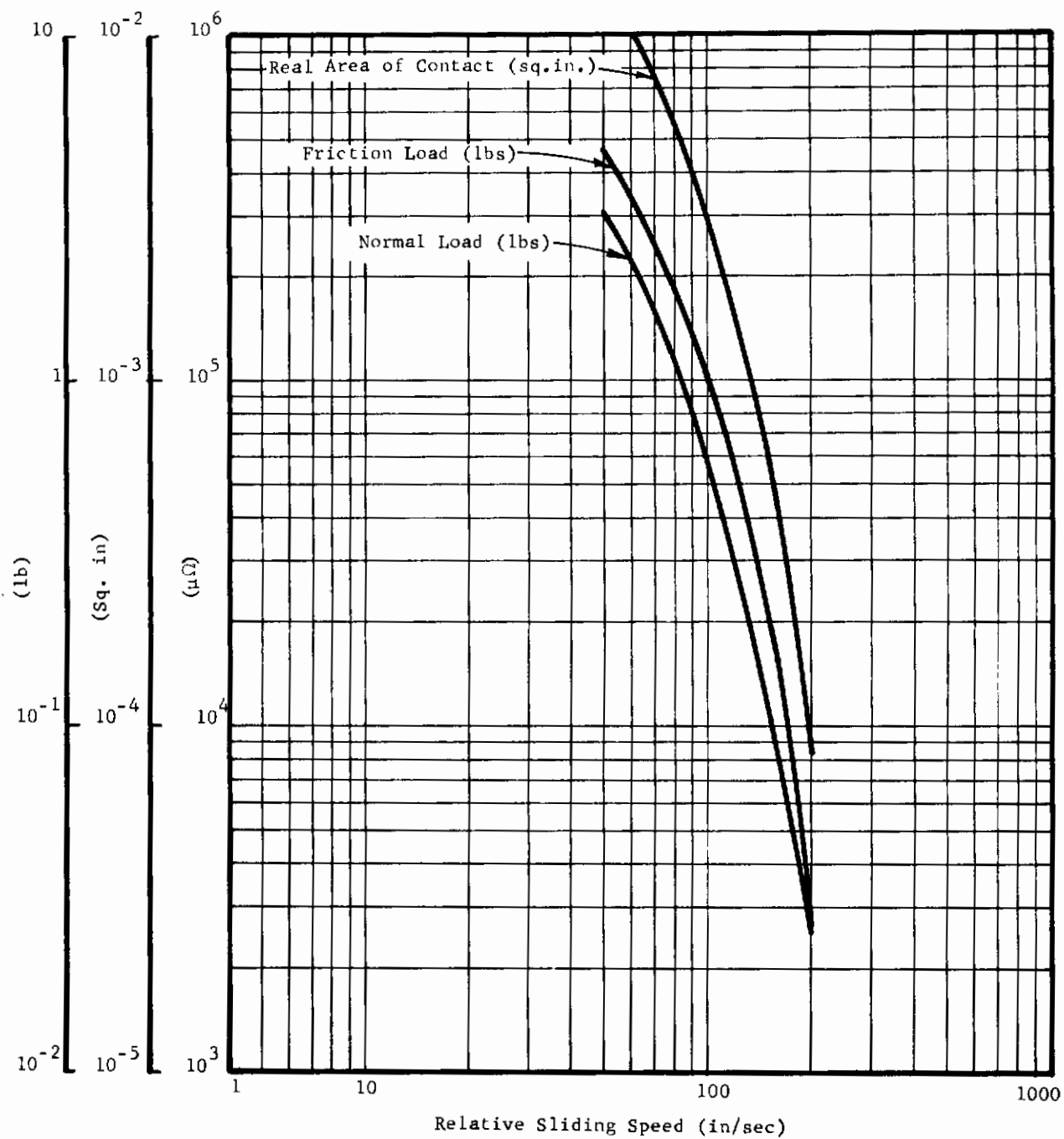


Fig. 67 Asperity Loads and Real Contact Area as a Function of Rolling Speed

Contraails

$$\xi = \frac{10^{-22}}{2} \cdot \frac{A^2}{1 + AB} e^{AB} \text{ ohm-cm}^2$$

where

$$A = 7.32 \times 10^5 [t - (7.2/\phi)]$$

$$B = 1.265 \times 10^{-6} \phi - (10/t \epsilon_r)$$

$$t = \text{surface film thickness, (\AA)}$$

$$\phi = \text{work function for electron emission, (eV)}$$

$$\epsilon_r = \text{relative permittivity of the material in the gap}$$

The total resistance may be obtained by summation over all the microcontacts.

If a model for film thickness as a function of speed is assumed, then it is possible to estimate the electrical contact resistance if the tunnel resistivity is known.

A computation of tunnel resistivity based on the range of expected lubricant adsorbed layers (as per table in Reference 20) showed that the constriction resistance as compared to tunnel resistance at the microasperities is generally very small and thus the computed resistance can approximately be stated as directly proportional to the tunnel resistance. With $\psi = 0.5$ eV and $\epsilon_r = 4$, the values of ξ as a function of layer thickness t are shown in Figure 68.

For a unit tunnel resistivity and a unit apparent contact area the computed resistance may be plotted as a function of lubricant film thickness as in Figure 69. Now for any given load knowing the Hertzian or apparent area the total contact resistance at a given film thickness and tunnel resistivity may be directly determined from Figure 69. For the 760 pound load, the average film thickness as a function of speed was estimated using Grubin's formula (10) and thus the mean resistance was computed as a function of speed for three values of fixed tunnel resistivity. The results are shown in Figure 70 along with the experimentally-determined exponential variations of resistance with speed.

The extremely high sensitivity of contact resistance with speed, as compared with analytical predictions, could be explained in several ways. It is possible that a few scratches on the surface of the discs may introduce highly non-Gaussian characteristics in the surfaces. However, it is not clear as to what degree such deviations would change the resistance speed relationships except that the presence of a very small number of large asperities could radically steepen the resistance-speed curves. Additional analysis with non-Gaussian and nonisotropic surfaces is needed to determine the sensitivity of any such effects. Conduction through very thin adsorbed films at interacting asperities is another possible factor which could cause a high sensitivity of contact resistance with speed. The resistance would be very low when there was metal contact, but as the micro film built up with speed the interactions would cease with a small increase in speed and resistance would increase. When the separation between the mating asperities was in the range of 0 to 0.2 microinch,

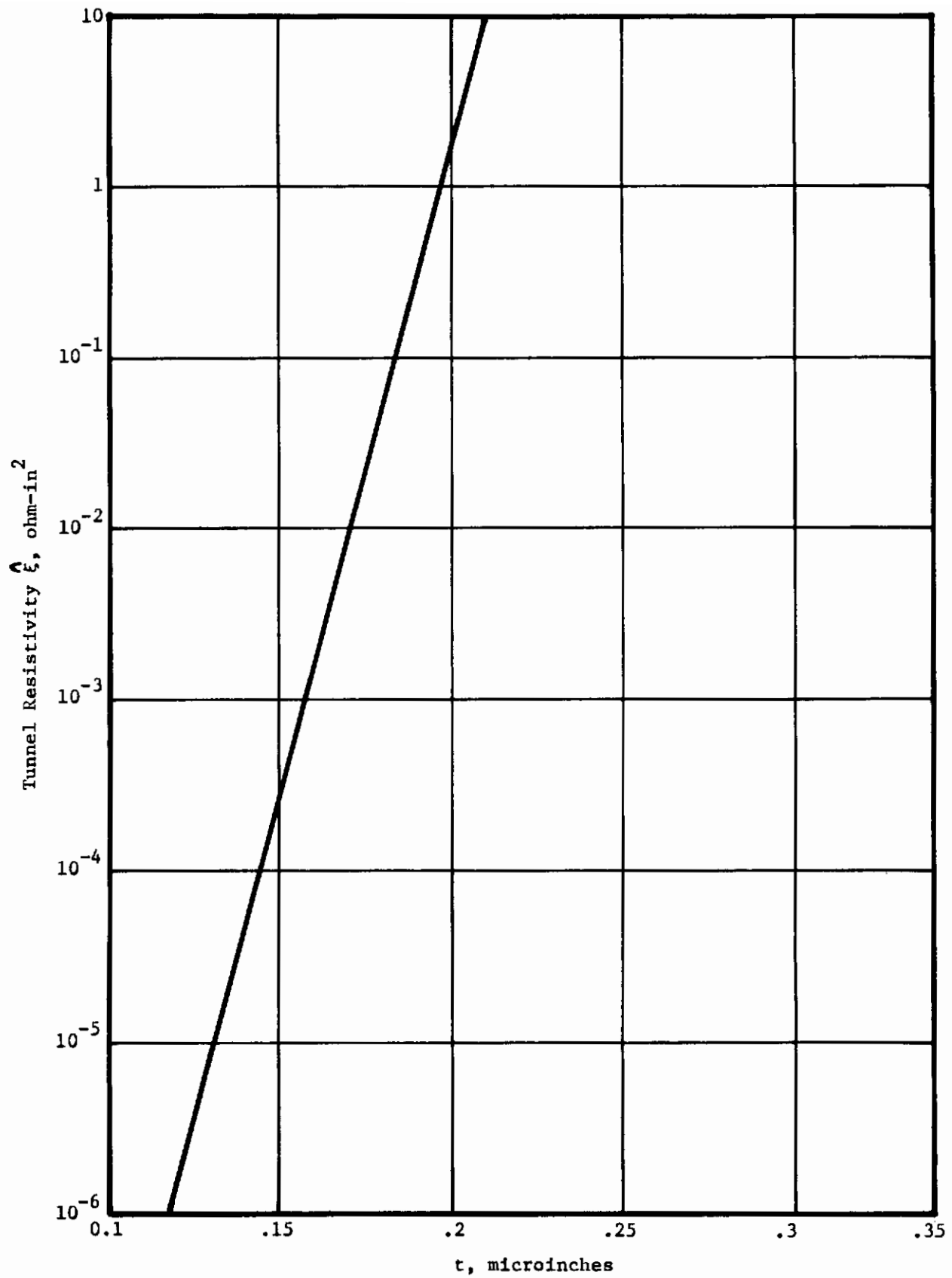


Fig. 68 Variations of Tunnel Resistivity as a Function of Adsorped Layer Thickness

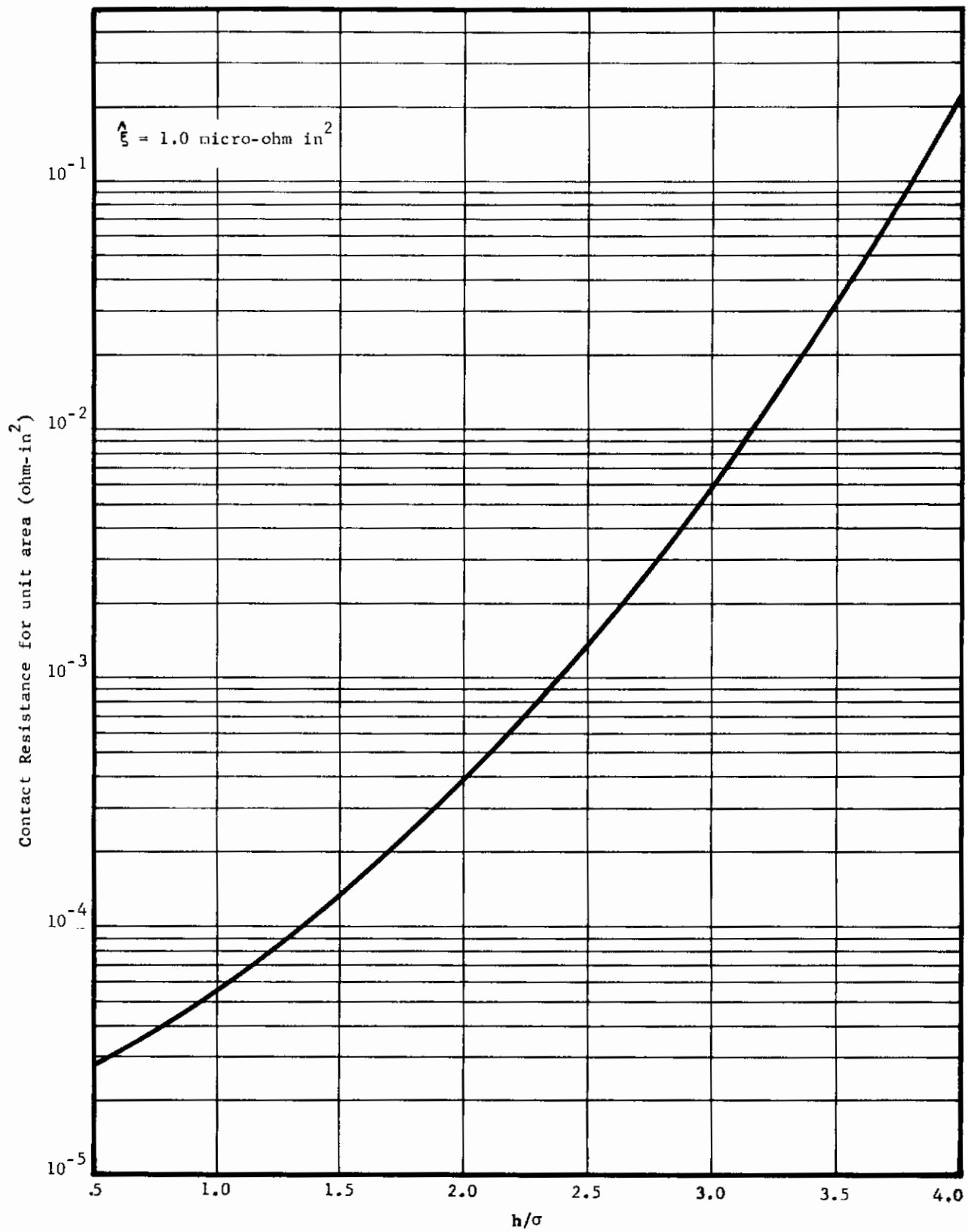


Fig. 69 Contact Resistance for a Unit Apparent Area as a Function of Separation Between Mean Planes

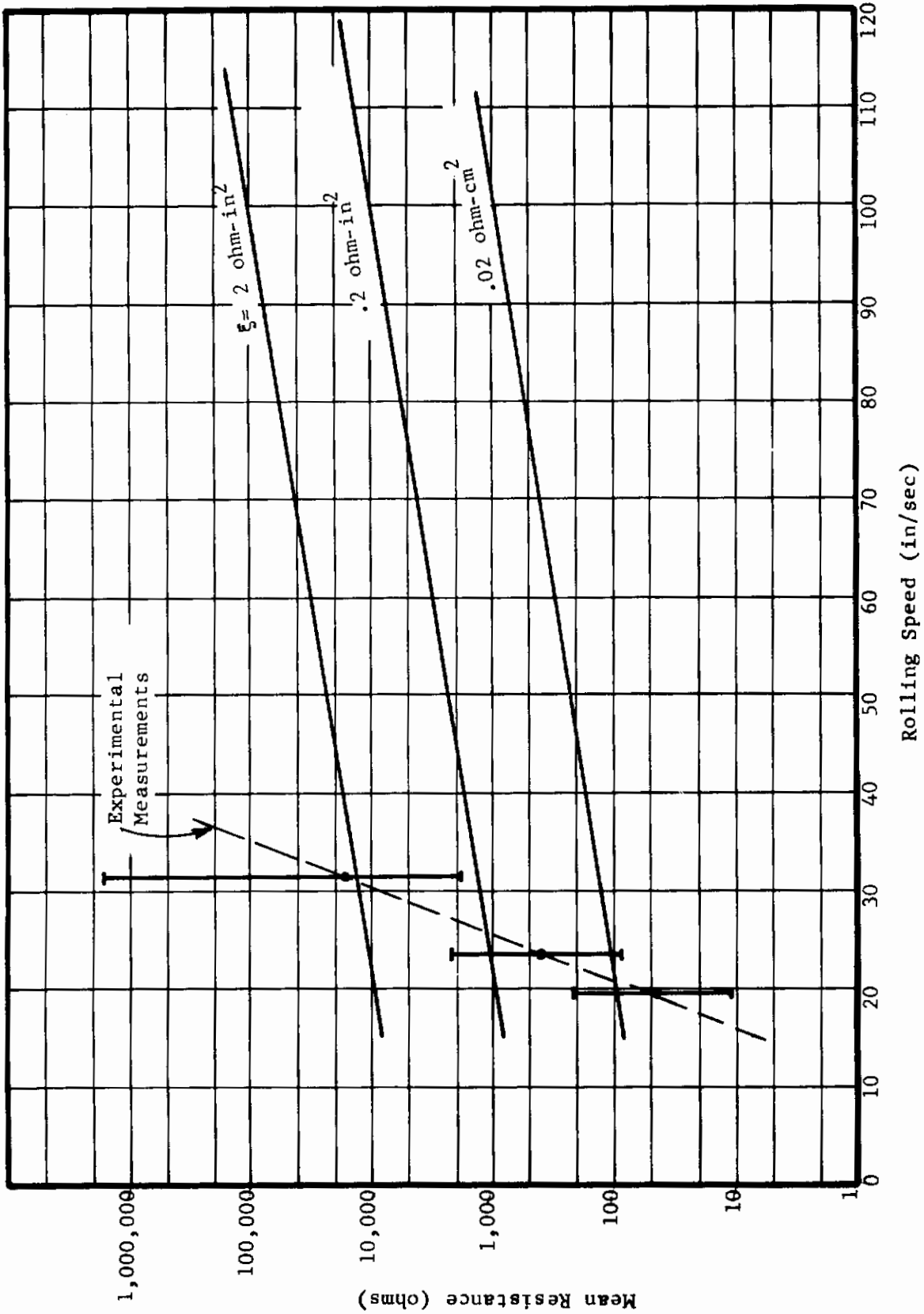


Fig. 70 Resistance Speed Relationships for Rolling Discs at 760 lb. Load. Grubin's Formula is Used to Determine the Film Thickness

Contrails

the resistances due to a thin absorbed film would be in the range measured. Since this resistance is a strong function of the separations between the asperities, a high resistance speed sensitivity would be expected.

The Asperitac measurements may be used to provide a good indication of the relative extent of surface contact, particularly in the incipient contact regime. The higher goal, using this device for extraction of film thickness in partial EHD lubrication, requires better agreement between theory and experiment than has been achieved thus far. It is anticipated that more analytical and experimental investigation along the lines given above would yield a technique for determining lubricant film thicknesses under partial elastohydrodynamic conditions.

Contrails

SECTION VII

CONCLUSIONS

The traction data obtained with the MIL-L-7808 oil showed both quantitative and qualitative dissimilarities with the 5P4E data, even under conditions where conventional viscosities and pressure coefficients of viscosity were similar. Order of magnitude differences in tractions measured under these conditions show that great caution must be taken when specifying lubricant properties in that conventional properties do not appear to determine lubricant traction behavior. In general, the MIL-L-7808 oil produced markedly lower tractions at all temperatures studied and showed a significant temperature dependence which was not exhibited by the polyphenyl ether. A hypothetical viscosity model has been put forth (as was done for polyphenyl ether) which mathematically represents the traction data over the ranges of loads, speeds, and temperatures studied experimentally. It was necessary, however, to allow for time effects when obtaining this correlation since the variations in traction with rolling speed are much larger than can be accounted for by predicted variations in film thickness alone.

Film thicknesses were measured by means of optical and capacitance techniques. The optical measurements provided the high degree of accuracy observed by other investigators who have used this technique. In particular, it showed the trailing edge dip which for the conditions of highly-elliptical contact extended across the back but did not appear to come around the sides. The optical measurements obtained with one cylindrical transparent quartz disc and one polished steel disc at fairly low pressures and speeds seem to be in reasonably good agreement with Dowson and Higginson's isothermal theory. This agreement has been borne out by optical measurements obtained by Cameron, particularly regarding the insensitivity of film thickness to load.

Capitance measurements, on the other hand, indicated similar speed variations as predicted by elastohydrodynamic theory; but showed considerably higher variations with load at the relatively higher loads and speeds that were studied. These load variations are borne out in part by the Battelle X-ray data where even stronger variations in load were indicated under these conditions. The full cause of these variations is still at this time not fully understood, although it is believed that the Battelle measurements have been at least qualitatively substantiated.

Asperitac measurements indicated partial elastohydrodynamic contact to start at speeds somewhat below 100 inches per second which corresponds to predicted film thicknesses below 20 microinches. More work is needed in this important area to fully correlate Asperitac data with asperity interaction analyses so that effective film thickness data in the partial elastohydrodynamic regime can be established and used to predict partial elastohydrodynamic performance characteristics. It is believed that this overall approach, if continued, would be quite fruitful.

Contrails

APPENDIX I
PHYSICAL PROPERTIES OF MIL-L-7808
LUBRICANT USED IN THIS INVESTIGATION

Index of Refraction - 1.395

Density - See Figure 71

Viscosity - See Figures 16, 72, and 73

Bulk Modulus - See Figure 74

Pressure-Viscosity Coefficient - See Formula in Text (Page 22)

Temperature-Viscosity Coefficient - See Formula in Text (Page 22)

Thermal Conductivity - .056 Btu/hr/ft/°F

Specific Heat - .5 Btu/lb-°F

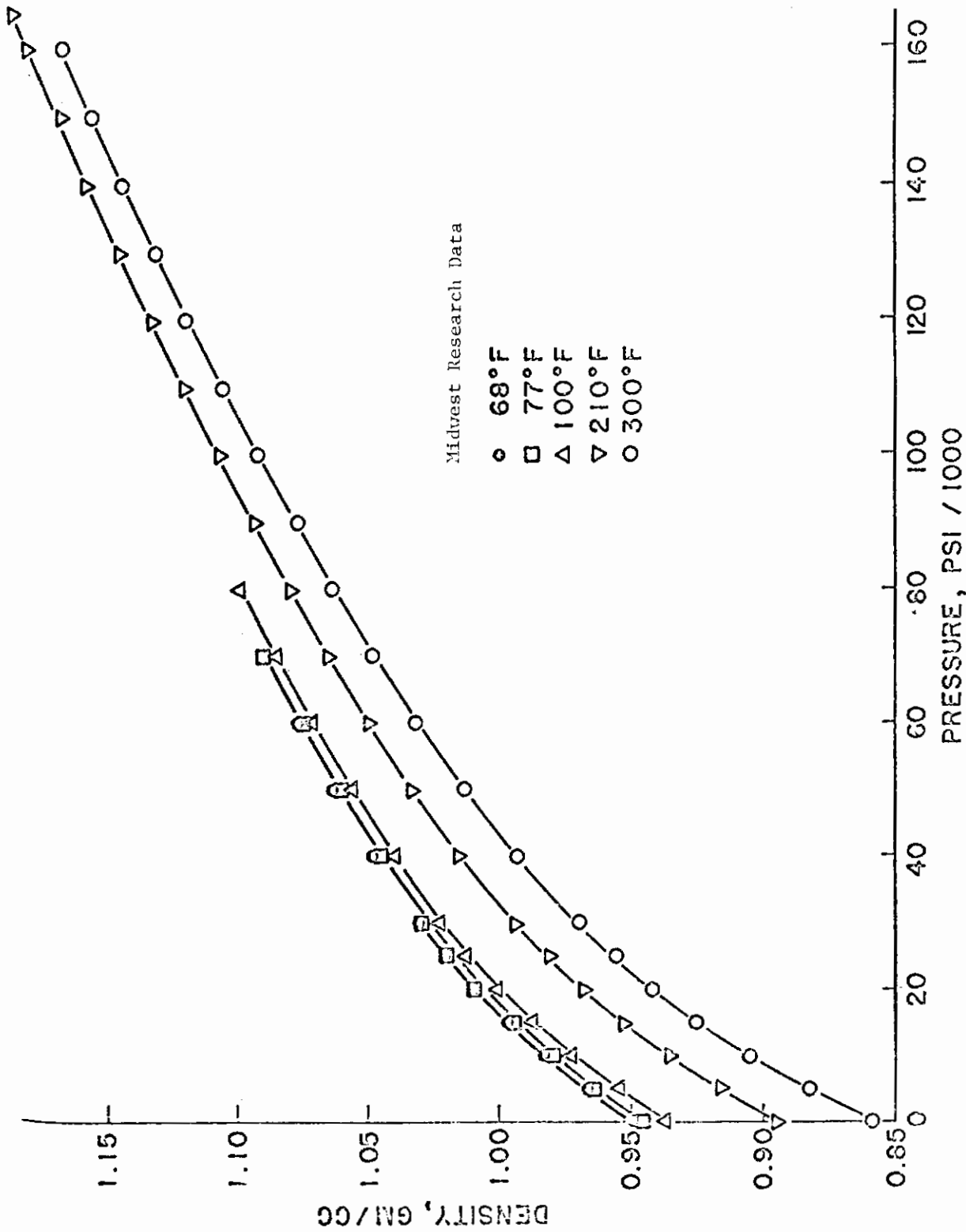


Fig. 71 Density as a Function of Temperature and Pressure for 0-67-29 (MIL-L-7808)

MTI-13384

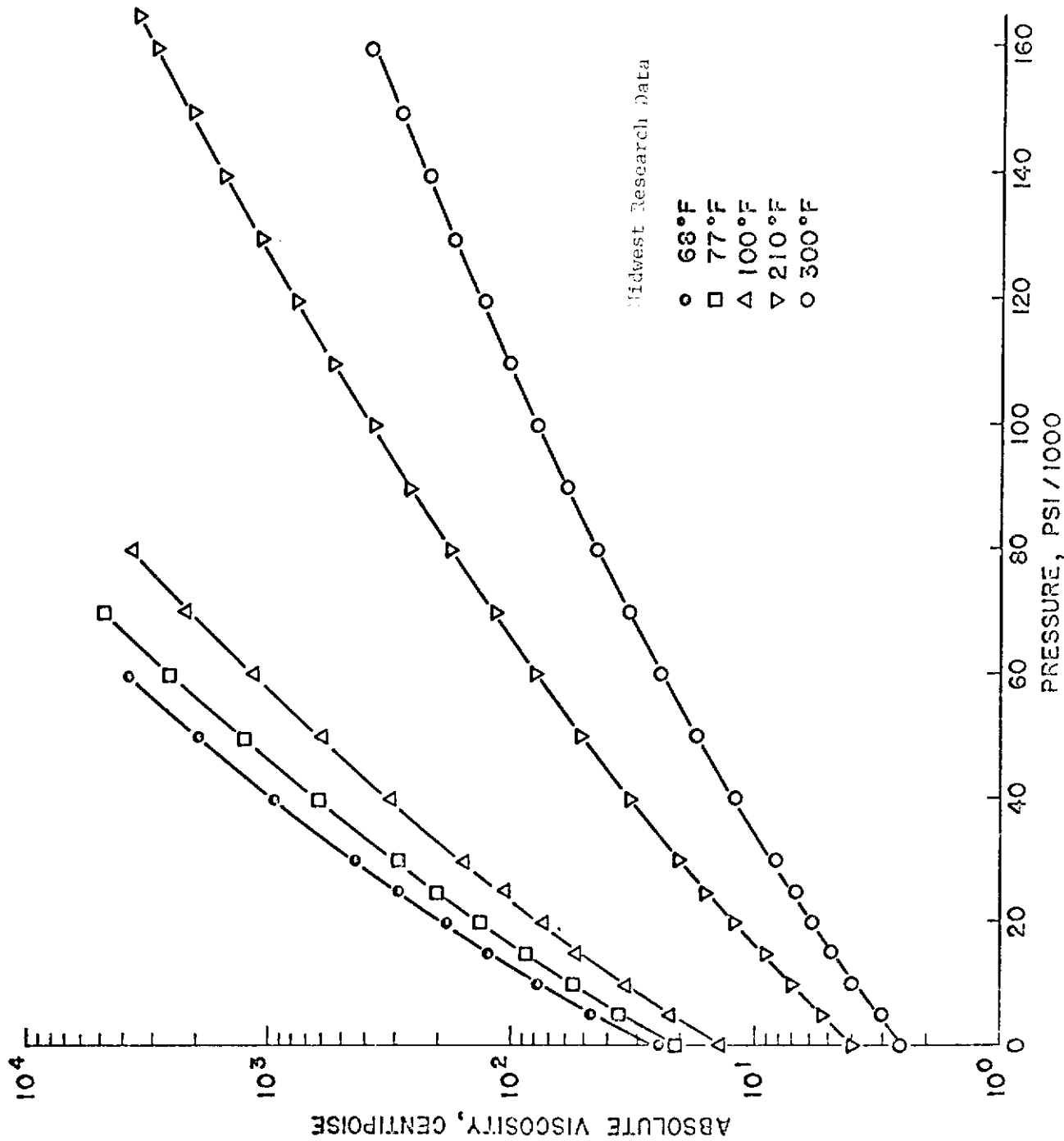


Fig. 72 Absolute Viscosity as a Function of Temperature and Pressure for 0-67-20 (MIL-L-7808)

F-11348K

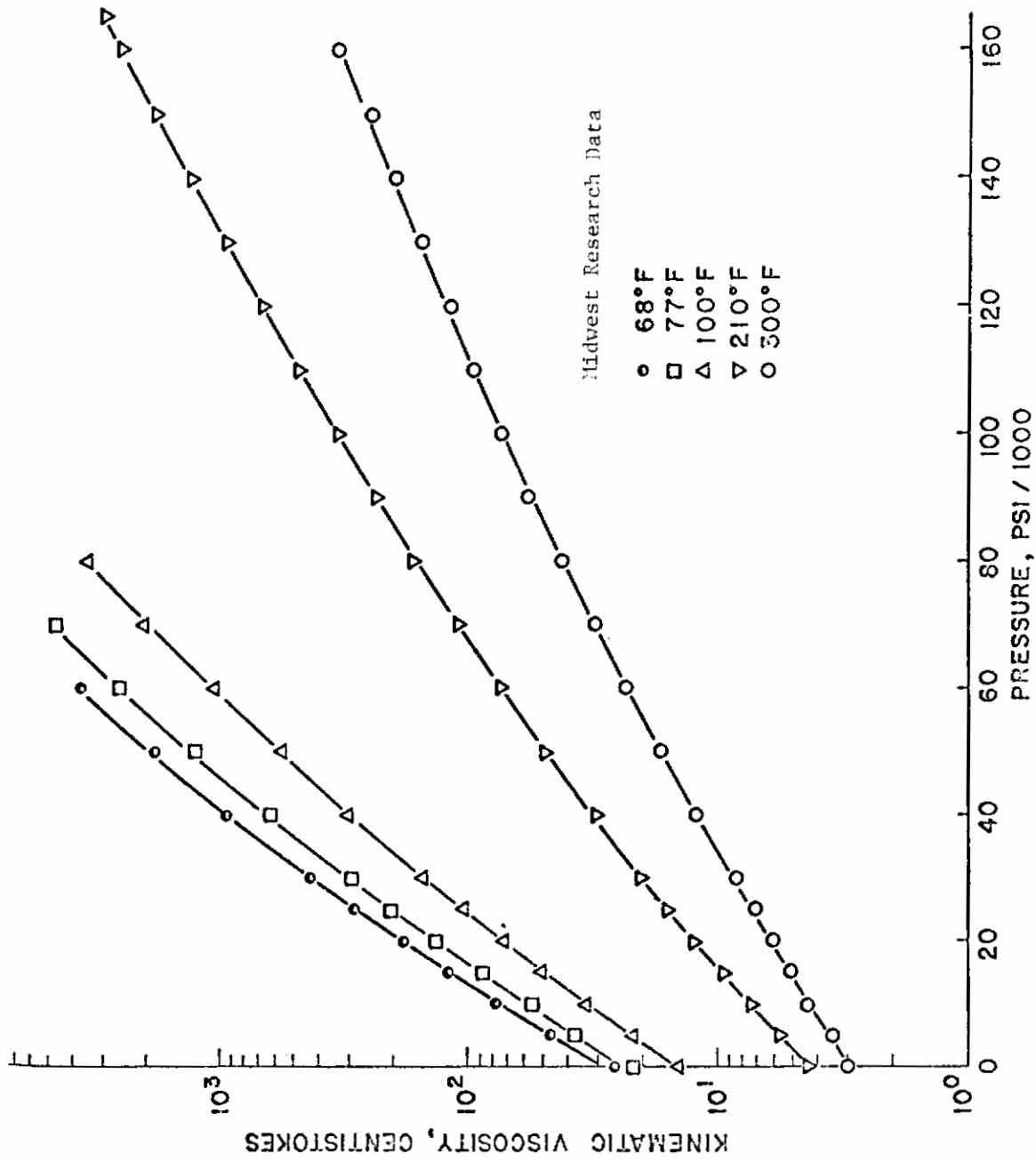


Fig. 73 Kinematic Viscosity as a Function of Temperature and Pressure for 0-67-20 (MIL-L-7808)

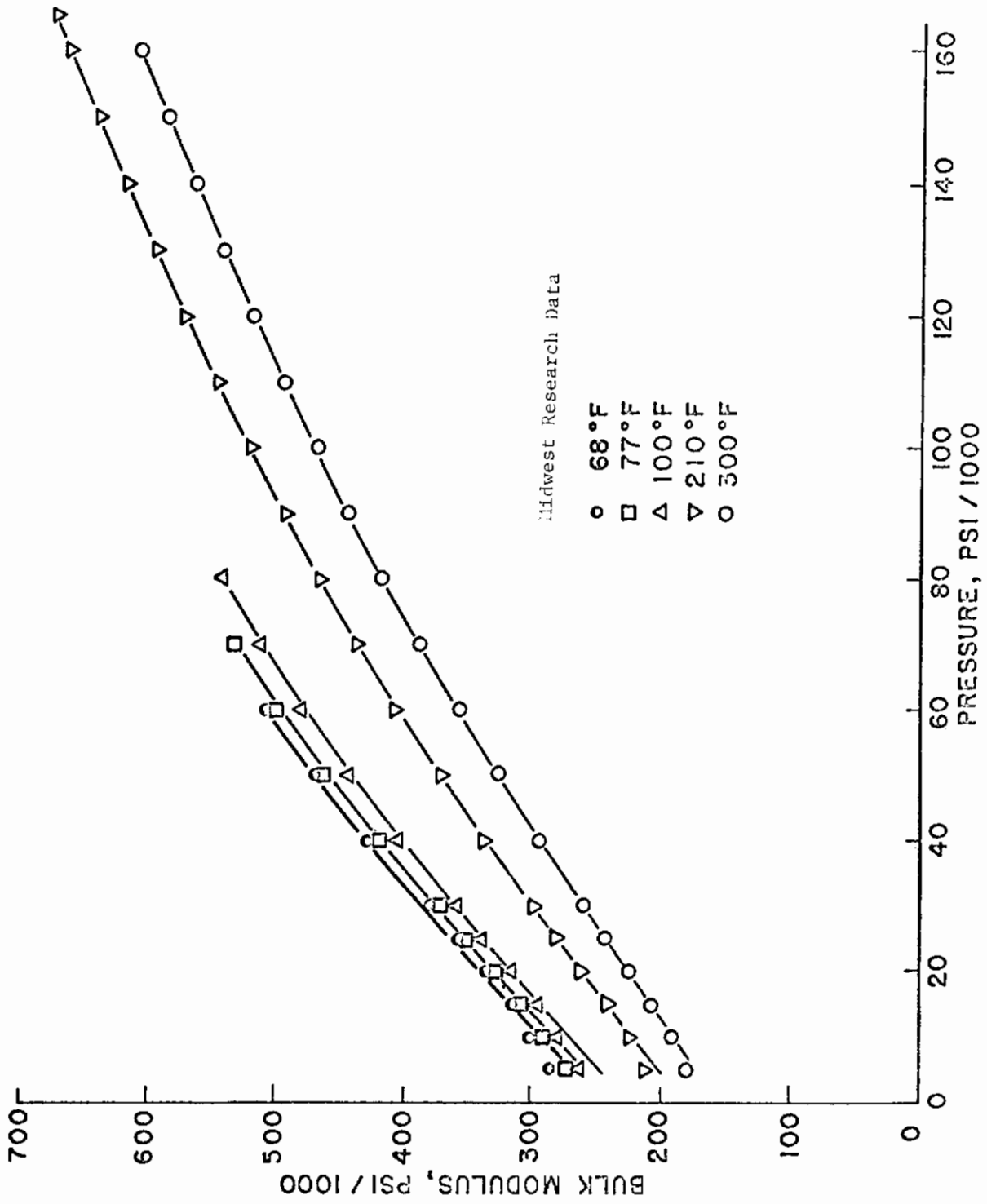


Fig. 74 Isothermal Secant Bulk Modulus as a Function of Temperature and Pressure for 0-67-20 (MIL-L-7808)

Contrails

APPENDIX II

TRACTION DATA SUMMARY FOR TURBINE ENGINE LUBRICANT
MIL-L-7808G AIR FORCE CODE 0-67-23 (SEE APPENDIX I FOR IDENTIFICATION)

Test Condition Summary

MTI Computer Data Bank Curve Number	Rolling Speed in/sec	Hertzian Contact Pressure, psi	Lubricant Test Temperature, °F
62	448.	100,000.	78.
63	448.	120,000.	78.
64	448.	130,000.	74.
65	448.	130,000.	78.
66	448.	100,000.	100.
67	448.	120,000.	100.
68	448.	130,000.	100.
69	448.	130,000.	100.
70	448.	100,000.	120.
71	448.	120,000.	120.
72	448.	130,000.	120.
73	448.	130,000.	120.
74	448.	140,000.	120.
75	448.	100,000.	140.
76	448.	120,000.	140.
77	448.	130,000.	140.
78	448.	130,000.	140.
79	448.	140,000.	140.
80	895.	100,000.	78.
81	895.	120,000.	78.
82	895.	130,000.	78.
83	895.	140,000.	78.
84	895.	100,000.	101.
85	895.	120,000.	101.
86	895.	130,000.	101.
87	895.	140,000.	101.
88	895.	100,000.	120.
89	895.	120,000.	120.
90	895.	130,000.	120.
91	895.	140,000.	120.
92	895.	100,000.	140.
93	895.	120,000.	140.
94	895.	130,000.	140.
95	895.	140,000.	140.
96	1351.	100,000.	75.

Contrails

Test Condition Summary (Continued)

MTI Computer Data Bank Curve Number	Rolling Speed in/sec	Hertzian Contact Pressure, psi	Lubricant Test Temperature, °F
97	1351.	120,000.	75.
98	1351.	130,000.	75.
99	1351.	140,000.	75.
100	1351.	100,000.	102.
101	1351.	120,000.	102.
102	1351.	130,000.	102.
103	1351.	140,000.	102.
104	1351.	100,000.	120.
105	1351.	120,000.	120.
106	1351.	130,000.	120.
107	1351.	140,000.	120.
108	1351.	100,000.	140.
109	1351.	120,000.	140.
110	1351.	130,000.	140.
111	1351.	140,000.	140.
112	1351.	100,000.	150.
113	1351.	120,000.	150.
114	1351.	130,000.	150.
115	1351.	140,000.	150.
116	1351.	100,000.	160.
117	1351.	120,000.	160.
118	1351.	130,000.	160.
119	1351.	140,000.	160.
120	1351.	150,000.	160.
121	1822.	100,000.	80.
122	1822.	120,000.	80.
123	1822.	130,000.	80.
124	1822.	140,000.	80.
125	1822.	150,000.	80.
126	1822.	100,000.	100.
127	1822.	120,000.	100.
128	1822.	130,000.	100.
129	1822.	140,000.	100.
130	1822.	150,000.	100.
131	1822.	100,000.	140.
132	1822.	120,000.	140.
133	1822.	130,000.	140.
134	1822.	140,000.	140.
135	1822.	150,000.	140.

NOTE: Test Disc Diameter: 3.00 in.
Surface Finish : ~ 2 microinch rms
Crown Radius : 36 inches
Material : AISI 52100 bearing steel
Curves 1-61 : Contain polyphenyl ether data (Ref. 1)

TRACTION DATA

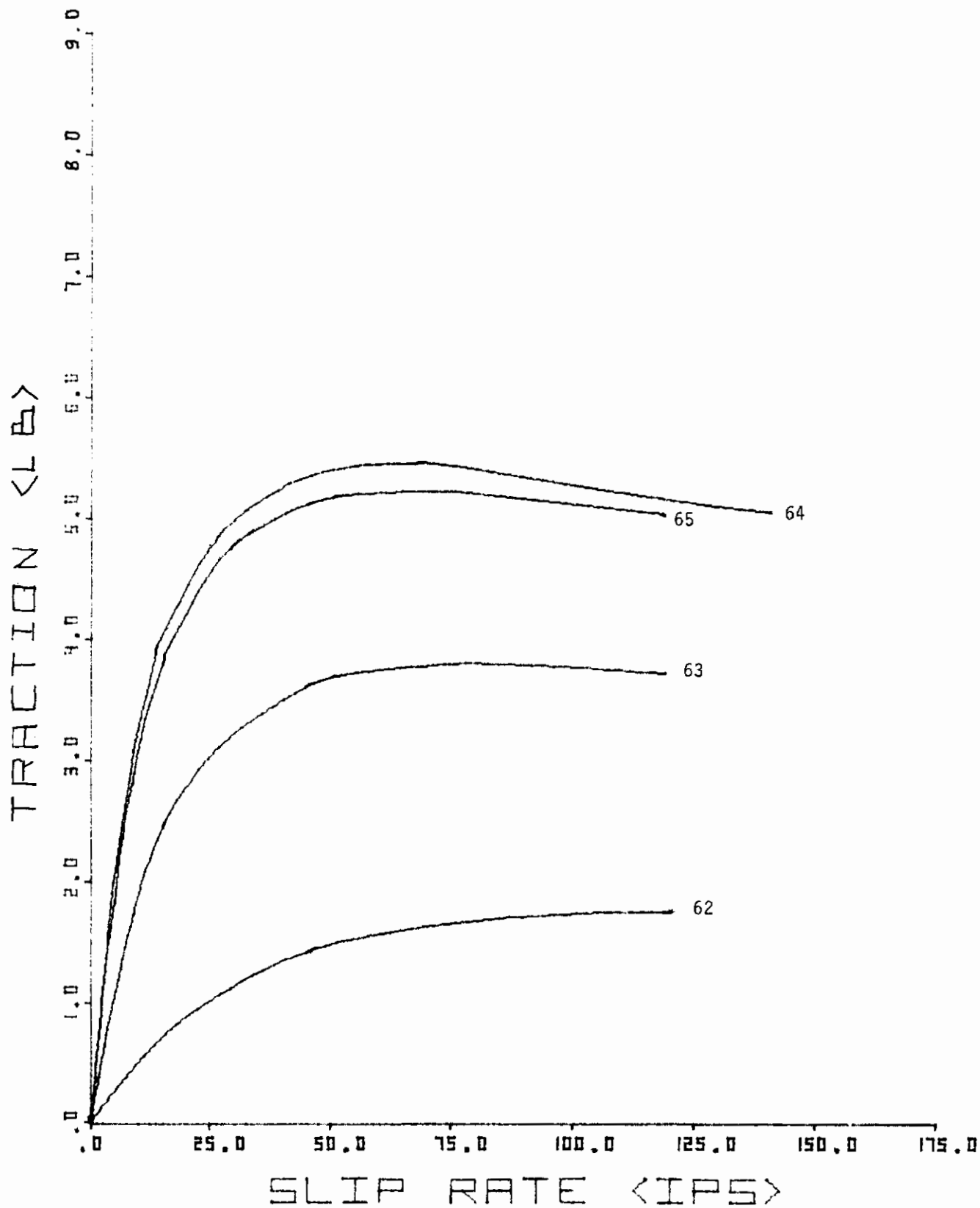


Fig. 75 Computer Plotted Experimental Traction Versus Slip Data

TRACTION DATA

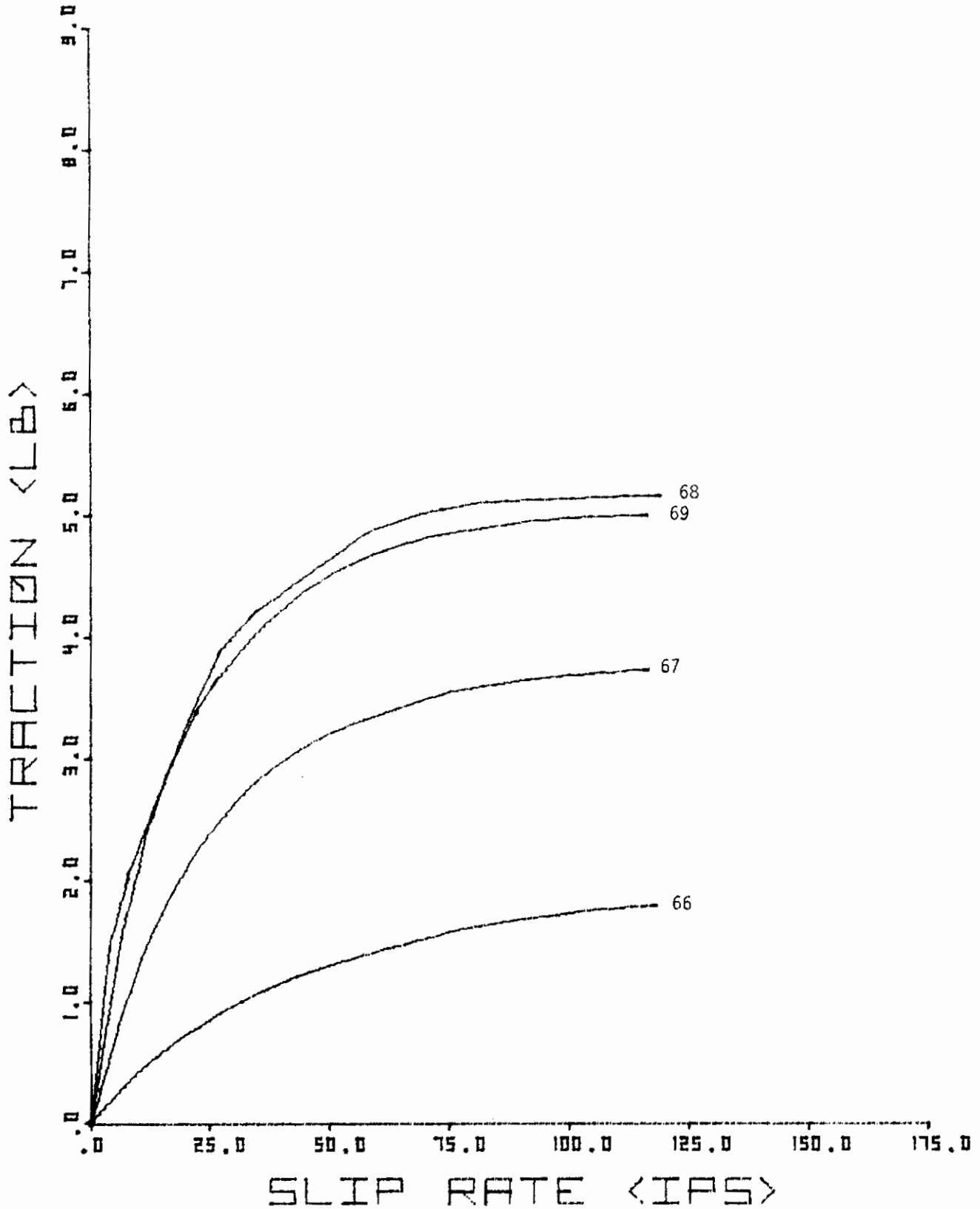


Fig. 76 Computer Plotted Experimental Traction Versus Slip Data

TRACTION DATA

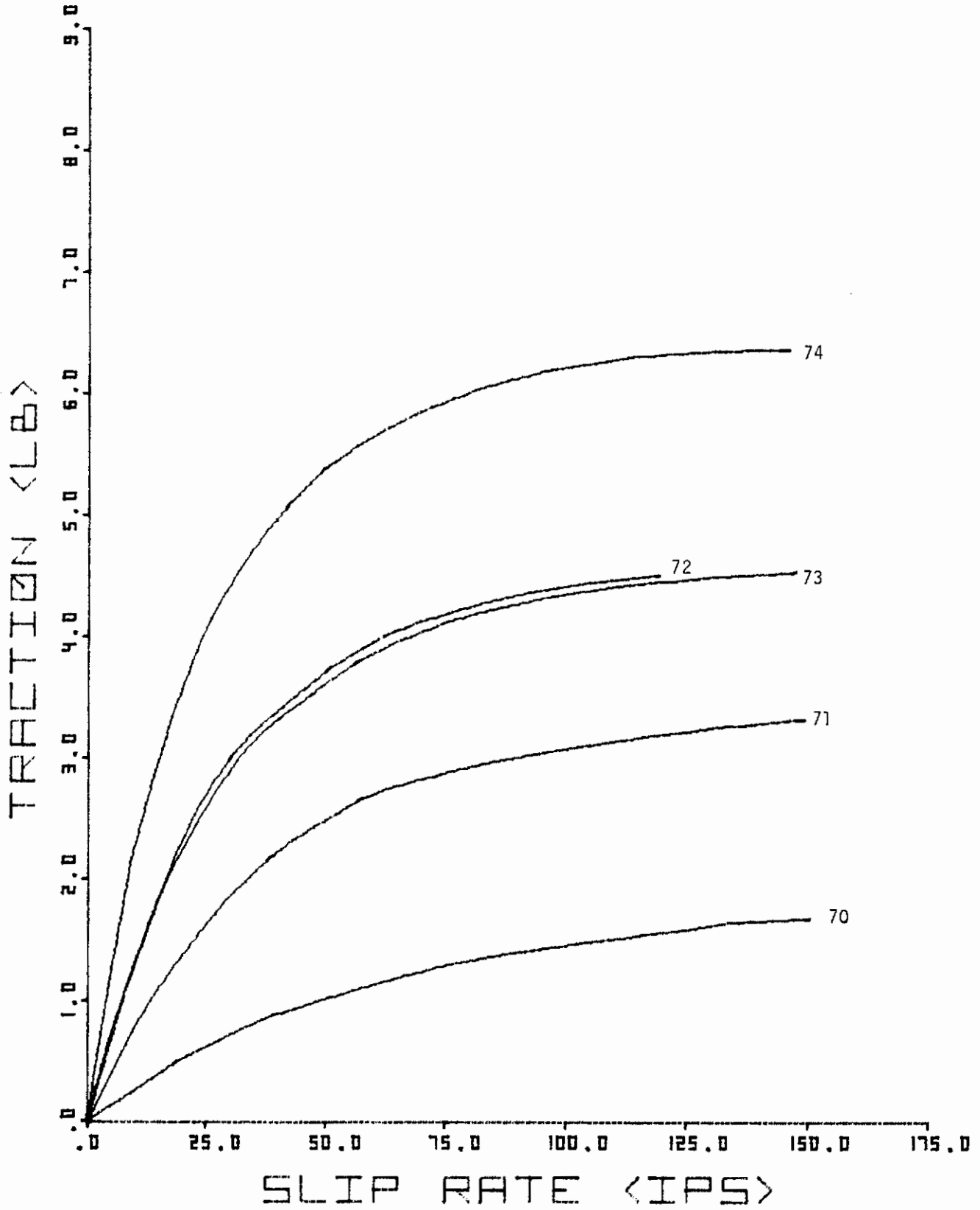


Fig. 77 Computer Plotted Experimental Traction Versus Slip Data

TRACTION DATA

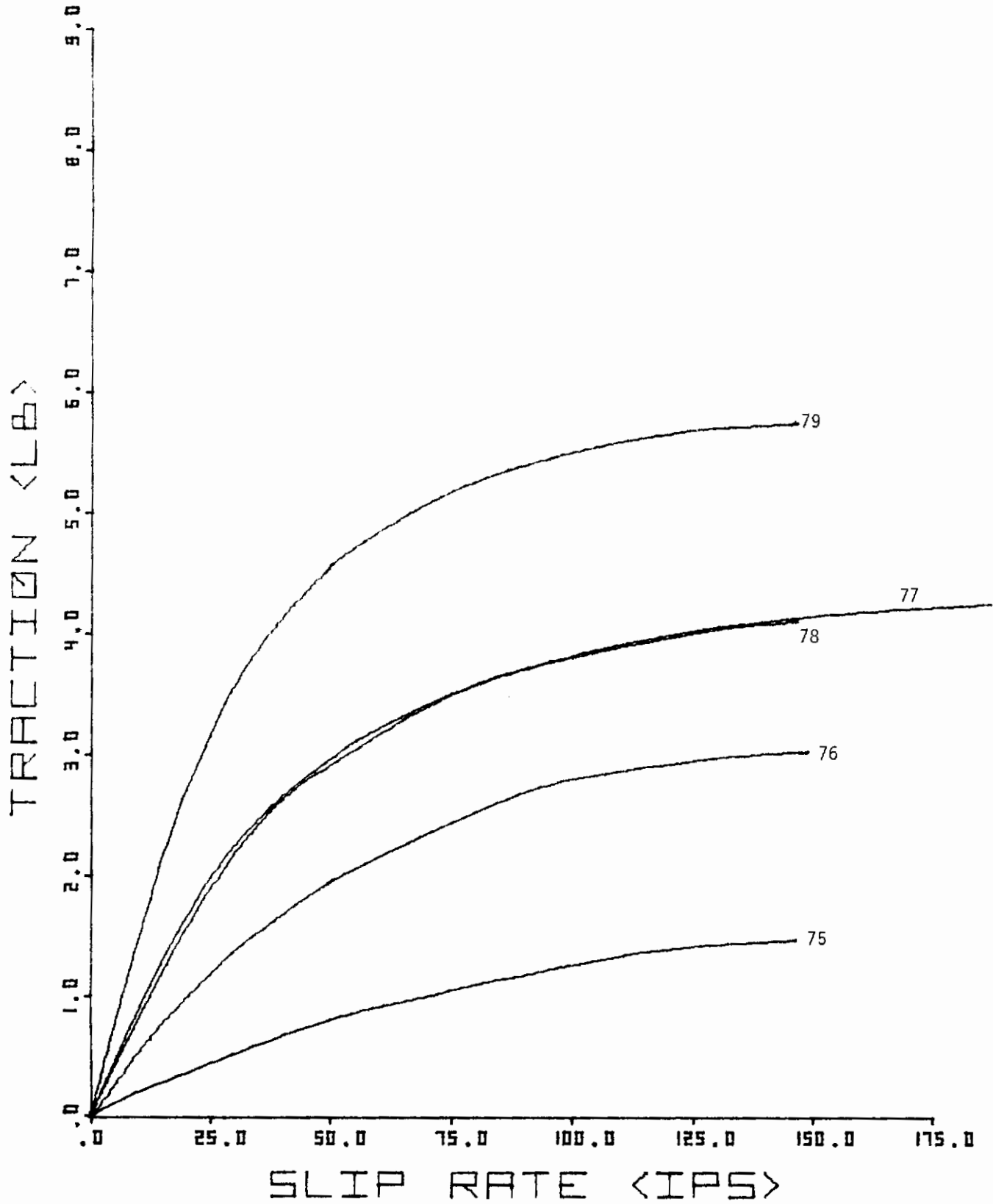


Fig. 78 Computer Plotted Experimental Traction Versus Slip Data

Contrails
TRACTION DATA

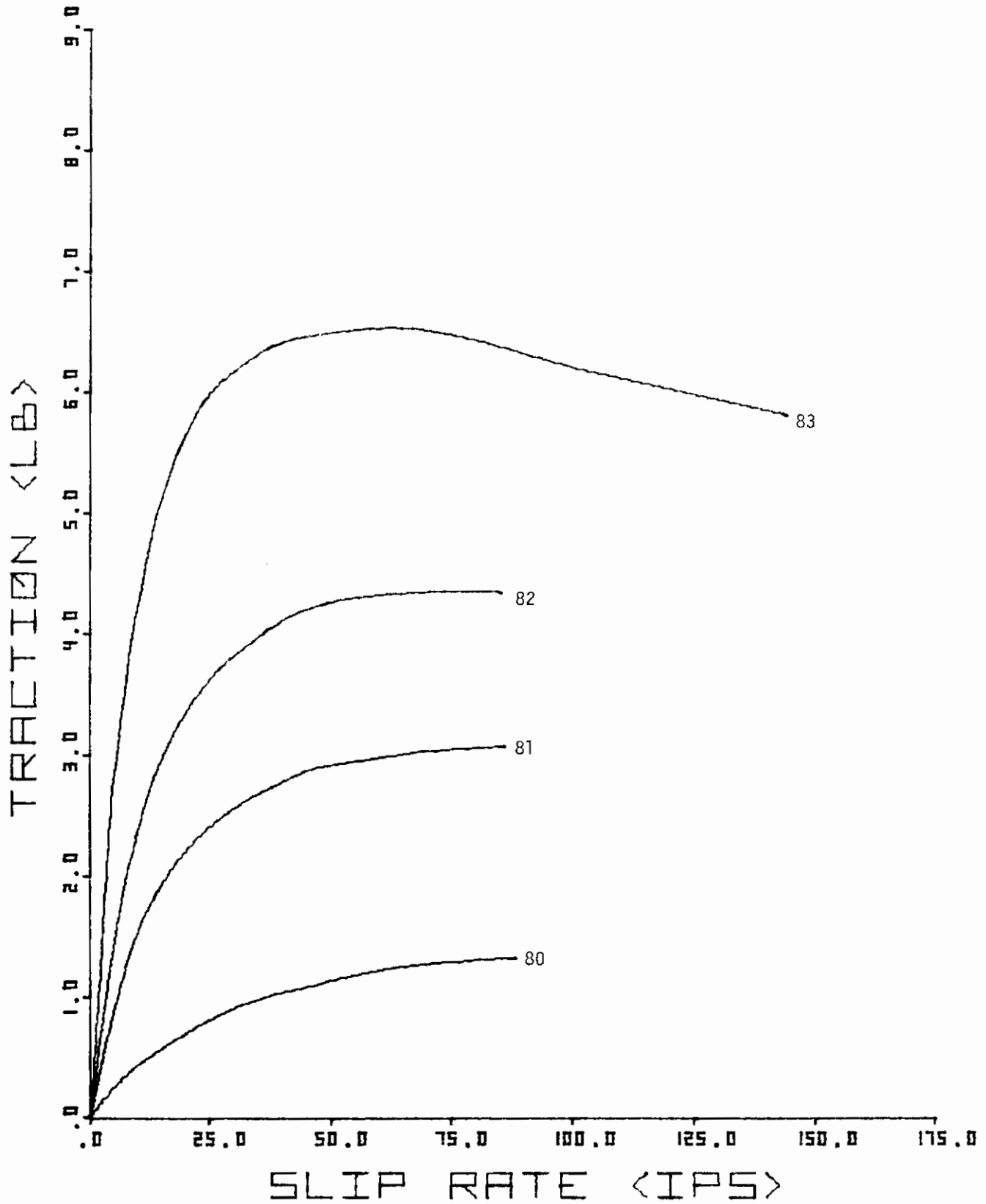


Fig. 79 Computer Plotted Experimental Traction Versus Slip Data

TRACTION DATA

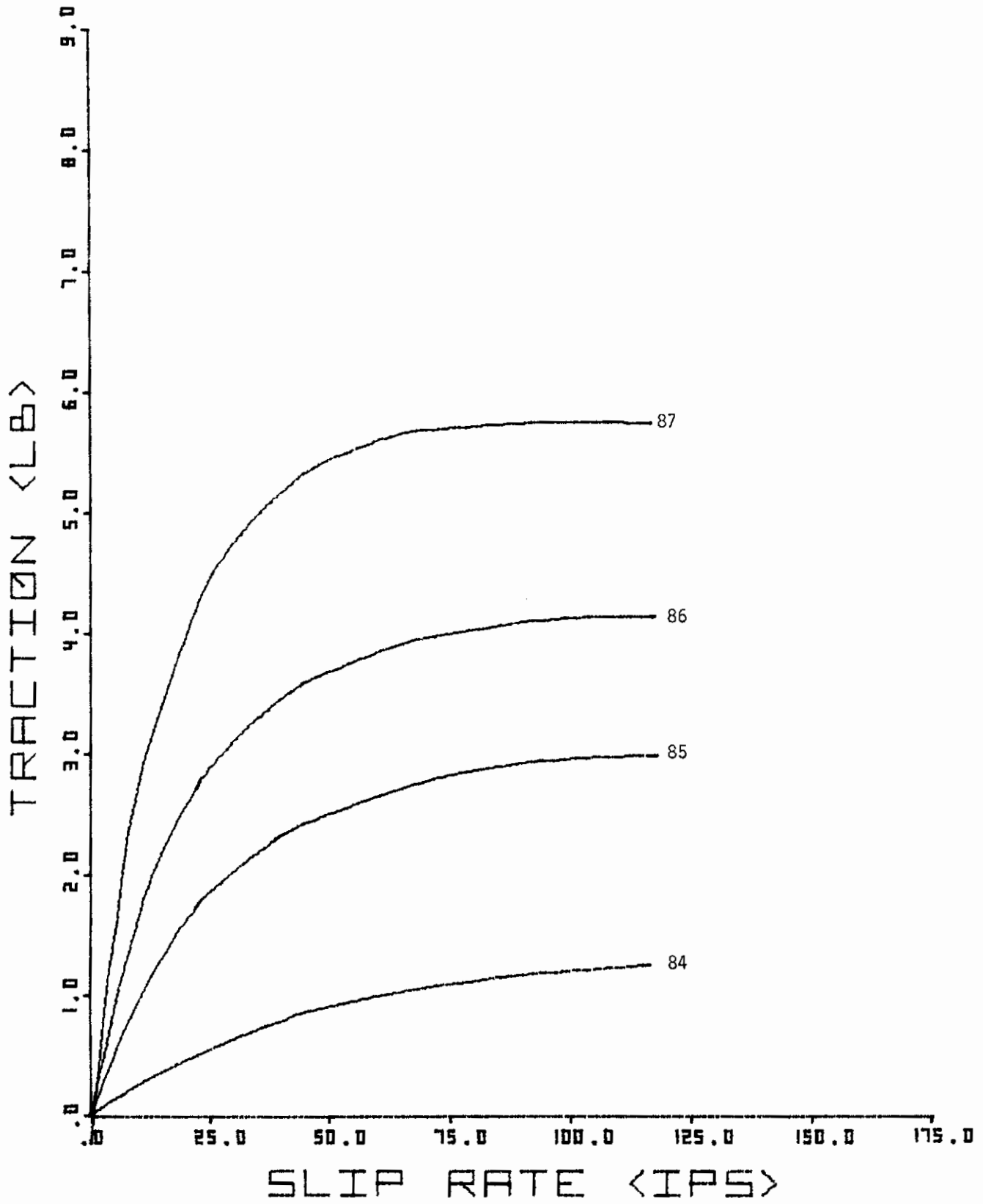


Fig. 80 Computer Plotted Experimental Traction Versus Slip Data

TRACTION DATA

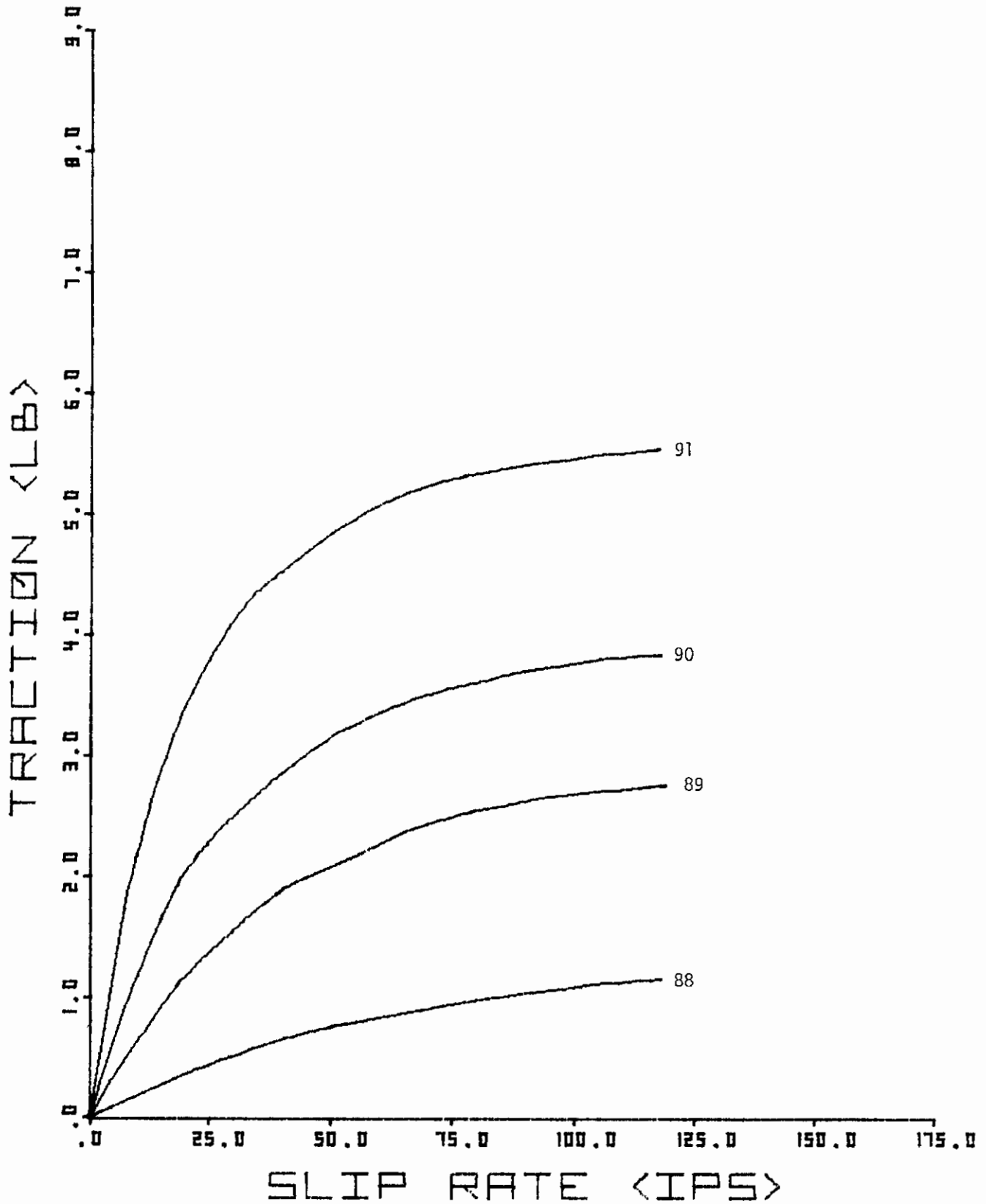


Fig. 81 Computer Plotted Experimental Traction Versus Slip Data

TRACTION DATA

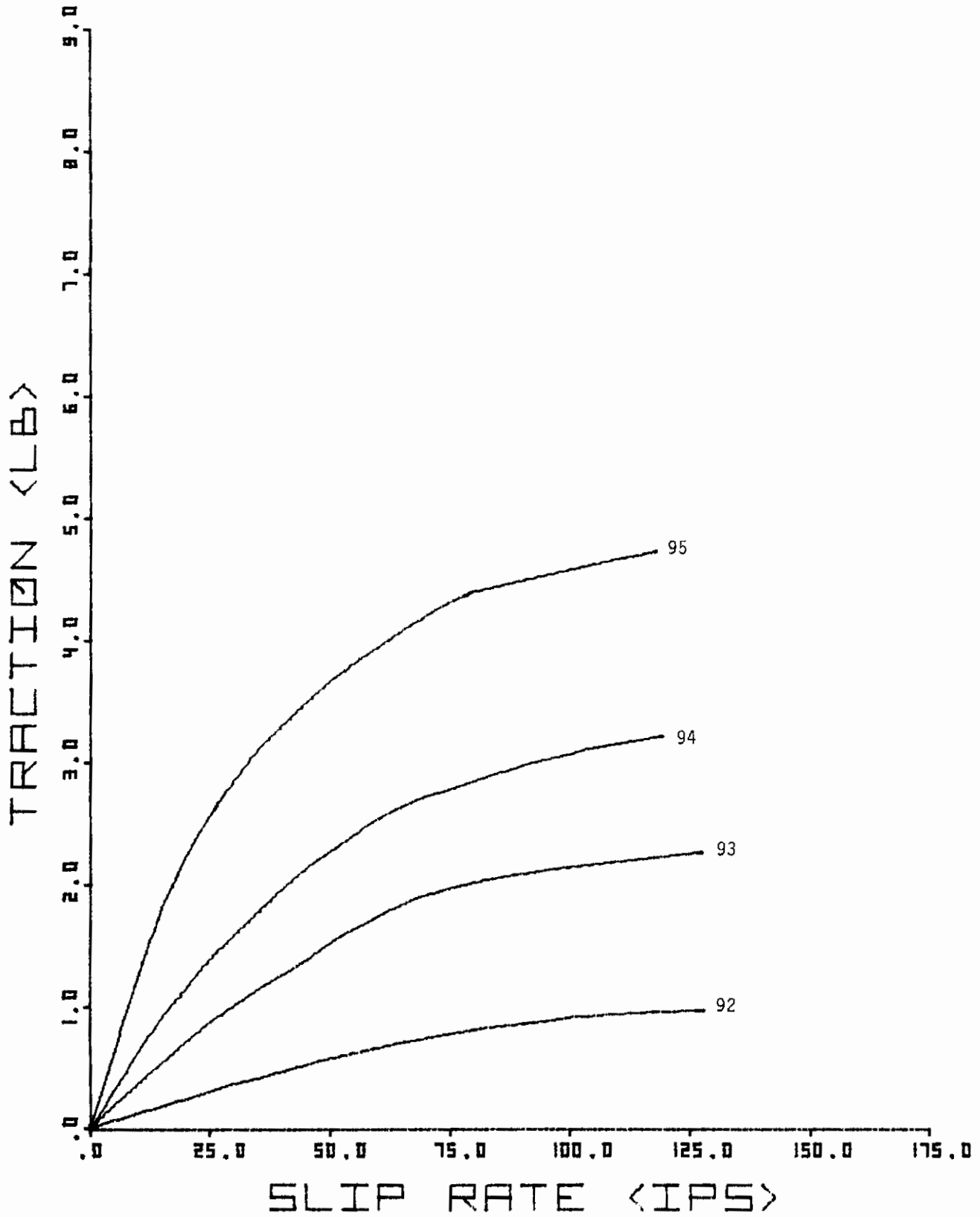


Fig. 82 Computer Plotted Experimental Traction Versus Slip Data

Contrails
TRACTION DATA

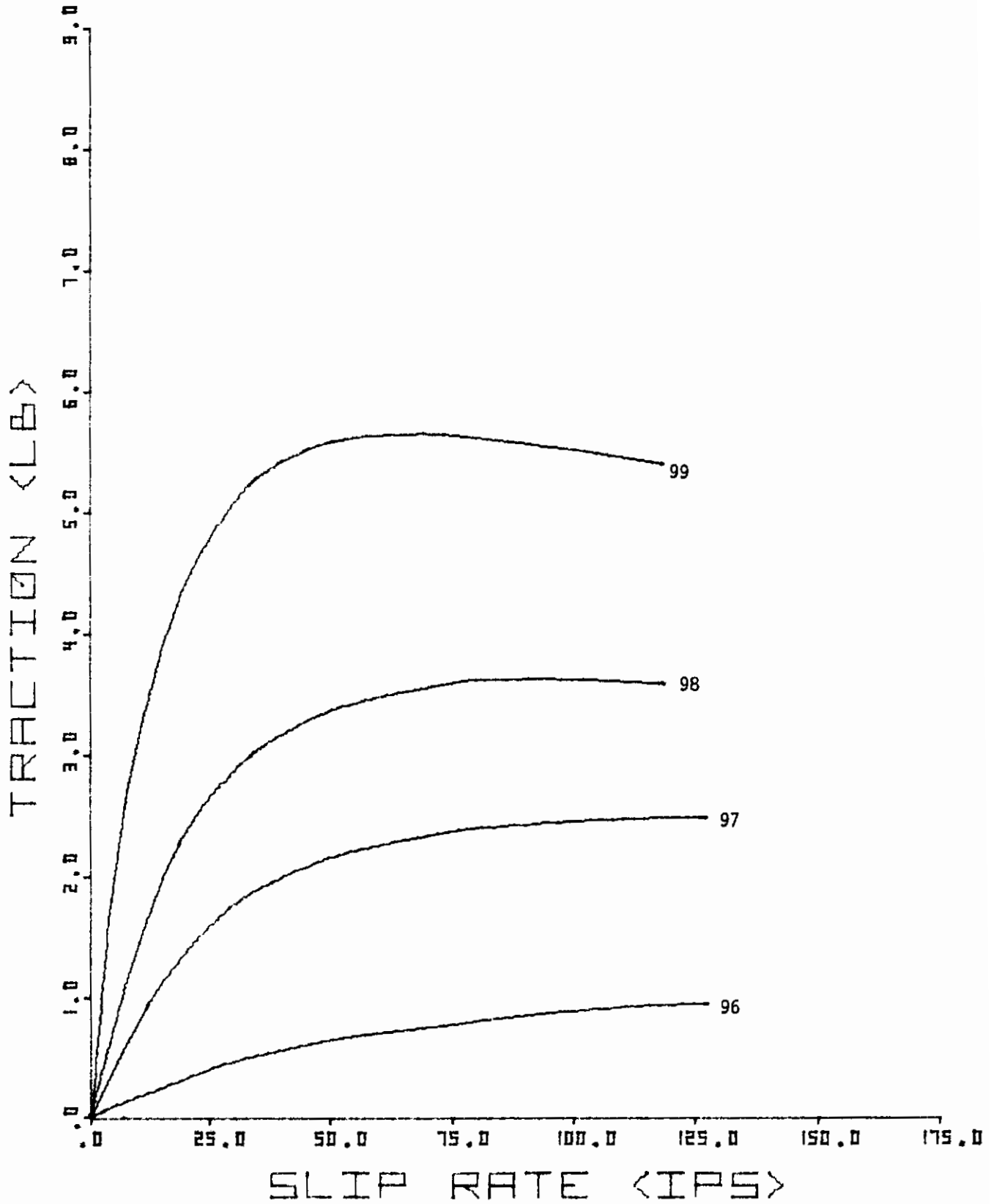


Fig. 83 Computer Plotted Experimental Traction Versus Slip Data

Contrails
TRACTION DATA

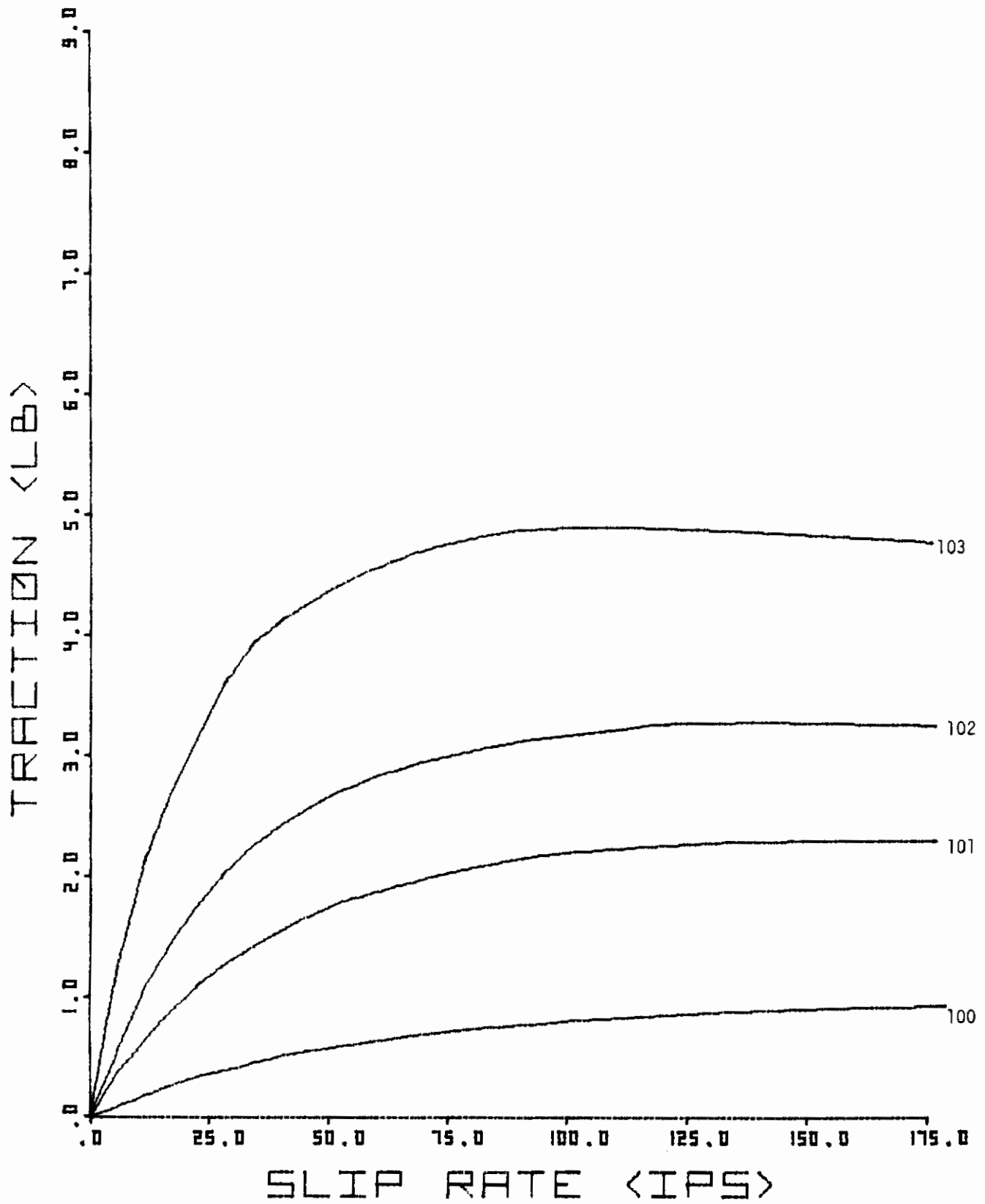


Fig. 84 Computer Plotted Experimental Traction Versus Slip Data

TRACTION DATA

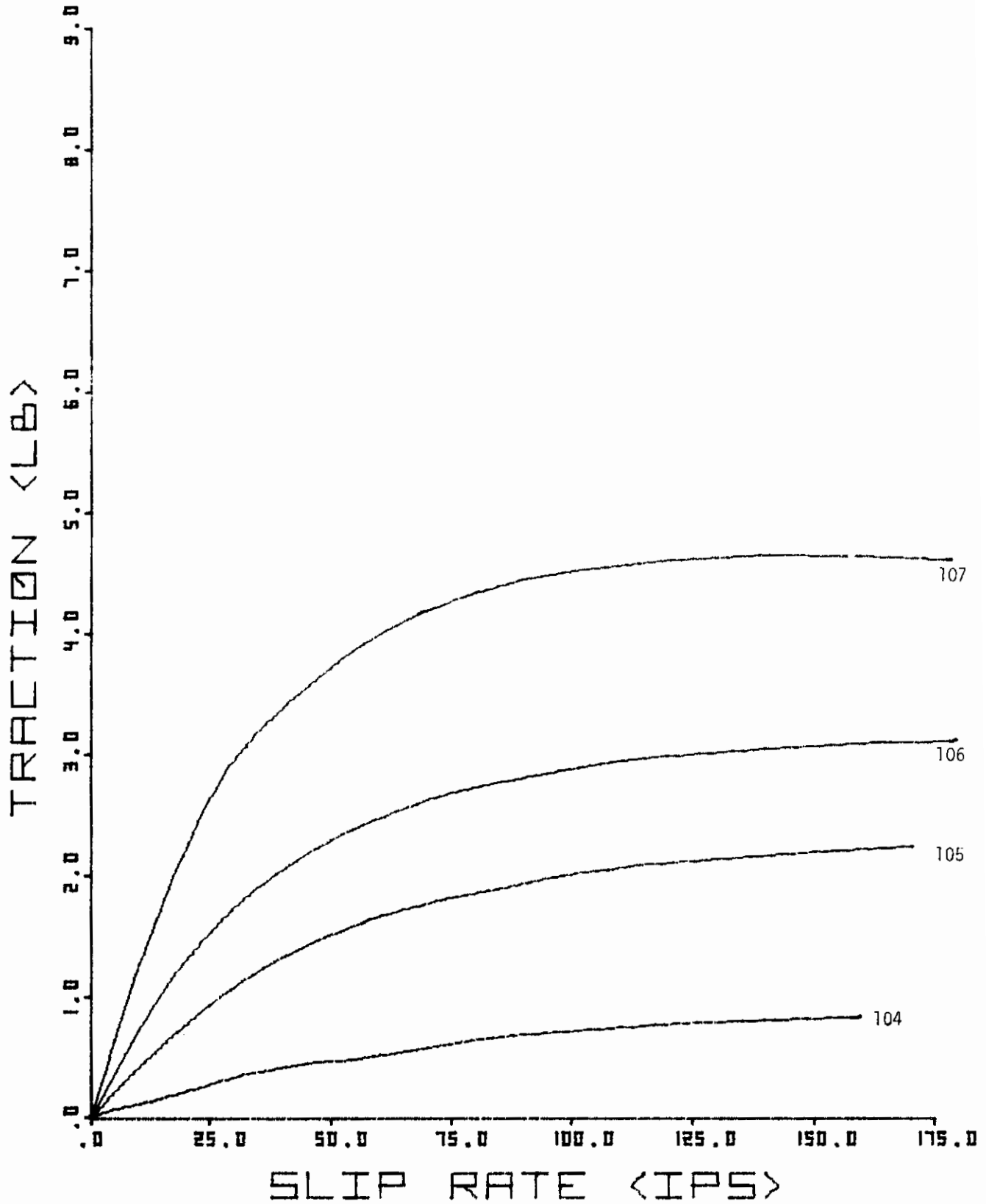


Fig. 85 Computer Plotted Experimental Traction Versus Slip Data

Contrails
TRACTION DATA

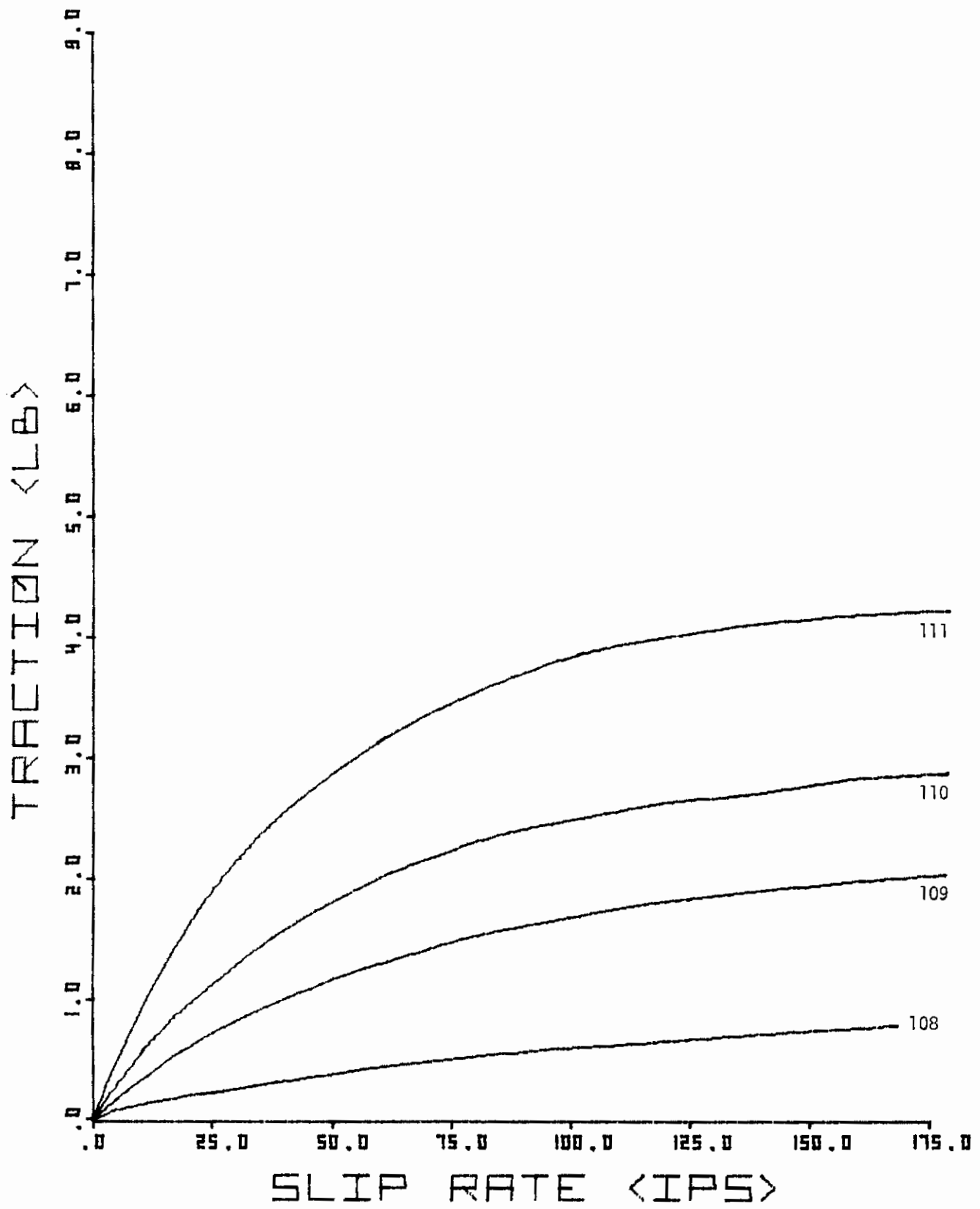


Fig. 86 Computer Plotted Experimental Traction Versus Slip Data

Contrails
TRACTION DATA

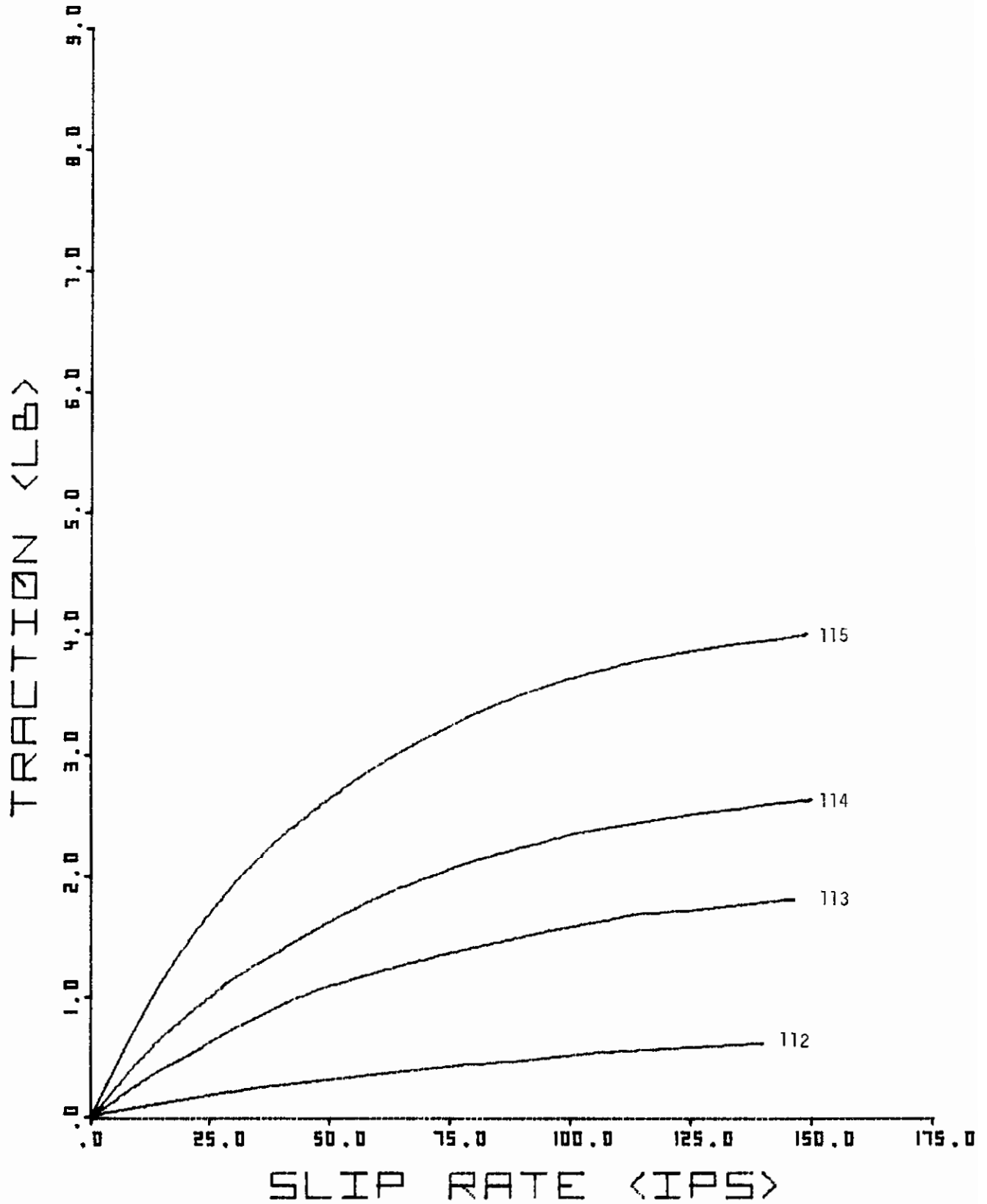


Fig. 87 Computer Plotted Experimental Traction Versus Slip Data

TRACTION DATA

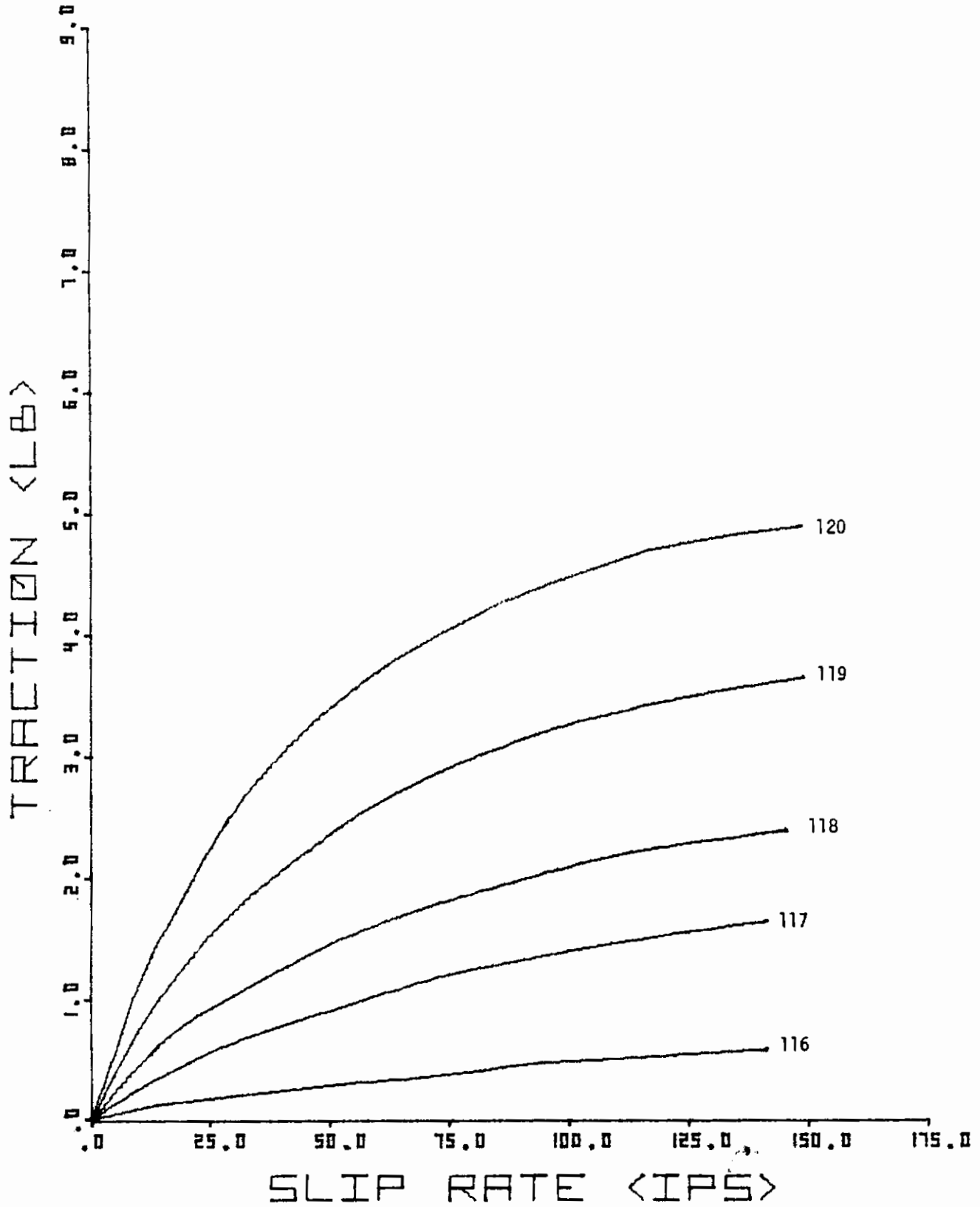


Fig. 88 Computer Plotted Experimental Traction Versus Slip Data

Contrails
TRACTION DATA

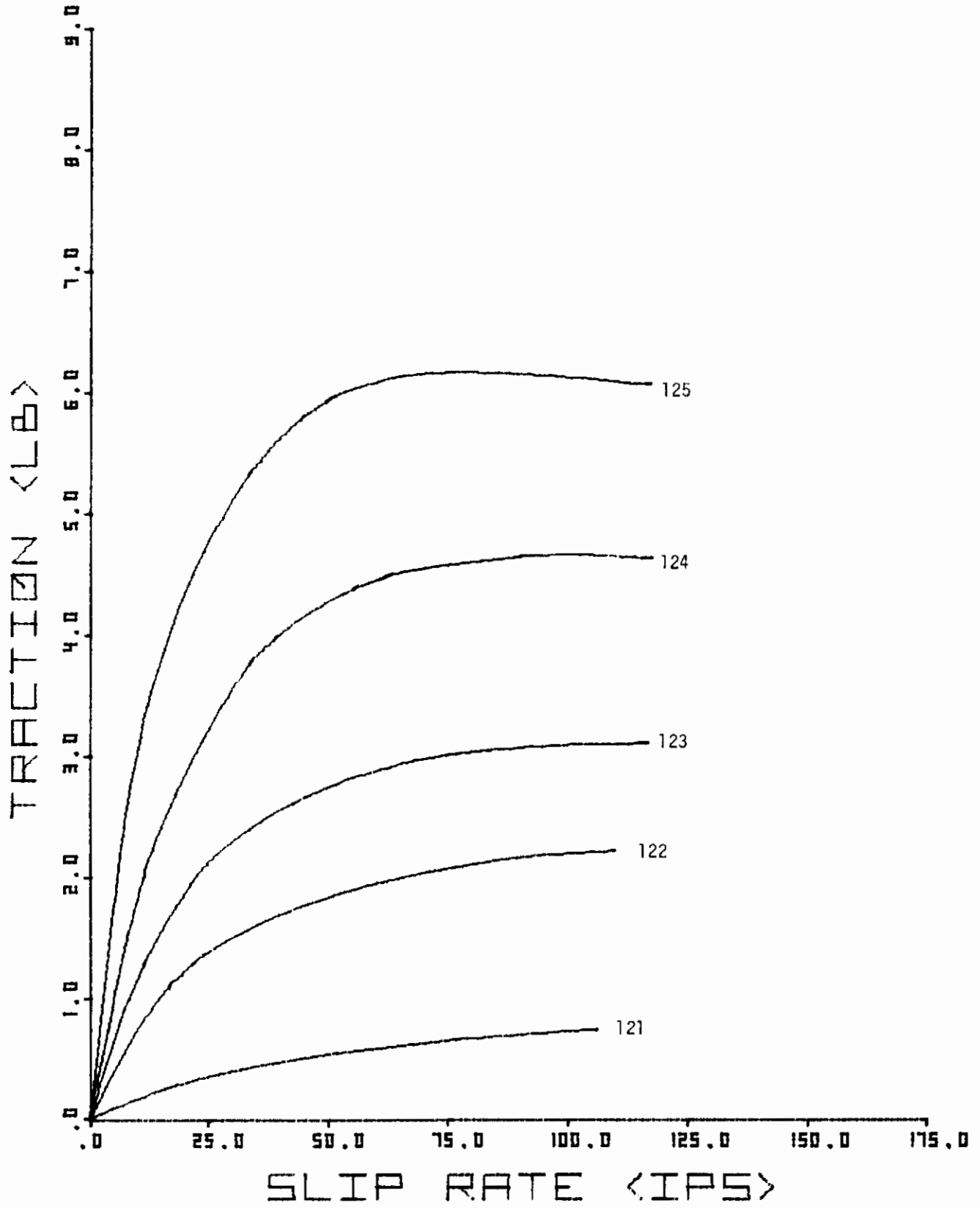


Fig. 89 Computer Plotted Experimental Traction Versus Slip Data

Contrails
TRACTION DATA

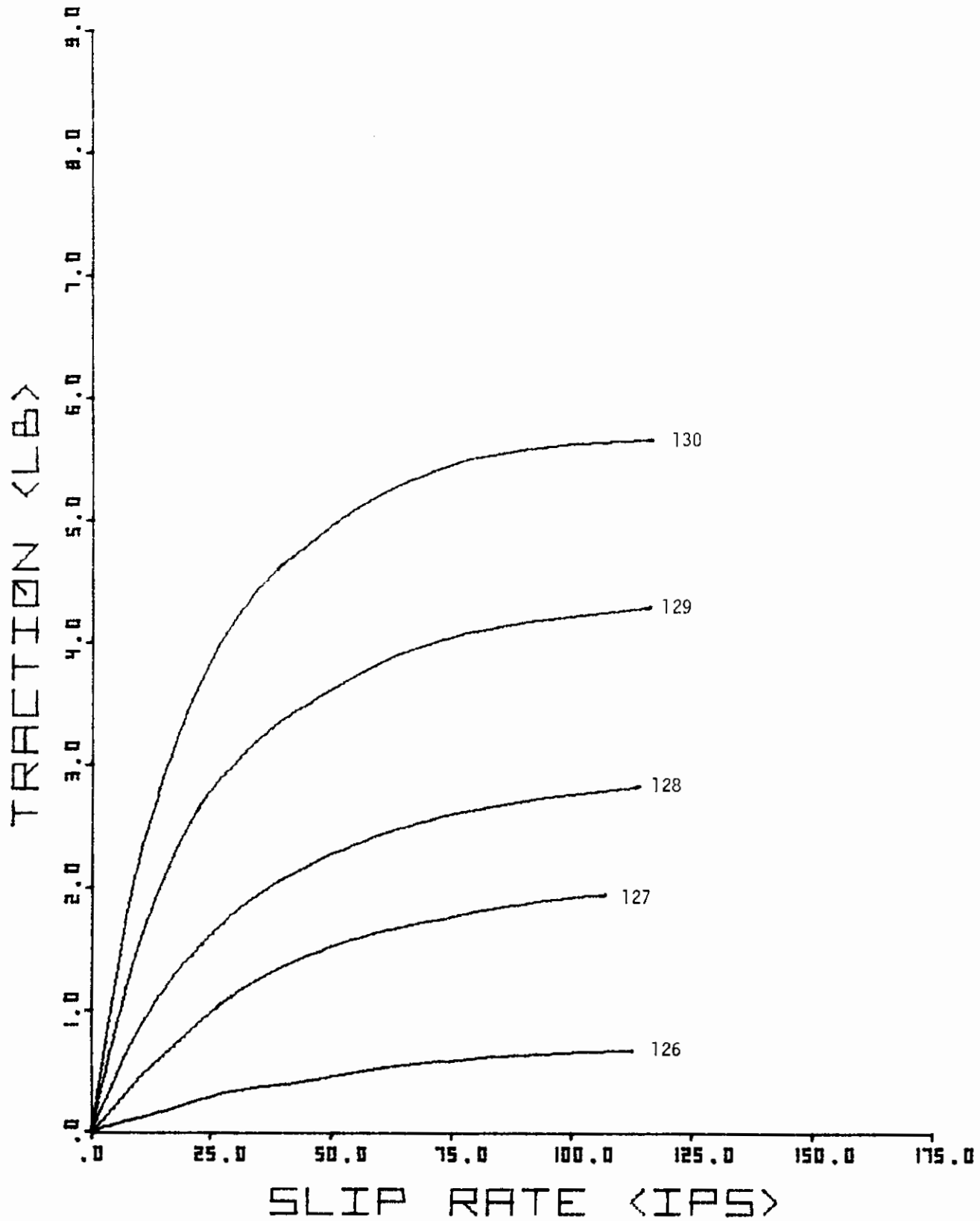


Fig. 90 Computer Plotted Experimental Traction Versus Slip Data

Contrails
TRACTION DATA

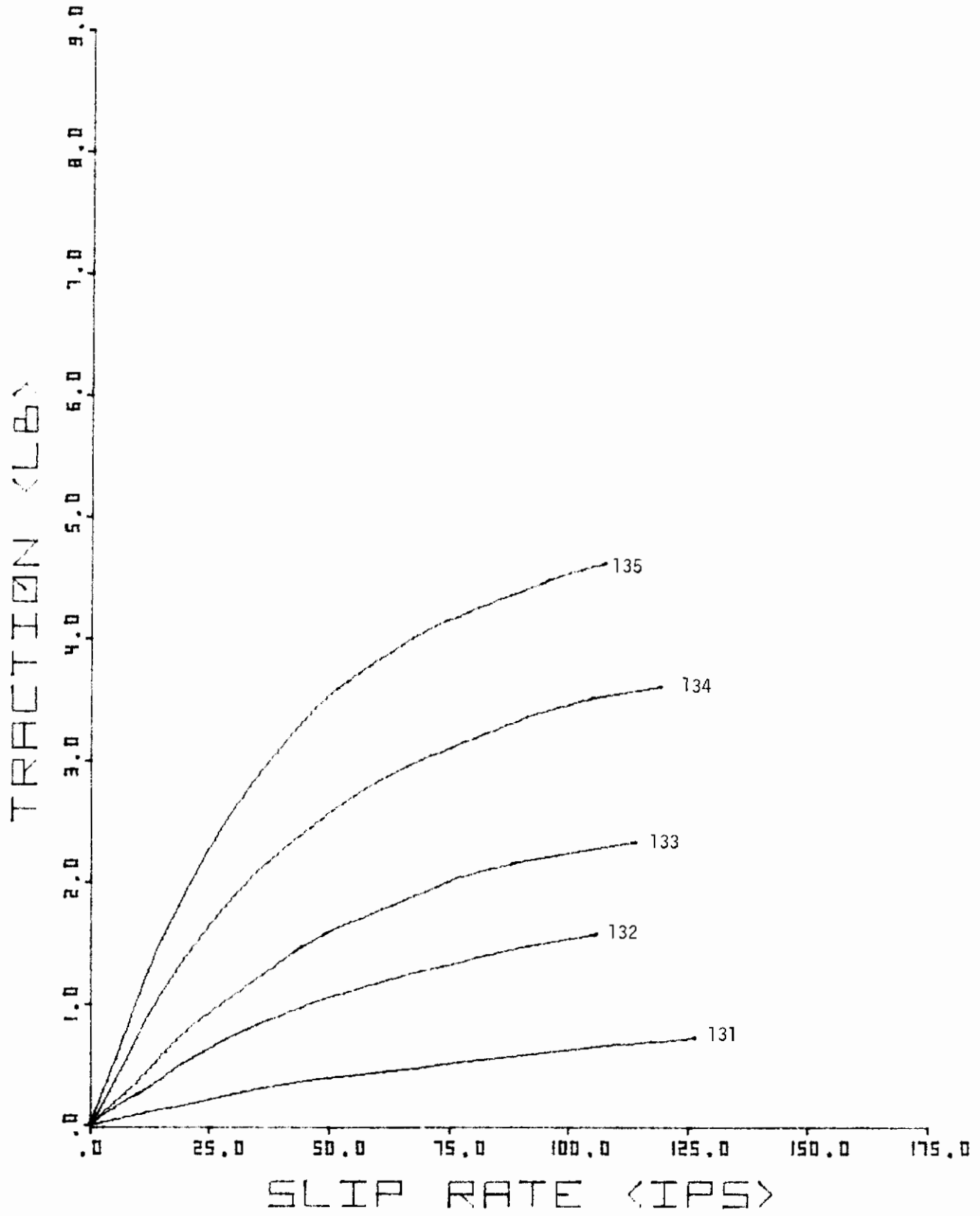


Fig. 91 Computer Plotted Experimental Traction Versus Slip Data

Contrails

APPENDIX III

ELASTIC DISTORTION ANALYSES USED FOR STATIC OPTICAL CALIBRATION AND CAPACITANCE CALIBRATIONS

The ability to determine the shape of the full exterior Hertz contact profile in elliptic contact is very useful in calibrating various electrical and optical film thickness in concentrated contact elements. The basic equation for determining the elastic distortion profiles were first put forth by Hertz. These equations were presented in convenient computational form in Reference (1) and were used to obtain comparisons between theoretical and measured optical interference fringe patterns for the particular disc geometry used in the investigation. This appendix will be devoted to the presentation of dimensionless curves and methods for extending these predictions to any elliptical contact geometry and to presenting the methods used in obtaining capacitance film thickness calibrations.

Formulas for Exterior Hertz Profile in Elliptic Contact

The formulas presented in Reference 1 are based upon those originally put forth by Hertz and are repeated here for completeness.

A plan and elevation view of an elliptical Hertz contact is shown in Figure III-1. The exterior Hertz profile h is expressed as a function of the coordinate x and y in terms of the elastic modulus and Poisson's ratio of contacting bodies 1 and 2 (denoted E_1 , E_2 , ν_1 , and ν_2 respectively), the applied load W and the contact ellipse dimensions a and b in terms of the dimensionless quantities $\bar{\phi}$, ξ , and η :

$$\bar{\phi} = \frac{2E'a}{3W} h, \quad \xi = \frac{x}{b}, \quad \eta = \frac{y}{a}, \quad \bar{\beta} = \frac{b}{a}$$

where

$$\frac{1}{E'} = \frac{(1 - \nu_1^2)}{\pi E_1} + \frac{(1 - \nu_2^2)}{\pi E_2}$$

The dimensionless separation $\bar{\phi}(\xi, \eta)$ is determined for Hertz contact theory which may be put in the form

$$\bar{\phi}(\xi, \eta) = J_2 \xi^2 + J_3 \eta^2 - J_1 \tag{A3.1}$$

where

$$J_1 = \int_0^{\bar{u}} \frac{d\zeta}{(1 + \zeta^2)^{1/2} (1 + \bar{\beta}^2 \zeta^2)^{1/2}} \tag{A3.2}$$

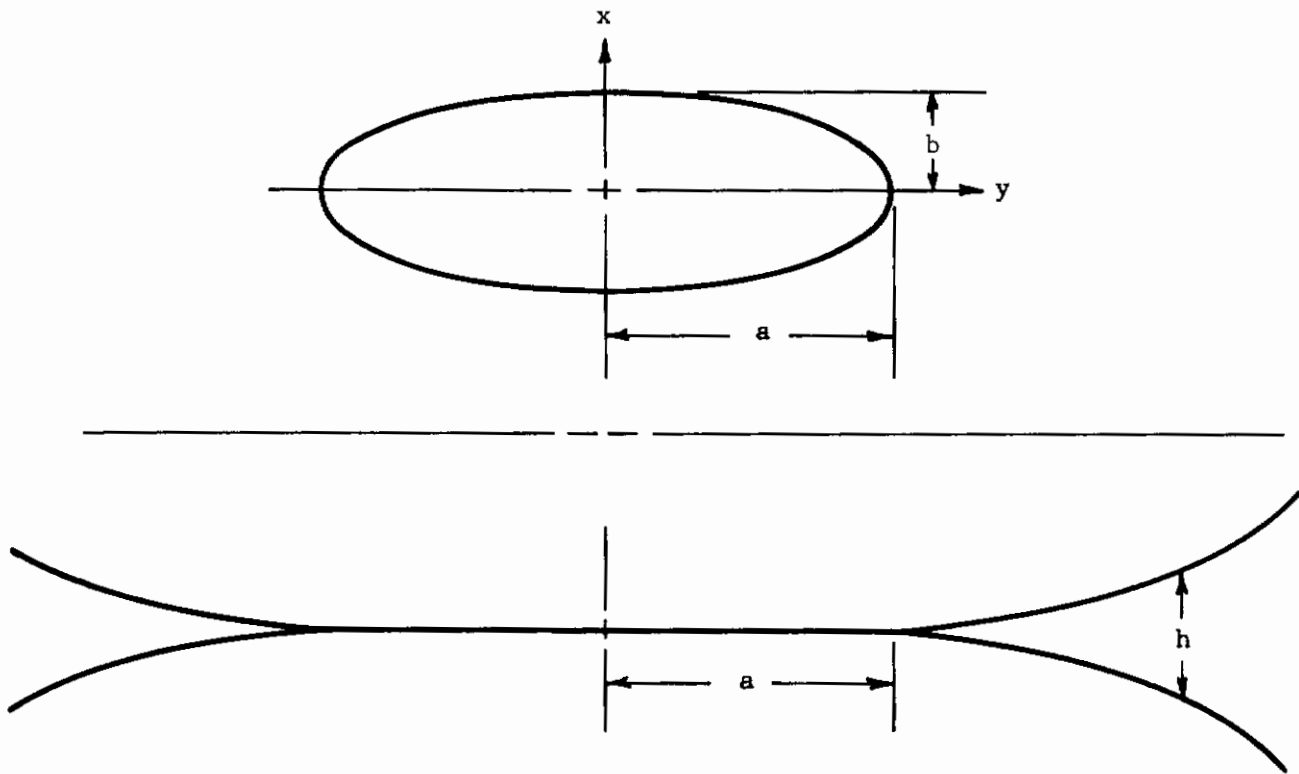


Fig. 92 Schematic of Hertz Profile

$$J_2 = \int_0^{\bar{u}} \frac{d\zeta}{(1 + \zeta^2)^{3/2} (1 + \bar{\beta}^2 \zeta^2)^{1/2}} \quad (A3.3)$$

$$J_3 = \int_0^{\bar{u}} \frac{d\zeta}{(1 + \zeta^2)^{1/2} (1 + \bar{\beta}^2 \zeta^2)^{3/2}} \quad (A3.4)$$

and \bar{u} is determined from the relationship

$$\frac{\xi^2}{1 + \bar{u}^2} + \frac{\eta^2}{1 + \bar{\beta}^2 \bar{u}^2} = 1 \quad (A3.5)$$

The integrals J_1 , J_2 , and J_3 may be expressed in terms of the elliptic integrals $F(\emptyset, k)$ and $E(\emptyset, k)$ as follows:

$$J_1 = F(\emptyset, k), \quad J_2 = \frac{1}{(1 - \bar{\beta}^2)} [E(\emptyset, k) - \bar{\beta}^2 F(\emptyset, k)]$$

and

$$J_3 = \frac{1}{(1 - \bar{\beta}^2)} [F(\emptyset, k) - E(\emptyset, k)] + \frac{\bar{u}}{(1 + \bar{\beta}^2 \bar{u}^2)^{1/2} (1 + \bar{u}^2)^{1/2}}$$

where

$$k = \sqrt{1 - \bar{\beta}^2} \quad \text{and} \quad \emptyset = \tan^{-1} \bar{u}$$

and $F(\emptyset, k)$ and $E(\emptyset, k)$ denote the incomplete elliptic integrals of the first and second kind defined as

$$F(\emptyset, k) = \int_0^{\emptyset} \frac{d\theta'}{\sqrt{1 - k^2 \sin^2 \theta'}}, \quad \text{and} \quad E(\emptyset, k) = \int_0^{\emptyset} \sqrt{1 - k^2 \sin^2 \theta'} \, d\theta'$$

The aspect ratio of the contact ellipse β is related to the relative curvature parameter R/R' in accordance with the equation

$$\beta^2 \frac{[K(k) - E(k)]}{E(k) - \beta^2 K(k)} = \frac{R}{R'} \quad (A3.6)$$

where the effective radii of curvature in the rolling direction (R) and the crown direction (R') are defined as:

Contacts

$$\frac{1}{R} = \frac{1}{R_1} + \frac{1}{R_2}, \quad \frac{1}{R'} = \frac{1}{R'_1} + \frac{1}{R'_2}$$

The dimensional Hertz contact parameters are calculated from the relationship

$$b = \left(\frac{3}{2} \frac{\pi W}{E'} \frac{RR'}{R + R'} \right)^{1/3} \bar{n} \quad (\text{A3.7})$$

$$a = b/\bar{\beta} \quad (\text{A3.8})$$

and

$$P_{\text{HZ}} = \frac{3}{2} \frac{W}{\pi ab} \quad (\text{A3.9})$$

The relationships between $\bar{\beta}$, \bar{n} , and R/R' appear frequently in the literature but are repeated here in Figure III-2 for completeness.

The dimensionless exterior profile for elliptic contact as obtained from Equations (A3.1) through (A3.5) does not appear in the literature and results of computation for computing exterior Hertz separation profiles are given here in the form of values of $\bar{\phi}$ on the x and y axes respectively in Figures III-3 and III-4.

The family of curves in Figure III-3 is of the form ξ_0 versus $\bar{\phi}(\xi_0, 0)$ for various values of R/R' , where ξ_0 denotes values of ξ when $\eta = 0$.

Similarly, Figure III-4 shows values of η_0 versus $\bar{\phi}(0, \eta_0)$ where η_0 corresponds to values of η when $\xi = 0$. For a given dimensionless separation, $\bar{\phi}$, one may calculate the values of ξ_0 and η_0 corresponding to the extreme points of the closed curve representing the locus points of constant separation $\bar{\phi}$ (we will refer to these curves subsequently as fringe lines).

Complete fringe lines for values of $\eta_0 = 1, 2, 3, 4,$ and 5 and $R/R' = 1/24$ (corresponding to 3 inch diameter discs with 36 inch crown radii) are shown in Figure III-5. These are plots of η versus ξ at constant $\bar{\phi}$. The curves are very nearly elliptical in nature and in the extreme cases $\eta_0 = 1$ and $h_0 \rightarrow \infty$, the curves approach those of true ellipses. These represent the Hertz contact ellipse and rigid body separation fringe lines respectively. Good approximations to the fringe lines can be obtained with the ellipses having major and minor semi-axes of η_0 and ξ_0 . Hence, lines of constant separation $\bar{\phi}$ may be approximated by

$$\left(\frac{\xi}{\xi_0} \right)^2 + \left(\frac{\eta}{\eta_0} \right)^2 = 1 \quad (\text{A3.10})$$

where η_0 and ξ_0 may be obtained as functions of $\bar{\phi}$ from Figures III-3 and III-4.

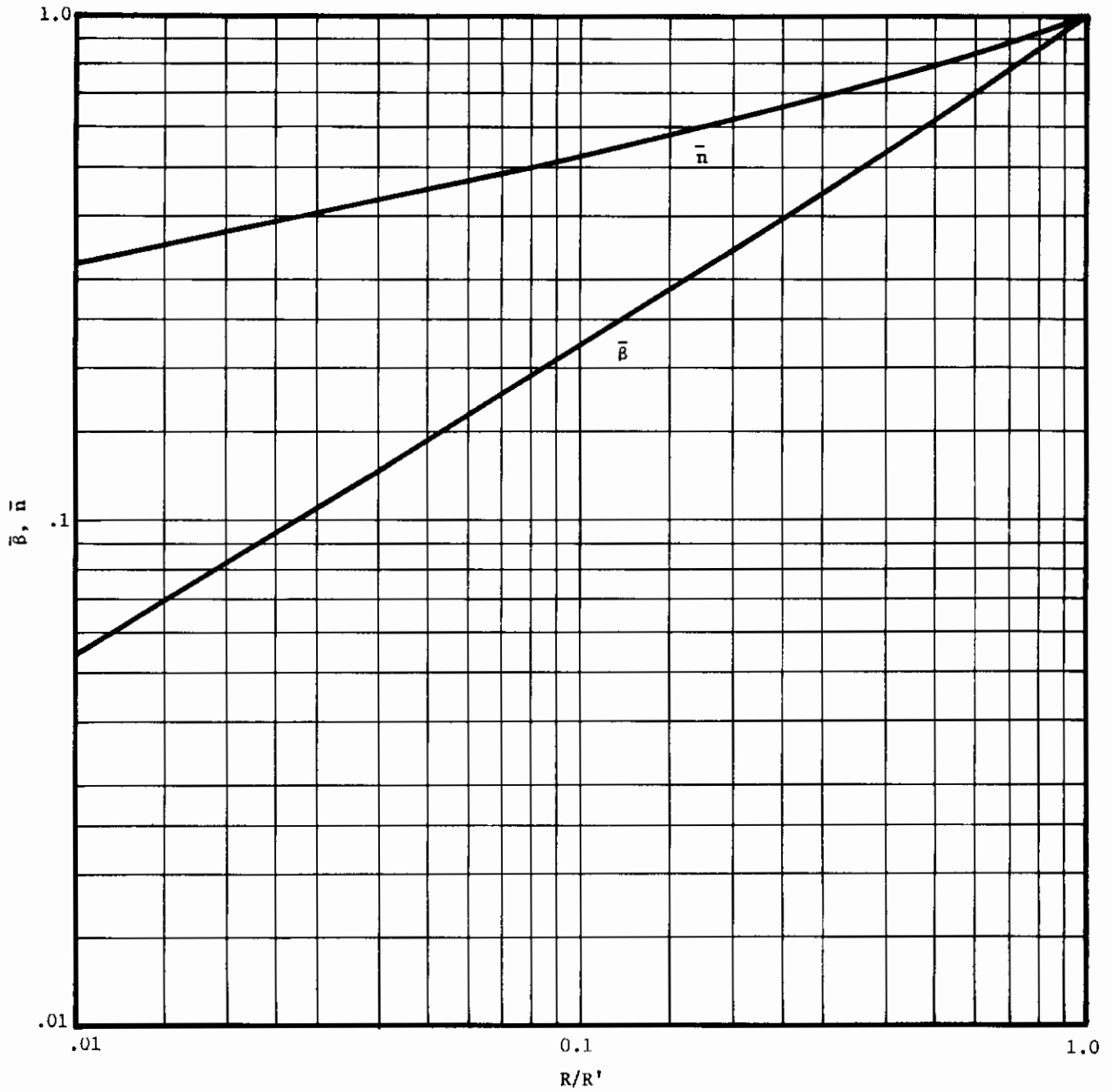


Fig. 93 Hertz Contact Parameters

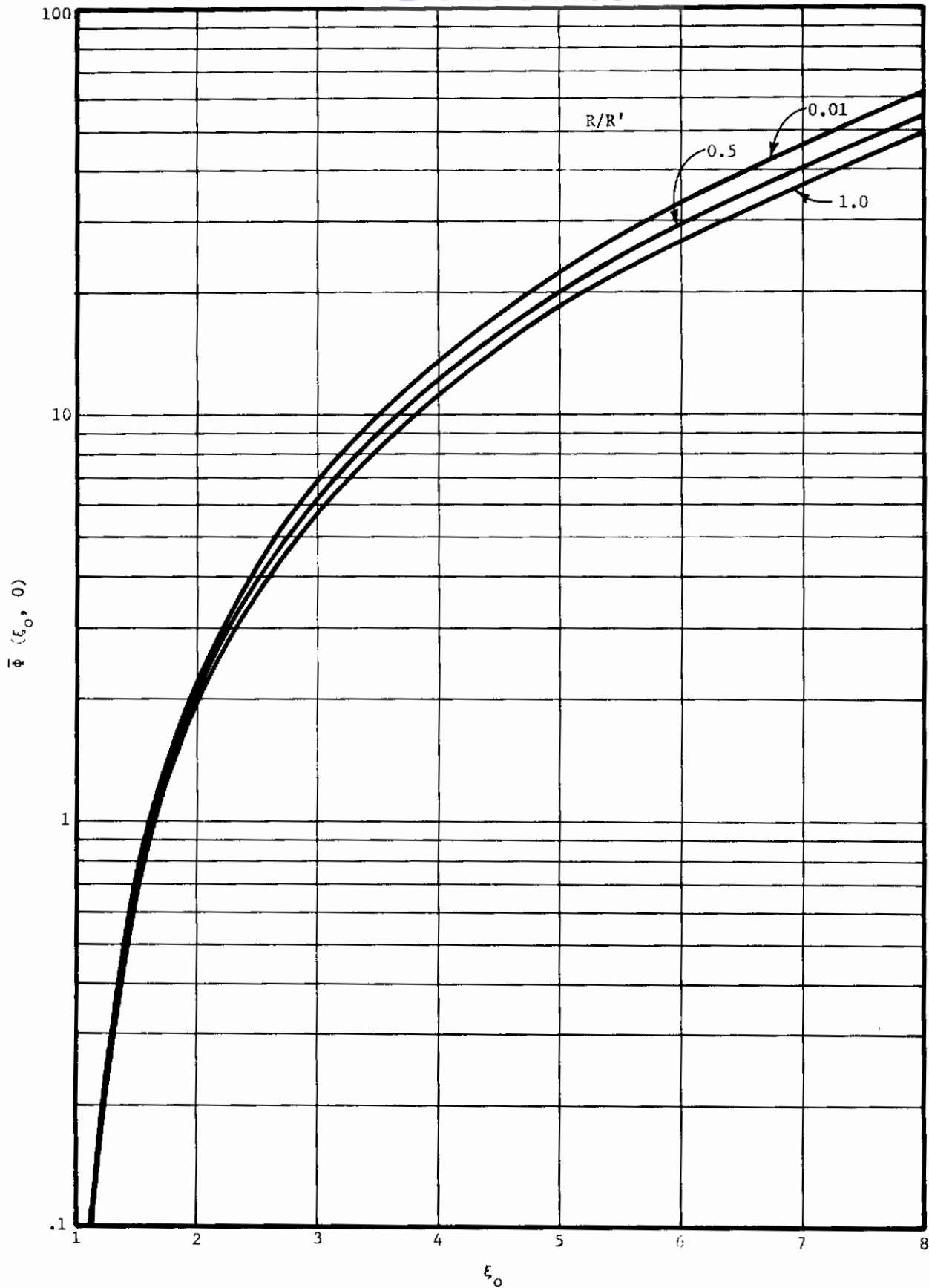


Fig. 94 Dimensionless Elastic Distortion Along Minor Axis of Contact

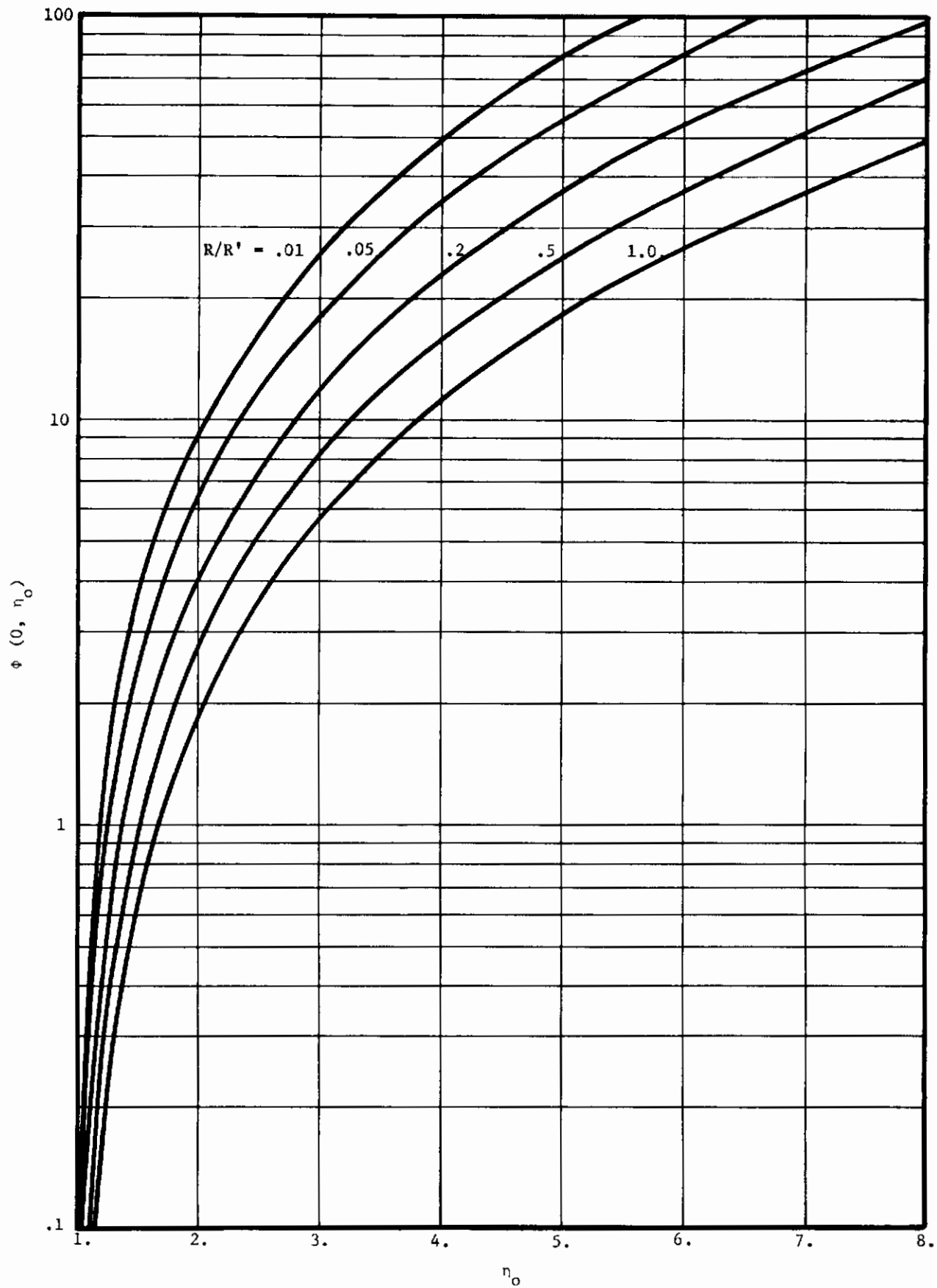


Fig. 95 Elastic Distortion Along Major Axis of Contact

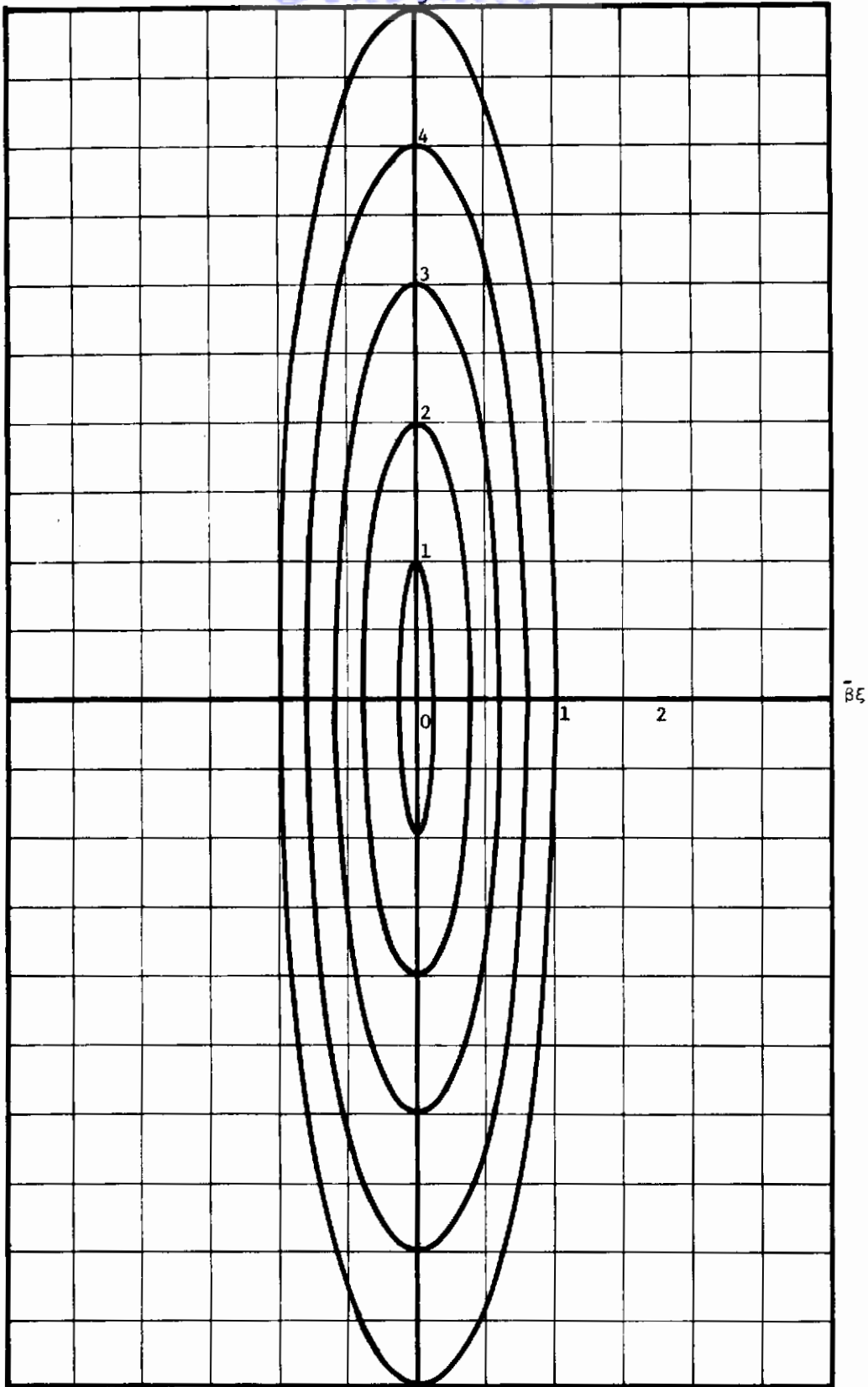


Fig. 96 Dimensionless Fringe Lines for $R/R' = 1/24$

Contrails

The maximum error for the test case under consideration ($R/R' = 1/24$) is about 6 percent and occurs when $\eta_0 = 1.2$. The elliptical and true fringe lines for this case are shown in Figure 24 appearing in Section III of this report.

This approximation will be used in the following section when calculating capacitance and will provide a considerable savings in computer costs with little error in accuracy.

Capacitance Calculations

In order to calculate capacitance it is necessary to obtain an effective area-to-displacement relationship ($\overline{A/h}$). If h is to be assumed constant on elliptical fringe lines, then ($\overline{A/h}$) may be calculated by dividing differential elliptical bands by the separation at the band and integrating over the entire space bounded by the discs. The elliptical bands under consideration are shown schematically in Figure III-6. They fall into two categories corresponding to whether the fringe line falls completely between the two discs as shown in Figure III-6a or is truncated by the end of the discs having axial half length, L , as shown in Figure III-6b.

The area, A , bounded by a line of constant separation approximated by the ellipse having semi-axes x_0, y_0 is given by

$$A = \pi x_0 y_0, \quad y_0 < L \quad (A3.11)$$

When these ellipses go beyond the edge of the disc having half thickness, L , then the area A bounded by the solid lines in Figure III-6b is given by

$$A = 2 x_0 y_0 \left[\frac{L}{y_0} \sqrt{1 - \left(\frac{L}{y_0}\right)^2} + \sin^{-1} \left(\frac{L}{y_0}\right) \right], \quad y_0 > L \quad (A3.12)$$

For any given value of R/R' and $\bar{\phi}$ one can determine $x_0 = b\xi_0$ within the use of Figure III-3 and $y_0 = a\eta_0$ within the use of Figure III-4, and the necessary crossplots may be obtained to provide x_0 as a function of y_0 which are presented in the dimensionless form of η_0 versus ξ_0 in Figure III-7.

If we adopt the Grubin assumption that the shape of the film thickness profile follows that of the exterior Hertz profile, then the EHD film thickness profile h may be expressed mathematically as

$$h = \begin{cases} h_1 & y_0 \leq a \\ h_1 + \frac{3W}{2E'a} \bar{\phi}(0, y_0/a), & y_0 > a \end{cases} \quad W \neq 0 \quad (A3.13)$$

together with the constraint that h is assumed constant on the fringe lines given by

$$\left(\frac{y}{y_0}\right)^2 + \left(\frac{x}{x_0}\right)^2 = 1 \quad (A3.14)$$

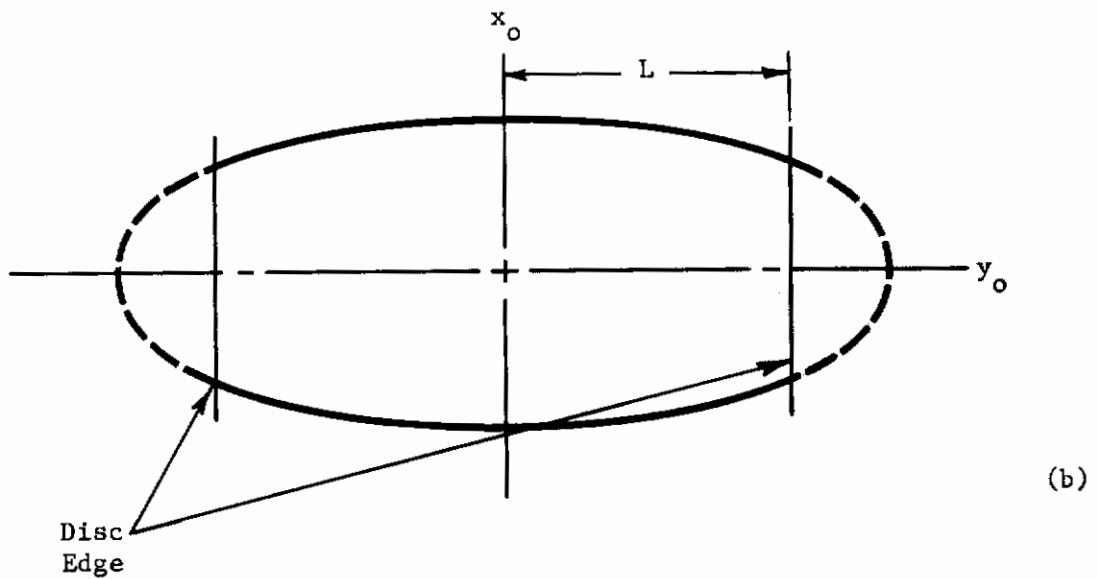
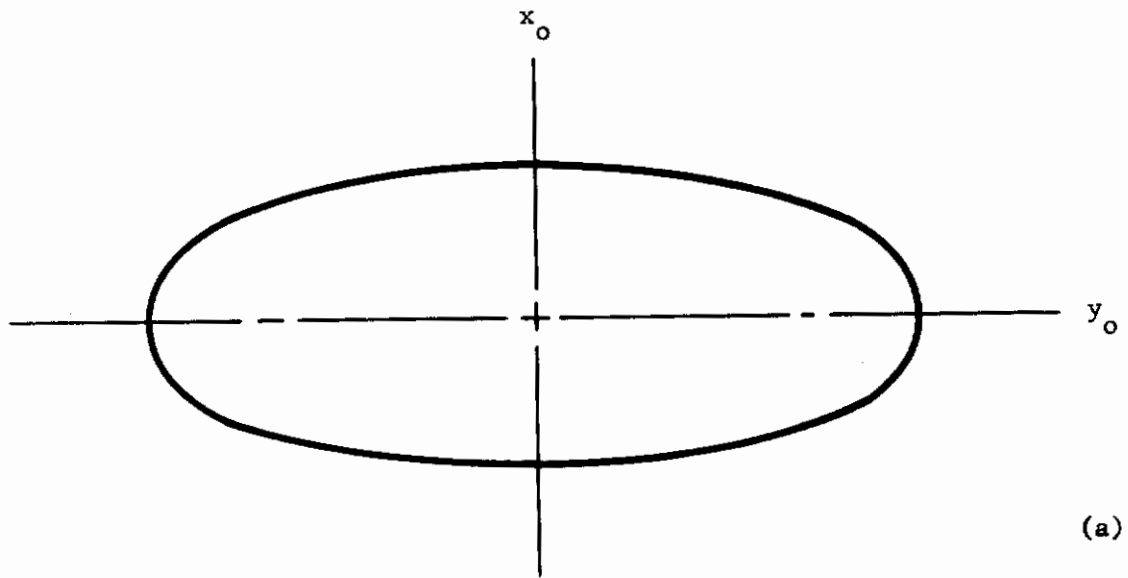


Fig. 97 Schematic of Elliptical Fringe Lines Used in Capacitance Calculations

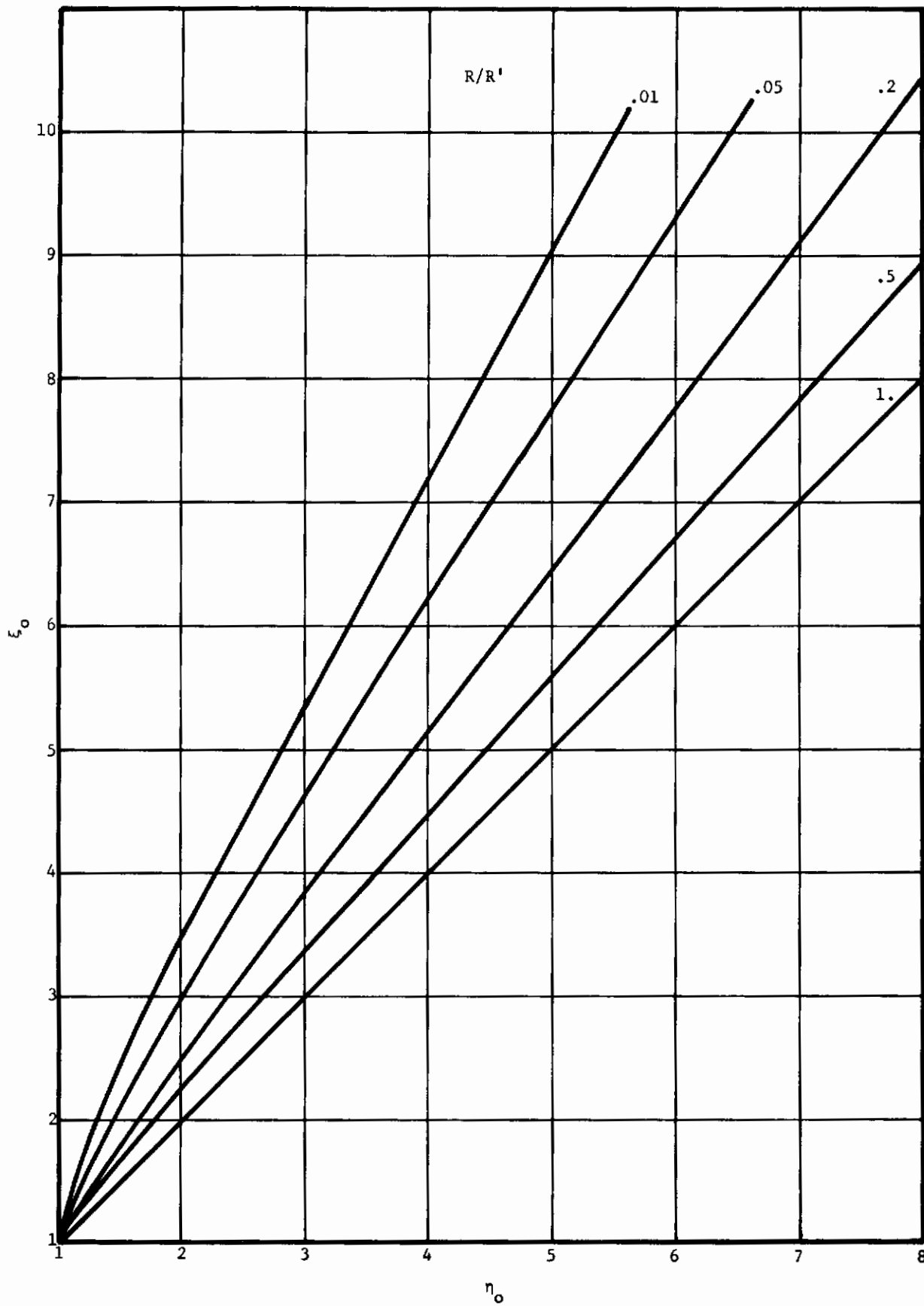


Fig. 98 The Relationship Between Major and Minor Axis for Fringe Lines

Contrails

The capacitance is thus calculated from an effective area-to-film ratio

$$\left(\frac{\bar{A}}{h}\right) = \int \frac{dA}{h} \quad (A3.15)$$

where h is given by Equation (A3.13).

If we consider x_o and $\bar{\Phi}$ to be functions of y_o , then we may write the complete expression for $\left(\frac{\bar{A}}{h}\right)$ as

$$\left(\frac{\bar{A}}{h}\right) = \frac{\pi ab}{h_1} + \int_{d_1}^{\infty} \frac{1}{h} \left(\frac{dA}{dy_o}\right) dy_o \quad (A3.16)$$

The indicated area derivative may be obtained by differentiation of Equations (A3.11) and (A3.12) and is given as

$$\frac{dA}{dy_o} = \begin{cases} \pi \left(x_o + y_o \frac{dx_o}{dy_o}\right) & , y_o < L \\ 2L \left(\frac{dx_o}{dy_o} - \frac{x_o}{y_o}\right) \sqrt{1 - \left(\frac{L}{y_o}\right)^2} + 2y_o \frac{dx_o}{dy_o} \sin^{-1} \left(\frac{L}{y_o}\right) & , y_o \geq L \end{cases} \quad (A3.17)$$

where $dx_o/dy_o = \bar{\beta} d_o/d\xi_o$ may be obtained by differentiation of Figure III-7.

When the discs are unloaded, Equations (A3.14) through (A3.17) remain the same; but the elastic distortion profile is replaced by the rigid body profile which may be expressed by mathematically replacing Equation (A3.13) with

$$h = h_1 + \frac{y_o^2}{2R^2} \quad , W = 0 \quad (A3.18)$$

where x_o is related to y_o by

$$x_o = \sqrt{R/R^2} y_o \quad , W = 0 \quad (A3.19)$$

It should be noted that a smooth transition does occur between lightly loaded and unloaded conditions.

Equation (A3.16) may be readily integrated numerically by Gaussian Quadrature to obtain capacitance computation in the form of $\left(\frac{\bar{A}}{h}\right)$ as functions of h_1 and W . The results of these computations are presented and described in the main text of this report.

APPENDIX IV

DISTORTION FACTOR DERIVATION FOR INTERFERENCE FRINGE SPACING IN ROLLING DIRECTION OF CONTACT ELLIPSE

The geometric arrangement depicted in Figure IV-1 shows an exaggerated example of how a fringe image observed to be at S' is offset from the actual position S in the contact area. The disc is cut from a cylinder with a center bore concentric to the outside diameter of the disc. Both inner and outer surfaces have been optically polished. The outside diameter has been chromium coated and provides a semi-transparent surface which produces interference patterns of the contact region gap.

Let S define the actual distance to any fringe in the rolling direction along a perpendicular line from the major axis of the contact ellipse. Let S' be the observed distance from the image plane to any fringe along the same perpendicular. For a fixed disc geometry and index of refraction, the distortion factor, f , between observed images and actual is

$$f_D = \frac{S'}{S} = f(r, R_1, n_G, \theta, L_1)$$

The microscope arrangement is such that $L_1 \gg R_1$ and for all fringing makes $\theta \leq 2^\circ$. The contact illuminating light can, therefore, be assumed as parallel to the axis line of the test disc.

Since the microscope is in air, Snell's Law states

$$\sin \theta = n_G \sin \tilde{\gamma} \quad (A4.1)$$

Small angle approximations provide that

$$\sin \tilde{\gamma} \approx \tan \tilde{\gamma} = \frac{\Delta S}{R_1 - r} \quad (A4.2)$$

$$\sin \theta \approx \theta = \frac{S'}{R_1} \quad (A4.3)$$

Also, from the diagram we note

$$\frac{S + \Delta S}{R_1} = \frac{S'}{r} \quad (A4.4)$$

Substituting Equations (A4.2) and (A4.3) into (A4.4) we get

$$\Delta S = \left(\frac{S'}{r}\right) \left(\frac{R_1 - r}{n_G}\right) \quad (A4.5)$$

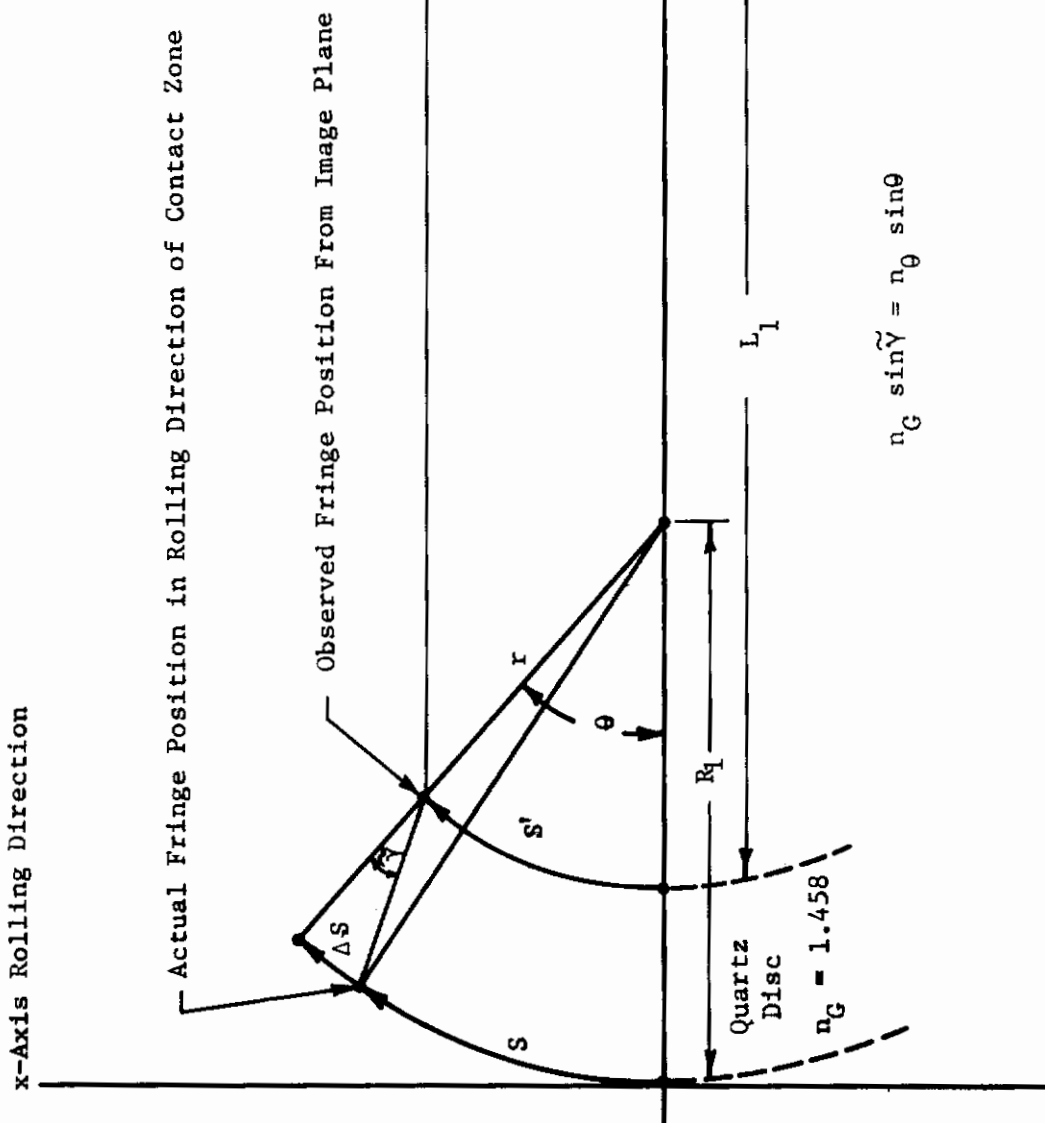


Fig. 99 Optical Distortion Off-Set Diagram

MEI-13470

Contrails

Evaluation of Equation (A4.4) with this value of ΔS results in

$$\frac{S + \left(\frac{S'}{r}\right) \left(\frac{R_1 - r}{n_G}\right)}{R_1} = \frac{S'}{r}$$

$$S = \frac{R_1}{r} S' - \left(\frac{R_1 - r}{r}\right) \frac{S'}{n_G}$$

$$\frac{S'}{S} + \frac{1}{\frac{R_1}{r} - \left(\frac{R_1 - r}{r}\right) \frac{1}{n_G}}$$

$$\frac{S'}{S} = \frac{rn_G}{R_1 n_G - (R_1 - r)} = \frac{rn_G}{R_1 (n_G - 1) + r}$$

$$\boxed{\frac{S'}{S} = \frac{n_G}{\frac{R_1}{r} (n_G - 1) + 1}}$$

(A4.6)

For the test setup evaluation yields

$$R_1 = 1.5 \text{ inches}$$

$$r = 1.00 \text{ inches}$$

$$n_G = 1.458$$

$$\therefore \frac{S'}{S} = .8641$$

In other words, the visually-observed fringe location will be .8641 times the actual location from the major axis line of the elliptical contact pattern.

Contrails

APPENDIX V
EQUIPMENT LIST

Capacitance Film Thickness Measurement

- MTI Rolling Disc Machine (described in detail in Reference 1)
- Wayne-Kerr autobalance precision bridge Model B331 MK11
- Two mercury-wetted rotating contacts
- One Mechanical Technology Incorporated differential tachometers (one side only for absolute speed output); Drawing No. 10D000068
- One Hewlett-Packard x-y recorder Model 7004A
- One Mitutoyo calibration tester micrometer Model (521-102)

Optical Film Thickness Measurement

- One Nikon microscope with 1X objective and 15X eyepiece lenses and colored filters
- Two Dell Optics cylindrical chromium-coated quartz discs per MTI Sketch No. SK-A-4211
- One Pentax 35mm camera with microscope mount
- One three-way directional microscope holder
- One 45-degree extension tube mirror holder
- One Honeywell 65C stroboscope
- Fotonic sensor
- Digital Monsanto counter

X-Ray Film Thickness Measurement

- Harshaw Chemical Company amplifier and pulse height discriminator Model N-301
- Harshaw Chemical Company regulated power supply Model N-401
- Harshaw Chemical Company linear count rate meter Model N-730
- One New England Nuclear Cd¹⁰⁹ source Serial No. D-111
- One Nuclear Associated Cd¹⁰⁹ calibration source Cat. No. 67-405A
- One Baird-Atomic X-ray safety survey meter Model 420
- Bendix safety pocket dosimeters Model 1200-MR
- One lead container MTI design Drawing No. 245-D-035

REFERENCES

1. Smith, R.L., Walowit, J.A., Gupta, P.K., and McGrew, J.M., "Research of Elastohydrodynamic Lubrication of High Speed Rolling-Sliding Contacts," Mechanical Technology Incorporated, Tech. Report # AFAPL-TR-71-54, prepared for Wright-Patterson Air Force Base, Ohio, (1971).
2. McGrew, J.M., Gu, A., Cheng, H.S., Murray, S.F., Elastohydrodynamic Lubrication - Preliminary Design Manual, Technical Report AFAPL-TR-70-27, Wright-Patterson Air Force Base, 1970.
3. Kannel, J.W., Bell, J.G., and Allen, C.M., A Study of the Influence of Lubricant on High-Speed Rolling-Contact Bearing Performance, Technical Report ASD-TR-61-643, Part III, Wright-Patterson Air Force, 1963.
4. Wilson, D.R., Bossert, A.J., "Exploratory Development on Advanced Fluids and Lubricants in Extreme Environments by Mechanical Characterization," Tech. Report AFML-TR-70-32, WPAFB, Ohio, 1971.
5. Kannel, J.W. and Walowit, J.A., "Simplified Analysis for Traction Between Rolling-Sliding Elastohydrodynamic Contacts," Vol. 93, Series F., No. 1, ASME, JOLT, 1971.
6. Crook, A.W., "The Lubrication of Rollers, II, Film Thickness with Relation to Viscosity and Speed," Phil. Trans. A 254; 223, 1961.
7. Hamilton, G.M., Moore, S.L., "Deformation and Pressure in an Elastohydrodynamic Contact," Proc. Roy. Soc. Lond. A, 322, 313-330 (1971).
8. Corson, D.R., and Lorrain, P., Introduction to Electromagnetic Fields and Waves, W.H. Freeman and Co., San Francisco, 1962.
9. Galvin, G.D., Naylor, H., and Wilson, A.R., Proc. Instn. Mech. Engrs. 178; 283, 1964.
10. Dowson, D. and Higginson, G.R., Elastohydrodynamic Lubrication, Pergamon Press, Oxford, 1966.
11. Cameron, A. and Gohar, R., "Theoretical and Experimental Studies of the Oil Film in Lubricated Point Contact," Proc. R. Soc., Series A, 1966.
12. Foord, C.A., Wedeven, L.D., Westlake, F.J., and Cameron, A., "Optical Elastohydrodynamics," Vol. 184, Part 1, Proceedings of the Mech. Eng., 1969-70.
13. Holden, J., "Multibeam Interferometry; Intensity Distribution in the Reflected System," Vol. 62, Part 7, Proceedings of the Physical Society, July 1949.

REFERENCES (Continued)

14. Andrews, C.L., Optics of the Electromagnetic Spectrum, Prentis-Hall, Inc., Englewood Cliffs, N.J., 1960.
15. Sibley, L.B., Bell, J.C., Orcutt, F.K. and Allen, C.M., A Study of the Influence of Lubricant Properties on the Performance of Aircraft Gas Turbine Engine Rolling-Contact Bearings, WADD Technical Report, 60-189, 1960.
16. Gupta, P.K. and Cook, N.H., "Statistical Analysis of Mechanical Interaction of Rough Surfaces," J. Lub. Tech., ASME Trans. 94F, 19-25, 1972.
17. Gupta, P.K. and Cook, N.H., "Junction Deformation Models for Asperities in Sliding Interaction," Wear 20, 73-87, 1972.
18. Nayak, P.R., "Random Process Model of Rough Surfaces," J. Lub. Tech., ASME Trans., 93F, 398-407, 1971.
19. Longuet-Higgins, M.S., "The Statistical Analysis of a Random Moving Surface," Philosophical Transactions of the Royal Society, Vol. 249, Series A, 1957, pp. 321-387.
20. Longuet-Higgins, M.S., "Statistical Properties of an Isotropic Random Surface," Philosophical Transactions of the Royal Society, Vol. 250, Series A, pp. 157-174, 1957.

Contrails

DOCUMENT CONTROL DATA - R & D

(Security classification of title, body of abstract and indexing annotation must be entered when the overall report is classified)

1. ORIGINATING ACTIVITY (Corporate author) Mechanical Technology Incorporated 968 Albany-Shaker Road Latham, New York 12110		2a. REPORT SECURITY CLASSIFICATION Unclassified	
		2b. GROUP N/A	
3. REPORT TITLE RESEARCH ON ELASTOHYDRODYNAMIC LUBRICATION ON HIGH-SPEED ROLLING-SLIDING CONTACTS			
4. DESCRIPTIVE NOTES (Type of report and inclusive dates) Final Report February 1971 - February 1972			
5. AUTHOR(S) (First name, middle initial, last name) Richard L. Smith Pradeep K. Gupta Jed A. Walowit John M. McGrew			
6. REPORT DATE July 1972	7a. TOTAL NO. OF PAGES 150	7b. NO. OF REFS 20	
8a. CONTRACT OR GRANT NO. F33615-69-C-1305	9a. ORIGINATOR'S REPORT NUMBER(S) MTI 71-TR-41		
b. PROJECT NO. 3048			
c. Task No. 30806	9b. OTHER REPORT NO(S) (Any other numbers that may be assigned this report) AFAPL-TR-72-56		
d.			
10. DISTRIBUTION STATEMENT Approved for public release; distribution unlimited			
11. SUPPLEMENTARY NOTES		12. SPONSORING MILITARY ACTIVITY Air Force Aero Propulsion Laboratory Fuel, Lubrication & Hazards Division Wright-Patterson AFB, Ohio 45433	
13. ABSTRACT The rolling disc apparatus that was built during Phase II of this research program has been used to obtain traction measurements for a MIL-L-7808 oil. A full matrix of data covering a range of loads, speeds, and temperatures are presented along with analytical correlation which reasonably describes the data over these parameters. Attempts have been made to measure film thickness with optical, capacitance, and X-ray measuring techniques. Optical measurements appear to be in good agreement with iso-thermal theory. Capacitance measurements obtained at higher loads and speeds indicate more significant load variations than existing theory would predict. The partial elastohydrodynamic regime has been studied analytically and experimentally. Electrical continuity and resistance data have been obtained and comparisons between measured electrical resistance and predictions obtained with the asperity interactions analysis put forth in Task 2 have been obtained.			

14 KEY WORDS	LINK A		LINK B		LINK C	
	ROLE	WT	ROLE	WT	ROLE	WT
Elastohydrodynamic Lubrication Tractions Film Thickness Rolling Disc Machine Asperity Interactions Polyphenyl Ether Partial Elastohydrodynamics Optical Viscosity Electrical Resistance Elliptical Contact Capacitance X-Ray MIL-L-7808						